MATERIALS FOR ADAPTIVE STRUCTURAL ACOUSTIC CONTROLS

Period February 1, 1993 to January 31, 1994

Annual Report

VOLUME III

OFFICE OF NAVAL RESEARCH
Contract No. N00014-92-J-1510

APPROVED FOR PUBLIC RELEASE -- DISTRIBUTION UNLIMITED

Reproduction in whole or in part is permitted for any purpose
of the United States Government

94-14609

L. E. Cross

PENNSTATE

THE MATERIALS RESEARCH LABORATORY
UNIVERSITY PARK, PA

94 5 16 069

REPORT DOCUMENTATION PAGE

1. AGENCY USE ONLY (Leave blank)	2. REPORT DATE 4/11/94	3. REPORT TYPE AND DATES COVERED ANNUAL REPORT 02/01/93 TO 01/31/94

4. TITLE AND SUBTITLE

MATERIALS FOR ADAPTIVE STRUCTURAL ACOUSTIC CONTROL

5. FUNDING NUMBERS

6. AUTHOR(S)

L. ERIC CROSS

7. PERFORMING ORGANIZATION NAME(S) AND ADDRESS(ES)

MATERIALS RESEARCH LABORATORY
THE PENNSYLVANIA STATE UNIVERSITY
UNIVERSITY PARK, PA 16802

8. PERFORMING ORGANIZATION REPORT NUMBER

9. SPONSORING/MONITORING AGENCY NAME(S) AND ADDRESS(ES)

OFFICE OF NAVAL RESEARCH   GERALD T. SMITH
CODE 1513:NRJ   OFFICE NAVAL RESEARCH RES. REP
800 NORTH QUINCY STREET   536 SOUTH CLARK STREET, RM 286
ARLINGTON, VA 22217   CHICAGO, ILLINOIS 60606-1588

10. SPONSORING/MONITORING AGENCY REPORT NUMBER

11. SUPPLEMENTARY NOTES

12a. DISTRIBUTION/AVAILABILITY STATEMENT

12b. DISTRIBUTION CODE

13. ABSTRACT (Maximum 200 words)

SEE FOLLOWING PAGE

Accesion For

NTIS CRA&I	☒
DTIC TAB	☐
Unannounced	☐
Justification	

By _____
Distribution /

Availability Codes

Dist	Avail and / or Special

A-1

14. SUBJECT TERMS

15. NUMBER OF PAGES

16. PRICE CODE

17. SECURITY CLASSIFICATION OF REPORT	18. SECURITY CLASSIFICATION OF THIS PAGE	19. SECURITY CLASSIFICATION OF ABSTRACT	20. LIMITATION OF ABSTRACT

ABSTRACT

The research goals of this ONR sponsored University Research Initiative entitled "Materials for Adaptive Structural Acoustics Control" relate directly to the sensing and actuating material which must be integrated to function in adaptive control of acoustic structures. This report documents work in the second year of the program and for convenience the activities are grouped under the headings General Summary Papers, Materials Studies, Composite Sensors, Actuator Studies, Integration Issues, Processing Studies, and Thin Film Ferroelectrics.

The general papers cover a new comprehensive description of ferroelectric ceramics and their applications, analysis of high temperature piezoelectric sensors and the possible application of nonlinearity in enhancing the "smartness" of ceramics and composites. Scale effects on ferroics are of increasing interest and the manner in which nano-scale polar regions control the properties of relaxor ferroelectrics is again emphasized.

For material studies the detailed examination of the evolution of diffuse, then relaxor behavior in lanthanum modified lead titanate has been completed. Interest in the soft PZTs, relaxor and phase switching materials continues, with a new thrust developing towards a more complete description of domain walls and morphotropic phase boundaries in perovskites. Materials issues in the wear out and fatigue effects in polarization switching systems have been subjected to detailed evaluation and the precautions necessary to fabricate long lasting materials which will stand 10^9 switches without any fatigue are delineated.

Sensor studies have continued to focus on flextensional composites and have demonstrated both the very high hydrostatic sensitivity and the amplified actuation response of this configuration. Integration of sensors with the "moonie" actuators has been accomplished in individual cells. Actuator studies cover the gamut from highly reproducible micro positioning using electrostrictive compositions to high strain polarization switching shape memory ceramics capable of driving a latching relay device. Studies of the destruct mechanisms in practical MLA systems complement the earlier materials work and show the importance of internal electrodes and consequent stress concentrations for crack initiation. Integration studies have focused upon more detailed evaluation of 1:3, 2:2 and tubular 1:3 composites and upon the influence of the polymer characteristic and of face plates and edge guards upon sensing and actuation capabilities. In processing, the interest in dielectrophoretic forming of composites is continuing and assembly of interesting 1:3 composites is demonstrated. Guidelines for the transducer application of electrostrictive materials have been formulated and a useful classification scheme proposed. In fiber PZTs techniques for fabricating thin (30 μ) fibers are demonstrated, the first successful technique for poling fibers is described and it is shown that properly poled fibers have electro-elastic characteristics similar to bulk material. Film papers are selected to reflect the transducer capabilities of lead titanate and of phase switching lead zirconate titanate stannate antiferroelectric compositions.

MATERIALS FOR ADAPTIVE STRUCTURAL ACOUSTIC CONTROLS

Period February 1, 1993 to January 31, 1994

Annual Report

VOLUME III

OFFICE OF NAVAL RESEARCH
Contract No. N00014-92-J-1510

APPROVED FOR PUBLIC RELEASE -- DISTRIBUTION UNLIMITED

Reproduction in whole or in part is permitted for any purpose
of the United States Government

L. E. Cross

PENNSTATE

THE MATERIALS RESEARCH LABORATORY
UNIVERSITY PARK, PA

TABLE OF CONTENTS

APPENDICES

General Summary of Papers

1. Turner, R. C. , P. A. Fuierer, R. E. Newnham, and T. R. Materials for High Temperature Acoustic and Vibration Sensors: A Review. Applied Acoustics 41:1-26 (1993).

2. Uchino, K. Ferroelectric Ceramics. Materials Science and Technology, Edited by R.W. Cahn, P. Haasen, E.J. Kramer, Vol. I, VCH 1994.

3. Newnham, R. E. Smart, Very Smart and Intelligent Materials, MRS Bulletin XVIII(4), 24-26 (April 1993).

General Summary of Papers (continued)

4. Newnham, R. E. Size Effects and Nonlinear Phenomena in Ferroic Ceramics. 3rd European Ceramic Society Conference, Madrid (1993).

5. Cross, L. E. Relaxor Ferroelectrics: Useful Electron Nanocomposite Structures, Proc. IUMRS, Ikabakura, Tokyo (September 1993).

Materials Studies

6. Rossetti, G. A., Jr., W. Cao, and C. A. Randall. Microstructural Characterization and Diffuse Phase Transition Behavior of Lanthanum Modified Lead Titanate. Ferroelectrics: Proceedings of IMF8, Gaithersburg, Maryland (August 1993).

7. Cao, W. and L. E. Cross. Distribution Function of Coexisting Phases in a Complete Solid Solution System. J. Appl. Phys. 73(7), 3250 (1993).

8. Cao, W. Polarization Gradient Coefficients and the Dispersion Surface of the Soft Mode in Perovskite Ferroelectrics. J. Phys. Soc. Jpn. 63, 827 (1994).

9. Cao, W. and L. E. Cross. Nonlinear and Nonlocal Continuum Theory on Domain Walls in Ferroelectrics. Ferroelectrics: Proceedings of IMF8, Gaithersburg, Maryland (August 1993).

10. Cao, W. and C. Randall. Theory on the Fringe Patterns in the Study of Ferroelectric Domain Walls Using Electron Holograpy. Solid State Comm. 86, 435-439 (1993).

11. Zhang, Q. M., H. Wang, N. Kim, and L. E. Cross. Direct Evaluation of Domain Walls and Intrinsic Contributions to the Dielectric and Piezoelectric Constants and Their Temperature Dependence in Lead Zirconate Titanate Ceramics. J. Appl. Phys. 75 (1), 454 (1994).

12. Subbarao, E. C., V. Srikanth, W. Cao, and L. E. Cross. Domain Switching and Microcracking during Poling of Lead Zirconate Titanate Ceramics. Ferroelectrics 145, 271-281 (1993).

13. Li, S., W. Cao, R. E. Newnham, and L. E. Cross. Electromechanical Nonlinearity of Ferroelectric Ceramic and Related non 180° Domain Wall Motion. Ferroelectrics 139, 25-49 (1993).

14. Jiang, Q., W. Cao, and L. E. Cross. Electrical Fatigue in Lead Zirconate Titanate Ceramics. J. Am. Ceram. Soc. 77(1), 211-215 (1994).

15. Jiang, Q., E. C. Subbarao, and L. E. Cross. Grain Size Dependence of Electrical Fatigue Behavior in Hot Pressed PLZT Ferroelectric Ceramics. (Submitted to Acta. Met.)

16. Jiang, Q., E. C. Subbarao, and L. E. Cross. Effects of Composition and Temperature on electrical Fatigue of La Doped Lead Zirconate Titanate Ceramics. J. Appl. Phys. (in press).

17. Jiang, Q. and L. E. Cross. Effect of Porosity on Electrical Fatigue Behavior in PLZT and PZT Ceramics. J. Mat. Sci. 28, 4536-4543 (1993).

Materials Studies (continued)

18. Jiang, Q., E. C. Subbarao, and L. E. Cross. Effects of Electrodes and Electroding Methods on Fatigue Behavior in Ferroelectric Materials. Ferroelectrics: Proceedings of IMF8, Gaithersburg, Maryland (August 1993).

19. Jiang, Q., E. C. Subbarao, and L. E. Cross. Fatigue in PLZT: Acoustic Emission as a Discriminator Between Microcracking and Domain Switching. Ferroelectrics: Proceedings of IMF8, Gaithersburg, Maryland (August 1993).

20. Jiang, Q., E. C. Subbarao, and L. E. Cross. Field Induced Stress Concentration and Electrical Fatigue in Ferroelectric Ceramics. IEEE Trans. on Ultrasonic Ferroelectrics and Frequency Control (submitted).

21. Jiang, Q., E. C. Subbarao, and L. E. Cross. Dielectric Properties of Single Grain in PLZT Ferroelectric Ceramics. Ferroelectric Letters (in press).

22. Li, S., A. S. Bhalla, R. E. Newnham, and L. E. Cross. Quantitative Evaluation of Extrinsic Contribution to Piezoelectric Constant $d33$ in Ferroelectric PZT Ceramics. Materials Letters 17, 21-26 (1993).

23. Wang, H., Q. Zhang, and L. E. Cross. A High Sensitivity Phase Sensitive $d33$ Meter for Complex Piezoelectric Constant Measurement. Jpn. J. Appl. Phys. 32(Pt. 2; No. 9A), L1281-83 (1993).

Composite Sensors

24. Newnham, R. E., Q. C. Xu, and S. Yoshikawa. Metal-Electroactive Ceramic Composite Actuator. U.S. Patent# 5,276, 657.

25. Onitsuka, K., A. Dogan, J. A. Tressler, Q. C. Xu, S. Yoshikawa, and R. E. Newnham. Metal-Ceramic Composite Transducer–The Moonie. Ferroelectrics: IMF8, Gaithersburg, Maryland (August 1993).

26. Tressler, J. F., Q. C. Xu, S. Yoshikawa, K. Uchino, and R. E. Newnham. Composite Flextensional Transducer for Sensing and Actuating. Ferroelectrics: IMF8, Gaithersburg, Maryland (August 1993).

27. Newnham, R. E., A. Dogan, Q. C. Xu, K. Onitsuka, J. Tressler, and S. Yoshikawa. Flextensional "Moonie" Actuators. IEEE 1993 Ultrasonics Symp. Proc., Baltimore, Maryalnd; Vol. 2, pp. 509-514 (1993).

28. Harshe, G., J. P. Dougherty, and R. E. Newnham. Theoretical Modeling of Multilayer Magnetoelectric Composites. Int. J. of Appl. Mag. in Mtls. 4, 145-159 (1993).

29. Newnham, R. E. and G. R. Ruschau. Electromechanical Properties of Smart Materials. J. Intelligent Mtls. Systems and Structures 4, 289 (1993).

30. Onitsuka, K., A. Dogan, Q. Xu, S. Yoskikawa, and R. E. Newnham. Design Optimization for Metal-Ceramic Composite Actuator, "Moonie." Ferroelectrics: IMF8, Gaithersburg, Maryland (August 1993).

Actuator Studies

31. Uchino, K. Relaxor Ferroelectric Devices. Ferroelectrics: Proceedings IMF8, Gaithersburg, Maryland (August 1993).

32. Uchino, K. Recent Development of Piezoelectric Actuators for Adaptive Structures. 3rd International Conference on Adaptive Structures (1991).

33. Furuta, A. and K. Uchino. Dynamic Observation of Crack Propagation in Piezoelectric Multilayer Actuators. J. Am. Ceram. Soc. 76(6), 1615 (1993).

34. Uchino, K. Ceramic Actuators Principles and Applications. MRS Bull. (April 1993).

35. Uchino, K. Applications of Piezoelectric Ceramics in Smart Actuator Systems. ADPA/AIAA/ASME/SPIE Cont. on Active Mtls. (1992).

36. Uchino, K. and A. Furuta. Destruction Mechanism of Multilayer Ceramic Actuators. ISAF92, South Carlonia (1992).

37. Furuta, A. , K. Y. Oh, and K. Uchino. Shape Memory Ceramics and Their Application to Latching Relays. Sensors and Materials 3, 205 (1992).

38. Uchino, K. Piezoelectric Ceramics in Smart Actuators Systems. 1st European Conference on Smart Structures and Materials, Glasgow (1992).

39. Zhang, Q. M., J. Chen, and L. E. Cross. Electric Field Induced Piezoelectric Response in Ferroelectric Materials Near the Paraelectric-Ferroelectric Transition. Proceedings Ultrasonics Symposium, pp. 525 (1993).

Integration Issues

40. Zhang, Q. M., W. Cao, J. Zhao, and L. E. Cross. Piezoelectric Performance of Piezoelectric Polymer Composites with 2-2 Connectivity–A Combined Theoretical and Experimental Study. IEEE Transactions UFFC (accepted) (1993).

41. Chen, J., Q. M. Zhang, L. E. Cross, and C. M. Trottier. Modeling and Design of 1-3 Tubular Composites for Smart Transducer Applications. 1994 Proceedings International Conference on Intelligent Materials (submitted) (1994).

42. Wang, H., Zhang, and L. E. Cross. Piezoelectric Relaxation of P(VDF-TrFE) Copolymers. Ferroelectrics: IMF8, Gaithersburg, Maryland (August 1993).

43. Zhao, J., Q. M. Zhang, and W. Cao. Effects of Face Plates and Edge Strips on Hydrostatic Piezoelectric in 1-3 Composites. J. Mat. Sci. (submitted).

Processing Studies

44. Yoshikawa, S. and T. R. Shrout. Multilayer Piezoelectric Actuator Structures and Reliability. Proceedings Structural Dynamics, Materials Conference AIAA/ASM Adaptive Structures Forum, Pt. 6, 3581-3586 (1993).

45. Bowen, C. P., T. R. Shrout, R. E. Newnham, and C. Randall. Intelligent Processing of Composite Materials. J. Intelligent and Smart Materials (submitted) (1993).

46. Shrout, T. R., C. A. Randall, B. P. Brodeur, and S. J. Jang. Classification of Electrostrictive Based Materials for Transducers. U.S. Japan Meeting on Dielectrics, Lahaina, Hawaii (November 1994).

47. Yoshikawa, S., U. Selvaraj, P. Moses, Q. Jiang, and T. R. Shrout. Pb(ZrTi)O3 [PZT] Fibers–Fabrication and Properties. J. of Intelligent Material Systems and Structures (submitted) (1994).

48. Miller, D., C. A. Randall, A. S. Bhalla, R. E. Newnham, and J. Adair. Electrorheological Properties of BaTiO3 Suspensions. Ferroelectric Letters 15, 141-151 (1993).

49. Randall, C. A., C. P. Bowen, T. R. Shrout, A. S. Bhalla, and R. E. Newnham. Dielectrophoresis: A Means to Assemble Novel Electroceramic Composite Materials. Proceedings of Electrorheological Fluids. Feldrick, Austria (1993).

Thin Film Ferroelectrics

50. Udayakumar, K. R., S. B. Krupanidhi, K. Kushida, and L. E. Cross. Origina of Orientation in Sol-Gel-Derived Lead Titanate Films. J. Am. Ceram. Soc. 76, 1345 (1993).

51. Brooks, K. G., J. Chen, K. R. Udayakumar, and L. E. Cross. Electric Field Forced Phase Switching in La Modified Lead Zirconate Titanate Stannate Films. J. Appl. Phys. 75, 1399 (1994).

52. Sheen, J., R. Guo, A. S. Bhalla, and L. E. Cross. Measurements of Dielectric Constant and Quality Factor of Ba(Mg1/3Ta2/3) O3 at X Band Frequencies. Ferroelectric Letters 16, 33 (1993).

Graduating Students in the Program

53. Rossetti, George A., Jr. PhD Thesis (Abstract), Solid State Science. Structural and Thermodynamic Investigation of the Ferroelectric Phase Transition in Lanthona-Substitued Lead Titanate. May 1993.

54. Chen, Jaiyu. PhD Thesis (Abstract), Electrical Engineering. Electrical and Electromechanical Properties of Ferroelectric Thin Films for Microelectromechanical Applications. August 1993.

55. Alberta, Edward. MS Thesis (Abstract), Solid State Science. The Dielectric, Piezoelectric and Pyroelectric Properties of Lead Zirconate-Lead Zinc Niobate-Lead Titanate Ceramics. October 1993.

COMPOSITE SENSORS
(continued)

APPENDIX   26

COMPOSITE FLEXTENSIONAL TRANSDUCERS FOR SENSING AND ACTUATING

JAMES F. TRESSLER, Q.C.XU, SHOKO YOSHIKAWA, KENJI UCHINO, and ROBERT E. NEWNHAM
The Pennsylvania State University, Intercollege Materials Research Laboratory, University Park, PA 16802 USA

Abstract A ceramic-metal composite flextensional transducer has been developed which integrates both sensing and actuating functions into a single device for the purpose of suppressing low-level vibration noise. This prototype sensor/actuator composite is capable of detecting and completely suppressing in real time, small (<1µm) vibration displacements with low (<100gf) forces. The dynamic frequency range of the device spans from 100Hz to at least 2500Hz. The actuator portion of the composite consists of a standard (11mm diameter, 3mm thick) "moonie" transducer. The sensor is a separate piece of piezoceramic, 0.1mm thick, imbedded within the surface of the actuator. Vibrations are detected by the sensor; then, via a feedback loop, the vibration noise is suppressed by the actuator. Potential applications for this device include active optical systems, rotor suspension systems, and other low-level vibration suppression devices.

INTRODUCTION

The elimination of vibration noise has achieved considerable attention in recent years, both on the macroscopic (smart shock absorbers) and microscopic (active optic systems) scale. The fundamental parameters that must be considered for a vibration control device are its response time, as well as the force and vibration displacement amplitude that it must be able to cancel. Once these criteria have been met for a particular application, it then becomes advantageous to reduce costs by miniaturizing and/or reducing the power delivered to the device.

Multilayer piezoelectric actuators have seen extensive use as vibration control

devices because of their large generative forces, high precision, and quick response time. Unfortunately, large driving voltages are necessary to achieve displacements of several microns. By sandwiching a multilayer actuator between two moonie endcaps, the displacement is amplified,[1,2] thereby making it possible to reduce the driving voltage[3] or reduce the size of the device. The response time is only slightly slower.

Using this information, it became our objective to fabricate a vibration control device based on the moonie actuator. In order to produce the most efficient device, the sensing and actuating functions were integrated into a single composite. The design is shown in Figure 1. The actuator portion of the prototype device consists of the standard moonie, 11mm in diameter and 3mm thick. The sensor is a separate piece of piezoceramic (PZT), 0.1mm thick, which was imbedded within the upper endcap. The sensor detects sinusoidal vibrations, as shown in the Figure 1, then via a feedback loop, sends a signal of appropriate amplitude and phase back to the actuator so that the latter effectively cancels the external vibration.
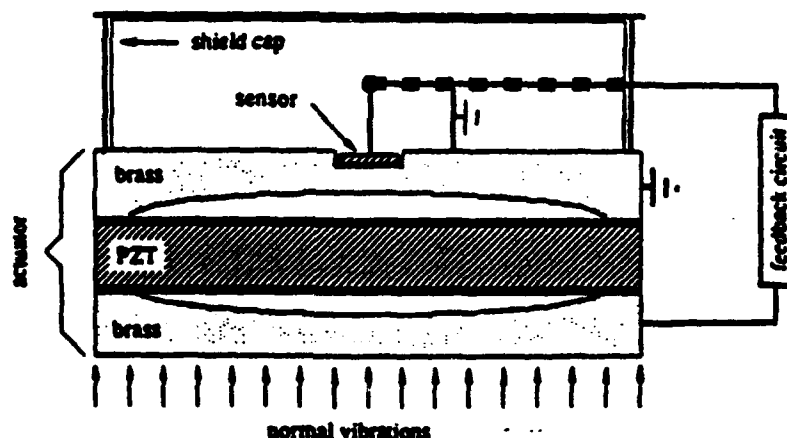

FIGURE 1   Integrated sensor and actuator

VIBRATION CONTOL RESULTS

The ability of the moonie actuator to actively control external vibrations was determined by adhering the device atop a vibrating multilayer actuator of known frequency and displacement amplitude. The dynamic frequency range of the sensor was found by applying a sinusoidal AC field to the moonie actuator and observing the resulting vibration

signal on an oscilloscope. The response remained relatively flat between 100 and 6000Hz.

The data in Figure 2 show that the integrated sensor/actuator device can indeed be used to cancel external vibrations. The horizontal axis shows the 1kHz electric field applied to the moonie actuator when the field applied (at 1kHz) to the multilayer vibration source was either 75V/mm, 125V/mm, or 250V/mm. The vertical axis shows the corresponding net vibration signal amplitude, which comes from the sum of the multilayer and moonie vibrations. The results show that whenever the applied field and phase shift into the moonie are adjusted to the appropriate magnitude, the net vibration signal goes to zero, indicating that the integrated sensor/actuator device has effectively cancelled the external vibration. The reason the phase shift is 1° rather than the expected 180° was due to the polarization direction of the sensor being opposite that of the actuator.
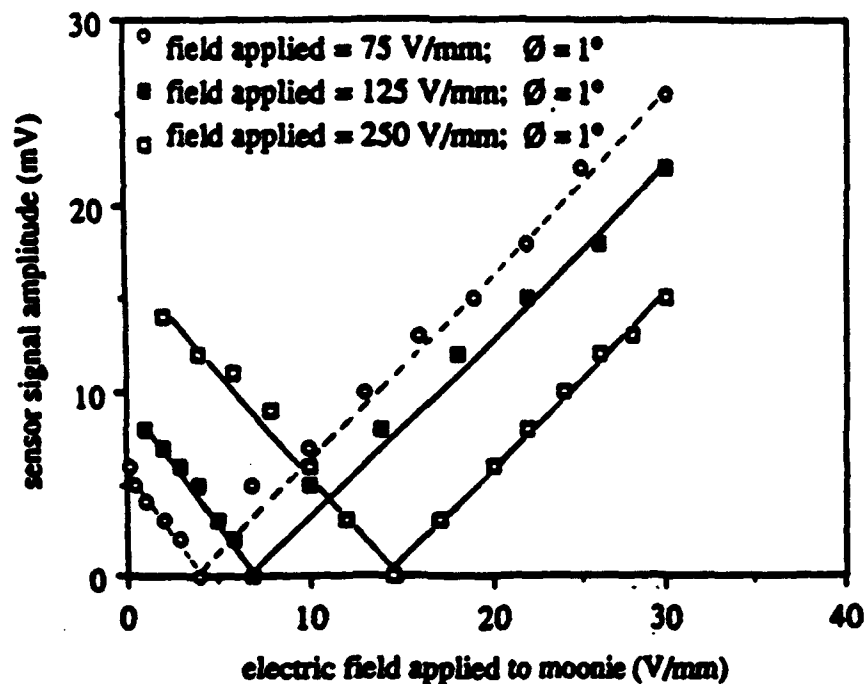

FIGURE 2   Net sensor signal response as a function of electric field applied to the multilayer vibration source at a frequency of 1kHz

Figure 3 shows how the net vibration signal amplitude changes with phase shift when the applied field to the multilayer is 125V/mm and the field applied to the moonie is 7.05V/mm. These data show that when the phase shift between the two fields is slightly greater than 0°, the moonie and multilayer vibrations have the same displacement amplitude
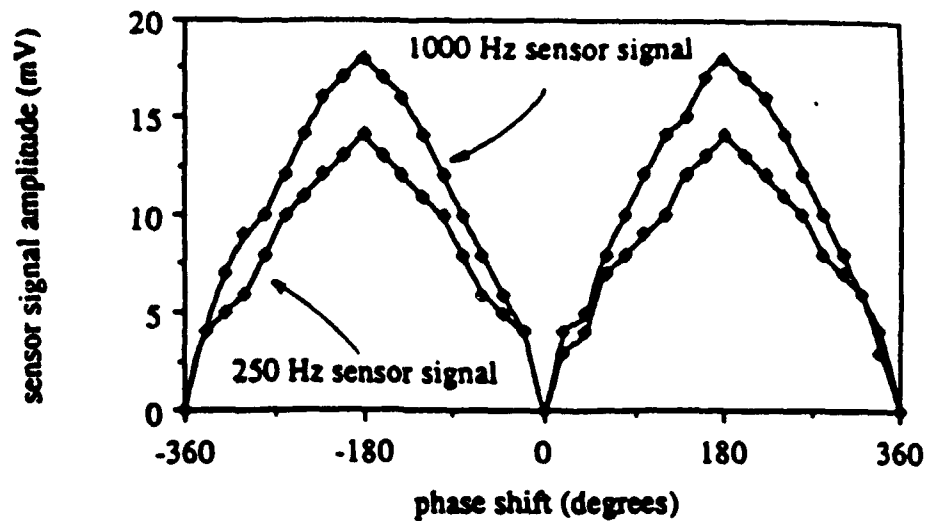
FIGURE 3 Sensor signal response as a function of phase shift of the electric field applied to the moonie

and are exactly 180° out-of-phase, resulting in no net vibration signal.

Figure 4 shows the applied electric field and phase shift (feedback signal) needed to be supplied to the moonie actuator in order to cancel the external vibration over the shown frequency range when the field applied to the multilayer was 75V/mm. Figure 5 superimposes the subsequent sensor signal amplitude detected from the multilayer vibration source both with and without the feedback signal activated. These data show that when the feedback field given in Figure 4 is activated, the multilayer vibration signal can be completely suppressed over this entire frequency range. The reason 2500Hz was chosen as the cut-off frequency was the inability to prevent "ultrasonic floating" (which arose from incomplete coupling) by the moonie atop the multilayer at higher frequencies.

The minimum and maximum electric fields into the moonie actuator for which the sensor signal remained sinusoidal were 200mV/mm and 370V/mm, respectively, and were independent of frequency. These fields thus define the dynamic displacememt range that the sensor is capable of detecting as being between 0.35nm and 0.65μm (as calculated by finite element analysis).[2]

The external force that the integrated sensor/actuator could detect was estimated from the output voltage of the sensor (Equation 1). Since the sensor was bonded to the actuator, it was assumed that g_{31} and g_{32} provided the major contribution to the output voltage. Also, since the sensor was square in shape, it was further assumed that $g_{31} = g_{32}$.
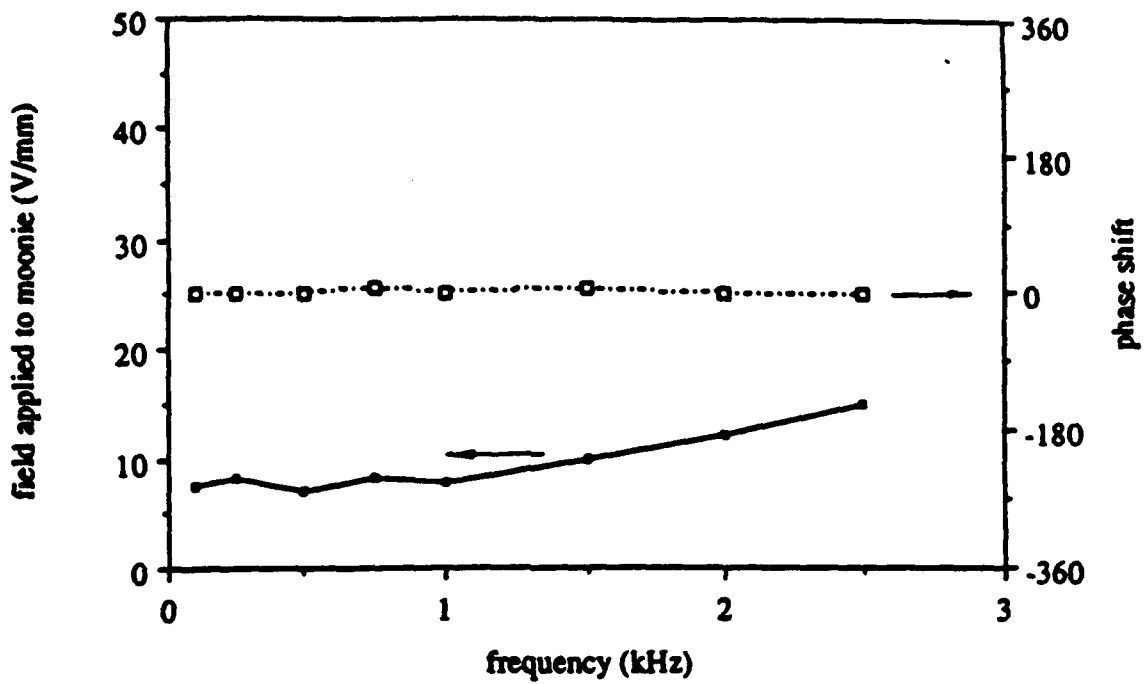
FIGURE 4 Field and phase shift applied to the moonie actuator needed to cancel the external vibration when the field applied to the multilayer vibration source is 75V/mm
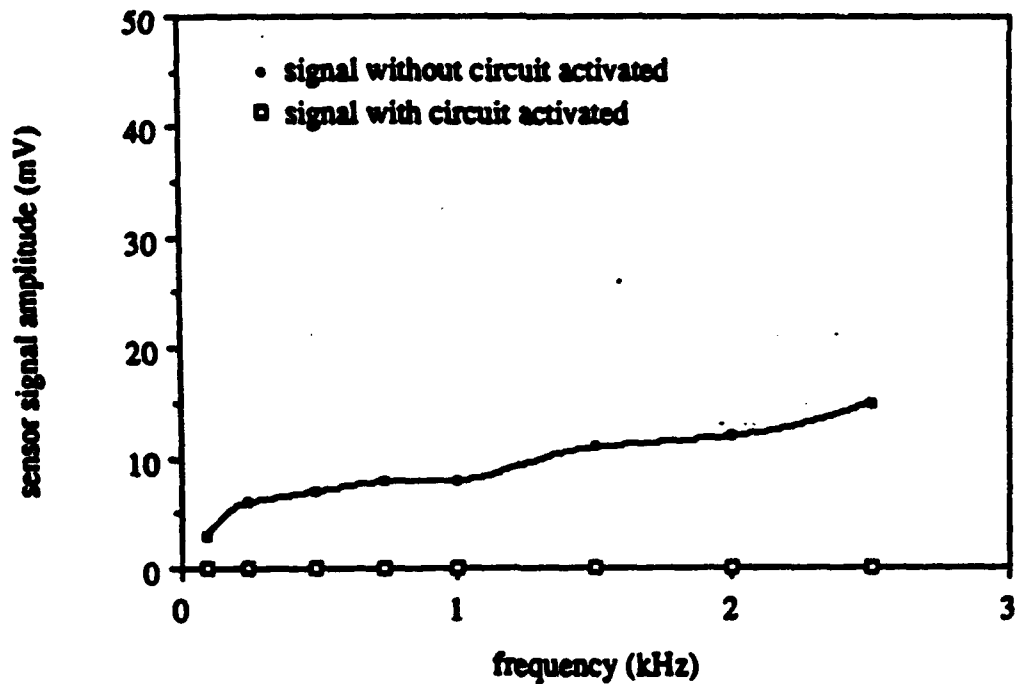

FIGURE 5 Sensor signal response both with and without the feedback circuit activated

$$F = \frac{A \, V_{out}}{2t \, |g_{31}|} \qquad (1)$$

where F = force detected by the sensor V_{out} = output voltage from the sensor

        t = thickness of the sensor g_{31} = piezoelectric charge coefficient

        A = area of the sensor

It was further assumed that the maximum and minimum force detected arose from the maximum and minimum electric fields reported previously. Table I provides a list of the values used for these calculations.

TABLE I   Values used to calculate force detected by the sensor at a frequency of 1kHz

sensor area = 6.25×10^{-6} m^2	sensor thickness = 1×10^{-4} m
g_{31} = -12.4×10^{-3} Vm/N	
$(V_{out})_{max}$ = 340mV	$(V_{out})_{min}$ = 0.2mV

Therefore F_{max} = 0.85N = 85gf and F_{min} = 0.5mN = 0.05gf. The reason for these rather small values is due to the sensor being located over the center of the cavity, which is the region of minimum generative force for the device.[2]

     Lastly, the response time of the device, 20μsec, was estimated from the resonance frequency of the actuator, 50kHz.

REFERENCES

1. Y. Sugawara, K. Onitsuka, S. Yoshikawa, Q.C. Xu, R.E. Newnham, and K. Uchino, J. Am. Ceram. Soc., 75, 996-998 (1992).
2. K. Onitsuka, Ph.D. thesis, Effects of Bonding and Geometry on the Flextensional Transducer "Moonie", The Pennsylvania State University (1993).
3. K. Imanaka, Proceedings of the SPIE, 1751, (1992).

APPENDIX 27

FLEXTENSIONAL "MOONIE" ACTUATORS

R. E. Newnham, A. Dogan, Q. C. Xu, K. Onitsuka, J. Tressler, and S. Yoshikawa
International Center of Actuators and Transducers
Materials Research Laboratory
The Pennsylvania State University
University Park, PA 16802

ABSTRACT

In recent years, piezoelectric and electrostrictive ceramics have been used in many actuators applications. A new type of composite actuator, which is based on the concept of a flextensional transducer, has been developed. (1-6) This ceramic-metal composite actuator, or "moonie" consists of either a piezoelectric ceramic disk or a multilayer stack sandwich between two specially designed metal end caps. This new design provides a sizeable displacement, as well as a large generative force. In other words, it bridges the gap between the two most common types of actuator; the multilayer and bimorph (7).

INTRODUCTION

The basic configuration of the ceramic-metal composite actuator (moonie) is shown in Figure 1. The metal end caps serve as mechanical transformers for converting and amplifying the lateral motion of the ceramic into a large axial displacement normal to the end caps. Both the d_{31} ($=d_{32}$) and d_{33} coefficients of the piezoelectric ceramic contribute to the axial displacement of the composite.

Sample Preparation and Measurement Technique

The composite actuators were made from electroded PZT-5A, PMN-PT, or multilayer ceramic disks (11-12.7 mm in diameter and 1 mm thick) and end caps (11-12.7 mm in diameter with thickness ranging from 0.3 to 3.0 mm). Shallow cavities 8.5 to 9.0 mm in diameter and about 200 μm center depth were machined into the inner surface of each of the end caps. The end caps were machined from brass, phosphor bronze, and acrylic. The ceramic disk and the end caps were bonded together around the circumference, taking care not to fill the cavity or short circuit the electrodes. Composite actuators were also stacked together to get higher displacement by using silver epoxy at the centers of end caps.

The displacement of the composite actuator in the low frequency range was measured with a Linear Voltage Differential Transducer (LVDT) having a resolution of approximately 0.05 μm. The effective piezoelectric coefficient, which is a device property, was measured at the center of the samples using a modified Berlincourt d_{33} meter at a frequency of 100 Hz. Resonant frequencies were obtained with a Hewlett-Packard Spectrum Analyzer HP-3585A or Network Analyzer HP-3577A.
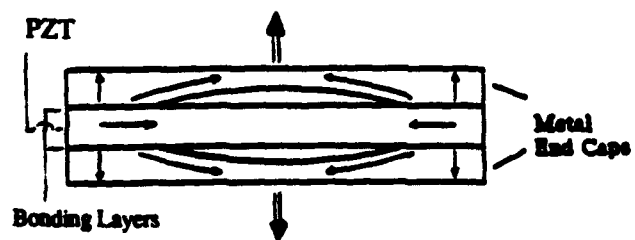

Figure 1. The geometry of the ceramic-metal composite actuator "Moonie". Arrows describe the direction of displacement.

FEA Modeling

Two commercially available FEA programs (ANSYS and SAP90) were used in this study for frequency response analysis. The relationship between admittance and frequency was calculated using 3-D axisymmetric piezoelectric elements in ANSYS. For the displacement analysis, the relationship between

displacement and applied electric field was calculated using 2D axisymmetric elements in SAP90. Each model was divided into three parts: the end cap, the PZT ceramic, and the bonding layer. Material parameters used in this analysis were Young's modulus, density, Poisson's ratio, piezoelectric constants, and dielectric constants.

EXPERIMENTAL RESULTS

Thickness Dependence of Displacement Values

Figure 2 shows the displacement at the cap center for composite actuators with different brass thickness at the same electric field, 1000 kV/mm. The results show that a composite actuator with 0.30 mm brass thickness can produce a displacement about 20 times larger than that of PZT alone. The displacement amplification is inversely related to the thickness of the metal end caps. FEA calculation agreed very well with the experimental results.
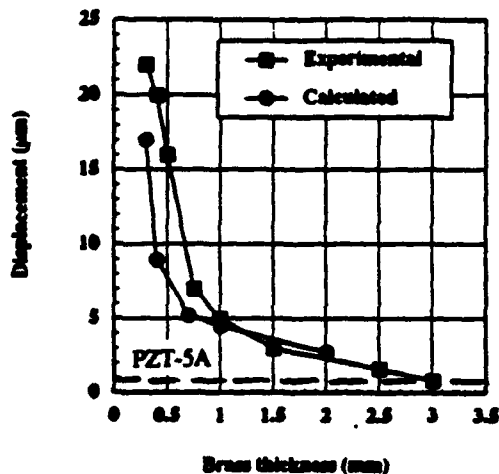

Figure 2. Comparison of the displacement calculated by FEA with experimental results as a function of end cap thickness.

Frequency Response of a Moonie Actuator

From the frequency response analysis, the lowest three resonant frequencies were calculated. Figure 3 shows the admittance spectrum of the moonie plotted as a function of the frequency from 10 to 300 kHz. The resonance peaks appearing at 50, 187, and 210 kHz, correspond to the lowest three flextensional vibration modes. The first flextensional mode can be effectively utilized up to nearly 50 kHz. Based on

these results, the coupling coefficient of the first mode was calculated to be 20%.
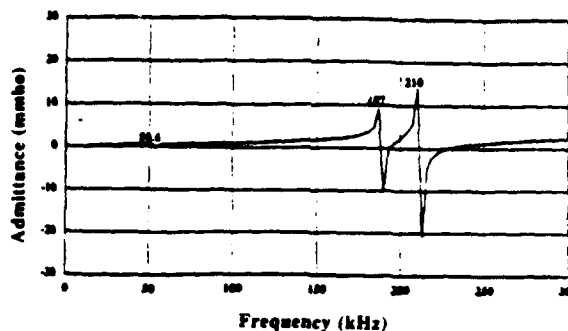
Figure 3. Admittance spectrum of the moonie (FEA)

Figure 4 compares the first flextensional resonant frequency calculated by FEA with those obtained experimentally, for a range of brass end cap thickness. FEA calculation agreed very well with the experimental results. The first resonant frequency is approximately proportional to the square root of the brass end cap thickness.
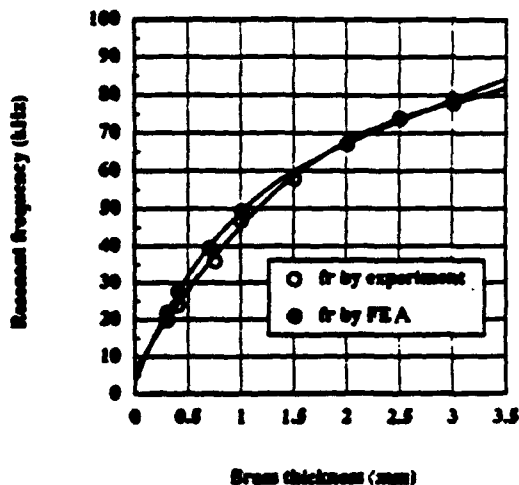

Figure 4. End cap thickness dependence of first resonance frequency.

Load Effect on Displacement of a Moonie Actuator

Normally, the displacement decreases when a load is applied to the actuator. Figure 5 shows the displacement profile across the exterior surface of the

moonie when four different loads are applied over an area 3 mm^2 under an applied E-field of 1 kV/mm. By increasing the load, the center displacement is gradually suppressed. The calculated maximum generative force of the moonie is 300 gf.
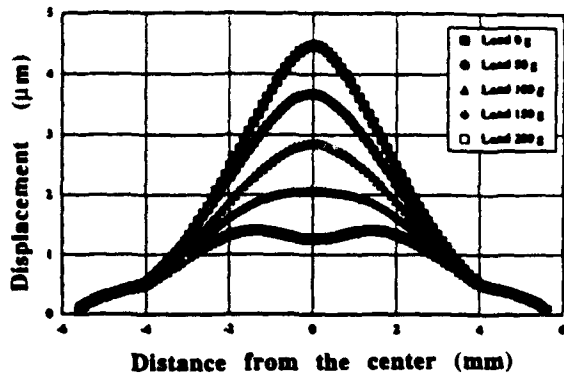

Figure 5. Calculated displacement profile across the exterior surface of the moonie actuator under the application of different loads.

Maximum Generative Force of the Moonie

Even though the flexural motion and displacement are the largest at the center of the end caps, the generative force is low. Fig. 6 shows the applied force-displacement relation of a moonie actuator operated at 1 kV/mm. A moonie actuator with 0.30 mm thick brass caps can withstand 210 gf while sacrificing 20% of its displacement value (load applied at the center of the end caps over 1mm^2). The maximum generative force of the moonie actuator with 0.30 mm thick brass end caps should be around 350 gf (i.e. the intercept on the force axis). The reason for the saturation near 150 gf is probably due to the increasing contact surface of the LVDT measurement tip.

Trade-off Between Maximum Generative Force and Displacement

The position dependence of displacement is shown in Fig. 7 for the moonie actuator with 0.30 mm thick brass end caps. A displacement of about 22 μm was obtained at the center of the moonie. Displacement decreases dramatically when moving from the center to the edge. Conversely, generative force increases when moving from the center to the edge, where it approaches that of PZT ceramic. Therefore, it

becomes possible to tailor the desired actuator properties by changing the contact area over the brass end caps.
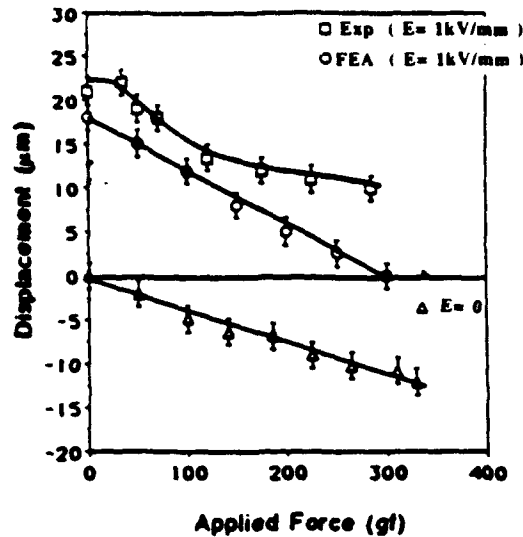

**Figure 6.** Displacement-applied force relation.
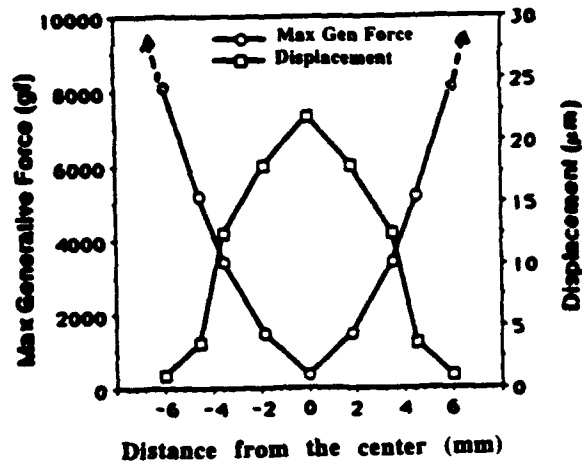
Figure 7.Position dependence of maximum generative force and displacement.

End Cap Material Effect

Four end cap materials: brass, aluminum, stainless steel and plastic were used for estimating their effect on the displacement of the moonie actuator. Since

they have different densities, Poisson's ratios, and Young's modulus, displacement is expected to be different for each end cap material.

Fig. 8 shows the effect of cap material on the displacement of the moonie actuator as a function of the cap thickness when applying a 1kV/mm electric field. It is observed that the lower the Young's modulus, the higher the displacement over the entire cap thickness range. All three metals, stainless steel, brass, and aluminum, show little difference in displacement when greater than 0.5 mm thick. Below a thickness of 0.5 mm, differences in displacement appear.
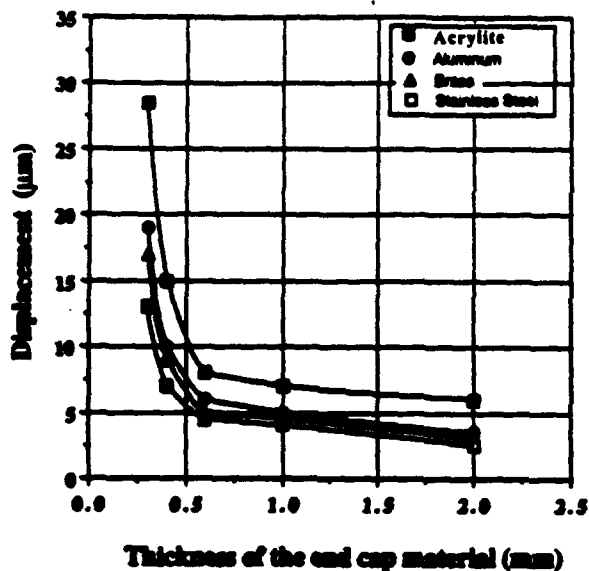

Figure 8. The effect of end cap material on the displacement value of moonie actuator.

Multistacked Moonie Actuator

A doubly stacked moonie actuator was fabricated by bonding together with silver epoxy two identical brass capped moonie actuators at the center of the cap. Figure 9 shows the displacement versus electric field curves for a doubly-stacked actuator driven by PZT-5A. A displacement of about 40 μm was obtained under an electric field of 1 kV/mm, which is almost twice the simple moonie displacement and nearly 20 times that of an uncapped ceramic. Displacement for the uncapped ceramic is also shown for comparison.
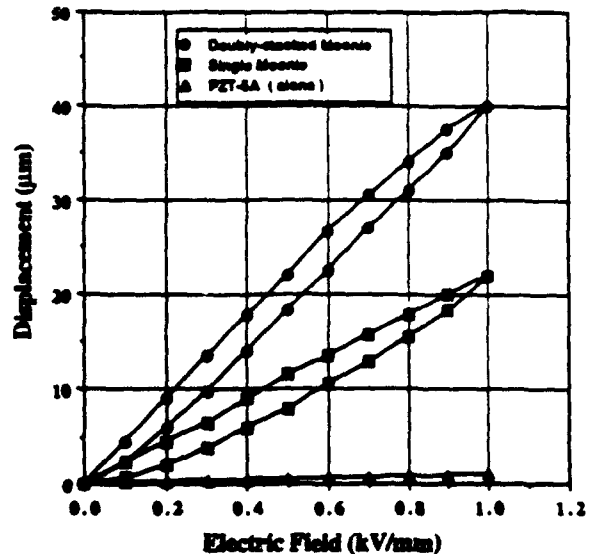

Figure 9. Displacament characteristic of a doubly-stacked moonie actuator .

Integrated Sensor and Actuator

By integrating both sensing and actuating functions into a single composite, the moonie device can be utilized for active vibration control. The prototype design (Fig. 10) consists of a 0.10 mm thick PZT-5A sensor, 2.5 mm on edge, imbedded within the upper end cap of a standard moonie actuator (11 mm in diameter, 3mm thick). External sinusoidal vibrations normal to the end cap surface are detected by the sensor. Then, via a feedback loop, a signal of appropriate amplititude and phase is applied to the actuatc. so that it effectively cancels the external vibration.

The sensitivity of the sensor was found by applying a sinusoidal AC electric field to the actuator portion of the device and observing the subsequent vibration signal on an oscilloscope. The minimum and maximum electric fields into the moonie actuator for which the sensor could detect a sinusoidal vibration signal were 200 mV/mm and 370V/mm. respectively. These minimum and maximum electric fields thus define the dynamic displacement range that the sensor is capable of detecting as being between 0.35 nm and 0.65 μm (as calculated by finite element analysis)
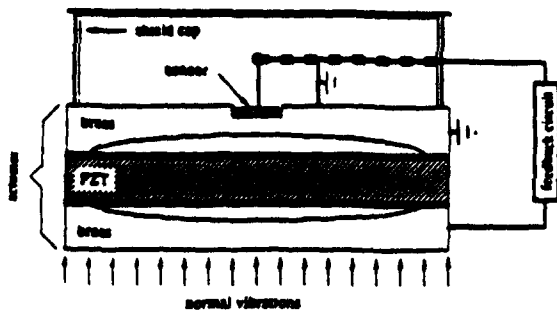
Figure 10. Integrated sensor and actuator.

The data in Figure 11 show that when the feedback circuit is activated, the prototype integrated sensor/actuator design can completely suppress the effects of an external vibration between 100 Hz and at least 2500 Hz. Over this frequency range, the electric field applied to the moonie actuator was nearly constant and its phase shift remained at nearly 180° due to the short propagation time as a result of the moonie actuator being in close proximity to the external vibration.
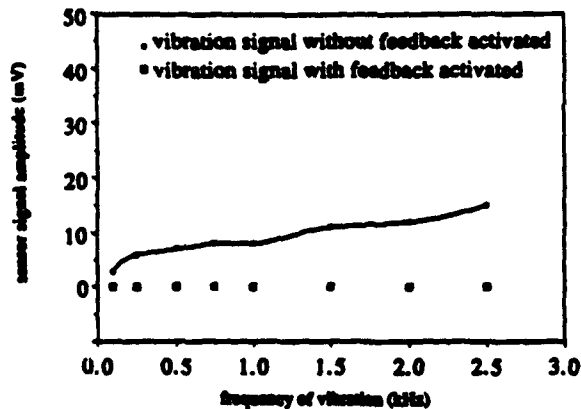

Figure 11. Sensor signal response both with and without the feedback circuit activated.

ACKNOWLEDGEMENT

The authors wish to thank Dr. L.E.Cross, and Dr .K. Uchino. The authors also wish to thank Dr. M. Megherhi of Piezo Kinetics Inc. for his technical support.

REFERENCES

1. R.E.Newnham, Q.C.Xu and S. Yoshikawa "Transformed stress direction-acoustic transducer" U.S Patent # 4,999,819 (March 12,1992).

2. Q.C.Xu, S.Yoshikawa, J.Belsick, R.E.Newnham, "Piezoelectric composites with high sensitivity and capacitance for use at high pressures.IEEE Transactions on Ultrasonics, Ferroelectrics and Frequency Control 38 [6] 634-39 (1991).

3. Y.Sugawara, K.Onitsuka, S.Yoshikawa, Q.Xu, R.E.Newnham, and K.Uchino, "Metal-Ceramic Composite Actuators " J.Am.Ceram.Soc.75[4]996-98(1992).

4. Q.C. Xu, A. Dogan, J. Tressler, S.Yoshikawa, and R.E.Newnham, "Ceramic-Metal Composite Actuator" IEEE Ultrasonic Symposium Proceedings (Florida, 1991).

5. A.Dogan, Q.C. Xu, K. Onitsuka, S.Yoshikawa, K. Uchino and R.E.Newnham. " High Displacement Ceramic-Metal Composite Actuators (Moonie)". Ferroelectric Special Issue for IMF-8 (in press).

6. K. Onitsuka, A.Dogan, Q.C. Xu, J. Tressler, S. Yoshikawa, and R.E.Newnham."Design Optimization for Ceramic-Metal Composite Actuators (Moonie)". Ferroelectric Special Issue for IMF8 (in Press).

7. K. Uchino "Piezoelectric and Electrostrictive Actuators", Morikita Publication, Tokyo, Japan, 1986.

APPENDIX 28

Theoretical modelling of multilayer magnetoelectric composites

Girish Harshé, J.P. Dougherty and R.E. Newnham

Materials Research Laboratory, The Pennsylvania State University, University Park, PA 16802, USA

Multilayer composites of a piezoelectric material and a piezomagnetic material can be designed to exhibit magnetoelectric (ME) effect. Such a composite is electrically polarized when it is placed in a magnetic field or is magnetized when an electric field is applied to it. Since the phases have anisotropic properties, the resulting ME coefficient depends on the boundary conditions of the composite. We have modelled four simple cases of two-layer structures of these composites and derived the theoretical expression for the ME coefficient for each arrangement.

1. Introduction

Magnetoelectric (ME) composites of a piezoelectric material and a piezomagnetic material can be designed to make use of different material coefficients depending on the application. Such composites show the ME effect similar to that observed in certain antiferromagnetic materials like Cr_2O_3. These materials are electrically polarized when placed in a magnetic field and also are magnetized when an electric field is applied to them. In composite piezoelectric–piezomagnetic (or magnetostrictive) materials, a phenomenon called 'product property' causes the ME effect [1]. Thus the piezomagnetic effect relating magnetic field to strain, the elastic property relating strain and stress, and the piezoelectric effect relating stress and electric polarization, together give rise to the ME effect in a composite. Since the product property magnetoelectricity in a composite depends on the piezoelectric, piezomagnetic and elastic coefficients of the component phases, theoretically it can be expressed in terms of all these coefficients of the components for different boundary conditions.

There can be various types of ME composites depending on the connectivity of phases for example 3–0, 3–1 and 2–2 [2]. In the past, most of the literature published has reported ME composites of the type 3–0 or 3–3 [3–6]. There is, however, no theoretical work reported to formulate the ME effect in a composite. The theoretical treatment reported by Zubkov [7] is not sufficient, since it does not consider all the relevant coefficients.

In the multilayer type of ME composites, there are different configurations possible as shown in fig. 1. We have developed theoretical models for bimorphs or two-layer composites. These configurations are relatively easy to make on a macroscopic scale and hence the models can be tested experimentally.

2. General theory

Since magnetoelectricity in composites involves piezoelectricity and magnetostriction, these properties of the individual phases are reviewed here. Piezoelectricity is expressed as:

$$P = dT , \tag{1}$$

Correspondence to: Dr. R.E. Newnham, Materials Research Laboratory, The Pennsylvania State University, University Park, PA 16802, USA. Tel.: +1-814 865 1612; telefax: +1-814 865 2326.
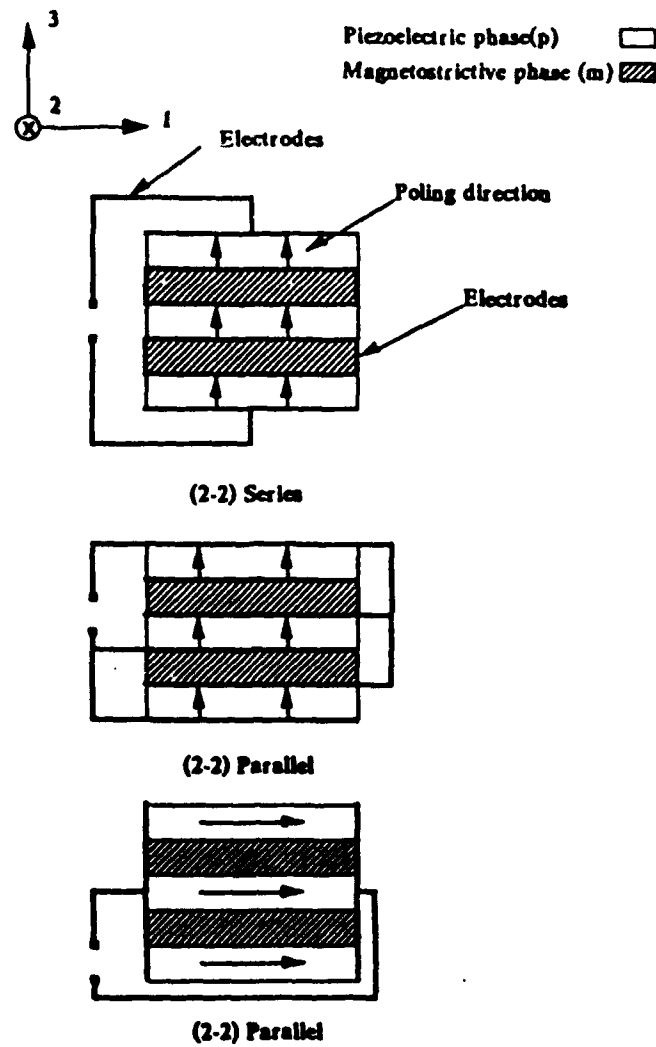
Fig. 1. Magnetoelectric multilayer composites with 2-2 connectivity.

where P is the polarization (3×1) matrix, d is the piezoelectric coefficient (3×6) matrix and T is the stress (6×1) matrix.

Piezoelectricity can be expressed in a different manner by using the piezoelectric voltage coefficient matrix g, as follows:

$$E = gT , \tag{2}$$

where E is the electric field (3×1) matrix, g is the piezoelectric voltage coefficient (3×6) matrix. The matrix g can be determined if d and the dielectric permittivity matrix ε^T are known, because the electric displacement D is

$$D = dT + \varepsilon^T E \tag{3}$$

and when $D = 0$, i.e. for open circuit condition,

$$E = (-d/\varepsilon^T)T . \tag{4}$$

From eqs. (2) and (4)

$$g = -d/\varepsilon^T . \tag{5}$$

Magnetostriction can be expressed as follows, assuming no hysteresis (at low magnetic fields):

$$S = \lambda H^2 , \tag{6}$$

where S is the strain (6×1) matrix, λ is the magnetostriction coefficient (6×6) matrix and H^2 is the magnetic field squared (6×1) matrix.

However, the magnetostriction at a particular bias field H_0, can give rise to pseudo-piezomagnetism over a small range where the slope of the magnetostriction curve dS/dH can be assumed to be constant. Thus pseudo-piezomagnetism at a bias field H_0 can be expressed as:

$$S = qH , \tag{7}$$

where q is the pseudo-piezomagnetic coefficient (6×3) matrix. Therefore for a material, a general expression for the strain, which takes into account the contribution from the stress field (elastic effect), the electric field (piezoelectric effect) and the magnetic field (piezomagnetic effect), can be written as:

$$S = sT + dE + qH , \tag{8}$$

where s is the compliance coefficient (6×6) matrix.

The magnetoelectric coefficient α is defined as

$$P = \varepsilon_0 \kappa E - \alpha H , \tag{9}$$

where κ is the dielectric susceptibility. Also

$$D = P + \varepsilon_0 H . \tag{10}$$

Therefore from eqs. (9) and (10)

$$D = \varepsilon_0 \kappa E + \alpha H + \varepsilon_0 E , \tag{11}$$

i.e. $\quad D = \varepsilon E + \alpha H . \tag{12}$

At open circuit condition $D = 0$, therefore

$$E = -(\alpha/\varepsilon)H . \tag{13}$$

We thus define a magnetoelectric voltage coefficient $\alpha_{(E)}$ which is

$$\alpha_{(E)} = -(\alpha/\varepsilon) . \tag{14}$$

Table 1
Non-zero coefficients for piezoelectric and magnetostrictive phases

Piezoelectric ceramic	
Piezoelectric coefficients	Compliance coefficients
$^p d_{15} = {}^p d_{24}$	$^p s_{11} = {}^p s_{22}$
$^p d_{31} = {}^p d_{32}$	$^p s_{12} = {}^p s_{21}$
$^p d_{33}$	$^p s_{13} = {}^p s_{23} = {}^p s_{31} = {}^p s_{32}$
	$^p s_{33}$
	$^p s_{44} = {}^p s_{55}$
	$^p s_{66} = 2({}^p s_{11} - {}^p s_{12})$

Piezomagnetic ceramic	
Piezomagnetic coefficients	Compliance coefficients
$^m q_{15} = {}^m q_{24}$	$^m s_{11} = {}^m s_{22} = {}^m s_{33}$
$^m q_{31} = {}^m q_{32}$	$^m s_{12} = {}^m s_{13} = {}^m s_{21} = {}^m s_{23} = {}^m s_{31} = {}^m s_{32}$
$^m q_{33}$	$^m s_{44} = {}^m s_{55} = {}^m s_{66}$

In order to determine $\alpha_{(E)}$ theoretically, for a composite material, it is necessary to derive an expression for the electric field E developed across the sample under the action of an applied magnetic field H. Then the ratio E/H is equal to the ME voltage coefficient $\alpha_{(E)}$.

It becomes very difficult to operate with matrices because the different connectivities make it necessary to use different formulae for different elements of the matrices. Hence the derivations for magnetoelectric coefficients are carried out using only relevant terms, necessary to be considered for a particular composite model. Table 1 lists the various coefficient matrices for a spinel ferrite with cubic symmetry and a poled piezoelectric with a 6 mm (or ∞ m) symmetry about the poling axis.

3. Composites with 2–2 connectivity

Composites in which the component phases have connectivity only in two directions are called 2–2 composites. There are several cases possible in the 2–2 type of ME composites. These include the variations due to the directions of E and H with respect to each other and the boundary conditions such as clamped ends and mechanical bonding between the two phases. Fig. 2 shows four cases of ME bimorphs due to different boundary conditions considered in this paper. The expressions for these cases have been derived below. It is assumed that there is no electric field present within the magnetostrictive phase as the piezoelectric phase has electrodes on the two opposite faces which are connected to the external electric field. Also the magnetic field is assumed to be constant through out the space so that the presence of the piezoelectric phase with magnetic permittivity of approximately 1 does not affect the magnetic field and induction experienced by the magnetostrictive phase.

3.1. Case I: free body with both phases perfectly bonded together

As shown in fig. 2(a) the composite in this case is a stacked arrangement of the magnetostrictive phase m and the piezoelectric phase p, bonded together with a glue. Since under free body condition there are no stresses present along the 3 direction in both the phases, hence

$$^mT_3 = {}^pT_3 = 0 \tag{15}$$

where prefixes m and p denote magnetostrictive phase and piezoelectric phase respectively: suffixes 1, 2 and 3 denote the three axes direction and T_i is the stress along i. Since the composite is assumed to be rigid, the strains in both the phases along the transverse directions 1 and 2 are equal, therefore

$$S_1 = {}^mS_1 = {}^pS_1 , \tag{16}$$

$$S_2 = {}^mS_2 = {}^pS_2 , \tag{17}$$

where S_i represents the strain along the i direction. Also the total force, acting on the composite along the direction 1 or 2, which is the product of the stress T_1 or T_2, and the cross sectional area, is zero. The cross sectional area is proportional to the volume fraction ^mv or ^pv, as the layer dimensions (along 1 and 2) except the thickness of both the phases are equal. Therefore

$$^mT_1 \, {}^mv = -{}^pT_1 \, {}^pv , \tag{18}$$

$$^mT_2 \, {}^mv = -{}^pT_2 \, {}^pv . \tag{19}$$

Finally, the electric displacement vector D in the piezoelectric layer is zero under open circuit condition, therefore

$$D = 0 . \tag{20}$$
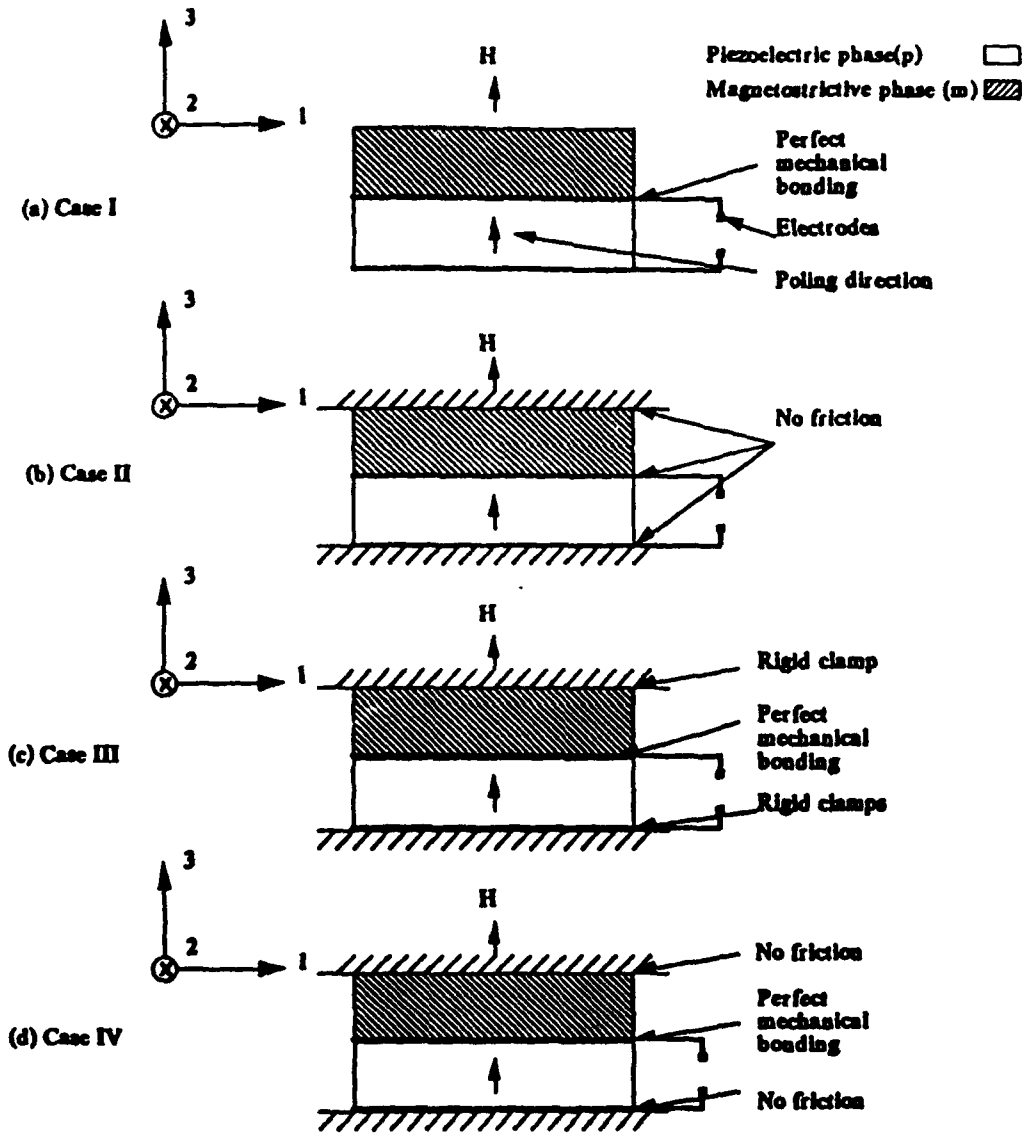
Fig. 2. Different cases of ME 2-2 type composites due to different boundary conditions.

Now using eq. (8) the strains along 1 are given by

$$^{m}S_1 = {}^{m}s_{11}{}^{m}T_1 + {}^{m}s_{12}{}^{m}T_2 + {}^{m}s_{13}{}^{m}T_3 + {}^{m}q_{31}H_3 \tag{21}$$

and

$$^{p}S_1 = {}^{p}s_{11}{}^{p}T_1 + {}^{p}s_{12}{}^{p}T_2 + {}^{p}s_{13}{}^{p}T_3 + {}^{p}d_{31}E_3 , \tag{22}$$

since the piezoelectric coefficient of the magnetostrictive phase $^{m}d_{ij} = 0$ and the piezomagnetic coefficient of the piezoelectric phase $^{p}q_{ij} = 0$. Also since $^{m}q_{31} = {}^{m}q_{32}$ and $^{p}d_{31} = {}^{p}d_{32}$ it can be assumed that $^{m}T_1 = {}^{m}T_2$ and $^{p}T_1 = {}^{p}T_2$. Hence with these assumptions and from eqs. (15), (16), (21) and (22) we get

$$(^{m}s_{11} + {}^{m}s_{12})^{m}T_1 + {}^{m}q_{31}H_3 = ({}^{p}s_{11} + {}^{p}s_{12})^{p}T_1 + {}^{p}d_{31}E_3 . \tag{23}$$

Substituting for $^{m}T_1$ from eq. (18) in eq. (23) we get

$$-(^{m}s_{11} + {}^{m}s_{12})^{p}T_1(^{p}v/^{m}v) + {}^{m}q_{31}H_3 = ({}^{p}s_{11} + {}^{p}s_{12})^{p}T_1 + {}^{p}d_{31}E_3 . \tag{24}$$

From eq. (20) we get

$$D_3 = {}^pd_{31}{}^pT_1 + {}^pd_{32}{}^pT_2 + {}^pd_{33}{}^pT_3 + {}^p\varepsilon^T_{33}E_3 = 0 , \tag{25}$$

and using ${}^pT_1 = {}^pT_2$ and ${}^pd_{31} = {}^pd_{32}$ we get

$$ {}^pT_1 = -({}^p\varepsilon^T_{33})E_3/(2{}^pd_{31}) . \tag{26}$$

From eqs. (24) and (26) after eliminating ${}^pT_1$ we get

$$- ({}^ms_{11} + {}^ms_{12})(-({}^p\varepsilon^T_{33})E_3/(2{}^pd_{31}))({}^pv/{}^mv) + {}^mq_{31}H_3$$

$$= ({}^ps_{11} + {}^ps_{12})(-({}^p\varepsilon^T_{33})E_3/(2{}^pd_{31})) + {}^pd_{31}E_3 .$$

After rearranging

$$[({}^ms_{11} + {}^ms_{12})({}^p\varepsilon^T_{33}){}^pv + ({}^ps_{11} + {}^ps_{12})({}^p\varepsilon^T_{33}){}^mv - 2({}^pd_{31})^2{}^mv]E_3 = (-2{}^mq_{31}{}^pd_{31}{}^mv)H_3 . \tag{27}$$

Now the magnetoelectric voltage coefficient, defined as the ratio of the electric field produced across the sample to the applied magnetic field is

$$\alpha_{(E)33} = E_3/H_3$$

$$\therefore \quad \alpha_{(E)33} = \frac{(-2{}^mq_{31}{}^pd_{31}{}^mv)}{[({}^ms_{11} + {}^ms_{12})({}^p\varepsilon^T_{33}){}^pv + ({}^ps_{11} + {}^ps_{12})({}^p\varepsilon^T_{33}){}^mv - 2({}^pd_{31})^2{}^mv]} . \tag{28}$$

3.2. Case II: clamped ends with no friction along transverse directions (axes 1 and 2) between all the surfaces in contact with each other

As shown in fig. 2(b) the composite in this case is a stacked arrangement of the magnetostrictive phase m and the piezoelectric phase p, clamped at both ends with thin layers of lubricant between all the surfaces in contact with each other in order to minimize the friction along axes 1 and 2. Since there is no friction along the interface (along the axes 1 and 2) the stresses in each layer along the axes 1 and 2 are zero, therefore

$$ {}^mT_1 = {}^pT_1 = 0 , \tag{29}$$

$$ {}^mT_2 = {}^pT_2 = 0 . \tag{30}$$

Also because the composite is stationary the stress along the vertical 3 direction in each layer is equal, therefore

$$ {}^mT_3 = {}^pT_3 . \tag{31}$$

Further, due to the rigid clamps total strain which is the sum of the strain along 3 in a layer times the volume fraction of that layer is zero. Hence

$$S_3 = {}^mS_3{}^mv + {}^pS_3{}^pv = 0 . \tag{32}$$

The electrical displacement D is zero under open circuit condition:

$$D = 0 . \tag{33}$$

Now using the general strain expression (8) and since ${}^md_{ij} = 0$ and ${}^pq_{ij} = 0$, from eq. (32) we have

$$({}^ms_{33}{}^pT_3 + {}^mq_{33}H_3){}^mv + ({}^ps_{33}{}^pT_3 + {}^pd_{33}E_3){}^pv = 0 . \tag{34}$$

Since $D = 0$ we have

$$D_3 = {}^P d_{33} {}^P T_3 + {}^P T_3 + {}^P \varepsilon^T_{33} E_3 = 0 , \tag{35}$$

$$\therefore \quad {}^P T_3 = -({}^P \varepsilon^T_{33} / {}^P d_{33}) E_3 . \tag{36}$$

Substituting for ${}^P T_3$ from eq. (36) in eq. (34) we get

$$({}^m s_{33} [-({}^P \varepsilon^T_{33} / {}^P d_{33}) E_3] + {}^m q_{33} H_3) {}^m v + ({}^P s_{33} [-({}^P \varepsilon^T_{33} / {}^P d_{33}) E_3] + {}^P d_{33} E_3) {}^P v = 0 ,$$

$$\therefore \quad [{}^P \varepsilon^T_{33} ({}^m s_{33} {}^m v + {}^P s_{33} {}^P v) - ({}^P d_{33})^2 {}^P v] E_3 = {}^m q_{33} {}^P d_{33} {}^m v H_3 .$$

Now the magnetoelectric voltage coefficient is

$$\alpha_{(E)33} = E_3 / H_3 ,$$

$$\therefore \quad \alpha_{(E)33} = \frac{{}^m q_{33} {}^P d_{33} {}^m v}{[{}^P \varepsilon^T_{33} ({}^m s_{33} {}^m v + {}^P s_{33} {}^P v) - ({}^P d_{33})^2 {}^P v]} . \tag{37}$$

3.3. Case III: clamped ends and both phases perfectly bonded together

As shown in fig. 2(c) the composite in this case is a stacked arrangement of the magnetostrictive phase m and the piezoelectric phase p, bonded together with a glue and clamped rigidly at both ends. In this case the transverse strains are zero due to the rigid bonding of the layers and the clamping, however, the stresses along 1 and 2 need not be zero. Other things remain same as in the previous case. The boundary conditions then are

$$^m T_3 = {}^P T_3 , \tag{38}$$

$$S_1 = {}^m S_1 = {}^P S_1 = 0 , \tag{39}$$

$$S_2 = {}^m S_2 = {}^P S_2 = 0 , \tag{40}$$

$$S_3 = {}^m S_3 {}^m v + {}^P S_3 {}^P v = 0 , \tag{41}$$

$$D = 0 , \tag{42}$$

where the notations denote the same quantities as in the previous case. Now using the general strain expression (8) and since ${}^m d_{ij} = 0$ and ${}^P q_{ij} = 0$ we have

$$^m S_3 = {}^m s_{31} {}^m T_1 + {}^m s_{32} {}^m T_2 + {}^m s_{33} {}^m T_3 + {}^m q_{33} H_3$$

and

$$^P S_3 = {}^P s_{31} {}^P T_1 + {}^P s_{32} {}^P T_2 + {}^P s_{33} {}^P T_3 + {}^P d_{33} E_3 .$$

Therefore from eqs. (38), (41) and also assuming ${}^m T_1 = {}^m T_2$ and ${}^P T_1 = {}^P T_2$ since ${}^m q_{31} = {}^m q_{32}$ and ${}^P d_{31} = {}^P d_{32}$ we get

$$^m v[({}^m s_{31} + {}^m s_{32}) {}^m T_1 + {}^m s_{33} {}^P T_3 + {}^m q_{33} H_3] + {}^P v[({}^P s_{31} + {}^P s_{32}) {}^P T_1 + {}^P s_{33} {}^P T_3 + {}^P d_{33} E_3] = 0 .$$

On rearranging we get

$$({}^m s_{31} + {}^m s_{32}) {}^m T_1 {}^m v + ({}^P s_{31} + {}^P s_{32}) {}^P T_1 {}^P v + ({}^m s_{33} {}^m v + {}^P s_{33} {}^P v) {}^P T_3 + {}^P d_{33} {}^P v E_3 = -{}^m q_{33} {}^m v H_3 . \tag{43}$$

Since ${}^m S_1 = 0$ and ${}^P S_1 = 0$, using eq. (38) we get

$$^m S_1 = ({}^m s_{11} + {}^m s_{12}) {}^m T_1 + {}^m s_{13} {}^P T_3 + {}^m q_{31} H_3 = 0 ,$$

$$\therefore \quad {}^m T_1 = -({}^m q_{31} H_3 + {}^m s_{13} {}^P T_3) / ({}^m s_{11} + {}^m s_{12}) . \tag{44}$$

Similarly

$$^pT_1 = -(^pd_{31} E_3 + {}^ps_{13} {}^pT_3)/(^ps_{11} + {}^ps_{12}) .$$ (45)

Substituting for $^mT_1$ from eq. (44) and $^pT_1$ from eq. (45) in eq. (43) we get

$$[-(^ms_{31} + {}^ms_{32})(^mq_{31} H_3 + {}^ms_{13} {}^pT_3)^m v/(^ms_{11} + {}^ms_{12})]$$

$$+ [-(^ps_{31} + {}^ps_{32})(^pd_{31} E_3 + {}^ps_{13} {}^pT_3)^p v/(^ps_{11} + {}^ps_{12})]$$

$$+ (^ms_{33} {}^m v + {}^ps_{33} {}^p v)^pT_3 + {}^pd_{33} {}^p v E_3 = -{}^mq_{33} {}^m v H_3 .$$

Rearranging this we get

$$[-(^ms_{31} + {}^ms_{32})^ms_{13} {}^m v/(^ms_{11} + {}^ms_{12})$$

$$- (^ps_{31} + {}^ps_{32})^ps_{13} {}^p v/(^ps_{11} + {}^ps_{12}) + (^ms_{33} {}^m v + {}^ps_{33} {}^p v)]^pT_3$$

$$+ [^pd_{33} {}^p v - (^ps_{31} + {}^ps_{32})^pd_{31} {}^p v/(^ps_{11} + {}^ps_{12})]E_3$$

$$= [-{}^mq_{33} {}^m v + (^ms_{31} + {}^ms_{32})^mq_{31} {}^m v/(^ms_{11} + {}^ms_{12})]H_3 ,$$

$$\therefore \quad [-(^ms_{31} + {}^ms_{32})(^ps_{11} + {}^ps_{12})^ms_{13} {}^m v - (^ps_{31} + {}^ps_{32})(^ms_{11} + {}^ms_{12})^ps_{13} {}^p v$$

$$+ (^ms_{33} {}^m v + {}^ps_{33} {}^p v)(^ms_{11} + {}^ms_{12})(^ps_{11} + {}^ps_{12})]^pT_3$$

$$+ [(^ms_{11} + {}^ms_{12})(^ps_{11} + {}^ps_{12})^pd_{33} {}^p v$$

$$- (^ps_{31} + {}^ps_{32})(^ms_{11} + {}^ms_{12})^pd_{31} {}^p v]E_3$$

$$= [-(^ms_{11} + {}^ms_{12})(^ps_{11} + {}^ps_{12})^mq_{33} {}^m v$$

$$+ (^ms_{31} + {}^ms_{32})(^ps_{11} + {}^ps_{12})^mq_{31} {}^m v]H_3 .$$ (46)

Since $D = 0$ we have

$$D_3 = 2^pd_{31} {}^pT_1 + {}^pd_{33} {}^pT_3 + {}^p\varepsilon^T_{33} E_3 = 0 .$$ (47)

Substituting for $^pT_1$ from eq. (45) we get

$$2^pd_{31}[-(^pd_{31} E_3 + {}^ps_{13} {}^pT_3)/(^ps_{11} + {}^ps_{12})] + {}^pd_{33} {}^pT_3 + {}^p\varepsilon^T_{33} E_3 = 0 .$$ (48)

$$\therefore \quad {}^pT_3 = [[2(^pd_{31})^2 - {}^p\varepsilon^T_{33}(^ps_{11} + {}^ps_{12})]/[^pd_{33}(^ps_{11} + {}^ps_{12}) - 2^pd_{31} {}^ps_{13}]]E_3 .$$ (49)

Substituting for $^pT_3$ from eq. (49) in eq. (46) we get

$$\therefore \quad [-(^ms_{31} + {}^ms_{32})(^ps_{11} + {}^ps_{12})^ms_{13} {}^m v - (^ps_{31} + {}^ps_{32})(^ms_{11} + {}^ms_{12})^ps_{13} {}^p v$$

$$+ (^ms_{33} {}^m v + {}^ps_{33} {}^p v)(^ms_{11} + {}^ms_{12})(^ps_{11} + {}^ps_{12})][2(^pd_{31})^2 - {}^p\varepsilon^T_{33}(^ps_{11} + {}^ps_{12})]$$

$$/[^pd_{33}(^ps_{11} + {}^ps_{12}) - 2^pd_{31} {}^ps_{13}]]E_3 + [(^ms_{11} + {}^ms_{12})(^ps_{11} + {}^ps_{12})^pd_{33} {}^p v$$

$$- (^ps_{31} + {}^ps_{32})(^ms_{11} + {}^ms_{12})^pd_{31} {}^p v]E_3 = [-(^ms_{11} + {}^ms_{12})(^ps_{11} + {}^ps_{12})^mq_{33} {}^m v$$

$$+ (^ms_{31} + {}^ms_{32})(^ps_{11} + {}^ps_{12})^mq_{31} {}^m v]H_3 ,$$

$$\therefore \quad [[-(^ms_{31} + {}^ms_{32})(^ps_{11} + {}^ps_{12})^ms_{13} {}^m v - (^ps_{31} + {}^ps_{32})(^ms_{11} + {}^ms_{12})^ps_{13} {}^p v$$

$$+ (^ms_{33} {}^m v + {}^ps_{33} {}^p v)(^ms_{11} + {}^ms_{12})(^ps_{11} + {}^ps_{12})][2(^pd_{31})^2 - {}^p\varepsilon^T_{33}(^ps_{11} + {}^ps_{12})]$$

$$+ [(^ms_{11} + {}^ms_{12})(^ps_{11} + {}^ps_{12})^pd_{33} {}^p v - (^ps_{31} + {}^ps_{32})(^ms_{11} + {}^ms_{12})^pd_{31} {}^p v]$$

$$\times [^pd_{13}(^ps_{11} + {}^ps_{12}) - 2^pd_{31} {}^ps_{13}]]E_3$$

$$= [[-(^ms_{11} + ^ms_{12})(^ps_{11} + ^ps_{12})^mq_{33}\,^mv + (^ms_{31} + ^ms_{32})(^ps_{11} + ^ps_{12})^mq_{31}\,^mv]$$
$$\times [^pd_{33}(^ps_{11} + ^ps_{12}) - 2^pd_{31}\,^ps_{13}]]H_3 .$$

(50)

Now the magnetoelectric voltage coefficient is

$$\alpha_{(E)33} = E_3/H_3$$

$$\therefore \quad \alpha_{(E)33} = \frac{\begin{array}{l}[[-(^ms_{11} + ^ms_{12})^mq_{33}\,^mv + (^ms_{31} + ^ms_{32})^mq_{31}\,^mv] \\ [^pd_{33}(^ps_{11} + ^ps_{12}) - 2^pd_{31}\,^ps_{13}](^ps_{11} + ^ps_{12})]\end{array}}{\begin{array}{l}[[-(^ms_{31} + ^ms_{32})(^ps_{11} + ^ps_{12})^ms_{13}\,^mv - (^ps_{31} + ^ps_{32})(^ms_{11} + ^ms_{12})^ps_{13}\,^pv \\ + (^ms_{33}\,^mv + ^ps_{33}\,^pv)(^ms_{11} + ^ms_{12})(^ps_{11} + ^ps_{12})][2(^pd_{31})^2 - ^p\varepsilon^T_{33}(^ps_{11} + ^ps_{12})] \\ + [(^ms_{11} + ^ms_{12})(^ps_{11} + ^ps_{12})^pd_{33}\,^pv - (^ps_{31} + ^ps_{32})(^ms_{11} + ^ms_{12})^pd_{31}\,^pv] \\ \times [^pd_{33}(^ps_{11} + ^ps_{12}) - 2^pd_{31}\,^ps_{13}]]\end{array}}$$

(51)

3.4. Case IV: clamped ends with no friction along traverse directions (axes 1 and 2) between the clamps and the sample with two phases perfectly bonded together

As shown in fig. 2(d) the composite in this case is a stacked arrangement of the magnetostrictive phase m and the piezoelectric phase p, clamped at both ends with thin layers of lubricant between the surfaces of the clamps and the sample in contact with each other in order to minimize the friction along axes 1 and 2, and the two phases are perfectly bonded with a glue. In this case the total transverse forces are zero, that is the force on each layer along the direction 1 or 2 is exactly equal and opposite of that in the other layer which gives us the eqs. (52) and (53) below. The stress along 3 in each layer are equal to each other which corresponds to eq. (54). Also the transverse strains in each layer is equal due to perfect bonding between the layers, which results in the eqs. (55) and (56) below.

$$^mv\,^mT_1 = -^pv\,^pT_1 ,$$

(52)

$$^mv\,^mT_2 = -^pv\,^pT_2 ,$$

(53)

$$^mT_3 = ^pT_3 ,$$

(54)

$$^mS_1 = ^pS_1 ,$$

(55)

$$^mS_2 = ^pS_2 .$$

(56)

Finally the total strain along 3 is zero due to the clamping and the electric displacement D is also zero due to the open circuit condition. Therefore

$$S_3 = ^mS_3\,^mv + ^pS_3\,^pv = 0 ,$$

(57)

$$D = 0 .$$

(58)

Now using the general strain expression (8) and since $^md_{ij} = 0$ and $^pq_{ij} = 0$ from eqs. (54) and (57) with the assumptions that $^mT_1 = ^mT_2$ and $^pT_1 = ^pT_2$, we have

$$(^ms_{31}\,^mT_1 + ^ms_{32}\,^mT_1 + ^ms_{33}\,^pT_3 + ^mq_{33}\,H_3)^mv + (^ps_{31}\,^pT_1 + ^ps_{32}\,^pT_1 + ^ps_{33}\,^pT_3 + ^pd_{33}\,E_3)^pv = 0 .$$

Substituting for eq. (52) from the above and on rearranging we get

$$[(^ps_{31} + ^ps_{32}) - (^ms_{31} + ^ms_{32})]^pv\,^pT_1 + (^ms_{33}\,^mv + ^ps_{33}\,^pv)^pT_3 + ^pd_{33}\,^pv E_3 = -^mq_{33}\,^mv H_3 .$$

(59)

Since $^mS_1 = ^pS_1$ from eq. (55) we have

$$({}^m s_{11} + {}^m s_{12}){}^m T_1 + {}^m s_{13}{}^p T_3 + {}^m q_{31} H_3 = ({}^p s_{11} + {}^p s_{12}){}^p T_1 + {}^p s_{13}{}^p T_3 + {}^p d_{31} E_3 . \tag{60}$$

From eq. (52) and on rearranging we get

$$-({}^m s_{11} + {}^m s_{12}){}^p v\,{}^p T_1 + ({}^m s_{13} - {}^p s_{13}){}^m v\,{}^p T_3 - ({}^p s_{11} + {}^p s_{12}){}^m v\,{}^p T_1 - {}^p d_{31}{}^m v E_3 = -{}^m q_{31}{}^m v H_3$$

$$\therefore \quad [({}^m s_{11} + {}^m s_{12}){}^p v + ({}^p s_{11} + {}^p s_{12}){}^m v]{}^p T_1 - ({}^m s_{13} - {}^p s_{13}){}^m v\,{}^p T_3 + {}^p d_{31}{}^m v E_3 = {}^m q_{31}{}^m v H_3 . \tag{61}$$

Since $D = 0$ we have

$$D_3 = 2\,{}^p d_{31}{}^p T_1 + {}^p d_{33}{}^p T_3 + {}^p \varepsilon^T_{33} E_3 = 0 ,$$

$$\therefore \quad {}^p T_1 = -({}^p \varepsilon^T_{33} E_3 + {}^p d_{33}{}^p T_3)/2\,{}^p d_{31} . \tag{62}$$

Substituting for ${}^p T_1$ from (62) in (59) we get

$$-[({}^p s_{31} + {}^p s_{32}) - ({}^m s_{31} + {}^m s_{32})]{}^p v({}^p \varepsilon^T_{33} E_3 + {}^p d_{33}{}^p T_3)$$
$$+ ({}^m s_{33}{}^m v + {}^p s_{33}{}^p v)2\,{}^p d_{31}{}^p T_3 + 2\,{}^p d_{31}{}^p d_{33}{}^p v E_3 = -2\,{}^p d_{31}{}^m q_{33}{}^m v H_3 .$$

After rearranging

$$[-[({}^p s_{31} + {}^p s_{32}) - ({}^m s_{31} + {}^m s_{32})]{}^p v\,{}^p d_{33} + ({}^m s_{33}{}^m v + {}^p s_{33}{}^p v)2\,{}^p d_{31}]{}^p T_3$$
$$+ [-[({}^p s_{31} + {}^p s_{32}) - ({}^m s_{31} + {}^m s_{32})]{}^p v\,{}^p \varepsilon^T_{33} + 2\,{}^p d_{31}{}^p d_{33}{}^p v]E_3 = -2\,{}^p d_{31}{}^m q_{33}{}^m v H_3 , \tag{63}$$

$$\therefore \quad {}^p T_3 = \frac{[[({}^p s_{31} + {}^p s_{32}) - ({}^m s_{31} + {}^m s_{32})]{}^p v\,{}^p \varepsilon^T_{33} - 2\,{}^p d_{31}{}^p d_{33}{}^p v]E_3 - 2\,{}^p d_{31}{}^m q_{33}{}^m v H_3}{[-[({}^p s_{31} + {}^p s_{32}) - ({}^m s_{31} + {}^m s_{32})]{}^p v\,{}^p d_{33} + ({}^m s_{33}{}^m v + {}^p s_{33}{}^p v)2\,{}^p d_{31}]} . \tag{64}$$

Substituting for ${}^p T_1$ from eq. (62) in eq. (61) we get

$$\therefore \quad -[({}^m s_{11} + {}^m s_{12}){}^p v + ({}^p s_{11} + {}^p s_{12}){}^m v]({}^p \varepsilon^T_{33} E_3 + {}^p d_{33}{}^p T_3)$$
$$- ({}^m s_{13} - {}^p s_{13}){}^m v 2\,{}^p d_{31}{}^p T_3 + 2({}^p d_{31})^2{}^m v E_3 = 2\,{}^p d_{31}{}^m q_{31}{}^m v H_3 .$$

After rearranging

$$\therefore \quad [-[({}^m s_{11} + {}^m s_{12}){}^p v + ({}^p s_{11} + {}^p s_{12}){}^m v]{}^p d_{33} - ({}^m s_{13} - {}^p s_{13}){}^m v 2\,{}^p d_{31}]{}^p T_3$$
$$+ [-[({}^m s_{11} + {}^m s_{12}){}^p v + ({}^p s_{11} + {}^p s_{12}){}^m v]{}^p \varepsilon^T_{33} + 2({}^p d_{31})^2{}^m v]E_3 = 2\,{}^p d_{31}{}^m q_{31}{}^m v H_3 . \tag{65}$$

Substituting for ${}^p T_3$ from eq. (64) in eq. (65) we get

$$\therefore \quad [-[({}^m s_{11} + {}^m s_{12}){}^p v + ({}^p s_{11} + {}^p s_{12}){}^m v]{}^p d_{33} - ({}^m s_{13} - {}^p s_{13}){}^m v 2\,{}^p d_{31}]$$
$$\times [[({}^p s_{31} + {}^p s_{32}) - ({}^m s_{31} + {}^m s_{32})]{}^p v\,{}^p \varepsilon^T_{33} - 2\,{}^p d_{31}{}^p d_{33}{}^p v]E_3$$
$$- 2\,{}^p d_{31}{}^m q_{33}{}^m v[-[({}^m s_{11} + {}^m s_{12}){}^p v + ({}^p s_{11} + {}^p s_{12}){}^m v]{}^p d_{33} - ({}^m s_{13} - {}^p s_{13}){}^m v 2\,{}^p d_{31}]H_3$$
$$+ [-[({}^m s_{11} + {}^m s_{12}){}^p v + ({}^p s_{11} + {}^p s_{12}){}^m v]{}^p \varepsilon^T_{33} + 2({}^p d_{31})^2{}^m v]$$
$$\times [-[({}^p s_{31} + {}^p s_{32}) - ({}^m s_{31} + {}^m s_{32})]{}^p v\,{}^p d_{33} + ({}^m s_{33}{}^m v + {}^p s_{33}{}^p v)2\,{}^p d_{31}]E_3$$
$$= 2\,{}^p d_{31}{}^m q_{31}{}^m v[-[({}^p s_{31} + {}^p s_{32}) - ({}^m s_{31} + {}^m s_{32})]{}^p v\,{}^p d_{33} + ({}^m s_{33}{}^m v + {}^p s_{33}{}^p v)2\,{}^p d_{31}]H_3 .$$

After rearranging

$$\therefore \quad [[-[({}^m s_{11} + {}^m s_{12}){}^p v + ({}^p s_{11} + {}^p s_{12}){}^m v]{}^p d_{33} - ({}^m s_{13} - {}^p s_{13}){}^m v 2\,{}^p d_{31}]$$
$$\times [[({}^p s_{31} + {}^p s_{32}) - ({}^m s_{31} + {}^m s_{32})]{}^p v\,{}^p \varepsilon^T_{33} - 2\,{}^p d_{31}{}^p d_{33}{}^p v]$$
$$+ [-[({}^m s_{11} + {}^m s_{12}){}^p v + ({}^p s_{11} + {}^p s_{12}){}^m v]{}^p \varepsilon^T_{33} + 2({}^p d_{31})^2{}^p v]$$

$$\times [-[(^{P}s_{31} + {}^{P}s_{32}) - (^{m}s_{31} + {}^{m}s_{32})]^{P}v\,{}^{P}d_{33} + (^{m}s_{33}{}^{m}v + {}^{P}s_{33}{}^{P}v)2\,{}^{P}d_{31}]]E_3$$

$$= [{}^{m}q_{31}[-[(^{P}s_{31} + {}^{P}s_{32}) - (^{m}s_{31} + {}^{m}s_{32})]^{P}v\,{}^{P}d_{33} + (^{m}s_{33}{}^{m}v + {}^{P}s_{33}{}^{P}v)2\,{}^{P}d_{31}]$$

$$+ {}^{m}q_{33}[-[(^{m}s_{11} + {}^{m}s_{12})^{P}v + (^{P}s_{11} + {}^{P}s_{12})^{m}v]^{P}d_{33} - (^{m}s_{13} - {}^{P}s_{13})^{m}v\,2\,{}^{P}d_{31}]]2\,{}^{P}d_{31}{}^{m}v\,H_3 \ .$$

Now the magnetoelectric voltage coefficient is

$$\alpha_{(E)33} = E_3/H_3 \ ,$$

$$\therefore \quad \alpha_{(E)33} = \frac{\begin{array}{l}[{}^{m}q_{31}[-[(^{P}s_{31} + {}^{P}s_{32}) - (^{m}s_{31} + {}^{m}s_{32})]^{P}v\,{}^{P}d_{33} + (^{m}s_{33}{}^{m}v + {}^{P}s_{33}{}^{P}v)2\,{}^{P}d_{31}]\\ + {}^{m}q_{33}[-[(^{m}s_{11} + {}^{m}s_{12})^{P}v + (^{P}s_{11} + {}^{P}s_{12})^{m}v]^{P}d_{33} - (^{m}s_{13} - {}^{P}s_{13})^{m}v\,2\,{}^{P}d_{31}]]2\,{}^{P}d_{31}{}^{m}v\end{array}}{\begin{array}{l}[[-[(^{m}s_{11} + {}^{m}s_{12})^{P}v + (^{P}s_{11} + {}^{P}s_{12})^{m}v]^{P}d_{33} - (^{m}s_{13} - {}^{P}s_{13})^{m}v\,2\,{}^{P}d_{31}]\\ \times [[(^{P}s_{31} + {}^{P}s_{32}) - (^{m}s_{31} + {}^{m}s_{32})]^{P}v\,{}^{P}\varepsilon^{T}_{33} - 2\,{}^{P}d_{31}\,{}^{P}d_{33}\,{}^{P}v]\\ + [-[(^{m}s_{11} + {}^{m}s_{12})p_v + (^{P}s_{11} + {}^{P}s_{12})^{m}v]^{P}\varepsilon^{T}_{33} + 2(^{P}d_{31})^{2\,m}v]\\ [-[(^{P}s_{31} + {}^{P}s_{32}) - (^{m}s_{31} + {}^{m}s_{32})]^{P}v\,{}^{P}d_{33} + (^{m}s_{33}{}^{m}v + {}^{P}s_{33}{}^{P}v)2\,{}^{P}d_{31}]]\end{array}} \tag{66}$$

Thus the ME coefficients for four cases of 2–2 composites have been derived. Fig. 3 shows all other possible variations of these by having the magnetic field an the electric field in different directions instead of parallel to each other along 3 axis as was considered in above cases. However these cases do not yield much different results other than only the coefficients $^{m}q_{31}$ and $^{m}q_{33}$, and $^{P}d_{31}$ and $^{P}d_{33}$ will be interchanged in the final expressions. Since the above cases were simple stacking of the two phases and since it is not difficult to measure the E_3 field developed across the piezoelectric phase in actual composites, E_3 field has been taken as the one developed across the piezoelectric layer only and not the whole composite.
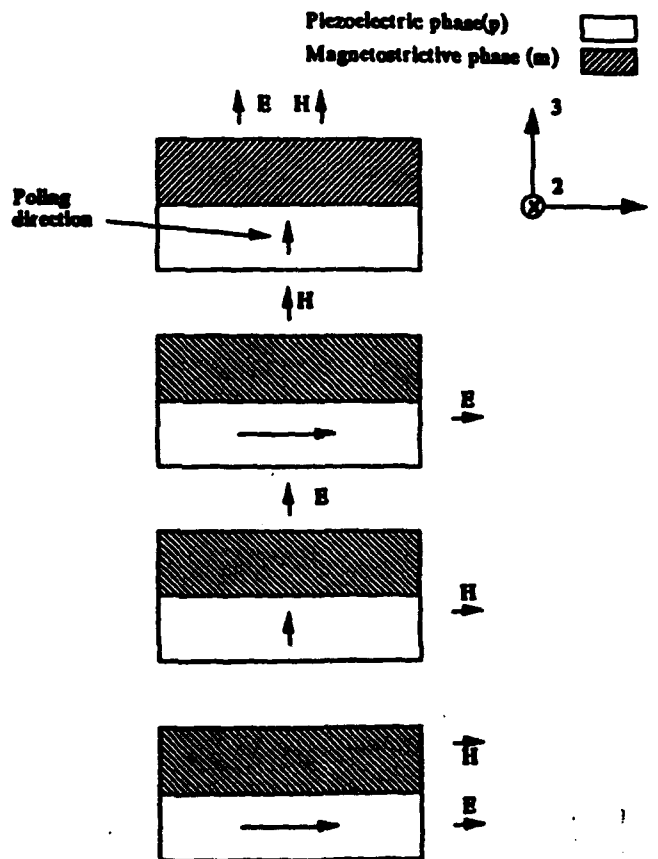

Fig. 3. Possible variations of 2–2 composites due to different directions of E and H.

Table 2

Properties of different materials used for calculations of ME effect in composites [8-10]. ${}^m q$: piezomagnetic coefficient. ${}^p d$: piezoelectric coefficient, ϵ: dielectric permittivity, ϵ^T: dielectric permittivity at constant stress for piezoelectric materials, s: compliance coefficient, s^E: compliance coefficient at constant electric field for piezoelectric material

Material	CoFe₂O₄	BaTiO₃	PZT-4	PZT-5A	PZT-5H	PZT-8
${}^m q_{31}$ [10^{-12} m/A]	556	-	-	-	-	-
${}^m q_{33}$ [10^{-12} m/A]	1880	-	-	-	-	-
${}^p d_{31}$ [10^{-12} C/N]	-	-78	-123	-171	-274	-90
${}^p d_{33}$ [10^{-12} C/N]	-	190	289	374	593	225
s_{11} or s^E_{11} [10^{-12} m²/N]	6.48	7.25	12.3	16.4	16.5	11.5
s_{12} or s^E_{12} [10^{-12} m²/N]	-2.37	-3.15	-4.05	-5.74	-4.78	-3.7
s^E_{13} [10^{-12} m²/N]	-	-3.26	-5.31	-7.22	-8.45	-4.8
s^E_{33} [10^{-12} m²/N]	-	10.8	15.5	18.8	20.7	13.5
ϵ_{33}/ϵ_0 or $\epsilon^T_{33}/\epsilon_0$	10	1345	1300	1700	3400	1000

Table 3

Magnetoelectric voltage coefficients in $(V/m)/(A/m)$ for 2-2 composites of different materials calculated using theoretical models: ${}^m v$ is the volume fraction of piezomagnetic phase; ${}^p v$ is the volume fraction of piezoelectric phase; $\alpha_{(E)33}$ is the ME voltage per unit thickness of the piezoelectric phase; $\alpha^*_{(E)33}$ is the ME voltage coefficient per unit thickness of the composite obtained by multiplying $\alpha_{(E)33}$ by the volume fraction of the piezoelectric phase ${}^p v$

${}^m v$	${}^p v$	Case I		Case II		Case III		Case IV	
		$\alpha_{(E)33}$	$\alpha^*_{(E)33}$	$\alpha_{(E)33}$	$\alpha^*_{(E)33}$	$\alpha_{(E)33}$	$\alpha^*_{(E)33}$	$\alpha_{(E)33}$	$\alpha^*_{(E)33}$
CoFe₂O₄ and BaTiO₃									
0.10	0.90	0.184	0.166	-0.391	-0.352	-0.181	-0.162	-0.191	-0.172
0.30	0.70	0.583	0.408	-1.214	-0.850	-0.573	-0.401	-0.612	-0.428
0.50	0.50	1.028	0.514	-2.097	-1.048	-1.015	-0.508	-1.094	-0.547
0.70	0.30	1.526	0.458	-3.046	-0.914	-1.516	-0.455	-1.648	-0.494
0.90	0.10	2.089	0.209	-4.071	-0.407	-2.088	-0.209	-2.288	-0.229
CoFe₂O₄ and PZT-4									
0.10	0.90	0.284	0.256	-0.586	-0.527	-0.329	-0.296	-0.292	-0.263
0.30	0.70	0.796	0.557	-1.837	-1.286	-1.084	-0.759	-1.032	-0.722
0.50	0.50	1.244	0.622	-3.208	-1.604	-2.000	-1.000	-1.977	-0.989
0.70	0.30	1.640	0.492	-4.717	-1.415	-3.135	-0.941	-3.135	-0.940
0.90	0.10	1.992	0.199	-6.386	-0.639	-4.580	-0.458	-4.518	-0.452
CoFe₂O₄ and PZT-5A									
0.10	0.90	0.294	0.265	-0.508	-0.457	-0.278	-0.250	-0.246	-0.221
0.30	0.70	0.786	0.550	-1.631	-1.142	-0.921	-0.645	-0.877	-0.614
0.50	0.50	1.182	0.591	-2.924	-1.462	-1.717	-0.858	-1.699	-0.849
0.70	0.30	1.508	0.452	-4.429	-1.329	-2.727	-0.818	-2.726	-0.818
0.90	0.10	1.780	0.178	-6.202	-0.620	-4.050	-0.405	-3.992	-0.399
CoFe₂O₄ and PZT-5H									
0.10	0.90	0.236	0.212	-0.423	-0.381	-0.234	-0.211	-0.217	-0.195
0.30	0.70	0.632	0.442	-1.347	-0.943	-0.767	-0.537	-0.746	-0.522
0.50	0.50	0.951	0.475	-2.391	-1.196	-1.406	-0.703	-1.400	-0.700
0.70	0.30	1.21	0.364	-3.582	-1.075	-2.188	-0.656	-2.187	-0.656
0.90	0.10	1.43	0.143	-4.952	-0.495	-3.165	-0.317	-3.122	-0.312
CoFe₂O₄ and PZT-8									
0.10	0.90	0.291	0.262	-0.625	-0.562	-0.356	-0.321	-0.332	-0.298
0.30	0.70	0.813	0.569	-1.940	-1.358	-1.156	-0.809	-1.125	-0.788
0.50	0.50	1.26	0.634	-3.352	-1.676	-2.096	-1.048	-2.087	-1.043
0.70	0.30	1.66	0.501	-4.870	-1.461	-3.217	-0.965	-3.216	-0.965
0.90	0.10	2.02	0.202	-6.508	-0.651	-4.578	-0.458	-4.514	-0.451

4. Results and discussion

Table 2 gives the coefficients for various materials used for calculations using the formulae derived above. The ME coefficient $\alpha_{(E)33}$ values, have been calculated for composites of piezoelectric $BaTiO_3$, or $Pb(Zr,Ti)O_3$ with magnetostrictive $CoFe_2O_4$. Table 3 shows the results of the calculations for different volume fractions. These models suggest that theoretically, a large ME effect can be obtained as shown by the calculations of $\alpha_{(E)33}$ values. The values show maxima at 50–50 vol% composition for each composite. Composite of Co ferrite with PZT-8 shows the largest ME effect under the boundary conditions of Case II namely, $\alpha_{(E)33} = -1.676$ (V/m)/(A/m) which is equal to 1.34 (V/cm Oe). That is, when such a composite is placed in a magnetic field of 1 Oe (79.58 A/m) the voltage generated across a sample of thickness is 1.34 V.

The effect of dielectric constant variation and piezoelectric coefficient variation on the ME voltage coefficient is shown in figs. 4 and 5. The graphs in fig. 4 show that as the ε value increases, the $\alpha_{(E)33}$ value decreases rapidly. This is obvious because the ME voltage coefficient is inversely proportional to the dielectric constant. The effect of piezoelectric coefficient variation is reported as the extent of poling since for calculation purpose it was necessary to assume different values for both, d_{31} and d_{33} which is equivalent to considering partially poled composite. The dependence of $\alpha_{(E)33}$ on the extent of poling shows more or less a linear behavior.

Magnetoelectric coupling coefficient (k_{ME}) cannot be predicted using the mechanical coupling coefficients for the piezomagnetic an piezoelectric materials because the boundary conditions are different for the single phase materials and for the composite.

We have prepared multilayer ME composites of $CoFe_2O_4$–PZT which showed encouraging results [11, 12]. Table 4 compares the experimental values of the ME voltage coefficients with the theoretical values, for three different types of multilayer composites, for free body type boundary conditions (Case I). The experimental values are lower because the composites could not be poled completely (in $CoFe_2O_4$:PZT4) or the presence of the bonding medium at the interface (in $CoFe_2O_4$:PZT8 and $CoFe_2O_4$:PZT5H) reduced the stress-strain interaction of the layers of the two phases. The maximum ME voltage coefficient $\alpha_{(E)33}$ was 92.8 (V/m)/(kA/m) in the case of cofired multilayer composites of $CoFe_2O_4$:PZT4.
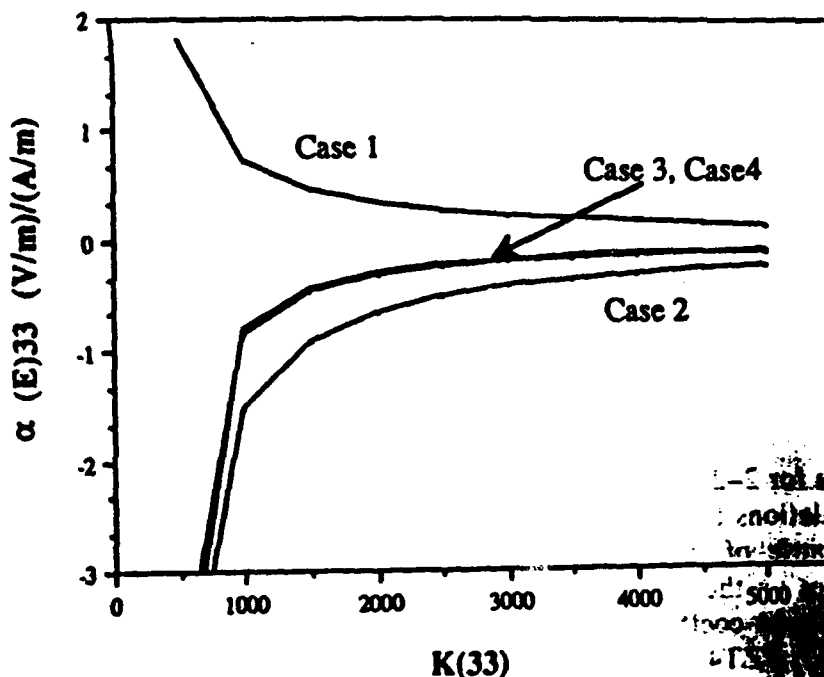

Fig. 4. Effect of dielectric constant variation on the ME coefficient.
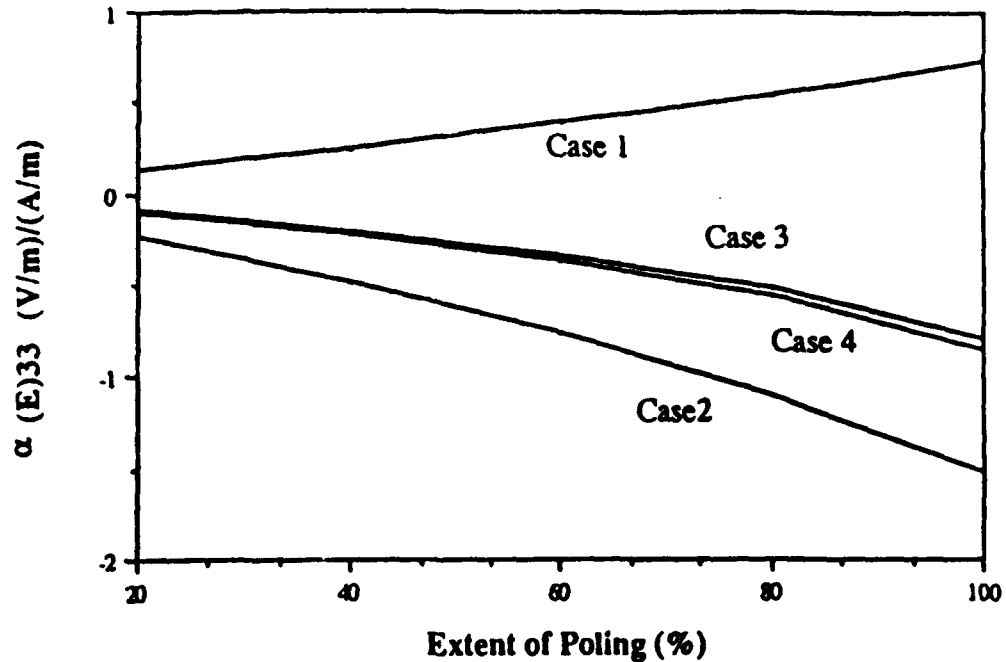
Fig. 5. Effect of extent of poling on the magnetoelectric coefficient.

Table 4
Experimental values of magnetoelectric voltage coefficients for mechanically bonded and cofired multilayer composites at 1 kH
$H_{ac} = 0.35$ kA/m, $H_{dc} = 39.78$ to 1193 kA/m

Materials	Piezoelectric coefficient d_{33} [10^{-12} C/N]	Maximum ME coefficient $\alpha_{(E)33}$ [(V/m)/(kA/m)]	Theoretical ME coefficient $\alpha_{(E)33}$ [(V/m) (kA/m]
CoFe$_2$O$_4$:PZT-4 (tape cast)	140	92.8	199 to 622
CoFe$_2$O$_4$:PZT-8 (glued thick disks)	285	18.6	202 to 634
CoFe$_2$O$_4$:PZT-5H (thin disks bimorph)	550	74.4	143 to 475

5. Conclusions

Theoretical models for 2-2 ME composites have been developed for four different sets of bounda conditions. The calculations for different composites show that large voltages can be generated acro such composites because of the product property, magnetoelectricity. The effect of dielectric ar piezoelectric properties on the ME properties has been studied. The experimental results showed th the maximum ME voltage coefficient $\alpha_{(E)33}$ was 92.8 (V/m)/(kA/m) in the case of cofired multilay composites of CoFe$_2$O$_4$:PZT4.

ferences

] J. van Suchtelen, Philips Res. Rep. 27 (1972) 28.
] R.E. Newnham, D.P. Skinner and L.E. Cross, Mater. Res. Bull. 13 (1978) 525.
] J. van den Boomgaard, D.R. Terrell, R.A.J. Born and H.F.J.I. Giller, J. Mater. Sci. 9 (1974) 1705;
   A.M.J.G. van Run, D.R. Terrell and J.H. Scholing, J. Mater. Sci. 9 (1974) 1710.
] J. van den Boomgaard, A.M.J.G. van Run and J. van Suchtelen, Ferroelectrics 10 (1976) 295.
] J. van den Boomgaard, A.M.J.G. van Run and J. van Suchtelen, Ferroelectrics 14 (1976) 227.
] J. van den Boomgaard and R.A.J. Born, J. Mater. Sci. 13 (1978) 1538.
] A.S. Zubkov, Elektrichestvo 10 (1978) 77.
] Landolt-Börnstein; Numerical Data and Functional Relationships in Science and Technology, Group III, Crystal and Solid State Physics 4, Magnetic and Other Properties of Oxides, eds. K.-H. Hellwege and A.M. Hellwege (Springer, New York, 1970).
] Landolt-Börnstein; Numerical Data and Functional Relationships in Science and Technology, New Series, Group III, Crystal and Solid State Physics 16/a, Ferroelectrics and Related Substances, eds. K.-H. Hellwege and A.M. Hellwege (Springer, New York, 1981).
0] Vernitron; Piezoelectric Technology, Data for Designers, Vernitron Piezoelectric Division.
1] G.R. Harshé, Magnetoelectric Effect in Piezoelectric-Magnetostrictive Composites, Ph.D. Thesis, The Pennsylvania State University, University Park, PA, USA (1991).
2] G. Harshé, J.P. Dougherty and R.E. Newnham, in: Proc. of Symp. on Smart Structures and Materials, 1–4 February 1993, Albuquerque, NM, USA, in press.

APPENDIX 29

Electromechanical Properties of Smart Materials

R. E. NEWNHAM* AND GREGORY R. RUSCHAU
Materials Research Laboratory
Pennsylvania State University
University Park, PA 16802

ABSTRACT: A smart material is one that can perform both sensor and actuator functions. This definition allows for some flexibility in deciding how to qualify a material as "smart", since the fundamental mechanisms of operation may differ greatly between types of smart materials. From the point of view of an electroceramist, piezoelectric materials, which show reversible electromechanical coupling, may be thought of as "naturally" smart materials since the same piezoelectric material may act as a sensor and/or an actuator. Piezoelectric single crystals, polymers, and poled polycrystalline ceramics all show good electromechanical coupling. In addition, they may be combined in a composite material that exaggerates their beneficial properties by eliminating their detrimental properties. Some common piezoelectric materials are reviewed, along with some examples of smart materials that incorporate piezoelectric ceramics.

INTRODUCTION

THE concept of creating a higher form of materials and structures by providing the necessary life functions of sensing, actuating, control, and intelligence to those materials is a prime motivation for studying smart materials. Smart materials are part of smart systems—functional materials for a wide variety of engineering applications.

This notion of a smart system has implications in a number of otherwise unrelated areas: smart medical systems for the treatment of diabetes with blood sugar sensors and insulin delivery pumps; smart airplane wings that achieve greater fuel efficiency by altering their shape in response to air pressure and flying speed; smart toilets that analyze urine as an early warning system for health problems; smart structures in outer space incorporating vibration cancellation systems that compensate for the absence of gravity and prevent metal fatigue; smart houses with electrochromic windows that control the flow of heat and light in response to weather changes and human activity; smart tennis rackets with rapid internal adjustments for overhead smashes and delicate drop shots; smart muscle implants made from rubbery gels that respond to electric fields; smart dental braces made from shape memory alloys; smart hulls and propulsion systems for navy ships and submarines that detect flow noise, remove turbulence, and prevent detection; and smart water purification systems that sense and remove noxious pollutants.

To begin our discussion, we first define "smart" to set the limits for classifying smart materials. In the simplest terms, a smart material is not simply an actuator or a sensor, but a material that performs *both* functions. It is a material that senses not only a change in its environment, but also responds to that change in some positive, useful way. There

are many degrees of smartness possible in materials; often, a merely "smart" material can be engineered into a "very smart" tunable device or even an "intelligent" material, where the sensor and actuator functions are integrated with the information processing chip. Many modern day materials have been cleverly designed to carry out useful functions, and, it seems that we are justified in calling them "smart". They are decidedly better than the "sensible" materials of the past.

One distinction that should be made immediately is that of passive as opposed to active smartness. A *passively smart material* has the ability to respond to environmental conditions in a useful manner, often incorporating self-repair mechanisms or stand-by phenomena which enable the material to withstand sudden changes in its surroundings. Ceramic varistors and PTC thermistors are good examples of passively smart materials. When struck by high-voltage lightning, a zinc oxide varistor loses most of its electrical resistance and the current is by-passed to the ground. The resistance change is reversible and acts as a stand-by protection phenomenon. In a similar way, barium titanate PTC thermistors show a very large increase in electrical resistance at the ferroelectric phase transformation near 130°C. The jump in resistance enables the thermistor to arrest current surges, acting as a protection element.

An *actively smart material* senses a change in the environment, and using a feedback system, makes a useful response. Again, it is both a sensor and an actuator. One example of this is the electrically controlled automobile suspension system currently produced by Toyota for their Lexus line [1]. A piezoelectric sensor detects road irregularities and feeds the signal into a piezoelectric actuator system, which automatically resets the suspension to compensate for the irregularity. The whole process takes only a few milliseconds, thus continuously damping bumps and dips to give a smooth ride.

Two schools of thought exist in the development of smart

*Author to whom correspondence should be addressed.

materials. One of these involves the integration of dissimilar components performing separate functions into one device, either as an integrated circuit or as a bulk composite material. In this type of approach, the individual material properties are well defined; the challenge lies in maintaining these properties during the co-processing, and packaging into an individual unit.

The other approach is to discover or develop materials that can intrinsically perform both sensor and actuator functions. Piezoelectric ceramics, which have the ability to convert mechanical energy into electrical energy and vice versa, fit into this category. It is this dual-function capability that allows them to perform both sensor and actuator functions; thus, these are intrinsically smart materials. Although many materials exhibit piezoelectricity, it is the magnitude and the efficiency of the electromechanical coupling in these materials that ultimately determines their suitability as smart materials.

MATERIALS FOR ELECTROMECHANICAL COUPLING

History of Piezoelectricity

Piezoelectricity, according to the original definition of the phenomenon discovered by J. and P. Curie in 1880 [2], is the ability of certain crystalline materials to develop an electric charge that is proportional to a mechanical stress. Very soon after this discovery, it was realized that the converse effect, that of a geometric strain developing upon the application of a voltage, was also inherent in these materials. Thus, in dealing with piezoelectrics, we speak of the direct piezoelectric effect and the converse piezoelectric effect.

The variety of crystals that exhibit piezoelectricity have one common feature: the absence of a center of symmetry within the crystal. This absence of symmetry gives rise to polarity, the "one-wayness" of the charge vector. Piezoelectricity is therefore limited to 20 of the 32 crystal classes, known as point groups, for all crystalline materials. Most of the important piezoelectric materials are also ferroelectric, which results in a transformation to a high symmetry, non-piezoelectric phase at higher temperatures. The piezoelectric effect is present only in the lower temperature phase, and the transformation temperature is known as the Curie temperature.

For some time after the discovery of piezoelectricity, the effect was thought to be limited to single crystals, because polycrystalline materials have randomly oriented grains that cancel each other, resulting in a zero net effect. In the 1940s, the discovery of high dielectric constant ceramics with the perovskite structure was soon followed by the development of the poling process, in which the randomly oriented domain pattern is given a high degree of orientation by the application of a strong electric field at elevated temperatures. The resulting polycrystalline material has a high net piezoelectric effect, and thus today we speak of piezoelectric ceramics more frequently than piezoelectric crystals.

Coupling Coefficients

The direct piezoelectric effect, as previously stated, is the development of an electric charge upon the application of a mechanical stress. The electric polarization, P, is the charge per unit area, and is related to the stress, σ, by the piezoelectric coupling coefficient, d:

$$P = d\sigma \qquad (1)$$

For the converse effect, the strain (S) produced by an applied electric field (E) is given by:

$$S = dE \qquad (2)$$

In both cases, the coefficient d is numerically identical. Another important constant, the voltage coefficient (g), describes the electric field produced by a stress, and is related to d through the permittivity (ϵ):

$$g = d/\epsilon \qquad (3)$$

A high d constant is desirable for actuator materials that are intended to develop motion or vibration, such as high power sonar, while a high g constant is desirable for sensor materials in which high voltages are to be generated from weak mechanical stresses, such as in a phonograph needle.

Another significant coefficient is the electromechanical coupling factor, k, which measures the efficiency of the electromechanical conversion. It is defined in terms of k^2, the fraction of electrical energy converted to mechanical energy, or vice versa. Since this conversion can never be complete, k and k^2 are always <1.

Because piezoelectric crystals are necessarily asymmetric, the coupling coefficients are given in tensor form. The first subscript of the tensor gives, by convention, the direction of the electric field or polarization, while the second gives the component of mechanical stress or deformation. Due to the sometimes competing piezoelectric effect in various directions within the crystal, we must identify the important coupling coefficient tensors for smart materials. For a number of applications, it is possible to select the appropriate candidate material by comparing the magnitude of the coupling coefficients.

Piezoelectric Materials

Table 1 lists the intrinsic piezoelectric properties of some common piezoelectric materials. The first three represent three completely different classes of materials: single crystals, polymers, and poled ceramics. A fourth class, composite piezoelectrics, will be discussed in the next section.

Quartz, the low temperature form of single crystal SiO_2, is the classic example of the piezoelectric single crystal. Figure 1(a) shows the transformation of quartz from its high temperature and high symmetry β form to the low temperature, lower symmetry α form at 573°C. Quartz crystals are grown from hydrothermal solutions, and these crystals can be cut in precise orientation for use as time and frequency standards.

PVDF, or polyvinylidine fluoride, is a piezoelectric polymeric material. The polarization arises from the asymmetric F^- and H^+ side groups, which create electric dipoles perpendicular to the carbon backbone [Figure 1(b)]. While the d coefficients are quite low for PVDF, the low dielectric

Table 1. Room temperature piezoelectric properties of selected materials.

Material	T_{cure} (°C)	d_{33} ($\times 10^{-12}$ C/N)	g_{33} ($\times 10^{-3}$ C/N)	ϵ	$d_h g_h$ ($\times 10^{-15}$ C/N)
Quartz (SiO$_2$)	573	-2.3^*	-57.5^*	4	0
PVDF	41	30	200	15	9
PZT 52/48	386	223	39.5	1500	200
PLZT 8/65/35	65	682	20	3400	—
BaTiO$_3$	125	191	11.4	2000	88
PbNb$_2$O$_6$	560	85	42	250	20

*Actually d_{11} and g_{11}, but for comparison purposes they are equivalent.

constant results in large g coefficients relative to other piezoelectrics.

PZT, or Pb(Zr,Ti)O$_3$, is the prototypical piezoelectric ceramic, and represents the largest portion of the commercial market for electromechanical transducers due to its high coupling coefficients and its versatility with regard to chemical substitutions. The 52/48 designation is for the composition PbZr$_{0.52}$Ti$_{0.48}$O$_3$, which lies at the morphotropic phase boundary on the PbZrO$_3$–PbTiO$_3$ phase diagram. Compositions near this boundary exhibit the greatest electromechanical coupling coefficients due to the fact that they are on the verge of instability. Many tailor-made piezoelectric properties can result from small compositional modifications on the basic PZT-based ceramics. For example, lanthanum-doped PZT, known as PLZT, is an extraordinary electrooptic material.

Composite Strategies

Too often in the field of materials research, we put too much emphasis on the synthesis of new materials and too little emphasis on new and unique designs for old materials. Because all piezoelectric materials have some inherent limitations for certain applications, it becomes necessary to modify these materials in order to take advantage of the beneficial properties, while cancelling or limiting the detrimental properties. An effective means by which to accomplish this is in a composite material with controlled connectivity.

Connectivity in a composite may be defined as the way in which the different phases are arranged, and designated by numbers such as 1–3, 3–2, etc. The numbers represent the number of dimensions in which each phase is self-connected. Figure 2 shows some different composite connectivities, each with specific advantages over single-phase materials for certain applications.

One example of the advantage of the composite strategy is the use of PZT-based composites for hydrophone materials. The figure of merit for hydrophone materials is the product of the hydrostatic piezoelectric charge coefficient (d_h) and the piezoelectric voltage coefficient (g_h). While PZT has high d_{33} and d_{31} piezoelectric coupling coefficients, the d_h value is only about 45 pC/N because d_{33} and d_{31} are opposite in sign, and $d_h = d_{33} + 2d_{31}$. $d_h g_h$ is also inversely related to the dielectric permittivity, ϵ, so that low dielectric constants are desirable as well.

A composite design with 1–3 connectivity [Figure 2(a)] consists of thin PZT rods embedded in a polymer matrix.

The 1–3 piezocomposites have excellent sensitivity to pressure waves in water. The large d_{33} is maintained because the parallel connection results in stress transfer from polymer to piezoceramic, while the d_{31} is destroyed because of series connection in the lateral dimension where the mechanical load is absorbed by the polymer and not transferred to the PZT rods. Finally, ϵ is minimized due to the large volume fraction of polymer present in the composite [3–4].

Another piezoelectric hydrophone [Figure 2(d)] composite maximizes d_h by simply re-directing the applied stresses using specially shaped electrodes. These are flextensional transducers with shallow air spaces positioned under the metal electrodes and a PZT ceramic disc. When subjected to a hydrostatic stress because of waves, the thick metallic electrodes convert a portion of the z-direction stress into large radial and tangential stresses of opposite signs. The result is that d_{31} changes from negative to positive, so that its contribution now adds to d_{33} rather than subtracting from it. The $d_h g_h$ of these composites is approximately 250 times that of pure PZT [5].

EXAMPLES OF SMART MATERIALS USING PIEZOELECTRICS

Two examples of smart piezoelectric materials are shown: in Figure 3(a) the "soft" ceramic, and in Figure 3(b) the tunable transducer.

Controlled Compliance and Soft Ceramics

For the first of these examples, a PZT sensor/actuator combination is used to produce "soft" ceramics, in which the sensor feels a stress and an actuator retracts the ceramic, giving the ceramic a rubber-like feel. In the controlled compliance test setup, one actuator is used as the external driver, and the other is used as the responder [6]. Sandwiched between the two actuator stacks are two sensors and a layer of rubber. The upper actuator is driven at a frequency of 100 Hz and the vibrations are monitored with the upper sensor. The pressure wave emanating from the driver passes through the upper sensor and the rubber separator and impinges on the lower sensor. The resulting signal is amplified using a low noise amplifier and fed back through a phase shifter to the lower actuator to control the compliance.

A smart sensor-actuator system can mimic a very stiff solid or a very compliant rubber. This can be done while retaining great strength under static loading, making the smart material especially attractive for vibration control.

O = Si at 0
● = Si at 1/3
● = Si at 2/3

(a)

● = carbon   ● = fluorine
O = hydrogen

(b)

● = Zr, Ti
● = Pb
○ = O

(c)
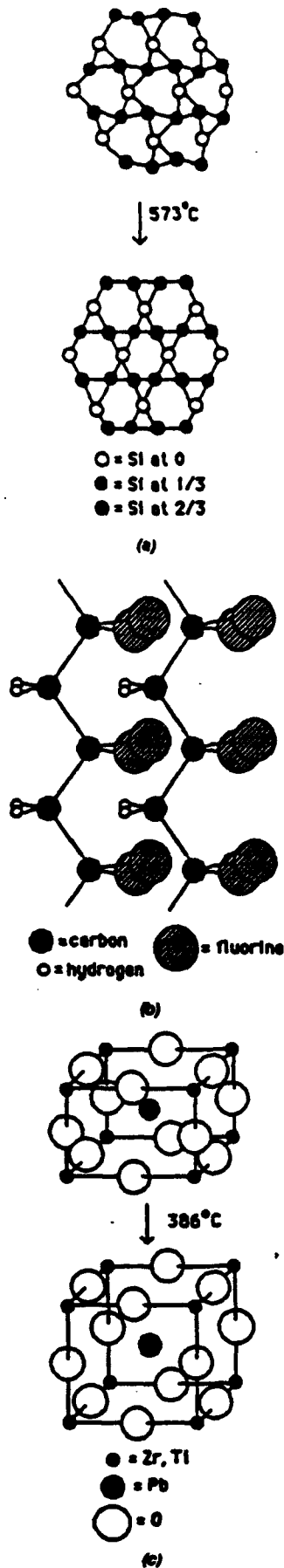
Figure 1. The crystal structure of (a) quartz, (b) polyvinylidine fluoride (PVDF), and (c) PZT.

(a)   (b)

(c)   (d)
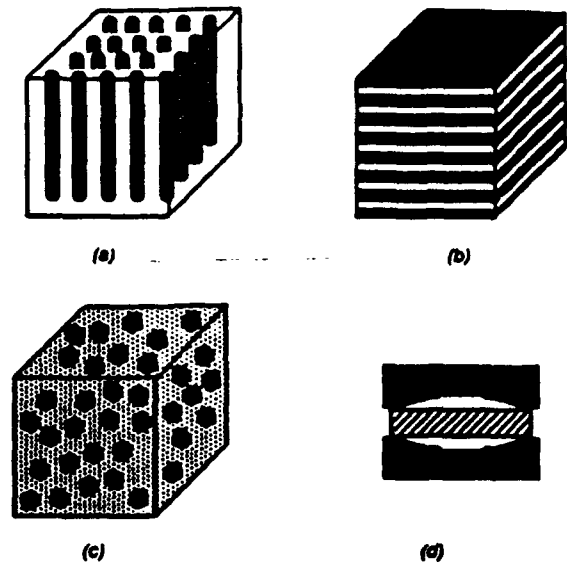
Figure 2. Different connectivities in composite materials. (a) 1–3 connectivity, with rods embedded in a continuous matrix; (b) 2–2 connectivity, found in multilayer ceramic capacitors and actuators; (c) 0–3 connectivity, useful in composite thermistors and chemical sensors; (d) the Moonie 2–2 composite, an advanced piezoelectric sensor and actuator.

STRESS
SENSOR
FEEDBACK AMPLIFIER
MULTILAYER ACTUATOR

(a)

STRESS BOLT
BRASS
RUBBER LAYER
PZT
RUBBER LAYER
BRASS
STRESS BOLT

(b)
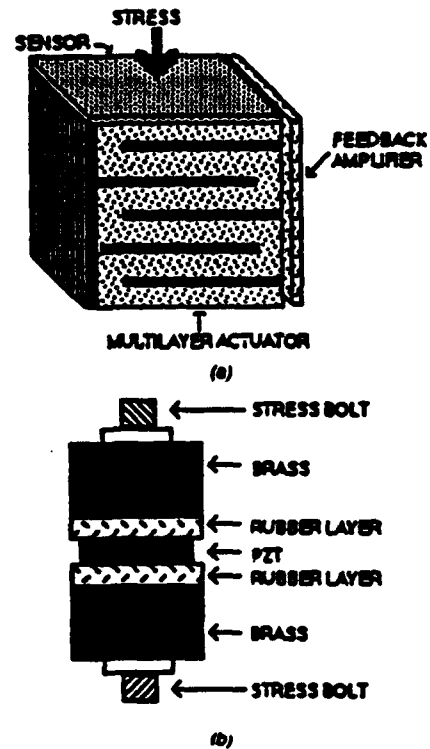
Figure 3. Examples of piezoelectric-based smart materials. (a) The "soft" ceramic, (b) the tunable transducer.

If the phase of the feedback voltage is adjusted to cause the responder to contract in length rather than expand. the smart material mimics a very soft, compliant substance. This reduces the force on the sensors and partially eliminates the reflected signal. The reduction in output signal of the upper sensor is a measure of the effectiveness of the feedback system.

Very Smart Materials—The Tunable Transducer

By building in a learning function, the definition of a smart material can be extended to a higher level of intelligence: a *very smart material* senses a change in the environment and responds by altering one or more of its property coefficients. Such a material can tune its sensor and actuator functions in time and space to optimize future behavior. With the help of a feedback system, a very smart material becomes smarter with age, something even human beings strive for. The distinction between smart and very smart materials is essentially one between linear and nonlinear properties. The physical properties of nonlinear materials can be adjusted by bias fields or forces to control response.

The second example illustrates the concept of a very smart material, the tunable transducer developed recently in our laboratory. Applications for transducers include fish finders, gas igniters, ink jets, micropositions, biomedical scanners, piezoelectric transformers and filters, accelerometers, and motors.

The resonant frequency of a tunable transducer can be adjusted over a wide range, giving it characteristics analogous to FM radio. Information is transmitted on electromagnetic waves in two ways: amplitude modulation (AM) and frequency modulation (FM). There are a number of advantages to FM signal processing, especially where lower noise levels are important. Atmospheric static is considerably lower in FM radio than in AM.

Signal-to-noise ratios are also important in the ultrasonic systems used in biomedical and nondestructive testing systems, but FM-modulation is difficult because resonant frequencies are controlled by stiffness (c) and (transducer) dimensions (t). Neither c, t, nor the density (ϱ) can be tuned significantly in ceramics and most other materials, but rubber is an exception. To tune the resonant frequency of a piezoelectric transducer, we designed and built a composite transducer incorporating thin rubber layers exhibiting nonlinear elasticity.

Rubber is a highly nonlinear elastic medium. In the unstressed compliant state, the molecules are coiled and tangled, but under stress, the molecules align and the material stiffens noticeably. Experiments carried out on rubber-metal laminates demonstrate the size of the nonlinearity. Young's modulus ($E = 1/s_{1111}$) was measured for a multilayer laminate consisting of alternating steel shim and soft rubber layers, each 0.1 mm thick. Under compressive stresses of 200 MPa, the stiffness is quadrupled from about 600 to 2400 MPa. The resonant frequency is therefore doubled, and can be modulated by applied stress.

Rubber, like most elastomers, is not piezoelectric. To take advantage of the elastic nonlinearity, it is therefore necessary to construct a composite transducer consisting of a piezoelectric ceramic (PZT) transducer, thin rubber layers,

and metal head and tail masses, all held together by a stress bolt [Figure 3(b)].

The resonant frequency and mechanical Q (important for vibration damping applications) of such a sandwich structure was measured as a function of stress bias ranging from 20 to 100 MPa in the experiments. Under these conditions, the radial resonant frequency changed from 19 to 37 kHz, approximately doubling in frequency as predicted from the elastic nonlinearity. At the same time, the mechanical Q increases from about 11 to 34 as the rubber stiffens under stress [7].

The changes in resonance and Q can be modeled with an equivalent circuit in which the compliance of the thin, rubber layers are represented as capacitors coupling together the larger masses (represented as inductors) of the PZT transducer and the metal head and tail masses. Under low stress bias, the rubber is very compliant and effectively isolates the PZT transducer from the head and tail masses. At very high stress, the rubber stiffens and tightly couples the metal end pieces to the resonating PZT ceramic. For intermediate stresses, the rubber acts as an impedance transformer, giving parallel resonance of the PZT-rubber-metal-radiation load.

FUTURE DIRECTIONS FOR SMART MATERIALS

The future for smart materials and systems appears to be quite bright, particularly as we enter a "new world order" in which the military will have to rely more upon efficient detection and prevention of instability rather than brute force and saturation bombings. None of us can soon forget the video images from Operation Desert Storm, in which one "smart" airborne missile enters the front door of an Iraqi military structure and destroys it. Likewise, the accuracy and success of the Patriot missile in contrast to the multitude of inefficient anti-aircraft missiles launched over Baghdad proved that in war, "smarter" is better than "bigger". (Of course, the peaceful use of smart technology is much preferred.)

Because the definition of smart materials is so broad, it is difficult to predict which area of materials research will lead the way. Electromechanical transducers have the advantage of performing as both sensors and actuators, so it is at least safe to say that they will continue to be important elements of smart systems.

Overall, there are some technologies applicable to all types of materials which will be critical to the performance of smart materials and systems. Integration and miniaturization of electroceramic sensors and actuators is an ongoing process in the automotive and consumer electronics areas. Multilayer packages containing signal processing layers made up of low-permittivity dielectrics and printed metal interconnections are in widespread production. Further integration with embedded resistors and capacitors are under development, and it seems likely that intelligent systems will make use of the same processing technology. Tape casting and screen printing are used most often. Varistors, chemical sensors, thermistors, and piezoelectric transducers can all be fabricated in this way, opening up the possibility of multicomponent, multifunction ceramics with both sen-

sor and actuator capabilities. Silicon chips can be mounted on these multifunctional packages to provide all or part of the control network. Processing is a major challenge because of the high firing temperatures of most ceramics, typically in the range 800°C to 1500°C. Differences in densification shrinkage and thermal contraction, together with adverse chemical reactions between the electroceramic phases, create formidable problems. Nevertheless, the rewards for such an achievement are substantial. An all-ceramic multifunction package would be small, robust, inexpensive, and sufficiently refractory to withstand elevated temperatures.

Electrodes are both a problem and a challenge. At present, precious metals such as palladium and platinum are used in multilayer ceramic components, greatly adding to the cost of the device. Copper and nickel electrodes require that the ceramic be fired in a reducing atmosphere, which may reduce the electroceramic layers and adversely affect the electrical properties. Copper and silver have high electrical conductivity, but the melting points (~ 1000°C) require lower firing temperatures and make it necessary to alter the ceramic compositions and fabrication procedures. Some headway has been made on this problem, but further work is needed. One interesting approach to the problem is ceramic electrodes. There are a number of ceramic phases with excellent conductivity which could be used, including the copper-oxide superconductors. In actuator devices, there are some special advantages in having electrodes and piezoceramics with matched elastic properties.

Composites are another approach to making sensor-actuator combinations. These can be formed at lower temperatures using low-firing ceramics and high temperature polymers, such as polyimides. Sol-gel and chemical precipitation methods are helpful in preparing ceramic powders with low calcining temperatures, but further work on composite fabrication is required to obtain reliable and reproducible electrical behavior.

To miniaturize the sensors and actuators, and to obtain complex shapes, we recommend the use of photolithography and other processing methods employed in the semiconductor industry. Ultraviolet curable polymers

incorporated into the tape-casting process make photolithographic processing comparatively easy and should find wide use in preparing ceramic or composite packages for intelligent systems.

The next logical step is to combine the sensor and actuator functions with the control system. This can be done by depositing electroceramic coatings on integrated circuit silicon chips, currently a very active area for materials research.

Reliability is a major requirement in all complex systems. Further research on electrical and mechanical breakdown of sensor-actuator materials is needed to elucidate the mechanisms responsible for failure.

Electroceramics have a vital role to play in intelligent systems, and many new developments will take place in the coming decade and the next century.

REFERENCES

1. Tsuka, H., J. Nakomo and Y. Yokoya. 1990. "A New Electronic Controlled Suspension Using Piezoelectric Ceramics". *IEEE Workshop on Electronic Applications in Transportation.*

2. Jaffe, W., R. Cook and H. Jaffe. 1971. *Piezoelectric Ceramics.* Marietta, Ohio: Academic Press.

3. Klicker, K. A., J. V. Biggers and R. E. Newnham. 1981. "Composites of PZT and Epoxy for Hydrostatic Transducer Applications". *J. Amer. Cer. Soc.*, 64:5–9.

4. Gururaja, T. R., W. A. Schulze, L. E. Cross, R. E. Newnham, B. A. Auld and J. Wang. 1984. "Resonant Modes in Piezoelectric PZT Rod-Polymer Composite Materials". *Proc. of IEEE Ultrasonic Symposium*, pp. 523–527.

5. Xu, Q. C., J. Belsick, S. Yoshikawa, T. T. Srinivasan and R. E. Newnham. 1991. "Piezoelectric Composites with High Sensitivity and High Capacitance for Use at High Pressures". *IEEE Transactions on UFFC*, 38:634–639.

6. Newnham, R. E., Q. C. Xu, S. Kumar and L. E. Cross. 1989. "Smart Ceramics". *J. Wave-Matl. Int.*, 4:3–10.

7. Xu, Q. C., R. E. Newnham, M. Blaskiewicz, T. T. Fang, T. T. Srinivasan and S. Yoshikawa. "Nonlinear Multilayer Composite Transducers", presented at the 7th International Symposium on Applications for Ferroelectrics, June 6–8, Urbana, Illinois.

APPENDIX   30

DESIGN OPTIMIZATION FOR METAL-CERAMIC COMPOSITE ACTUATOR, " MOONIE"

KATSUHIKO ONITSUKA, AYDIN DOGAN, QICHANG XU,
SHOKO YOSHIKAWA, ROBERT E. NEWNHAM
Materials Research Laboratory, The Pennsylvania State University
University Park, PA 16802

Abstract A piezoelectric ceramic-metal composite actuator has been developed to amplify the displacement of the piezoelectric ceramic. In this structure, the PZT ceramic is sandwiched between end caps with shallow cavities. This paper describes the design optimization of the flextensional transducer using finite element analysis (FEA). By using FEA, shape, material, and geometrical contributions to the displacement of the actuator were calculated. The effect of load on the displacement was also estimated. It was found that the displacement of the actuator increases with cavity diameter and depth, and that introducing a ring-shaped groove on the metal end caps of the actuator greatly enhances the displacement.

INTRODUCTION

A piezoelectric ceramic-metal composite actuator has been developed to amplify the displacement of a piezoelectric ceramic. The cross section of the moonie actuator is illustrated in the previous paper by Dogan et al. In this structure, the PZT ceramic is sandwiched between end caps with shallow cavities. Typical dimensions of these actuators are 11 mm in diameter and 2 mm in total thickness. The depth of the cavity is about 0.1 to 0.2 mm. The PZT and metal end caps are bonded together tightly using epoxy. By applying an electric field to the moonie actuator, the radial motion of PZT ceramic can be converted into flextensional motion creating a large displacement.

This paper describes the design optimization of the flextensional transducer using finite element analysis (FEA). The principal factors controlling the performance of the actuator were found to be the design of metal end caps and the bonding. Using FEA, the material and geometrical contributions to the displacement and generative force of the actuator were calculated. Load effects on the displacement were also estimated. Based on the modeling, changes in cap thickness and cavity size produced large effects on the displacement. It was also found that the displacement of the actuator increases with cavity diameter and depth, and that introducing a ring-shaped groove on the metal end

caps of the actuator greatly enhances the displacement. Finally, the displacement and generative force obtained experimentally were fitted to those calculated by FEA.

FEA Modeling

Two commercially available FEA programs (ANSYS and SAP90) were used for this study. For frequency response analysis, the relationship between admittance and frequency was calculated using 3-D axisymmetric piezoelectric elements in ANSYS. In the displacement analysis, the relationship between displacement and applied electric field was calculated using 2-D axisymmetric elements in SAP90. Each model was divided into three parts: the end cap, the PZT ceramic, and the bonding layer. Material parameters used in this analysis were Young's modulus, density, Poissons' ratio, piezoelectric constants, and dielectric constants.

CALCULATED AND EXPERIMENTAL RESULTS

(1) Frequency response of a moonie actuator

From the frequency response analysis, the lowest three resonant frequencies were calculated. Figure 1 shows admittance spectrum of the moonie plotted as a function of the frequency from 10 to 300 kHz. Three resonance peaks appear at 50, 187, and 210 kHz, corresponding the lowest three flextensional vibration modes. The first flextensional mode can be effectively utilized up to nearly 50 kHz. Based on these results, the coupling coefficient of the first mode was calculated as 20%.
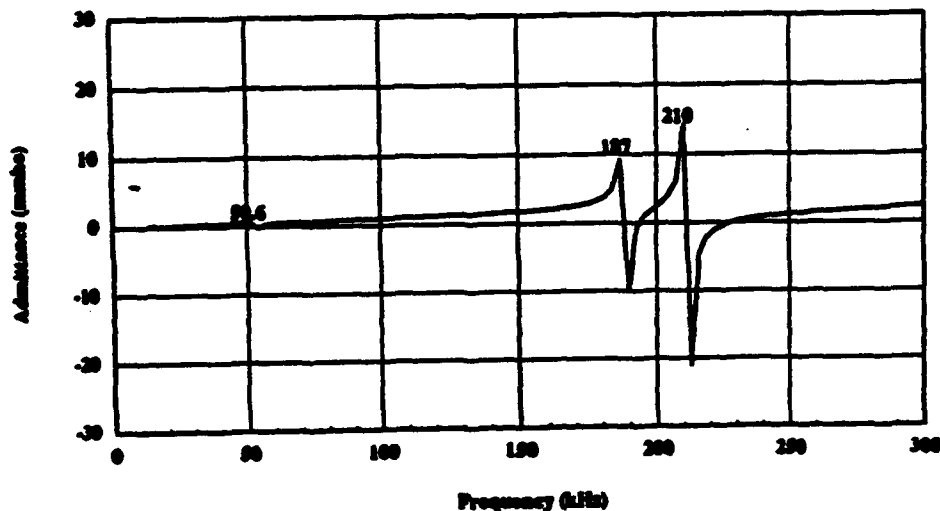
FIGURE 1 Calculated admittance curve of the 11 mm moonie actuator

Figure 2 compares the first resonant frequencies calculated by FEA with those obtained experimentally, for a range of brass cap thicknesses. Excellent agreement was obtained. The first resonant frequency is approximately proportional to the square root of the brass cap thickness.
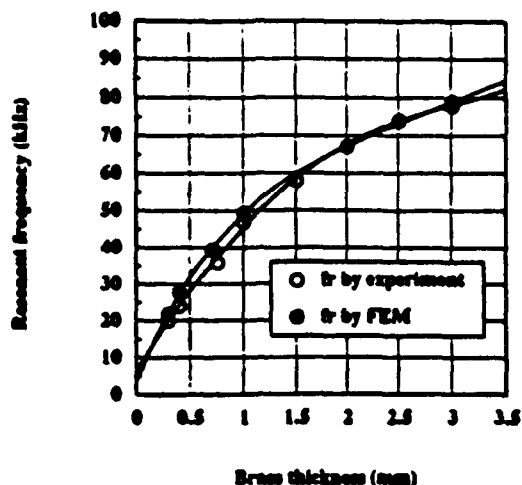
FIGURE 2 Calculated and measured first resonant frequencies of the moonie actuator

(2) Geometrical control of displacement for a moonie actuator

Figure 3 shows calculated displacement contour of the upper cap of a moonie actuator under an applied electric field of 1 kV/mm. The maximum displacement of 4.5 μm appears at the center of the moonie cap and gradually decreases toward the edge. The displacement profile of the moonie actuator corresponds to the effective d_{33} profile measured.
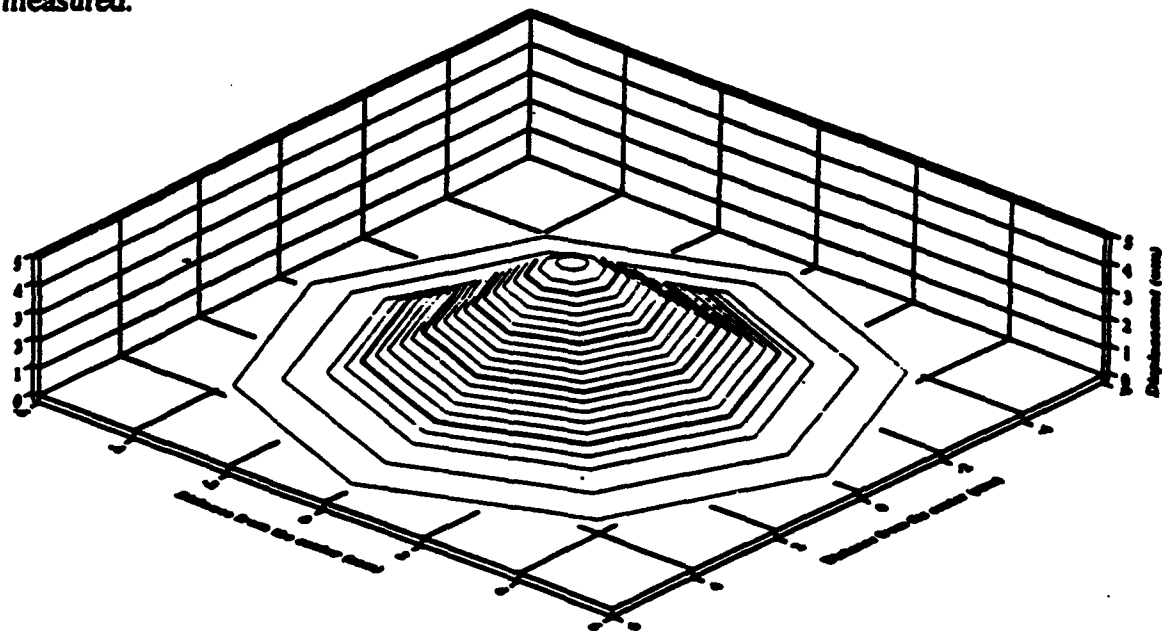
FIGURE 3 Calculated displacement contour of the upper cap of a moonie actuator

Figures 4 show the effect of geometry on displacement. The four variables are cap thickness, cavity size, cavity depth, and bonding thickness. Displacement decreases markedly with cap thickness and is inversely proportional to the brass cap thickness (Figure 5). Cavity diameter and cavity depth also affect the displacement. By increasing cavity size and cavity depth, displacement increases almost linearly. On the other hand, the thickness of the bonding layer has very little effect on the displacement in the range from 5 to 100 μm. In practice, the moonie has about 10 to 20 μm thick bonding layer.
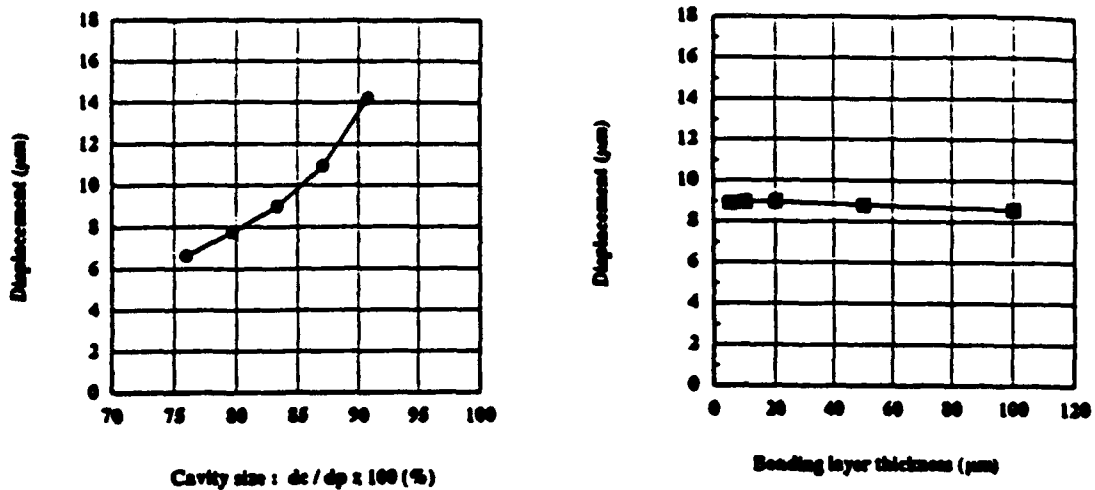
FIGURE 4 Effect of cavity diameter (left) and bonding layer thickness (right) on the displacement of the moonie actuator

Figure 5 compares the displacement calculated by FEA with those obtained by experiment, and plotted as a function of the brass thickness. This actuator is made of PZT-5, brass caps, and epoxy bonding with 20 μm thickness. There is very good agreement in displacement between the calculated and experimental values.
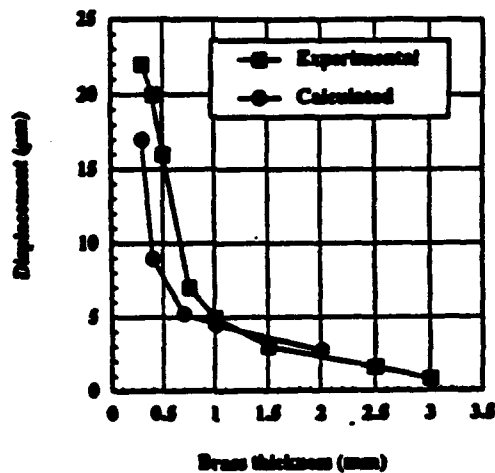
FIGURE 5 Calculated and measured displacements of the moonie actuator

In order to enhance the displacement of the moonie actuator, some modifications of the cap design were considered. It was found that introduction of a groove on the caps enhanced the displacement markedly. To determine the effect of the groove on displacement, the locations and dimensions of the groove were altered. Figure 6 compares the effect of groove position on the displacement (the maximum displacement is shown at the left side of each deformed shape) where g_p, g_d, and g_w are the groove position, groove depth, and groove width, respectively.

The most effective position of the groove is just above the edge of the inner cavity. In this case, a doubling of displacement (8.86 μm) was observed. Also the depth of the groove is important in enhancing the displacement. The deeper the groove, the higher the displacement. A displacement (12 μm) three times higher than the original is observed on the deepest grooved moonie.
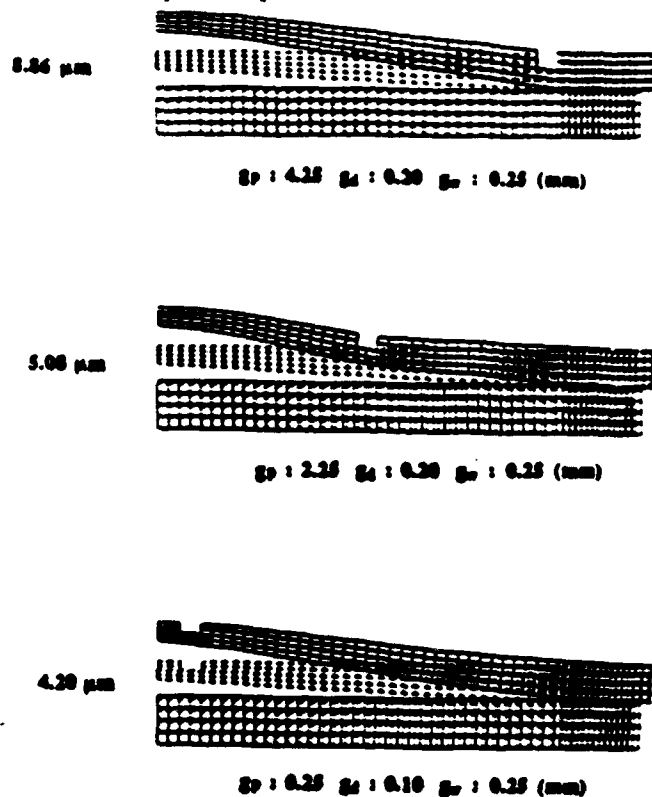
FIGURE 6 Groove positional effect on the displacement of the moonie actuator

(3) Effect of cap material effect on the displacement of a moonie actuator

Cap material partially controls the displacement of a moonie actuator. Four different cap materials stainless steel, brass, bronze, and plastic were selected for modeling. It was found that the higher the elastic stiffness, the lower the displacement. A plastic capped moonie actuator produces about 30 μm at a cap thickness of 0.3 mm.

(4) Load effect on displacements of a moonie actuator.

Normally the displacement decreases when a load is applied to the actuator. A moonie actuator also decreases under load, but shows rather peculiar behavior. Figure 7 compares the displacement profiles of the exterior surface of the moonie when four

different loads are applied over an area of 3 mm^2 under an applied E-field of 1 kV/mm. By increasing the load, the center displacement is suppressed gradually, and the center is no longer the maximum displacement point. The calculated load carrying capability of the moonie is 300 gf. for the effective working area of 3 mm^2 which corresponds to stress level of 10 kg/cm^2.
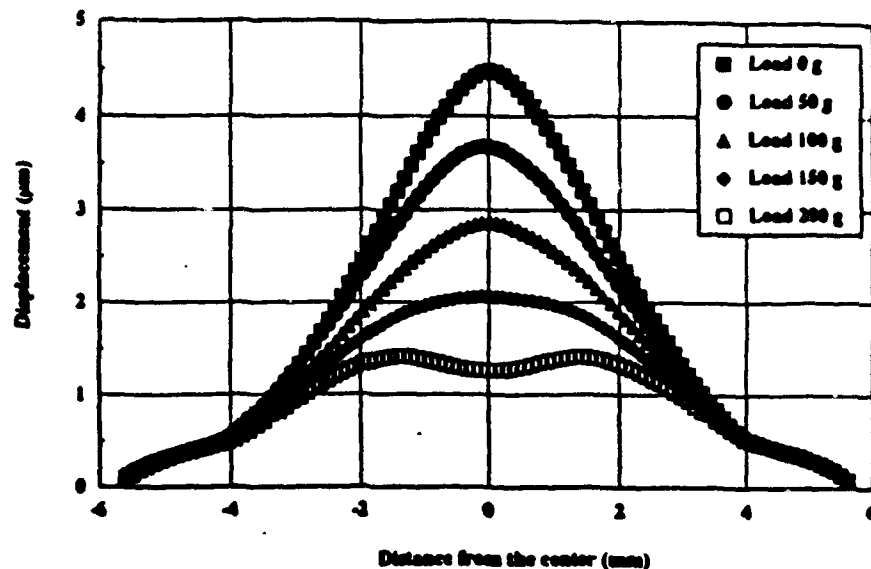
FIGURE 7 Calculated displacement profile on the exterior surface of the moonie actuator under the application of four different load

SUMMARY

1. Based on the frequency response analysis on the moonie actuator :
    (1) calculated resonant frequencies agreed well with the experimental results.
    (2) a coupling coefficient of the first mode was calculated as 0.2.
2. Based on the displacement analysis of the moonie actuator :
    (1) Among changeable geometrical parameters of the moonie actuator,
        (a) larger cavity diameter and higher cavity height lead to higher displacement.
        (b) thinner cap lead to higher displacement.
        (c) thickness of the epoxy bonding layer had little effect on the displacement.
        (d) Introduction of a groove on the caps above the bond edge enhanced the displacement.
    (2) The higher the stiffness of the cap material, the lower the displacement of the moonie.
    (3) The calculated maximum load (300 gf.) at the effective working area of 3 mm^2 agreed with that obtained by extrapolation of the experimental curve.

ACTUATOR STUDIES

APPENDIX 31

RELAXOR FERROELECTRIC DEVICES

KENJI UCHINO

International Center for Actuators and Transducers, Materials Research Laboratory, The Pennsylvania State University, University Park, Pennsylvania, USA

Abstract   Dielectric properties of relaxor ferroelectrics are characterized by giant and temperature-insensitive dielectric constants and large frequency dependence (dielectric relaxation), and therefore useful for high permittivity capacitors.   Relaxor ferroelectrics also reveal superior characteristics in electrostriction and electrooptic effects applicable to micropositioners, motors, light valves and displays. These properties are consistently explainable by the dynamic response of very small spindle-like domains in the materials.

INTRODUCTION

After Smolensky discovered that the ferroelectric phase transition of $Ba(Ti,Sn)_3$ becomes diffused drastically with increasing the $BaSnO_3$ content,[1] phenomena of the diffuse phase transition have been investigated intensively.   At a temperature several tens °C above the permittivity peak, where the phase is supposed to be paraelectric and non-piezoelectric, the solid solution specimen was found to exhibit piezoelectric resonance.[2]

Other than these solid solution systems, very similar diffused phase transition can be observed in complex perovskite oxides such as $Pb(Mg_{1/3}Nb_{2/3})O_3$ and $Pb(Zn_{1/3}Nb_{2/3})O_3$, where two kinds of ions share B sites randomly.[3]   Figure 1 shows the temperature dependence of the spontaneous polarization in $Pb(Zn_{1/3}Nb_{2/3})O_3$.[4] It is remarkable that the   spontaneous polarization remains further above the permittivity-peak temperature (140 °C). Temperature dependence of the permittivity of $Pb(Mg_{1/3}Nb_{2/3})O_3$ plotted in Fig. 2

also obeys a special quadratic law,[5,6] $1/\varepsilon \propto (T - T_0)^2$, instead of the normal ferroelectric Curie-Weiss law, $1/\varepsilon \propto (T - T_0)$, in the Curie temperature range. Dielectric properties are characterized by giant and temperature-insensitive dielectric constants and large frequency dependence (i. e. dielectric relaxation); this is the reason why these materials are called "relaxor ferroelectrics" and are useful for capacitor applications. Similar trailing phenomena are observed in electrostriction and electrooptic effects.[4]

Another interesting property of relaxor ferroelectrics is the very small thermal expansion effect throughout the Curie range. Figure 3 shows the thermal strain of $0.9Pb(Mg_{1/3}Nb_{2/3})O_3-0.1PbTiO_3$ plotted as a function of temperature.[7] In the temperature range -100 to +100°C, the thermal expansion coefficient is less than 1×10^{-6} K^{-1}, comparable to the best low-expansion ceramics or fused silica, which is extremely advantageous when this material is used as electrostrictive actuators.

In this paper, the crystallographic and domain structures of relaxor ferroelectrics are briefly summarized first, then superior characteristics in electrostriction and electrooptic effects are described with several practical device applications.

CRYSTALLOGRAPHIC & DOMAIN STRUCTURES OF RELAXOR FERROELECTRICS

Crystallographic Structures

Relaxor ferroelectrics contain three categories of crystal structure; 1) solid solutions with a non-polar component ($BaTiO_3-BaSnO_3$), 2) atomic deficiencies by a dopant ($Pb_{1-x}{}^{2+}La_x{}^{3+}(Zr,Ti)_{1-x/4}V_{x/4}O_3$), and 3) complex perovskites with a combination of different valence ions ($A^{2+}(B_{1/2}{}^{3+}B_{1/2}{}^{5+})O_3$, $A^{2+}(B_{1/3}{}^{2+} B_{2/3}{}^{5+})O_3$). All of them are associated with the disordered arrangement of constituent cations.

The ordering of the ionic arrangement gives a significant effect to ferroelectricity. Simple perovskites exhibit either ferroelectricity ($BaTiO_3$, $PbTiO_3$) or antiferroelectricity ($PbZrO_3$, $PbHfO_3$). On the other hand, the 1:1 ordered (NaCl-type) complex perovskites tend to be antiferroelectric ($Pb(Mg_{1/2}W_{1/2})O_3$, $Pb(Co_{1/2}W_{1/2})O_3$), and disordered perovskites tend to be ferroelectric ($Pb(Mg_{1/3}Nb_{2/3})O_3$, $Pb(Fe_{1/2}Ta_{1/2})O_3$). In addition, the phase transition of the disordered perovskite is rather diffused and the crystal structure in the low temperature phase is to be rhombohedral.

The close relation between dielectric and crystallographic properties is suggestively exemplified in the work on $Pb(Sc_{1/2}Ta_{1/2})O_3$.[8] The degree of cation ordering (Sc^{3+}, Ta^{5+}) is easily changeable only by thermal anneal without changing any composition. The disordered sample exhibits a "diffuse" transition from a ferroelectric to a paraelectric phase. With increasing the ordering, the phase transition becomes "sharp" and occurs at a higher temperature. Moreover, the polarization - electric field (P - E) curve at a temperature just below the transition shows a double hysteresis, indicating an antiferro- to ferroelectric field-induced transition.

Domains in Relaxor Ferroelectrics

Let us review the recent studies on the dynamic domain observation in relaxor ferroelectrics.[9,10] Figure 4 shows some examples of the ferroelectric domains observed in the solid solution system $(1 - x)$ $Pb(Zn_{1/3}Nb_{2/3})O_3 - x\ PbTiO_3$. The system exhibits a drastic change from a diffuse phase transition to a sharp transition with an increase of the $PbTiO_3$ content x, correlating to the existence of a morphotropic phase boundary from a rhombohedral to a tetragonal phase around x = 0.1. Very small spindle-like domains ($\sim 5\ \mu m$) with ambiguous boundaries in x = 0 become larger and clearer with increasing x. It is noteworthy that the specimen of x = 0.095 reveals a two-stage domain structure, i. e. spindle-like domains included in clear straight boundaries; this is probably due to the coexistence of the rhombohedral and tetragonal phases at room temperature.

Dynamic response to an electric field gives also important information. Figure 5 illustrates the domain reversal process in this system schematically. Sharp $90°$ domain walls corresponding to the tetragonal symmetry in the sample with x = 0.2 move abruptly and independently each other above a coercive field of 1 kV/mm. The situation resembles to the case in normal ferroelectrics such as $BaTiO_3$. On the contrary, pure lead zinc niobate (x = 0) reveals very different domain configurations. Long narrow spindle-like domains (aspect ratio ~ 10) are arranged perpendicularly to the applied electric field. When the field above 0.5 kV/mm is applied, the ambiguous curve domain walls move simultaneously in a certain size region, so that each micro-domain should change synchronously like cooperative phenomena, in good comparison with almost independent movement of the domain walls in the $PbTiO_3$-rich samples. The domain reversal front ($180°$ domain wall) moves rather slower than in the sample of x = 0.2; this is probably the reason of the dielectric relaxation. It is noteworthy that the stripe period of the dark and bright domains (corresponding to up and
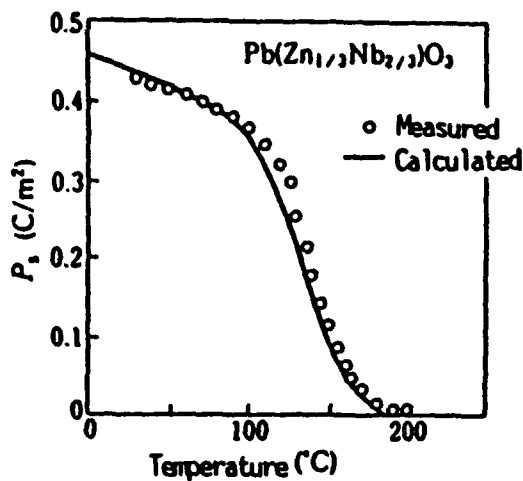
FIGURE 1 Temperature dependence of the spontaneous polarization in $Pb(Zn_{1/3}Nb_{2/3})O_3$.
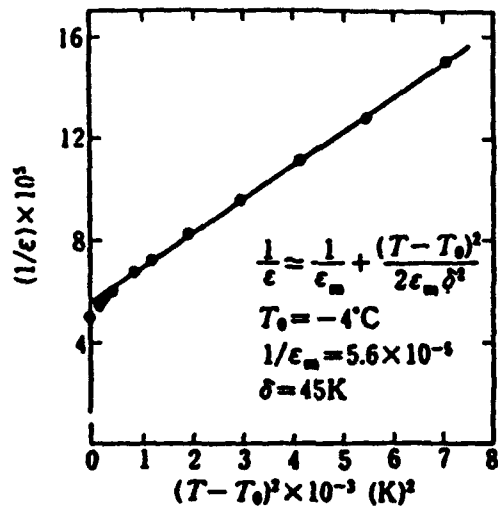
FIGURE 2 Dependence of the reciprocal permittivity on the square of temperature in $Pb(Mg_{1/3}Nb_{2/3})O_3$.
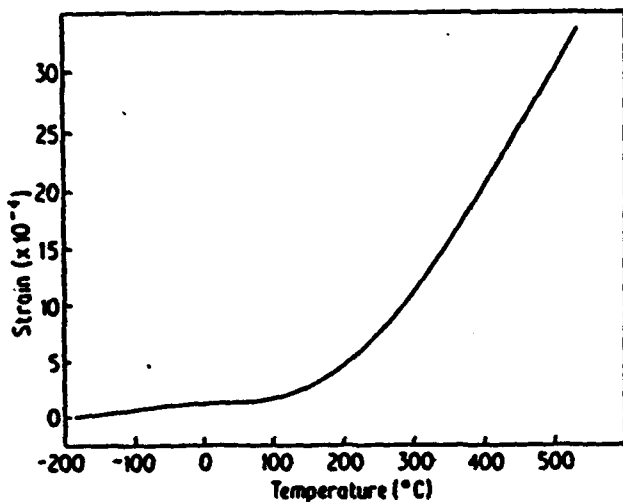

FIGURE 3 Thermal expansion in $0.9Pb(Mg_{1/3}Nb_{2/3})O_3$-$0.1PbTiO_3$.
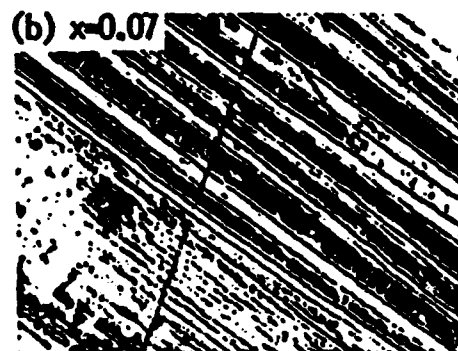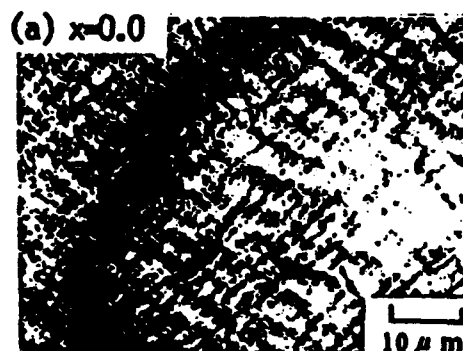
FIGURE 4 Ferroelectric domains in the $(1-x)Pb(Zn_{1/3}Nb_{2/3})O_3$-$x$ $PbTiO_3$.
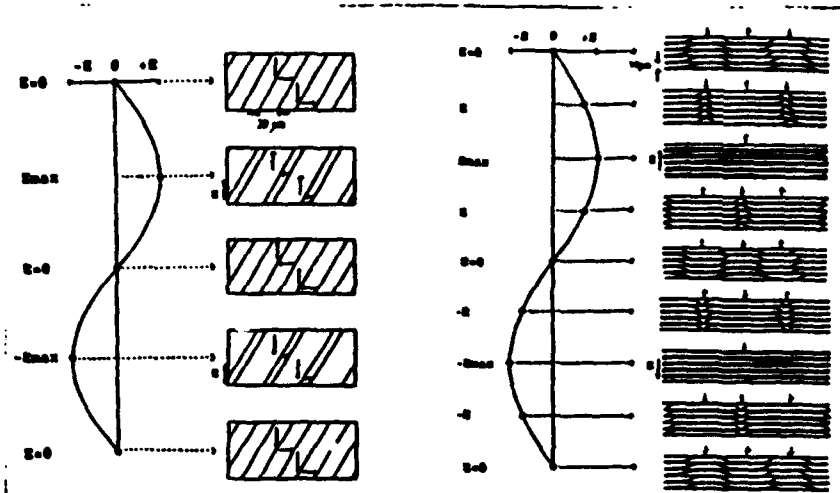
FIGURE 5 Mechanism of the domain reversal in $0.8Pb(Zn_{1/3}Nb_{2/3})O_3$-$0.2$ $PbTiO_3$ (left), and in pure $Pb(Zn_{1/3}Nb_{2/3})O_3$.

down polarizations) will not be changed by the domain reversal, and that each domain area changes under an AC external field with zero net polarization at zero field. This can explain large apparent secondary non-linear effects in physical properties such as electrostrictive and electrooptic phenomena, without exhibiting any hysteresis. The relaxor crystal is electrically-poled easily when an electric field is applied around the transition temperature, and depoled completely without any remanent polarization.

ELECTROSTRICTION IN RELAXOR FERROELECTRICS

Cencerning electric field induced strains, $Pb(Mg_{1/3}Nb_{2/3})O_3$ for example, exhibits a large electrostriction (i. e. a second-order electro-mechanical property where strain is induced in proportion to the square of the applied field) at room temperature in the small electric-field range. Figure 6 shows the strain curve of the transversely induced electrostriction in $0.9Pb(Mg_{1/3}Nb_{2/3})O_3$-$0.1PbTiO_3$.[7,11] The relaxor ceramics are anhysteretic, and retrace the same curve with rising and falling fields. For comparison, the piezoelectric strain (i. e. strain induced in proportion to the applied field) of a hard PZT 8 under cyclic field is also plotted in Fig. 6. This material has often been used in the fabrication of multi-dither mirrors and other active optical components. Note that the electrostriction is comparable to or larger than the magnitude of the typical piezoelectric strain induced in $Pb(Zr,Ti)O_3$ based ceramics and far more reproducible under cyclic drive conditions.

The superiority of the PMN electrostrictor to the PZT piezostrictor was demonstrated in a deformable mirror and a scanning tunneling microscope.

Deformable Mirror

In the field of optical information processing, deformable mirrors have been proposed to control the phase of the incident light wave. The deformable mirror can be made convex or concave on the surface as necessary. This type of mirror, which is applicable to an accessory device on observatory telescopes, effectively corrects for image distortions resulting from fluctuating airflow.

An example of a deformable mirror is the two-dimensional multimorph type illustrated in Fig. 7.[12,13] When three layers of thin electrostrictive ceramic plates are bonded to the elastic plate of a glass mirror, the mirror surface is deformed in various ways corresponding to the strain induced in the ceramic layers. The nature of the deformation is determined by the electrode configurations and the distribution of the applied electric field. Trial devices have been designed by finite element methods such that the first layer, with a uniform electrode pattern, produces a spherical deformation (i. e. refocusing), while the second layer, with a 6-divided electrode pattern, corrects for coma aberration. Figure 8 shows a parabolic deformation of the mirror measured by an interferometric technique on a cycle with rising and falling electric field. In comparison with the conventional PZT piezostrictor, the PMN mirror is much superior in the reproducibility at zero field.

Scanning Tunneling Microscope

The scanning tunneling microscope (STM) is a key instrument for analyzing surfaces in an atomic scale. Figure 9 shows an STM structure designed by us. A sharp tungsten needle probe installed on a tripod ceramic actuator is set very close to a sample surface, and a constant voltage is applied between the probe and the sample so that a tunneling current be detected. By scanning the x- and y-axis actuators, the current change is monitored, which can provide the surface contour in an angstrom scale.

The most important point in the development is to fabricate an anhysteretic reliable actuator; otherwise, the surface images obtained will be significantly deformed according to the scanning direction of the probe. Remarkable improvement in the image reproducibility has been obtained by using an electrostrictive PMN-PT actuator, replacing a conventional PZT device.[14]
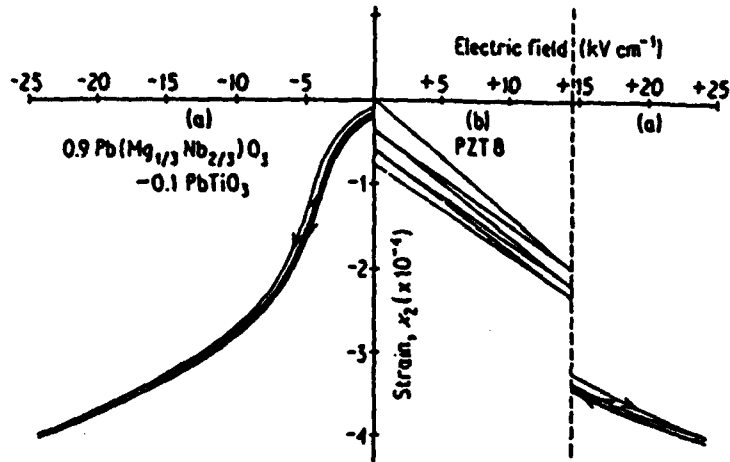
FIGURE 6 Transverse field-induced strain
in $0.9Pb(Mg_{1/3}Nb_{2/3})O_3$-$0.1PbTiO_3$ (a),
and in PZT8 (hard piezoelectric) (b).
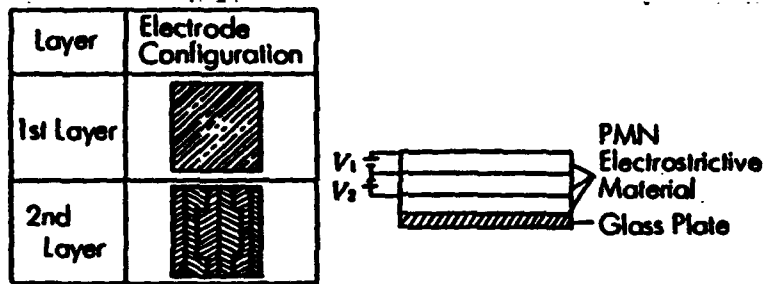
FIGURE 7 Structure of a multimorph
deformable mirror.
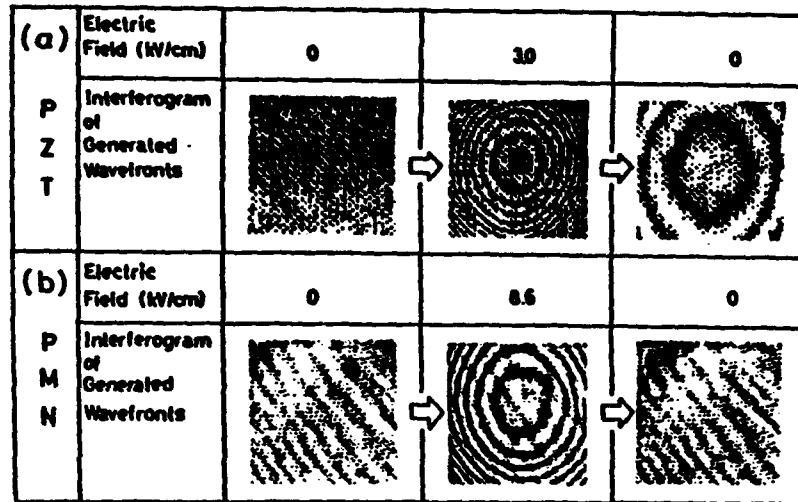
FIGURE 8 Actual control of the deformable mirrors made of
the PZT piezostrictor (a), and of the PMN electrostrictor (b).

ELECTROOPTIC EFFECT IN RELAXOR FERROELECTRICS

Relaxor ferroelectrics are also remarked in non-linear optic applications because an extraordinarily large apparent "electrooptic Kerr effect" can be observed even in the so-called paraelectric state. Figure 10 shows the birefringence versus electric field relation of $Pb(Zn_{1/3}Nb_{2/3})O_3$ in the paraelectric phase.[4] The parabolic curve in the low field region tends to approach a straight line in the high field region. This peculiar phenomenon is analyzed on the basis of the model that the crystal is composed of the ferroelectric and paraelectric phases mixed together. Suppose that the volume fraction of the paraelectric phase x(T) is given by the accumulated Gaussian distribution with respect to temperature, the birefringence Δn is estimated by the summation of linear and quadratic electro-optic effects:[15] $\Delta n = [1 - x(T)]n^3(r_{33} - r_{13})E/2 + x(T)n^3R_{44}E^2/2$, where n is the refractive index, and r and R represent electro-optic Pockels and Kerr coefficients, respectively. This suggests again the importance of the micro-domains in relaxor ferroelectrics.

Famous electrooptic transparent ceramics PLZT, i. e. $(Pb_{1-x}La_x)$ $(Zr_yTi_z)_{1-x/4}O_3$, are examples of relaxors, which have large electrooptic effect $(R = 9.1 \times 10^{-16} m^2V^{-2})$ and are applicable to light valves, displays etc. However, the PLZT with a deficient crystal structure has revealed a serious problem in fracture toughness $(K_{IC} = 0.9 MNm^{-3/2})$ or durability under repeating operation. We have developed new transparent ceramics of $(1 - x) Pb(Mg_{1/3}Nb_{2/3})O_3 - x PbTiO_3$ with high fracture toughness $(K_{IC} = 1.7 MNm^{-3/2})$ originally, and found twice larger electrooptic coefficients $(R = 21 \times 10^{-16} m^2V^{-2})$ than that of the PLZT. Figure 11 shows the compotition dependence of the electrooptic R coefficient in the PMN-PT system.

A two-dimensional light valve array for an image projector has been developed using transparent PLZT ceramics, as shown in Fig. 12.[16] A light shutter array with 10 x 10 pixels was fabricated by a sophisticated tape casting technique, starting from coprecipitated PLZT fine powder. Plate-through and separate internal electrodes are stacked alternately so as to make vertical addressing by an external electrode connecting separate electrodes and horizontal addressing by a plate-through electrode. A pair of shutter elements beside a plate-through electrode constitute an image pixel. The transmittance of 62% (at 633 nm) could be obtained by atmosphere controlled sintering of a green chip, which is in good comparison with 63% for the ideal sample prepared by hot pressing. A contrast ratio of 80 is realized with a response time of 10 μsec under a half-wavelength voltage of 100V applied. The applicative feasibility to a high definition projection-type TV's was verified.
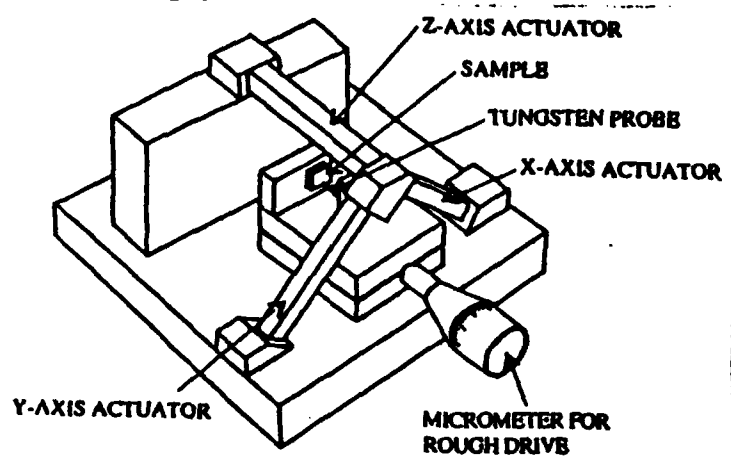
FIGURE 9 Structure of the STM.
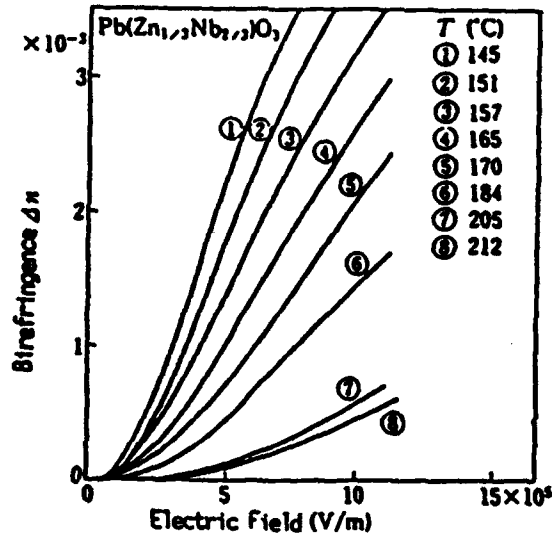
FIGURE 10 Birefringence vs. field in the paraelectric Pb(Zn$_{1/3}$ Nb$_{2/3}$)O$_3$.
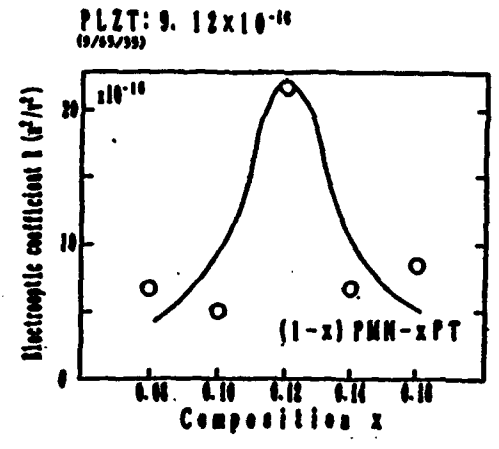
FIGURE 11 Composition dependence of the electrooptic Kerr Coefficient in the (1-x) Pb(Mg$_{1/3}$Nb$_{2/3}$)O$_3$-x PbTiO$_3$.

(a)

(b)
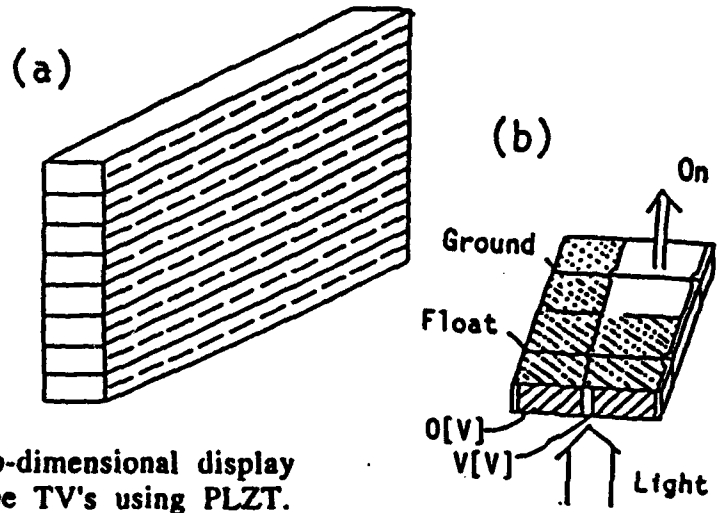
FIGURE 12 Two-dimensional display for projection-type TV's using PLZT.

CONCLUSIONS

Relaxor ferroelectrics are widely applicable to high capacitance condensers, electrostrictive positioners, electrooptic light valves/displays etc. Superior characteristics of these materials are mainly attributed to the easy poling of the ferroelectric micro-domains. Further intensive investigations on the peculiar domain reversal mechanism will be required to develop more sophisticated practical devices.

REFERENCES

1.   G.A. Smolensky, J. Phys. Soc. Jpn., 28, Suppl., 26 (1970).
2.   G.A. Smolensky and V.A. Isupov, Zh. Tech. Fiz., 24, 1375 (1954).
3.   G.A. Smolensky, V.A. Isupov, A.I. Agranovskaya and S.N. Popov, Sov. Phys.- Solid State, 2, 2584 (1961).
4.   F. Kojima, J. Kuwata and S. Nomura, Proc.1st Mtg. on Ferroelectric Mater.& Appl. (Kyoto,1977) p.155.
5.   V.V. Kirillov and V.A. Isupov, Ferroelectrics, 5, 3 (1973).
6.   K. Uchino, S. Nomura, L.E. Cross, S.J. Jang and R.E. Newnham, J. Appl. Phys., 51, 1142 (1980).
7.   L.E. Cross, S.J. Jang, R.E. Newnham, S. Nomura and K. Uchino, Ferroelectrics, 23, 187 (1980).
8.   N. Setter and L.E. Cross, J. Appl. Phys., 51, 4356 (1980).
9.   K. Kato, K. Suzuki and K. Uchino, J. Jpn. Ceram. Soc., 98, 840 (1990).
10.   R. Ujiie and K. Uchino, Proc. IEEE Ultrasonic Symp. (Hawaii,1990) p.725.
11.   K. Uchino, Ceram.Bull., 65, 647 (1986).
12.   K. Uchino, Y. Tsuchiya, S. Nomura, T. Sato, H. Ishikawa and O. Ikeda, Appl.Optics, 20, 3077 (1981).
13.   T. Sato, H. Ishikawa, O. Ikeda, K. Uchino and S. Nomura, J. Opt. Soc. Amer., 71, 1645 (1981).
14.   K. Uchino, in Ceramic Data Book '88 (Inst. Industrial Manufacturing Technology, Tokyo, 1988), Chap. Ceramic Actuator.
15.   J. Kuwata, K. Uchino and S. Nomura, Ferroelectrics, 22, 863 (1979).
16.   K. Uchino, K. Tokiwa, J. Giniewicz, Y. Murai and K. Ohmura, in Electro-Optics and Nonlinear Optic Materials, Ceramic Trans. Vol.14 (Amer. Ceram. Soc., 1990) p.297.

APPENDIX 32

Title: Recent Development of Piezoelectric Actuators for Adaptive Structures

Author: Kenji Uchino

ABSTRACT

The requirements for the actuator material for adaptive structures are (1) large stroke, (2) quick response, (3) energy saving and (4) reliability/durability. Especially in space applications, mechanical vibration suppression is occasionally required, and remote control/drive of the actuator is another key technology. This paper describes recent developments of piezoelectric and related ceramic actuators for adaptive structures.

INTRODUCTION

In these several years piezoelectric and related ceramic actuators have become very popular for micro-positioning in optical and precision machinery fields [1-5]. Very recently, these ceramic actuators have been trially utilized in big structures such as military vehicles and space constructions for realizing "smart skins" and active vibration suppression.

The requirements for the actuator materials for adaptive structures are (1) large stroke, (2) quick response, (3) energy saving and (4) reliability/durability. This paper reviews recent developments of piezoelectric/electrostrictive and related ceramic actuators from the above-mentioned viewpoints. New gigantic strain materials of antiferroelectrics and a displacement magnification mechanism called "moonie" are introduced, firstly. Then, low permittivity electrostrictors, which are essential to quick drive, are referred, followed by a pulse drive technique of the ceramic actuators. Thirdly, described are shape memory ceramics operated by a short pulse voltage with efficient energy saving. Concerning reliability/durability issues, donor-ion doping effects on eliminating the strain hysteresis are mentioned, and a destruction prediction system of ceramic actuators using acoustic emission detection is proposed.

Especially in space applications, mechanical vibration suppression is occasionally required, and remote control/drive of the actuator is another key technology. Piezo-ceramic:carbon:polymer composites for passive dampers and photostrictive actuators are introduced, finally.

LARGE STROKE

The magnitude of the maximum strain induced in piezoelectric/electrostrictive ceramics is usually about 0.1% and is not enough to some applications. Utilization of the strains associated with phase transitions such as an antiferroelectric-to-ferroelectric transition may give a breakthrough to this problem [6,7]. Figure 1 shows the field-induced strain curves taken for the lead zirconate-based system $Pb_{0.99}Nb_{0.02}(Zr_xSn_{1-x})_{1-y}Ti_y)_{0.98}O_3$. The longitudinally induced strain reaches up to 0.4%, which is much larger than that expected in piezostrictors. A sufficiently large hysteresis during a field cycle (Figure 1(a)) exhibits two on/off strain states, which can be referred to as a "digital displacement transducer." Devices

Professor Kenji Uchino, The Pennsylvania State University, 134 Materials Research Laboratory, University Park, PA 16802-4800

(a)

x=0.60,y=0.055

(b)
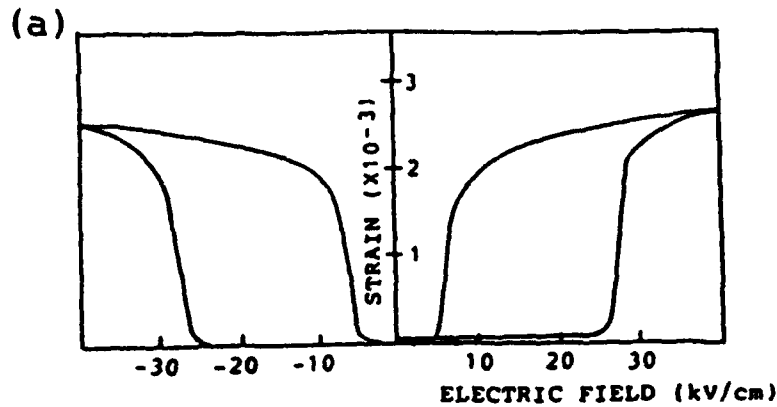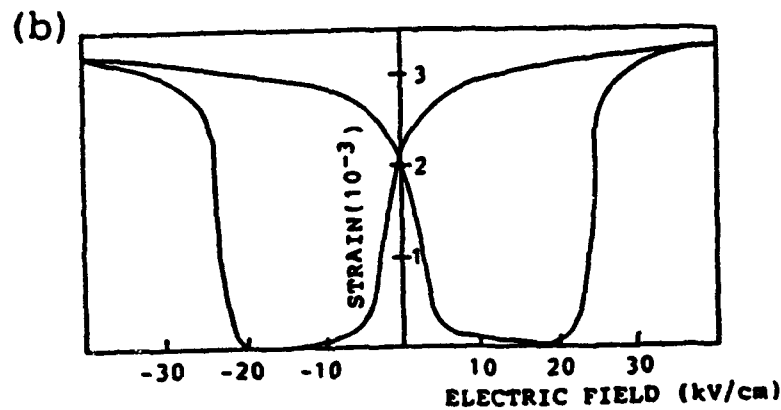
x=0.70,y=0.045

Figure 1   Longitudinally-induced strains in $Pb_{0.99}Nb_{0.02}((Zr_xSn_{1-x})_{1-y}Ti_y)_{0.98}O_3$ at room temperature.

based on this effect are currently being investigated for applications requiring precise micropositioning with a constant distance change such as in the production of optical diffraction gratings and photolithography.

A composite actuator structure called "moonie" has been developed to amplify the small displacement induced in a piezoelectric ceramic [8]. The moonie has intermediate characteristics between the conventional multilayer and bimorph actuators; this exhibits an order of magnitude larger displacement than the multilayer, and much larger generative force with quicker response than the bimorph. The device consists of a thin multilayer piezoceramic element and two metal plates with a narrow moon-shaped cavity bonded together as shown in figure 2. The moonie with a size of 5mm × 5mm × 2.5mm can generate a 20 μm displacement under 60V, which is eight times as large as the generative displacement of the multilayer with the same size (figure 3). The new compact actuator has been applied to make a miniaturized laser beam scanner [9].

QUICK RESPONSE

Lead magnesium niobate based ceramics (PMN) can exhibit a large electrostriction (~0.1%) without hysteresis, and have been utilized in various applications, as reviewed later. Because of a high permittivity more than 10,000, however, their application to pulse-drive motors has been limited. Lead barium zirconate titanate based electrostrictors
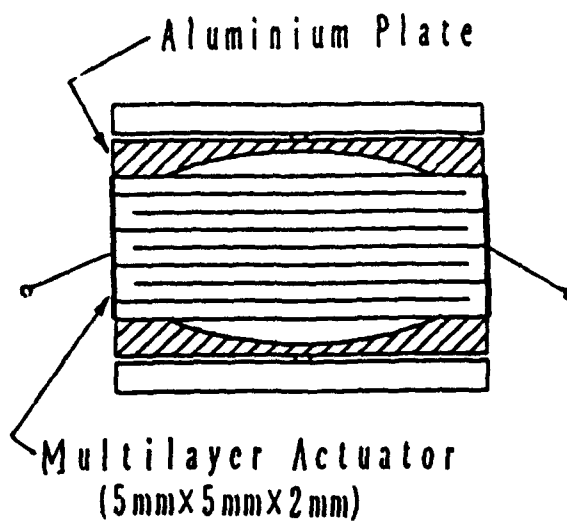
Figure 2   Structure of a composite actuator "moonie."
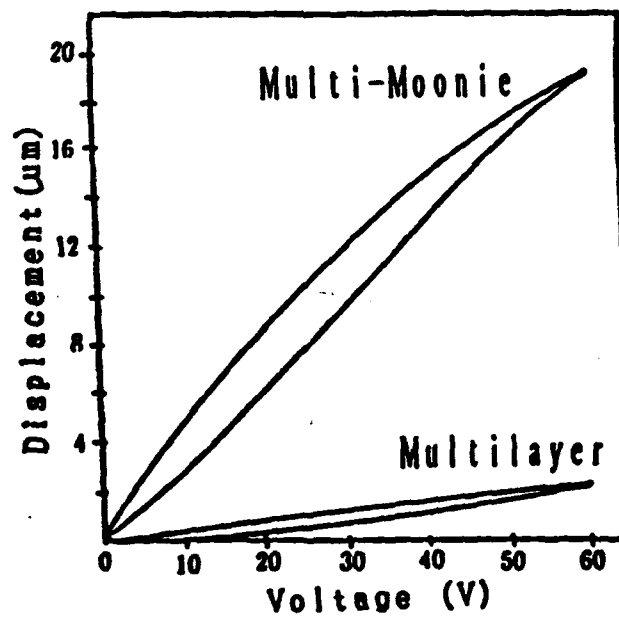
Figure 3   Displacement curves measured in a moonie and a multilayer actuator.

((Pb,Ba)(Zr,Ti)O$_3$) with a relatively low permittivity (~3000) are suitable for quick response applications [10].

Drive/control methods of the actuator reveal occasionally an apparently slow response. Figure 4 shows transient vibrations of a bimorph actuator excited after a pseudo-step voltage applied. The tip displacement induced, in general, is associated with overshoots and ringings. This noise vibration period is a loss time in a positioner system. When the rise time of the voltage is appropriately adjusted (i.e. equally to the resonance period), the overshoots/ringings are completely suppressed and the quickest response is realized [11].

A flight actuator consisting of a pulse-drive piezoelectric element and a steel ball is a very suggestive mechanism. A 2 mm steel ball can be hit up to 20 mm by a 5 mm displacement induced in a multilayer actuator with quick response. A dot-matrix printer head has seen trially manufactured using a flight actuator as shown in figure 5 [12]. By changing the drive voltage pulse width, the movement of the armature is easily controlled to realize no vibrational ringing or double hitting.
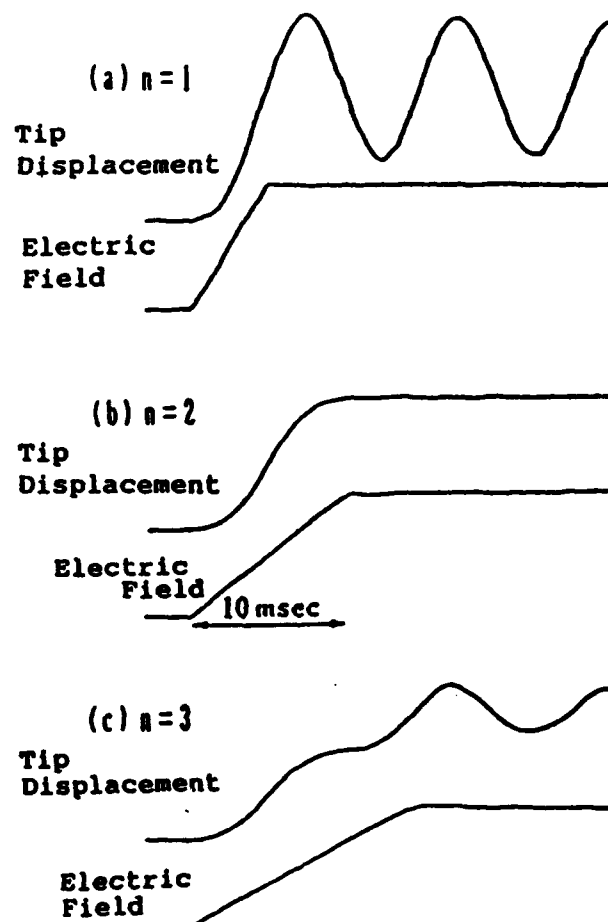

Figure 4   Transient vibration of a bimorph tip excited after a pseudo-step voltage applied. The n is a time scale in the unit of a half of the resonance period.
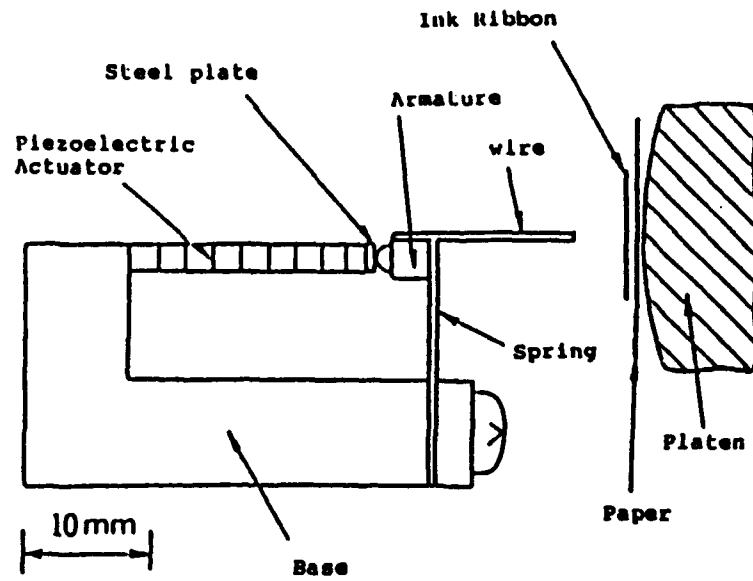
Figure 5   Dot-matrix printer head element using a flight actuator mechanism.
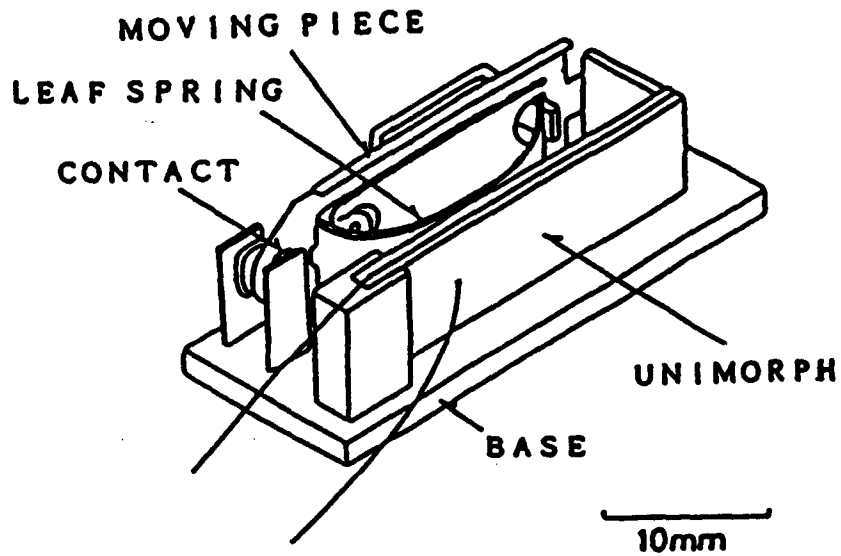
Figure 6   New latching relay using a shape memory ceramic unimorph.

ENERGY SAVING

The field-induced transition exhibits a shape memory effect in appropriate compositions. The lead zirconate based ceramics provide such an attractive effect as shown in figure 1(b). Once the ferroelectric phase is excited, the material will "memorize" its ferroelectric shape even under zero-voltage conditions, and the memory can be erased with the application of a small reverse bias field or a thermal anneal. This shape memory device can be operated by a short pulse voltage, not by a continuous voltage; this means remarkable energy saving in comparison with the conventional piezoelectric devices.

A new latching relay in figure 6 is composed of a shape memory ceramic unimorph and a mechanical snap action switch, which is driven by a pulse voltage of 3 ms [13]. Compared with the conventional electro-magnetic latching relays, the new relay is much simple and compact in structure with almost the same response time.

RELIABILITY/DURABILITY

The hysteresis in the electric field induced strains provides significant problems in practical devices. The investigations focused on compositions, dopants and polycrystal microstructures are introduced here.

Recently developed lead magnesium niobate based ceramics ($Pb(Mg_{1/3}Nb_{2/3})O_3$ - $PbTiO_3$) can exhibit a large nonlinear electrostriction ($\Delta l/l \sim 10^{-3}$) without any hysteresis and aging effect [14]. A simple deformable unimorph mirror using the PMN electrostrictor has been fabricated for refocusing a light beam [15]. Figure 7 shows parabolic deformation of the mirror measured by an interferometric technique on a cycle with rising and falling electric field. In comparison with the conventional lead zirconate titanate (PZT) piezostrictor, the PMN mirror is much superior in the reproducibility at zero field.

(a)	Electric Field (kV/cm)	0	3.0	0
P Z T	Interferogram of Generated Wavefronts			

(b)	Electric Field (kV/cm)	0	8.6	0
P M N	Interferogram of Generated Wavefronts			
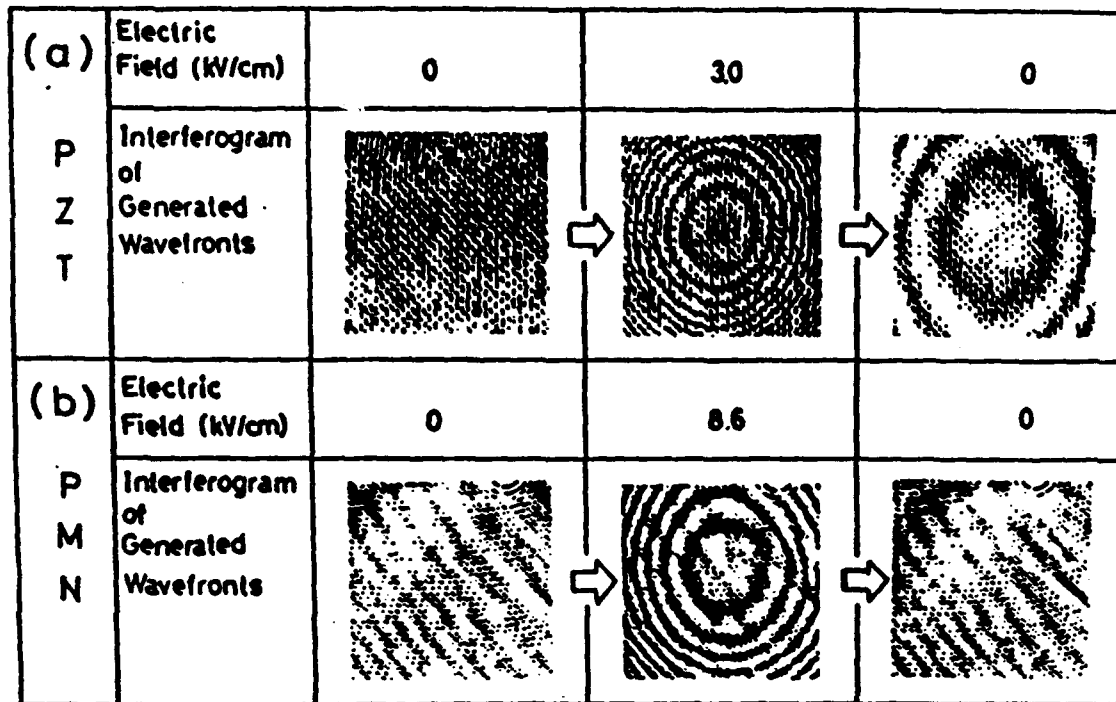
Figure 7   Interferometric fringe patterns generated by the deformable mi.. made of the PZT piezostrictor (a) and of the PMN electrostrictor (b).

The doping effect of various metal ions on the field induced strains has been investigated in (Pb,Ba)(Zr,Ti)O_3 ceramics [16]. Figure 8 plots a relation between the maximum strain and the degree of hysteresis. The maximum strain x_{max} is defined by the strain at the maximum field E_{max} = 1kV/mm, and the degree of hysteresis is calculated as the ratio (%) of the strain deviation Δx at $E_{max}/2$ over x_{max}. As doped with acceptor-type ions (small valence +1 to +3), the x_{max} decreases drastically and the hysteresis increases. On the contrary, the donor doping (large valence +5 to +6) provides a remarkable decrease in the hysteresis with keeping the magnitude of x_{max}. This phenomenon is explainable by considering a domain wall pinning effect caused by crystal deficiencies.

As the requirements for piezoelectric/electrostrictive actuators become more specific, inadequacies due to the preparation history of the ceramic arise in reproducibility of properties. High reproducibility is achieved only by precise control of the grain/particle size, which is not possible utilizing the conventional mixed-oxide method of preparation. Recent preparation technology of ultrafine ceramic powders has been very useful in producing reliable and durable ceramic actuators. The effect of grain size on the electrostrictive response and the mechanical fracture toughness in lead lanthanum zirconate titanate (PLZT 9/65/35) is shown in figure 9(a) and (b) [17]. A significant reduction in hysteresis and in the strain magnitude is observed for grain sizes less than 1.7 μm, as well as a remarkable increase in the fracture toughness.
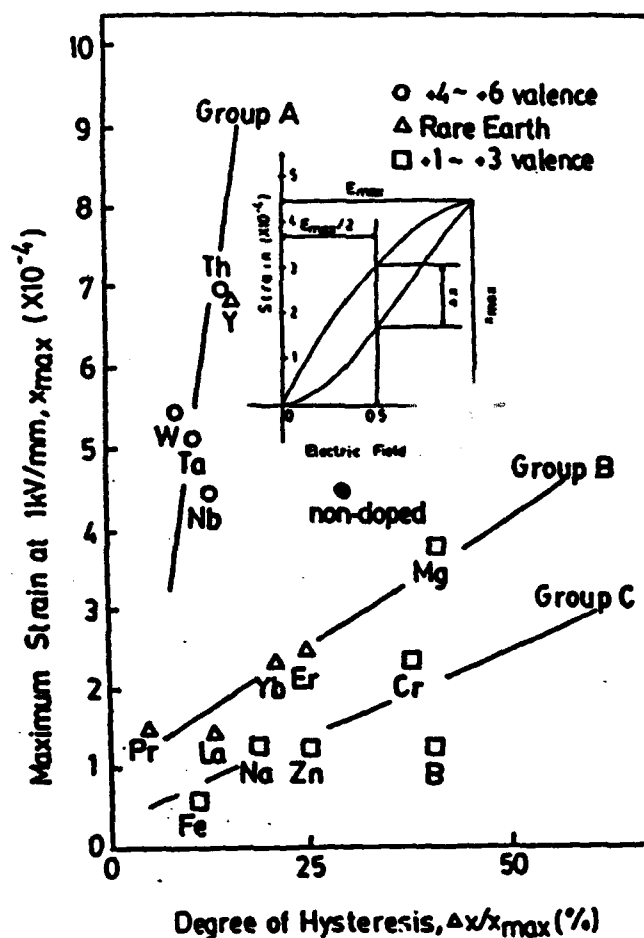
Figure 8   Ion doping effect on the electrostriction in (Pb,Ba)(Zr,Ti)O_3.
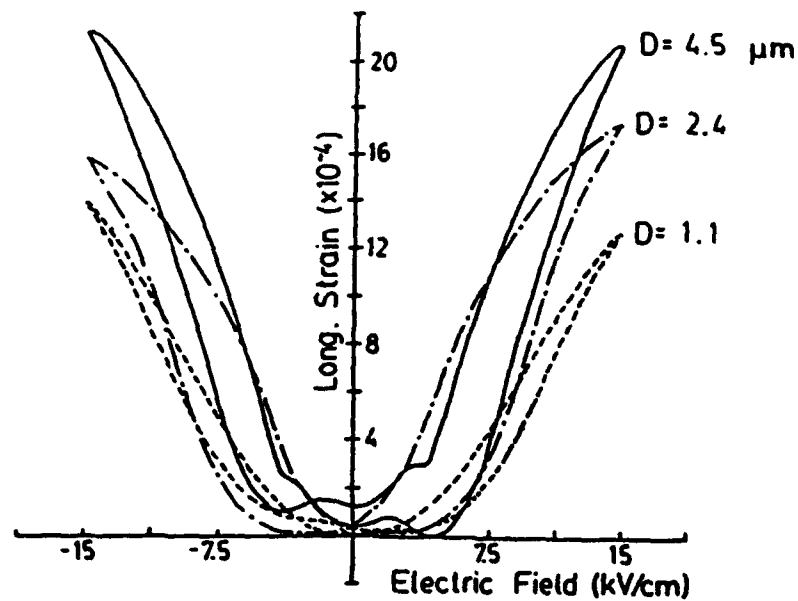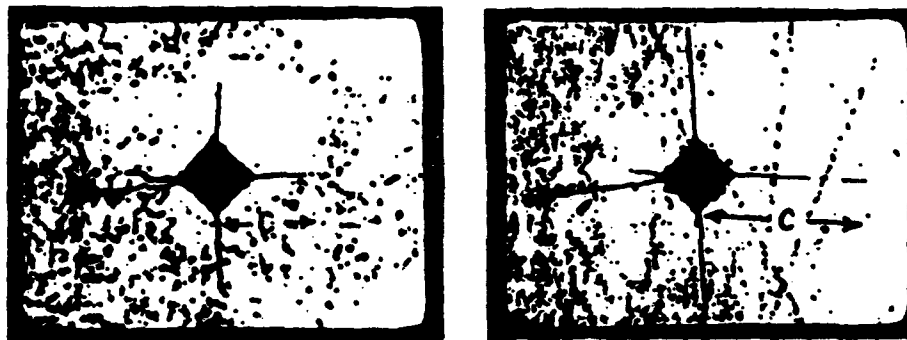
Figure 9   Grain size dependence of field-induced strain (a) and Vickers' indentation test (b) observed in PLZT 9/65/35.

Safety is the highest priority in actuator systems. A very smart system has been proposed, containing a reliability test system, which can stop an actuator system safely without causing any serious damages on to the work, e.g. in a lathe machine (fig. 10). Acoustic emission measurement of a piezo-actuator under a cyclic electric field is a good candidate for estimating the lifetime of the actuators [18]. Acoustic emission is detected largely when micro-cracks propagate in a ceramic sample. During a normal drive of the piezoelectric actuator, a drastic increase of AE number by three orders of magnitude was detected just before the final destruction (fig. 11).
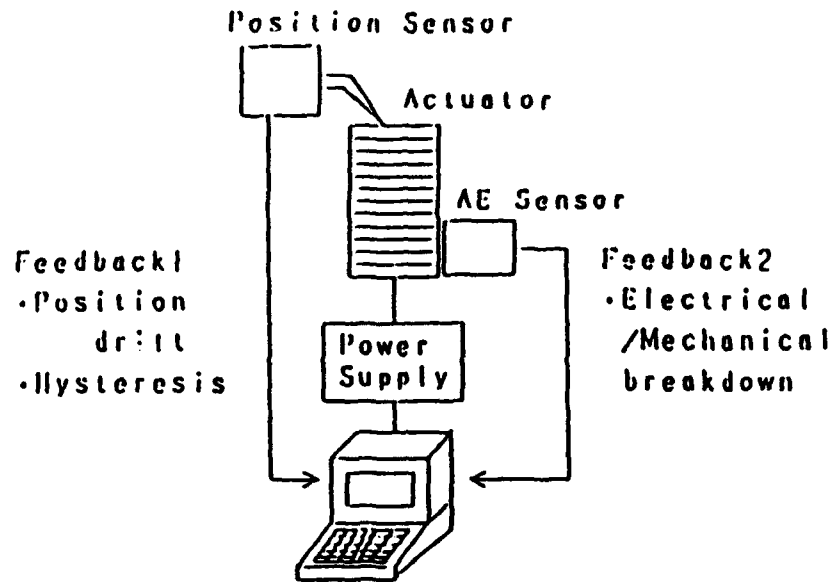
Figure 10   Very smart actuator system with a reliability test function as well as a position
   sensor.
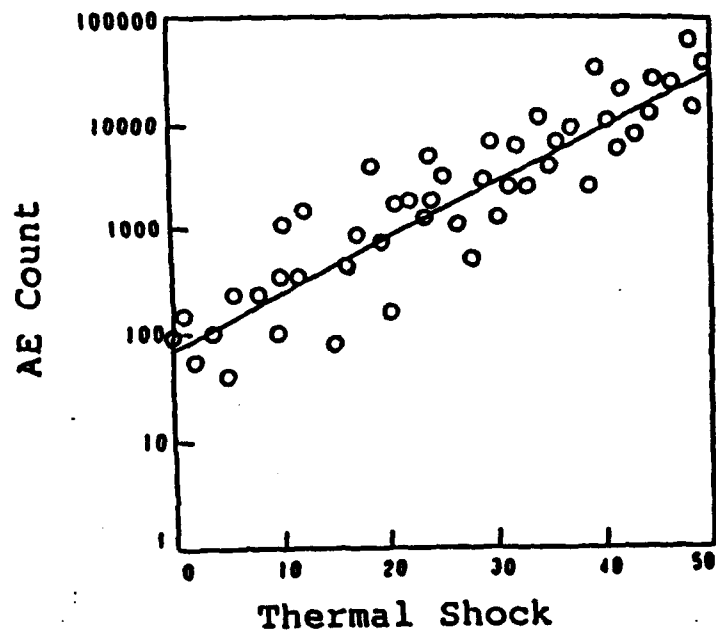
Figure 11   Acoustic emission measured during a normal drive of a multilayer piezoelectric
             actuator. Each measurement was done after successive thermal shock
             treatment.

VIBRATION SUPPRESSION

Passive damper application is a smart usage of piezoelectrics, where mechanical noise vibration is radically suppressed by the converted electric energy dissipation through Joule heat when a suitable resistance, equal to an impedance of the piezoelectric element $1/\omega C$, is connected to the piezo- element [19]. Piezoceramic:carbon black:polymer composites are promising useful designs for practical application. Figure 12 shows the damping time constant change with volume percentage of the carbon black [20]. The minimum time constant (i.e. quickest damping) is obtained at 6% of carbon black, where a drastic electric conductivity change is observed (percolation threshold). Notice that this effect is enhanced by using a higher electro-mechanical coupling material.

REMOTE CONTROL

A photostrictive actuator is the best example of intelligent materials including sensing of illumination, self production of drive/control voltage and final actuation in a unique material [21]. In certain ferroelectrics a phenomenon by which a constant electromotive force is generated with exposure of light has been observed. A photostrictive effect is expected as a result of the coupling of the bulk photovoltaic and inverse piezoelectric effects.

A unit bimorph is made from PLZT (3/52/48) ceramics with slight addition of niobium and tungsten. The remnant polarization of one PLZT is parallel to the plate and in the direction opposite to that of the other plate (refer to figure 13). When a violet light is applied to one side of the PLZT bimorph, photovoltaic voltage of (0.7 kV/mm) is generated, causing a bend as a whole. The displacement observed at the tip of a 20 mm long bimorph with 0.4 mm in thickness is 150 μm with the response time of 1 sec.
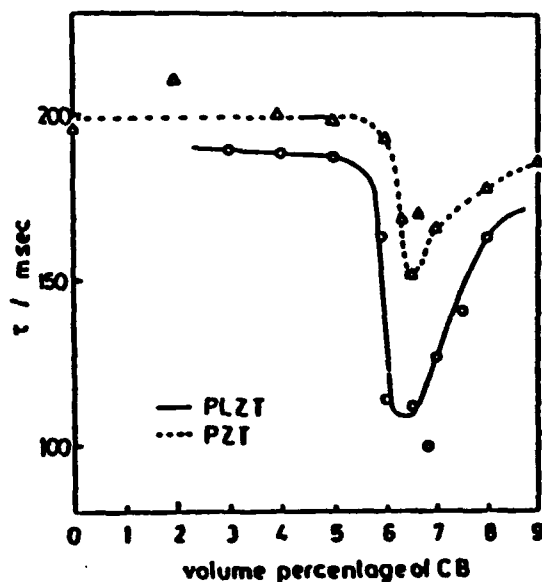

Figure 12   Damping time constant change with volume percentage of carbon black in polymer composite piezoelectric dampers.
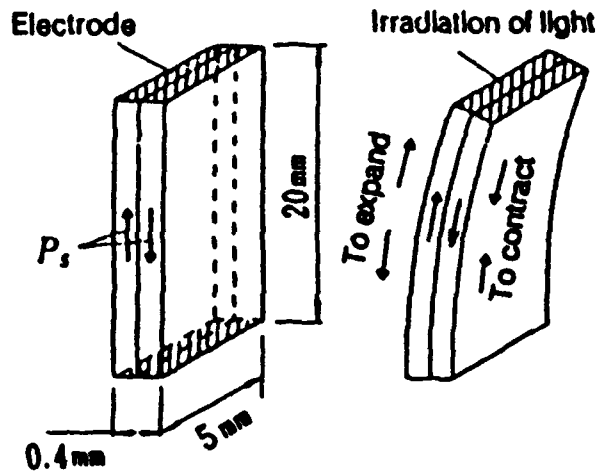
**Figure 13** Structure of a photo-driven bimorph.
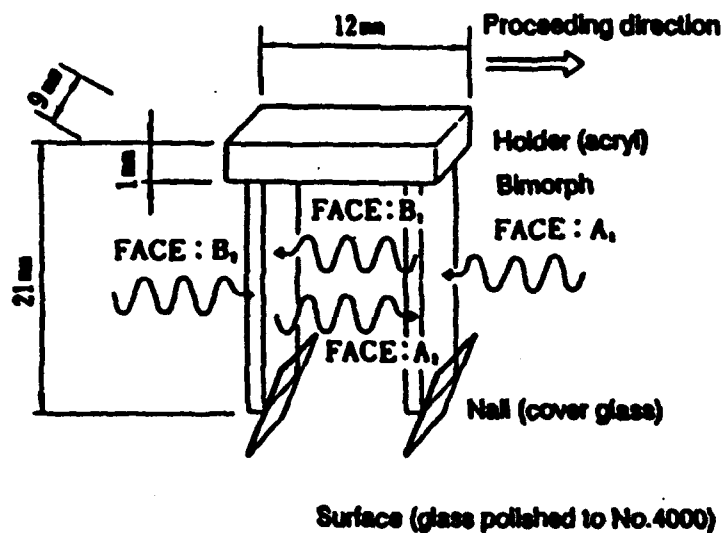
Figure 14 Structure of the walking element and the directions of illumination.

A photo-driven micro-waling device, which is designed to start moving by the irradiation of light, has been developed [22]. As shown in figure 14, it is simple in structure, having neither lead wires nor electric circuits. Only two bimorph legs are fixed to a plastic board. When light is irradiated to the legs alternately, the device moves like an inchworm.

CONCLUSION

The improvements of existing actuator materials are already well underway and the advances that lie ahead will be extensive. Bright future of piezoelectric and related ceramic actuator is anticipated in various application fields for adaptive structures.

REFERENCES

1. Uchino, K.. 1986. Piezoelectric/Electrostrictive Actuators, Tokyo: Morikita Pub. Co.

2. Uchino, K.. 1991. Problem Solving: Piezoelectric Actuators, Tokyo: Morikita Pub. Co.

3. Uchino, K.. 1986. "Electrostrictive Actuators: Materials and Applications." Bull. Amer. Ceram. Soc., 65(4):647-652.

4. Uchino, K.. 1988. "Ceramic Actuators." FC Report for Overseas Readers, pp. 23-31.

5. Uchino, K.. 1991. "Recent Topics in Ceramic Actuators." Proc. Int'l. Symp. Appl. Ferroelectrics '90, 153-158.

6. Uchino, K. and S. Nomura. 1983. "Electrostriction in PZT-Family Antiferroelectrics." Ferroelectrics, 50(1):191-196.

7. Uchino, K.. 1989. "Shape Memory Effect Associated with the Forced Phase Transition in Antiferroelectrics." Proc. Int'l. Mtg. on Adv. Mater., 9:489-503.

8. Sugawara, Y., K. Onitasuka, S. Yoshikawa, Q. C. Xu, R. E. Newnham, and K. Uchino. 1992. "Metal-Ceramic Composite Actuators." J. Amer. Ceram. Soc., 75(4):996-998.

9. Goto, H., K. Imanaka, and K. Uchino. 1992. "Piezoelectric Actuators for Light Beam Scanners." Ultrasonic Techno., (5):48-51.

10. Leung, K. M., S. T. Liu and J. Kyonka. 1980. "Electrostriction in PBZT." Ferroelectrics, 27(1):41-44.

11. Sugiyama, S. and K. Uchino. 1986. "Pulse Driving Method of Piezoelectric Actuators." Proc. 6th Int'l. Symp. Appl. Ferroelectrics, IEEE:637-640.

12. Ota, T., T. Uchikawa, and T. Mizutani. 1985. "Printing Flight Hammer Using Multilayer Piezoelectric Actuator." Jpn. J. Appl. Phys., 24(Suppl. 24-3):193-195.

13. Furuta, A., K. Y. Oh, and K. Uchino. 1992. "Shape Memory Ceramics and Their Application to Latching Relays." Sensors and Materials, 3(4):205-215.

14. Cross, L. E., S. J. Jang, R. E. Newnham, S. Nomura, and K. Uchino. 1980. "Large Electrostrictive Effects in Relaxor Ferroelectrics." Ferroelectrics, 23(3):187-192.

15. Uchino, K., Y. Tsuchiya, S. Nomura, T. Sato, H. Ishikawa, and O. Ikeda. 1981. "Deformable Mirror Using the PMN Electrostrictor." Appl. Optics, 20(17):3077-3080.

16. Hagimura, A. and K. Uchino. 1989. "Impurity Doping Effect on Electrostrictive Properties of $(Pb,Ba)(Zr,Ti)O_3$." Ferroelectrics, 93:373-378.

17. Uchino, K. and T. Takasu. 1986. "Evaluation Method of Piezoelectric Ceramics from a Viewpoint of Grain Size." Inspec., 10:29-33.

18.   Hirose, T. and K. Uchino. 1988. "Acoustic Emission in Ceramic Actuators." <u>Ferroelectrics</u>, 87:295-302.

19.   Uchino, K. and T. Ishii. 1988. "Mechanical Damper Using Piezoelectric Ceramics," <u>J. Jpn. Ceram. Soc.</u>, 96(8):863-867.

20.   Suzuki, Y., K. Uchino, H. Gouda, M. Sumita, R. E. Newnham and A. R. Ramachandran. 1991. "Mechanical Dampers Using Piezoelectric Composites." <u>J. Jpn. Ceram. Soc.</u>, 99(11):1135-1137.

21.   Tanimura, M. and K. Uchino. 1988. "Effect of Impurity Doping on Photostriction in Ferroelectric Ceramics." <u>Sensors and Materials</u>, 1:47-56.

22.   Uchino, K.. 1989. "Micro Walking Machines Using Piezoelectric Actuators." <u>J. Rob. Mech.</u>, 1(2):124-127.

APPENDIX 33

Dynamic Observation of Crack Propagation in Piezoelectric Multilayer Actuators

Atsushi Furuta

Department of Physics, Sophia University, Tokyo 102, Japan

Kenji Uchino*

Materials Research Laboratory, The Pennsylvania State University, University Park, Pennsylvania 16802

Crack propagation in multilayer piezoelectric actuators made of $Pb((Ni_{1/3}Nb_{2/3}),Ti,Zr)O_3$ ceramics with an interdigital electrode configuration was observed dynamically under an applied cyclic electric field using charge coupled device microscopy. The crack was observed only under a high electric field, and it healed under zero field. The crack was initiated at the internal electrode edge and propagated from the electrode edge in three directions. The electric-field-induced displacement was measured simultaneously with the propagation. The displacement of the multilayer actuator became gradually smaller and asymmetric with respect to the sign of the field with increased driving cycle.

I. Introduction

RECENTLY, ceramic actuators have been accepted for various applications, such as precision positioners in semiconductor manufacturing processes and precision cutting machines.[1-3] Multilayer actuators have several advantages: quick response, large generative force, and high electromechanical coupling. Many applications, such as a printer head[4]

and an X-Y stage,[5] have been attempted using the multilayer actuator. New applications of multilayer actuators make their endurance very important.

Figure 1(A) shows a typical interdigital-type structure of a multilayer actuator. The internally generated stress around the boundary between electrostrictively active and inactive parts (i.e., the electrode edge region) is expected to be large enough to cause self-destruction. The distribution of the internal stress under an electric field in this type multilayer actuator has been calculated by Takahashi et al.[6] using a finite-element method. The magnitude of the tensile stress is as high as 1×10^8 Pa, which is as large as the destruction strength of the ceramic (Fig. 1(B)). This suggests that a crack might be initiated around the electrode edge where a large internal stress is concentrated.

Although the theoretical estimation methods have been reported, the actual destruction mechanism of multilayer actuators has not been experimentally clarified as yet because of
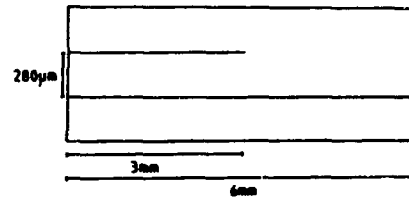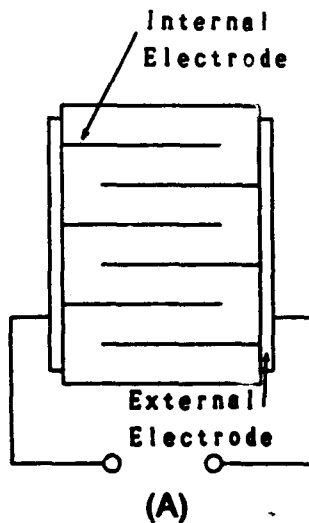
Fig. 2. Electrode configuration of a model multilayer actuator used in this experiment.

(A)

(B)
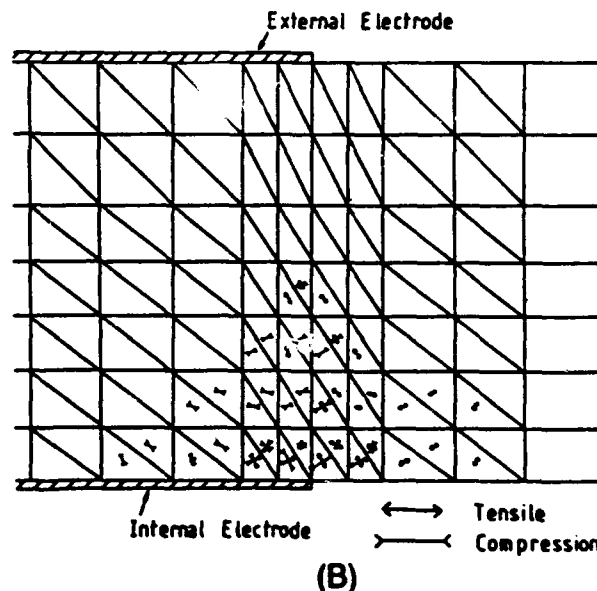
Fig. 1. (A) Structure of a multilayer actuator with an interdigital electrode configuration. (B) Internal stress distribution in a multilayer actuator with an interdigital electrode configuration (Ref. 6). Arrow length corresponds to the relative magnitude of the stress generated.

experimental difficulties. We have recently developed a new tool to observe the destruction mechanism. The purpose of this research is to visually observe dynamically the crack propagation in multilayer actuators with an interdigital electrode configuration by using a high-resolution charge coupled device (CCD) microscope, and to measure simultaneously the electric-field-induced displacement change during the destruction process.
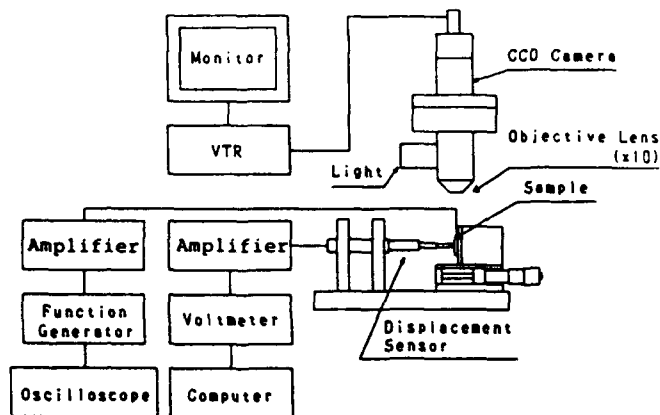
Fig. 3. Measuring system for crack propagation.

Note that the crack is observed only under a high electric field and is not detected under a zero field; this is probably what has provided the difficulty in previous experiments, which were performed without an electric field.

II. Experimental Procedure

The model multilayer actuators were prepared by a conventional tape-casting method.[2] The samples simulating the interdigital electrode configuration used in this experiment had only one layer, with a thickness of 280 μm (Fig. 2). The ceramic composition was a $Pb((Ni_{1/3}Nb_{2/3}),Ti,Zr)O_3$-based piezoelectric ceramic of the same composition as used in commercial multilayer actuators. Note that the model multilayer actuator used in this experiment exhibited a very large internal stress, concentrated around the electrode edge, so as to accelerate the multilayer actuator collapse.

Figure 3 shows the measuring system, composed of a CCD microscope (Model IK-C40, Toshiba, Tokyo, Japan) and a displacement sensor (Model 1301, Millitron). The CCD used here had 400 000 pixels, and 1-μm length of sample was magnified up to 1 mm on the monitor; this is probably the resolution of the CCD. The crack propagation process was video recorded. The sample was bipolar driven at 0.1 Hz, where a triangular wave of the electric field with E_{max} = 20 kV/cm was adopted.
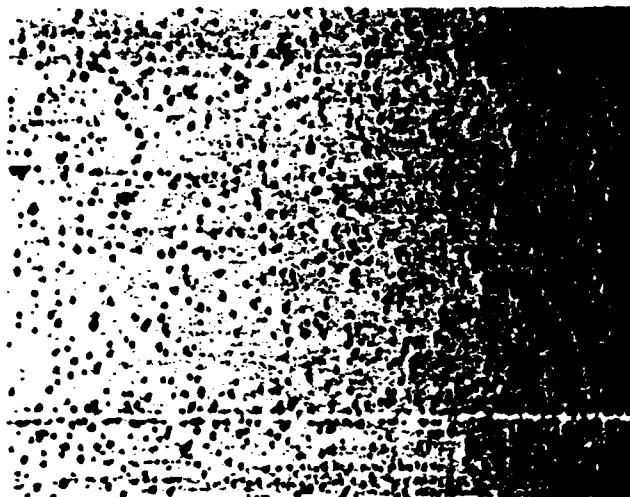

(A)
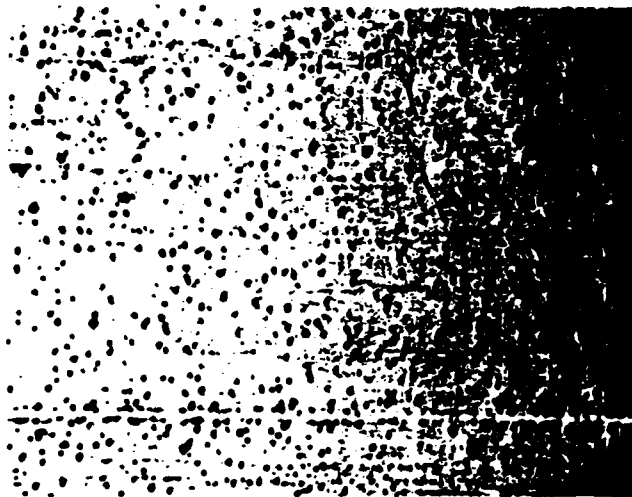
(B)
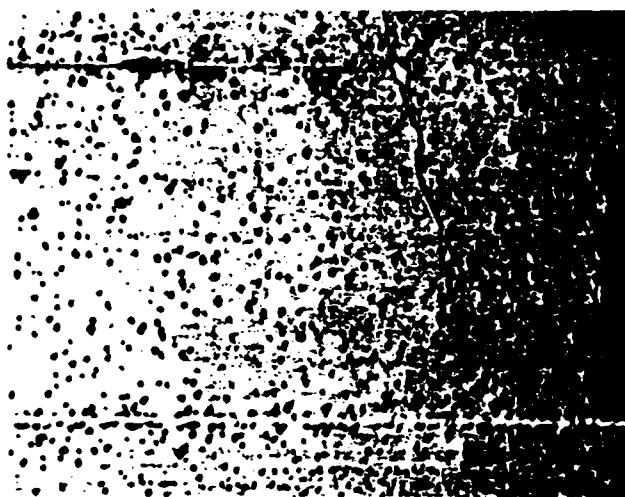
(C)

Fig. 4. Crack propagation process in the model multilayer actuator: (A) initial state, (B) after 2400 cycles, and (C) after 3000 cycles.
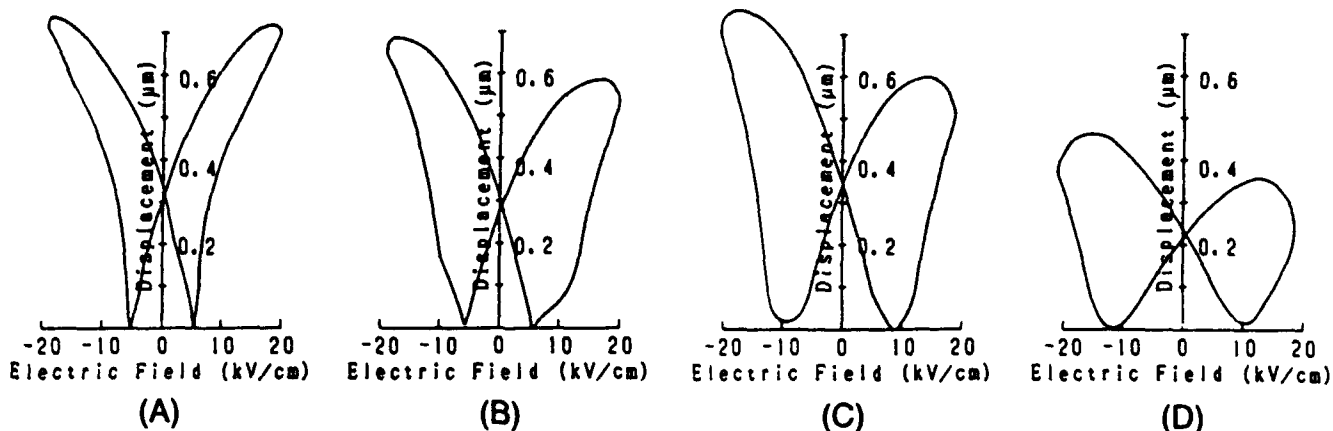
Fig. 5. Variation of the induced displacement during destruction: (A) initial state, (B) after 1800 cycles, (C) after 2400 cycles, and (D) after 3600 cycles.

III. Results

(1) Crack Propagation

Figures 4(A) to (C) show a typical crack propagation process. At first, the crack is initiated at one internal electrode edge; it propagates obliquely toward the paired electrode (Fig. 4(B)), which corresponds qualitatively to the result of the calculated internal stress distribution in Fig. 1(B), even if the calculation was made for somewhat different electrode configurations. The crack also propagates outward from the electrode edge, which is also expected from the electrode configuration, and along the metal electrode (Fig. 4(C)). The adhesive strength between the ceramic and the electrode metal is probably weaker than the mechanical strength of the ceramic itself, and the propagation speed of the crack along the ceramic–metal electrode boundary is the quickest path among the three branches.

Note that the crack is observed only under a high electric field and is not detected under zero field.

(2) Displacement Change during Destruction

The magnitude of the displacement induced in the model multilayer actuator was about 0.7 µm. The displacement curve in Fig. 5(A) shows a typical soft piezoelectric strain characteristic associated with the domain reversal. As the crack propagates, the displacement curve becomes asymmetric. A remarkable decrease in the strain occurs when a positive electric field is applied. This asymmetry is attributed to the asymmetric electrode configuration. By increasing the cycle of deformation, the magnitude of the displacement decreases, which is explained by a decrease of the effective electric field on the ceramic because of the narrow air gap generation (i.e., crack). The magnitude of the displacement decrease differed slightly in each sample, but the tendency was observed in most of the 10 samples.

IV. Summary

(1) To clarify the crack propagation mechanism in the piezoelectric multilayer actuator, we have set up a high-resolution CCD microscope, with the capability of simultaneously measuring the induced strain.

(2) We have made a model multilayer actuator so as to cause the crack to occur at a very high speed. The crack is observed only under an electric field and is closed under zero field.

(3) The crack is initiated at the internal electrode edge, and it branches basically into three directions from the electrode edge. This crack propagation process corresponds qualitatively to the result of the internal stress distribution calculated using a finite-element method.

This preliminary work will be followed by systematic observation on piezoelectric, electrostrictive, and phase-transition-related ceramic actuators, as well as detailed analysis based on the exact electrode configuration.

References

[1] E. Kouno, "A Fast Response Piezoelectric Actuator for Servo Correction of System Errors in Precision Engineering," *CIRP Ann.,* 33 [1] 369 (1984).

[2] K. Uchino, *Piezoelectric/Electrostrictive Actuators.* Morikita, Tokyo, Japan, 1986.

[3] K. Uchino, "Electrostrictive Actuators: Materials and Applications," *Am. Ceram. Soc. Bull.,* 65 [4] 647 (1986).

[4] T. Yano and S. Takahashi, "Utilization of Piezoelectric Stiffend Effects on Impact Printer Heads," *Trans. IEICE.* J71-C11, 1576 (1988).

[5] S. Moriyama and F. Uchida, "Precision X–Y Stage with a Piezo-Driven Fine Table," *JSPE,* 50 [4] 718 (1984).

[6] S. Takahashi, A. Ochi, M. Yonezawa, T. Yano, T. Hamatsuki, and I. Fukui, "Internal Electrode Piezoelectric Ceramic Actuator," *Jpn. J. Appl. Phys.,* 22 [Suppl. 22-2] 157 (1983). □

APPENDIX 34

Ceramic Actuators: Principles and Applications

Kenji Uchino

Introduction

Piezoelectric and electrostrictive actuators, capable of moving something electromechanically, are forming a new field between electronic and structural ceramics.[1,5] Application fields are classified into three categories: positioners, motors, and vibration suppressors. The manufacturing precision of optical instruments such as lasers and cameras, and the positioning accuracy for fabricating semiconductor chips, which must be adjusted using solid-state actuators, is of the order of 0.1 μm. Regarding conventional electromagnetic motors, tiny motors smaller than 1 cm^3 are often required in office or factory automation equipment and are rather difficult to produce with sufficient energy efficiency. Ultrasonic motors whose efficiency is insensitive to size are superior in the minimotor area. Vibration suppression in space

structures and military vehicles using piezoelectric actuators is also a promising technology.

New solid-state displacement transducers controlled by temperature (shape memory alloy) or magnetic field (amorphous magnetostrictive alloy) have been proposed, but are generally inferior to the piezoelectric/electrostrictive actuators because of technological trends aimed at reduced driving power and miniaturization.

This article reviews recent developments of piezoelectric and related ceramic actuators for smart/intelligent systems.

Ceramic Actuator Materials

What happens on an atomic scale when a ceramic expands or contracts in response to an applied electric field? There are three types of strain (defined by the ratio $\Delta L/L$:

the amount of deformation with respect to the original length) that may be induced by an electric field, depending on the crystal structure: piezoelectric, electrostrictive, and phase-change-related strains.

Figures 1a and b show rigid ion models for noncentrosymmetric (piezoelectric) and centrosymmetric (electrostrictive) crystals, respectively.[6] When an electric field is applied to the crystal, the cations are displaced in the direction of the field and the anions in the opposite direction. The ionic shift differences in noncentrosymmetric ceramic can be visualized as soft and hard springs, producing piezostriction. The induced strain is proportional to the applied field (i.e. $x = dE$). For the centrosymmetric structure in Figure 1b, anharmonicity of the springs is essential, resulting in a second-order electrostrictive effect. Here the induced strain is proportional to the square of the field ($x=ME^2$).

Actual strains in ceramics are induced in more complicated ways. The crystal pictured in Figure 1a possesses a spontaneous polarization. When a large reverse electric field is applied in the opposite direction of the spontaneous polarization, a transition phase is formed which is another stable crystal state in which the relative positions of the ions are reversed by 180°. This transition, referred to as polarization reversal, causes a jump and hysteresis of the strain during an electric-field cycle, superimposed on the pure piezostriction. Non-180° polarization reorientation, though not shown in the one-dimensional model in Figure 1a, also causes significant contribution to the strain hysteresis.

Modified lead zirconate titanate [PZT, $Pb(Zr,Ti)O_3$]-based ceramics are currently the leading materials for piezoelectric applications. The PLZT [$(Pb,La)(Zr,Ti)O_3$] 7/62/38 compound is one such composition.[7] The strain curve is shown in Figure 2a left. When the applied field is small, the induced strain is nearly proportional to the field. As the field becomes larger (i.e., greater than about 100 V/mm), however, the strain curve deviates from this linear trend and significant hysteresis is exhibited due to polarization reorientation. This sometimes limits the usage of this material in actuator applications that require nonhysteretic response.

An interesting new family of actuators has been fabricated from a barium stannate titanate [$Ba(Sn,Ti)O_3$] solid solution.[8] The useful property of $Ba(Sn_{0.15}Ti_{0.85})O_3$ is its unusual strain curve, in which the domain reorientation occurs only at low fields, and there is then a long linear range at higher fields (Figure 2a right); i.e., the coercive field is unusually small.

On the other hand, electrostriction in

$$x = (\delta_2 - \delta_1)/a_0 = dE$$

Ion Pair Potential Energy

(a) Piezoelectric Strain

$$x = (\delta_2 - \delta_1)/a_0 = ME^2$$

Ion Pair Potential Energy

(b) Electrostriction
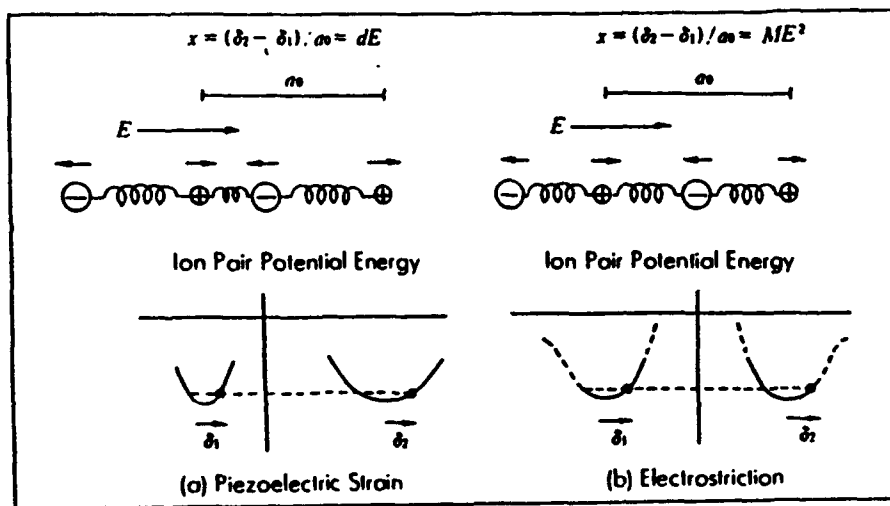
Figure 1. Diagrammatic explanation of the origins of piezoelectric strain (a) and electrostriction (b).

a) Piezostrictor

PLZT

BST

b) Electrostrictor

PMN-PT

c) Phase-Change Material

PNZST

DIGITAL DISPLACEMENT

PNZST
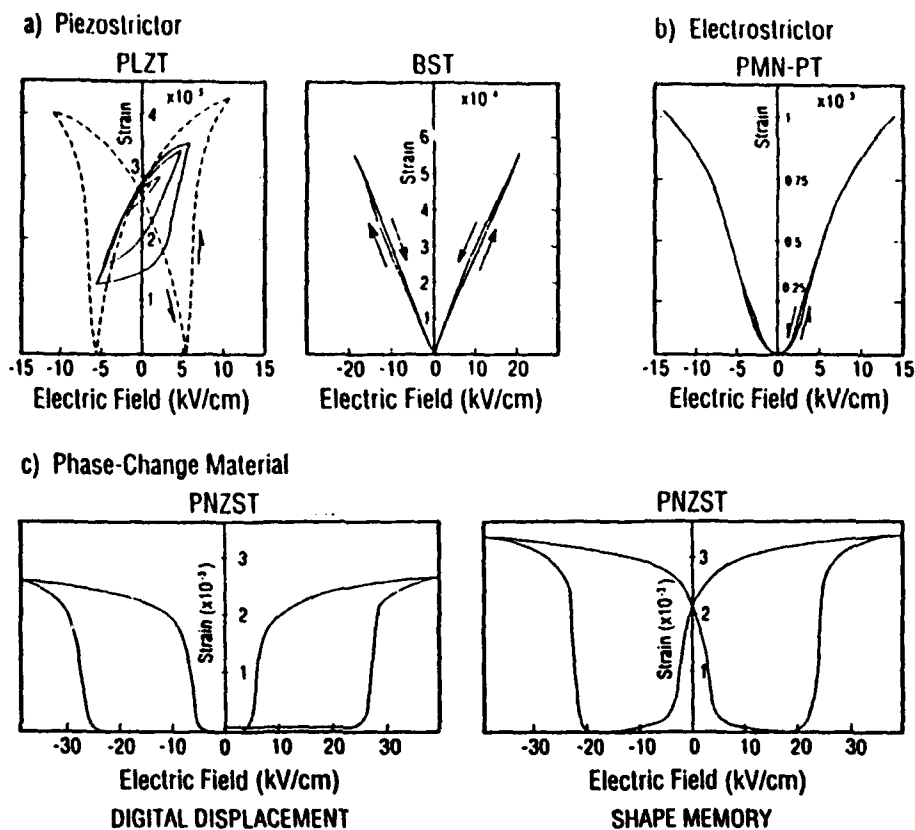
SHAPE MEMORY

Figure 2. Electric field-induced strains in ceramics: (a) Piezoelectric for $(Pb,La)(Zr,Ti)O_3$ and $Ba(Sn,Ti)O_3$. (b) Electrostrictor, $Pb(Mg_{1/3}Nb_{2/3}Ti)O_3$. (c) Phase-change material $Pb(Zr,Sn,Ti)O_3$.

a) Shape Memory Alloy

Parent Phase

Cool   Heat

(Initial State)   (Deformed State)

Stress Applied & Removed

Martensitic Phase   Deformed Martensitic Phase

b) Shape Memory Ceramic

Paraelectric Phase

Cool   Heat

(Deformed State)

Inverse Field Applied & Removed

(Initial State)

Field Applied & Removed

Antiferroelectric Phase   Ferroelectric Phase
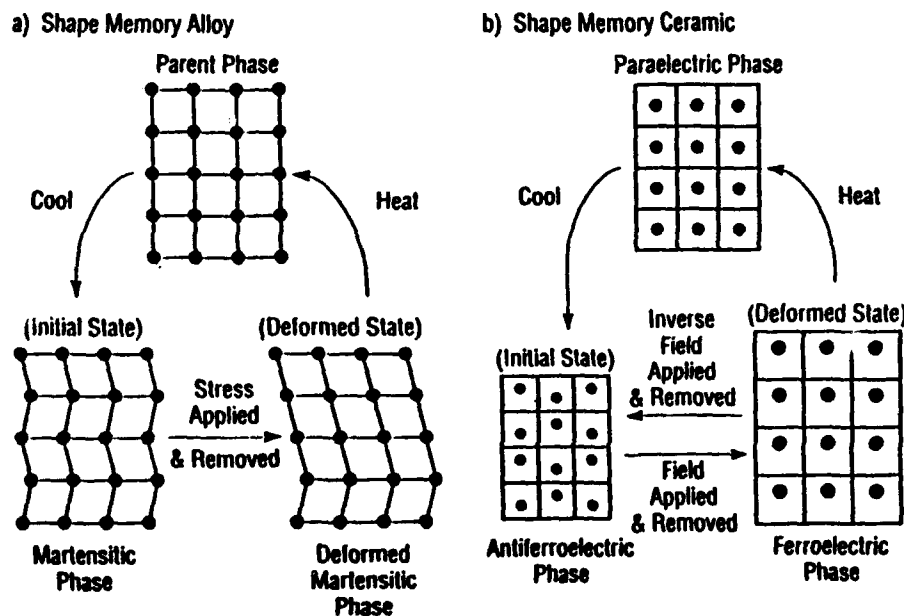
Figure 3. Shape-memory effects in an alloy (a) and an antiferroelectric ceramic (b).

$PMN [Pb(Mg_{1/3}Nb_{2/3})O_3]$-based ceramics, though a second-order phenomenon of electromechanical coupling, is extraordinarily large (more than 0.1%).[9] An attractive feature of these materials is the near absence of hysteresis (Figure 2b).

Concerning the phase-change-related strains, polarization induction by switching from a macroscopically nonpolar into a polar state, as in switching from an anti-ferroelectric to a ferroelectric state, has been proposed.[10] Figure 3 illustrates the phase transition mechanism under an applied electric field, in comparison with the phase change in a shape memory alloy.[11] Notice that the strain control is made thermally in shape memory alloys, leading to much slower response and higher drive power than in the antiferroelectrics.

Figure 2c shows the field-induced strain curves taken for the lead zirconate stannate-based system $[Pb_{0.99}Nb_{0.02}((Zr,Sn_{1-x})_{1-y}Ti_y)_{0.98}O_3]$. The longitudinally induced strain reaches up to 0.4%, which is much larger than that expected in normal piezostrictors/electrostrictors. A rectangular-shape hysteresis in Figure 2c left, referred to as a "digital displacement transducer" because of the two on/off strain states, is interesting. Moreover, this field-induced transition exhibits a shape memory effect in appropriate compositions (Figure 2c right). Once the ferroelectric phase has been induced, the material will "memorize" its ferroelectric state even under zero-field conditions, although it can be erased with the application of a small reverse bias field.[12] This shape memory ceramic is used in energy-saving actuators.

The fundamental features of ceramic actuators may be summarized as follows:

■ Displacements of up to several tens of microns that can be controlled with a precision of ±0.01 μm.
■ Response speeds on the order of 10 μsec.
■ Generative forces as large as 400 kgf/cm².
■ Driving power an order of magnitude smaller than electromagnetic motors.

As the requirements for ceramic actuators become more specific, inadequacies due to the preparation history of the ceramic arise in reproducibility of properties. High reproducibility is achieved only by precise control of the grain/particle size, which is not possible utilizing the conventional mixed-oxide method of preparation. Recent advances in preparation technology of ultrafine ceramic powders has been useful in producing reliable and durable ceramic actuators. The effect of grain size on the electrostrictive response and the mechanical fracture toughness in lead lanthanum zirconate titanate (PLZT 9/65/35) is shown in Figures 4a and 4b.[13] A significant reduction in hysteresis and in

the strain magnitude is observed for grain sizes less than 1.7 μm, as is a remarkable increase in the fracture toughness, suggesting the existence of an optimum grain size around 1 μm.

Actuator Designs

Two of the most popular actuator designs are multilayers and bimorphs (see Figure 5). The multilayer, in which roughly 100 thin piezoelectric/electrostrictive ceramic sheets are stacked together, has advantages in low driving voltage (100 V), quick response (10 μsec), high generative force (100 kgf) and high electromechanical coupling. But the displacement in the range of 10 μm is not sufficient for some applications. This contrasts with the bimorph, consisting of multiple piezoelectric and elastic plates bonded together to generate a large bending displacement of several hundred μm, but the response (1 msec) and the generative force (100 gf) are low.

A composite actuator structure called the "moonie" has been developed to provide characteristics intermediate between the multilayer and bimorph actuators;[14] this transducer exhibits an order of magnitude larger displacement than the multilayer, and much larger generative force with quicker response than the bimorph. The device consists of a thin multilayer piezoelectric element and two metal plates with narrow moon-shaped cavities bonded together as shown in Figure 5. The moonie with a size of 5 × 5 × 2.5 mm can generate a 20-μm displacement under 60 V, eight times as large as the generative displacement of the multilayer with the same size.[15] This new compact actuator has been applied to make a miniaturized laser beam scanner.

## Applications of Piezoelectric/Electrostrictive Actuators

Piezoelectric/electrostrictive actuators may be classified into two categories, based on the type of driving voltage applied to the device and the nature of the strain induced by the voltage (Figure 6): (1) rigid displacement devices for which the strain is induced unidirectionally along an applied dc field, and (2) resonating displacement devices for which the alternating strain is excited by an ac field at the mechanical resonance frequency (ultrasonic motors). The first can be further divided into two types: servo displacement transducers (positioners) controlled by a feedback system through a position-detection signal, and pulse-drive motors operated in a simple on/off switching mode. An actuator referred to as a flight actuator has been proposed that strikes a steel ball by means of a pulse-drive unit made from a multilayer piezo-device similar to that found in a pinball machine.[16]

The material requirements for these classes of devices are somewhat different, and certain compounds will be better suited to particular applications. The ultrasonic motor, for instance, requires a conventional hard-type piezoelectric with a high mechanical quality factor Q. The servo-displacement transducer suffers most from strain hysteresis and, therefore, a PMN electrostrictor is used for this purpose. The pulse-drive motor requires a low permittivity material aiming at quick response rather than a small hysteresis so that soft-PZT piezoelectrics are preferred to the high-permittivity PMN for this application.

Three typical application examples will now be considered.

Deformable Mirror

In the field of optical information processing, deformable mirrors have been proposed to control the phase of the incident light wave. The deformable mirror can be made convex or concave on the surface as necessary. This type of mirror, which is applicable to an accessory device

a)

b)

D = 1.1 (μm)
C = 208 ± 22 (μm)
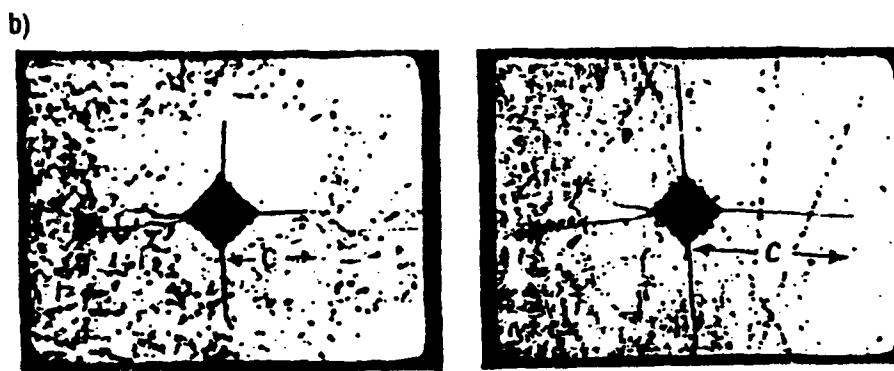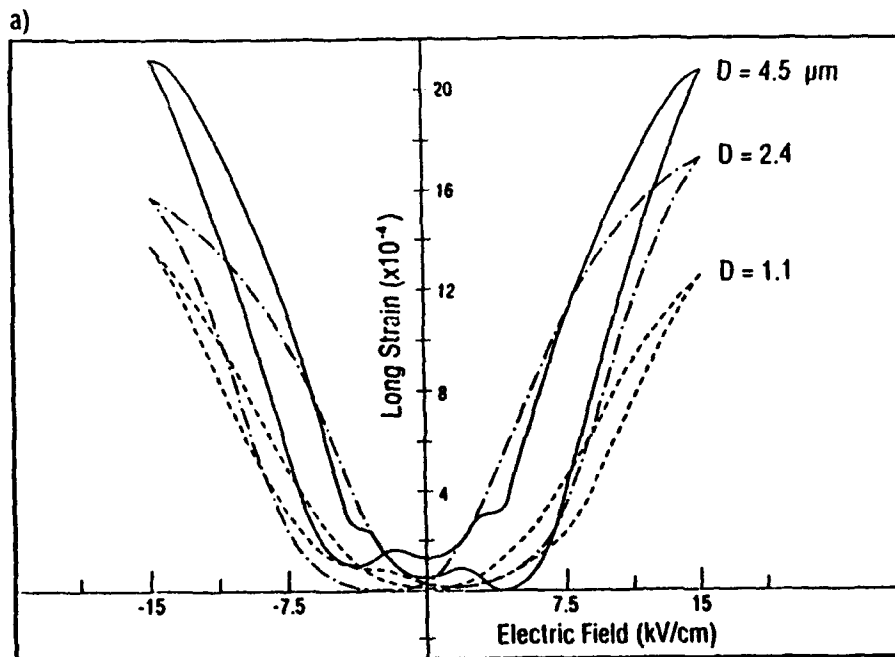
D = 2.4 (μm)
C = 275 ± 30 (μm)

Figure 4. Grain-size dependence of field-induced strain (a) and Vicker's indentation test (b), observed in PLZT 9/65/35.
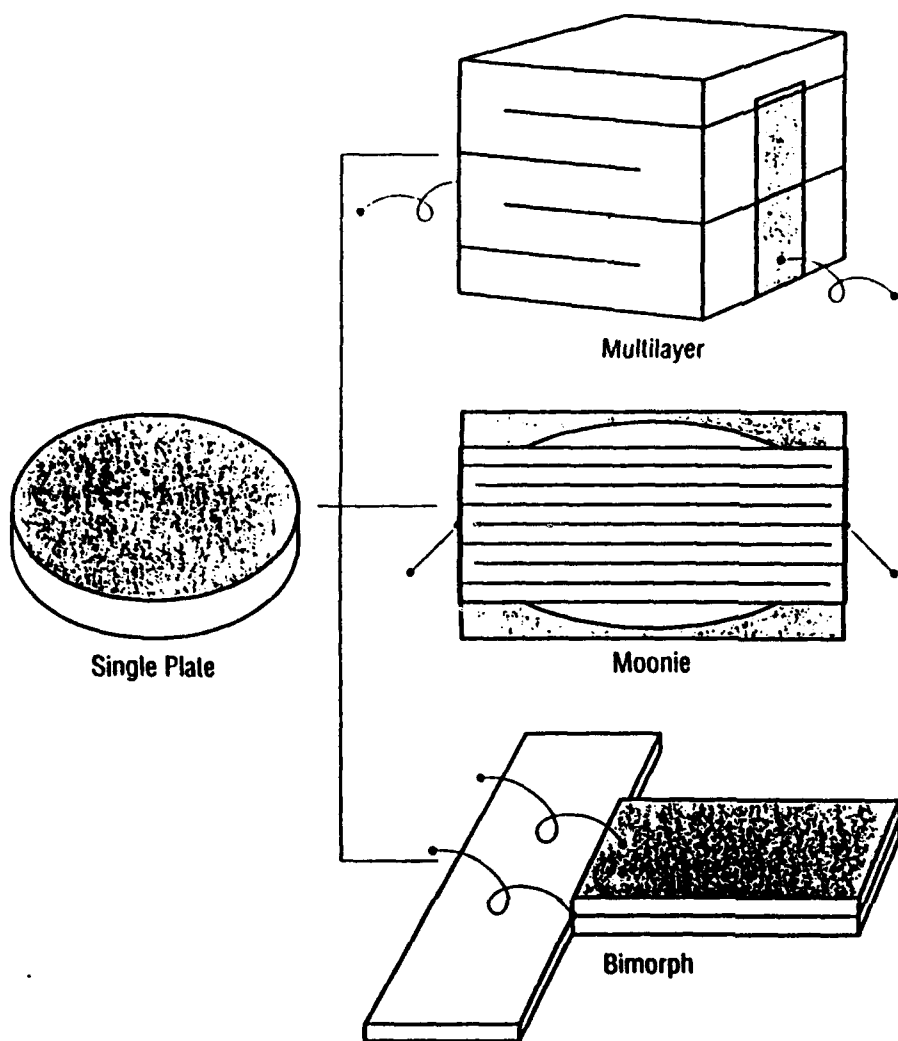
Figure 5. *Typical designs for ceramic actuators: multilayer, moonie, and bimorph.*
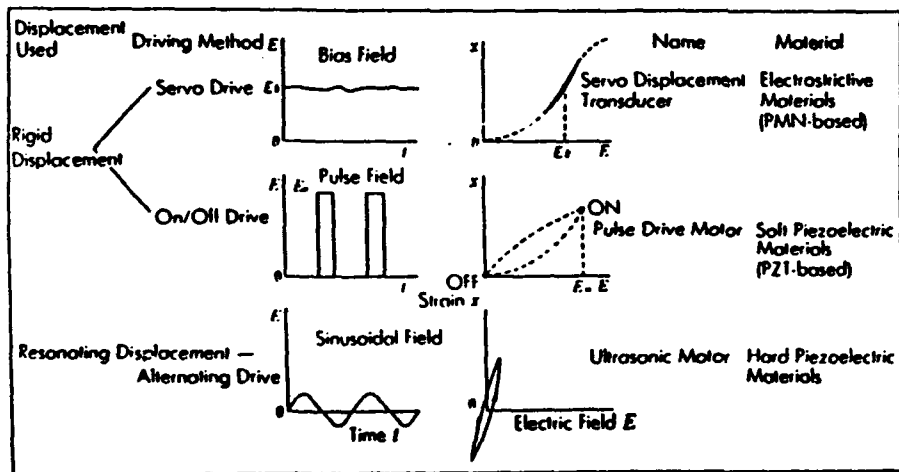
Figure 6. *Classification of piezoelectric/electrostrictive actuators.*

on observatory telescopes, effectively corrects for image distortions resulting from fluctuating airflow.

An example of a deformable mirror is the two-dimensional multimorph type illustrated in Figure 7.[17,18] When three layers of thin electrostrictive ceramic (PMN) plates are bonded to the elastic plate of a glass mirror, the mirror surface is deformed in various ways corresponding to the strain induced in the PMN layers. The nature of the deformation is determined by the electrode configurations and the distribution of the applied electric field. Trial devices have been designed by finite element methods such that the first layer, with a uniform electrode pattern, produces a spherical deformation (i.e., refocusing), while the second layer, with a 6-divided electrode pattern, corrects for coma aberration.

Aberration correction using such a simple three-layered device makes the image clear to the human eye. One may relate this situation to an eye examination at the optometrist. First you are asked "Which lens fits you best?" to adjust the focus degree. Then, "Do you have an uneven orientation distribution?" to correct the astigmatism. Usually, an optometrist does not further optically correct your lenses. Correction up to the second order is sufficient for the human eye.
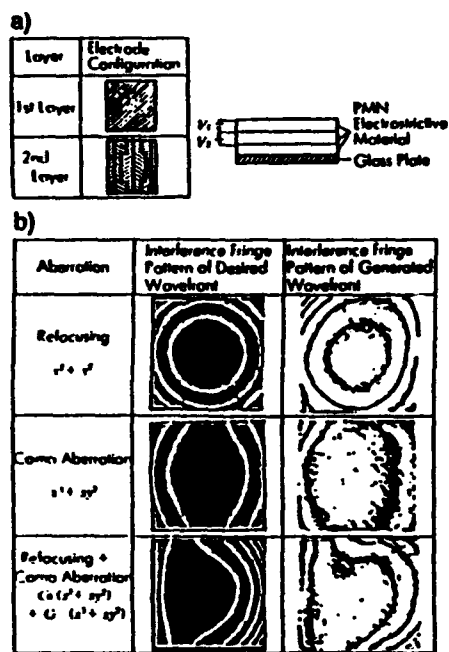

Figure 7. *Structure of a multimorph deformable mirror (a) and actual control of light wavefront (b).*

Impact Dot-Matrix Printer

Among the various types of printing devices, dot matrix printers are routinely employed at present. Each character formed by such a printer is composed of a 24 × 24-dot matrix. A printing ribbon is subsequently impacted by a multiwire array. A sketch of the printer head appears in Figure 8a."

The printing element is composed of a multilayer piezoelectric device, in which 100 thin ceramic sheets 100 μm in thickness are stacked, together with a sophisticated magnification mechanism (Figure 8b). The advantages of using a multilayer actuator for this particular application include a low driving voltage, large displacement, and a high electromechanical coupling. The magnification unit is based on a monolithic hinged lever with a magnification of 30, resulting in an amplified displacement of 0.5 mm and an energy transfer efficiency greater than 50%.

The merits of the piezoelectric impact printer compared with the conventional electromagnetic types are: (1) higher printing speed by an order of magnitude, (2) lower energy consumption by an order of magnitude, and (3) reduced printing noise, which can be obtained with a sound shield because the actuators do not generate much heat.

Ultrasonic Motor

Efforts have been made to develop high-power ultrasonic vibrators as replacements for conventional electromagnetic motors. Two categories are being investigated for ultrasonic motors: a standing-wave type and a propagating-wave type.

The standing-wave type is sometimes referred to as a vibratory-coupler type or a "woodpecker" type, where a vibratory piece is connected to a piezoelectric driver and the tip portion generates flat-elliptical movement. Attached to a rotor or a slider, the vibratory piece provides intermittent rotational torque or thrust. The standing-wave type has, in general, high efficiency, but lack of control in both clockwise and counterclockwise directions is a problem.

An ultrasonic linear motor equipped with a multilayer piezoelectric actuator and fork-shaped metallic legs has been developed as shown in Figure 9." Since there is a slight difference in the mechanical resonance frequency between the two legs, the phase difference between the bending vibrations of both legs can be controlled by changing the drive frequency. The walking slider moves in a way similar to a horse using its fore and hind legs when trotting. A trial motor 20 × 20 × 5 mm³ in dimension exhibited a maximum speed of 20 cm/s and a maximum thrust of
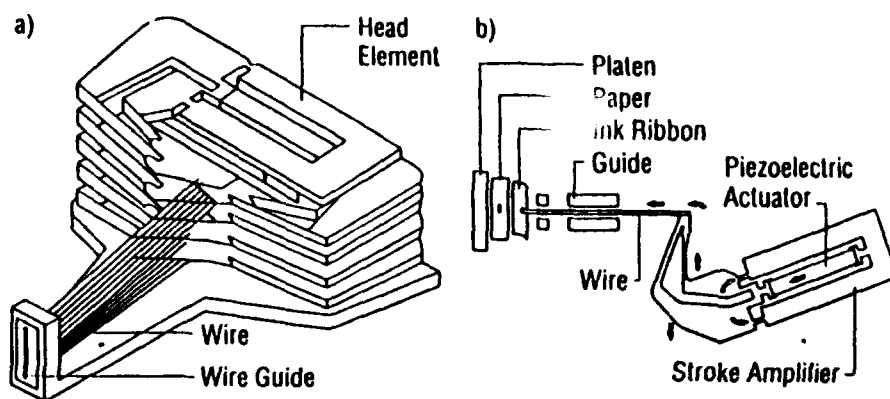

Figure 8. Structure of a printer head (a) and a differential-type piezoelectric printer-head element (b).
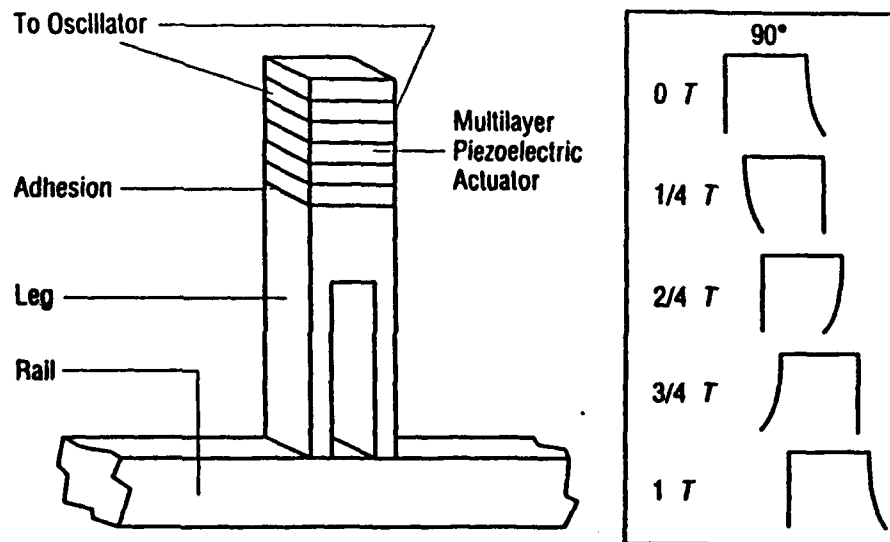

Figure 9. Ultrasonic linear motor of a vibratory coupler type.

0.2 kgf with a maximum efficiency of 20%, when driven at 98 kHz of 6 V (actual power ~0.7 W). This motor has been employed in a precision X-Y stage.

By comparison, the propagating-wave type (a surface-wave or "surfing" type) combines two standing waves with a 90° phase difference both in time and in space, and is controllable in both rotational directions.

By means of the traveling elastic wave induced by the thin piezoelectric ring, a ring-type slider in contact with the "rippled" surface of the elastic body bonded onto the piezoelectric is driven in both directions by exchanging the sine and cosine voltage inputs. Another advantage is its thin design, which makes it suitable for

installation in VCR or movie cameras as an automatic focusing device.[21]

Future Developments of Ceramic Actuators

It is evident that the application field of ceramic actuators is remarkably wide. There still remain, however, problems in durability and reliability that need to be addressed before these devices can become general-purpose commercialized products. Investigations are primarily focused on the areas of material preparation, device design, and systemization of the actuator.[22] In particular, current topics include the preparation of homogeneous fine-grained ceramics by means of wet chemical

methods,[13] moonie actuators,[14] pulse-drive techniques based on analysis of transient vibrations and vibration suppression,[23] and prediction of breakdown within a ceramic actuator by means of acoustic emission measurements.[24]

Piezoceramic:carbon:polymer composites and photostrictive actuators have been under recent development for mechanical vibration suppression and remote control/drive of the actuator. These devices are described in the closing sections.

Piezoelectric Damper

The passive damper application is a smart usage of piezoelectrics, where mechanical noise vibration is radically suppressed by the converted electric energy dissipation through Joule heat when a suitable resistance, equal to an impedance of the piezoelectric element $1/\omega C$, is connected to the piezo-element.[25] Piezoceramic:carbon black:polymer composites are promising designs for practical applications (see Figure 10). The minimum damping time constant (i.e., quickest damping) is obtained at 6 vol % of carbon black, where a drastic electric conductivity change is observed (percolation threshold).[26] The vibration suppression effect is greatly enhanced by using a higher electromechanical coupling material.

Photostrictive Actuator

A photostrictive actuator is a fine example of an intelligent material incorporating illumination sensing and self production of drive/control voltage together with final actuation. In certain ferroelectrics, a constant electromotive force is generated with exposure of light, and a photostrictive strain results from the coupling of this bulk photovoltaic effect to inverse piezoelectricity. .
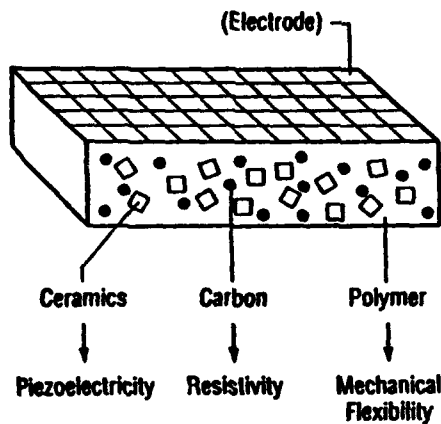

Figure 10. Passive damper using a piezoceramic/polymer composite.
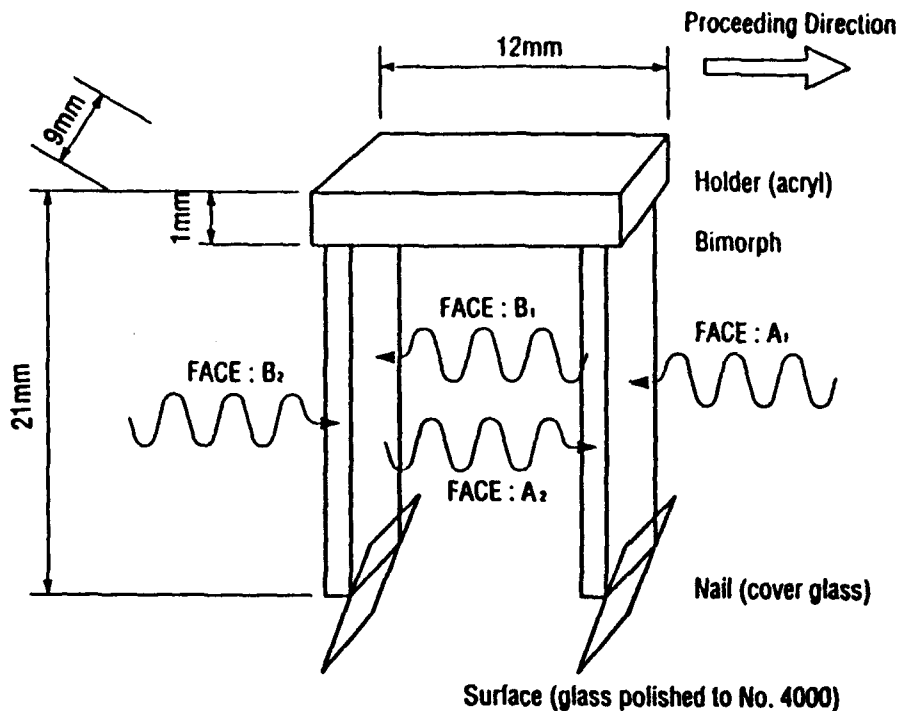
Figure 11. Structure of a photo-driven walking device and the illumination directions.

A bimorph unit has been made from PLZT (3/52/48) ceramic doped with slight additions of niobium and tungsten.[27] The remnant polarization of one PLZT layer is parallel to the plate and in the direction opposite to that of the other plate. When a violet light is irradiated to one side of the PLZT bimorph, a photovoltaic voltage of 0.7 kV/mm is generated, causing a bending motion. The displacement observed at the tip of a 20 mm bimorph 0.4 mm in thickness is 150 μm, with a response time of 1 sec.

A photo-driven micro walking device, designed to begin moving by light illumination, has been developed.[28] As shown in Figure 11, it is simple in structure, having neither lead wires nor electric circuitry, with two bimorph legs fixed to a plastic board. When the legs are irradiated alternately with light, the device moves like an inchworm with a speed of 100 μm/min.

Summary

In summary, piezoelectric/electrostrictive actuators and ultrasonic motors are expected to increase in market share to more than $10 billion in 1998, and a bright future is anticipated in many application fields.

References

1. K. Uchino, Piezoelectric/Electrostrictive Actuators (Morikita Publishing, Tokyo, 1986).
2. K. Uchino, Problem Solving-Piezoelectric Actuators (Morikita Publishing, Tokyo, 1991).
3. K. Uchino, Bull. Am. Ceram. Soc. 65 (4) (1986) p. 647.
4. K. Uchino, FC Report for Overseas Readers (1988) p. 23.
5. K. Uchino, Proc. Intl. Symp. Appl. Ferroelectrics '90 (1991) p. 153.
6. K. Uchino and S. Nomura, Jpn. J. Appl. Phys. 52 (7) (1983) p. 575.
7. K. Furuta and K. Uchino, Adv. Ceram. Mater. 1 (1986) p. 61.
8. J. von Cieminski and H. Beige, J. Phys. D 24 (1991) p. 1182.
9. L.E. Cross, S.J. Jang, R.E. Newnham, S. Nomura, and K. Uchino, Ferroelectrics 23 (3) (1980) p. 187.
10. K. Uchino and S. Nomura, Ferroelectrics 50 (1) (1983) p. 191.
11. K. Uchino, Proc. Intl. Mtg. Adv. Mater. 9 (1989) p. 489.
12. A. Furuta, K.Y. Oh, and K. Uchino, Sensors and Mater. 3 (4) (1992) p. 205.
13. K. Uchino and T. Takasu, Inspec. 10 (1986) p. 29.
14. Y. Sugawara, K. Onitsuka, S. Yoshikawa, Q.C. Xu, R.E. Newnham, and K. Uchino, J. Am. Ceram. Soc. 75 (4) (1992) p. 996.
15. H. Goto, K. Imanaka, and K. Uchino, Ultrasonic Technol. (5) (1992) p. 48.
16. T. Ota, T. Uchikawa, and T. Mizutani, Jpn. J. Appl. Phys. 24 (Suppl. 24-3) (1985) p. 193.
17. K. Uchino, Y. Tsuchiya, S. Nomura, T. Sato, H. Ishikawa, and O. Ikeda, Appl. Optics 20 (17) (1981) p. 3077.
18. T. Sato, H. Ishikawa, O. Ikeda, S. Nomura,

and K. Uchino, *Appl. Optics* 21 (1982) p. 3669.

19. T. Yano, I. Fukui, E. Sato, O. Inui, and Y. Miyazaki, *Electr. & Commun. Soc. Proc.* (Spring 1984) p. 1-156.

20. K. Uchino, *J. Rob. Mech.* 1 (1989) p. 124.

21. *Ultrasonic Motors/Actuators*, edited by Y. Akiyama (Triceps, Tokyo, 1986).

22. *Annual Report of Solid State Actuator Soc.*, edited by K. Uchino (Jpn. Tech. Transfer Assoc.,

Tokyo, 1991); *Smart Materials and Structures*, edited by R.O. Claus et al. (IOP, Philadelphia, 1992).

23. S. Sugiyama and K. Uchino, *Proc. Intl. Symp. Appl. Ferroelectrics '86* (IEEE, 1986) p. 637.

24. T. Hirose and K. Uchino, *Ferroelectrics 87* (1988) p. 295.

25. K. Uchino and T. Ishii, *J. Jpn. Ceram. Soc. 96* (8) (1988) p. 863.

26. Y. Suzuki, K. Uchino, H. Gouda, M. Sumita, R.E. Newnham, and A.R. Ramachandran, *J. Jpn. Ceram. Soc.* 99 (11) (1991) p. 1135.

27. M. Tanimura and K. Uchino, *Sensors and Mater.* 1 (1988) p. 47.

28. K. Uchino, *O plus E* (New Technology, Tokyo, May, 1989) p. 58.   □

APPENDIX 35

Applications of piezoelectric ceramics in smart actuators and systems

KENJI UCHINO
Materials Research Laboratory
The Pennsylvania State University
University Park, PA 16802-4801

Permanent Address:
Department of Physics
Sophia University, Kioi-cho 7-1
Chiyoda-ku, Tokyo 102
JAPAN

In these several years piezoelectric and electrostrictive actuators have become very popular for micro-positioning in optical and precision machinery fields.[1] Aiming at wide commercialization of these actuators, many investigations have been made in the improvement of ceramic materials for actuators, designs of the devices and control and systematization of the actuators. This paper reviews recent applications of piezoelectric/electrostrictive ceramics from a viewpoint of "smart" actuators and systems.

A passively smart material is exemplified by the lead magnesium niobate (PMN) based ceramic, which can exhibit a large electrostriction $(\Delta l/l - 10^{-3})$ without any hysteresis and aging effect during an electric field cycle.[2] A composite actuator structure called "moonie" has been developed to amplify the small displacement induced in a multilayer piezoelectric device. Passive damper application is another smart usage of piezoelectrics, where mechanical noise vibration is radically suppressed by the converted electric energy dissipation through Joule heat when a suitable resistance is connected to the piezoelectric plate.[3] Piezoceramic: carbon black: polymer composites are promising useful designs for practical use.

An actively smart material is exemplified by the video tape head positioner made from a lead zirconate titanate (PZT) bimorph with sensor and actuator-divided electrodes.[4]

Monomorphs and shape memory ceramics belong to very smart materials. A monomorph device made of a semiconductive piezoelectric plate generates the Schottky barrier when metal electrodes are coated on the faces, providing non-uniform distribution of the electric field even in a compositionally uniform ceramic. A superimposed effect of piezoelectricity and semiconductivity leads to a bending deformation in a total ceramic plate.[5] The strains associated with phase transitions such as an antiferroelectric-to-ferroelectric transition in lead zirconate stanate-based ceramics reach up to 0.4%, which is much larger than that expected in electrostrictors. Moreover, this field-induced transition exhibits a shape memory effect in appropriate compositions, and such ceramics are useful for the applications to latching relay and a mechanical clamper.[6]

A photostrictive actuator is the best example of intelligent materials including sensing, actuating and drive/control functions in a unique material.[7] In certain ferroelectrics a phenomenon by which a constant electromotive force is generated with exposure of light has been observed. A photostrictive effect is expected as a result of the coupling of the photovoltaic and inverse piezoelectric effects. A remote control miniature walking robot, which is activated with illumination, is currently being fabricated. Two photostrictive PLZT bimorphs were combined together and each plate exhibits a minute photo-induced displacement on the order of 150 µm. Alternative illumination causes a slow moving of the ceramic device.

A flight actuator consisting of a pulse-driven piezoelectric element and a steel ball is a very suggestive mechanism, even if it would not be denoted as a smart system. A 2mm steel ball can be hit up to 20 mm by a 5 μm displacement induced in a multilayer actuator with quick response.[8]

A smart system is typically exemplified by a precision lathe machine. A micro displacement actuator has been manufactured using an electrostrictive multilayer actuator, a magneto-resistive strain sensor and an adaptive control circuitry. The feedback control has suppressed the position deviation of the cutting edge when pushing stress is produced during cutting process. The cutting accuracy in less than ±0.01 μm is now available.

A very smart system contains a reliability test system, which can stop an actuator system safely without causing any serious damages on to the work, e.g. in a lather machine. Acoustic emission measurement of a piezo-actuator under a cyclic electric field is a good candidate for estimating the life time of the actuators.[9]

The bright future of piezoelectric/electrostrictive actuators has been initiated and even greater commercial participation in their continued growth and application is anticipated.

REFERENCES

1.   K. Uchino, Piezoelectric/Electrostrictive Actuators, Morikita Pub. Co., Japan (1986).

2.   L. E. Cross, S. J. Jang, R. E. Newnham, S. Nomura and K. Uchino, Ferroelectrics 23, 187 (1980).

3.   K. Uchino and T. Ishii, J. Ceram. Soc. Jpn. 96, 863 (1988).

4.   A. Ohgoshi and S. Nishigaki, Ceramic Data Book '81, Industrial Products Tech. Assoc., Japan, p. 35 (1981).

5.   K. Uchino, M. Yoshizaki, K. Kasai, H. Yamamura, N. Sakai and H. Asakura, Jpn. J. Appl. Phys. 26, 1046 (1987).

6.   K. Uchino, Proc. MRS Int'l. Mtg. on Adv. Mats. 9, 489 (1989).

7.   M. Tanimura and K. Uchino, Sensors and Mater. 1, 47 (1988).

8.   S. Sugiyama and K. Uchino, Proc. 6th IEEE Int'l Symp. Appl. Ferroelectrics, p. 637 (1986).

9.   T. Hirose and K. Uchino, Ferroelectrics 87, 295 (1988).

Kenji Uchino
Materials Research Laboratory
The Pennsylvania State University
University Park, PA 16802   USA

and

Atsushi Furuta
Tokyo Research Laboratory
Tokin Corporation
Shiboguchi, Takatsu-ku
Kawasaki 213, Japan

Destruction mechanism in multilayer ceramic actuators has been investigated under cyclic electric fields. Crack propagation has been observed dynamically using CCD microscopy, and the accompanying characteristics of the induced displacement and acoustic emission were measured simultaneously. The piezoelectric $Pb(Ni_{1/3} Nb_{2/3}) O_3$ - $PbTiO_3$ and the phase-transition-related actuator material (antiferroelectric) $PbZrO_3$ - $PbSnO_3$ - $PbTiO_3$ exhibit a remarkable difference in the destruction manner probably due to the strain induction mechanism. The effect of layer thickness on the destruction process has also been studied.

Introduction

In these several years piezoelectric/electrostrictive ceramic actuators have become very popular for micro-positioning in optical and precision machinery fields and active vibration suppression in mechanical structures.[1] The expanding number of applications of ceramic actuators has made the endurance of the devices very important.

This paper describes the destruction mechanism of multilayer-type ceramic actuators observed by optical microscopy, induced displacement and acoustic emission measurements, and proposes a safety system which can stop the actuator before its troublesome sudden complete collapse.

Experiments

Multilayer model actuators were prepared by tape casting method. The samples simulating the interdigital electrode configuration [Fig. 1(a)] used in this experiment have only one internal ceramic layer with a thickness of 100 µm, 200 µm or 300 µm, as shown in Fig. 1(b).

The piezoelectric $Pb(Ni_{1/3}Nb_{2/3})_{0.6} Ti_{0.4}O_3$ (PNNT) and the phase-transition-related actuator material $Pb_{0.99}Nb_{0.02}[(Zr_{0.7}Sn_{0.3})_{0.955}Ti_{0.045}]_{0.98}O_3$ (PNZST) were prepared, and the average grain size of the device was roughly the same (~5 µm), independent of the composition and the layer thickness. The PNZST is initially antiferroelectric, but changes into ferroelectric under an applied electric field.[2] Rather isotropic expansive strains are associated with this phase transition, and the magnitude of the strain (~1.5 × 10⁻³) is twice larger than that of the piezoelectric PNNT. The longitudinally and transversely induced strains in the piezoelectric PNNT are 0.8 × 10⁻³ and -0.3 × 10⁻³, respectively, with opposite sign.[3]

Note that the multilayer model actuator used in this experiment exhibits an exaggeratedly large internal stress concentrated around the electrode edge so as to accelerate the failure of multilayer actuators.

Figure 2 show the measuring system composed of a CCD microscope (Toshiba, IK-C40), a displacement sensor (Millitron, Nr. 1301) and an acoustic emission sensor (NF Circuit Design Block, AE-905). The sample was driven by a triangular electric field of E_{max} = 2-4 kV/mm at 0.1 Hz.

Results

Crack Propagation: Crack generation and propagation resulting from the internal stress was observed and recorded dynamically using a CCD microscope and a VCR. Figures 3(a) and 3(b) show typical crack propagation processes observed for the PNNT and PNZST samples (200 µm in layer thickness). The crack initiates at the internal electrode edge in the PNNT sample and propagates to another electrode obliquely, also outward of the electrode and along the ceramic-metal electrode interface. On the contrary, the crack starts between the pair electrodes slightly inside the electrode edge in the PNZST, then propagates along the center area, finally branching around the electrode edge. It is noteworthy that the crack opens wide under the electric field and closes at zero field.

This difference is probably due to the difference in internal stress distribution. The sign of the longitudinally - or transversely-induced strain is opposite in the piezoelectrics, while in antiferroelectrics undergoing a phase change, rather isotropic expansive strains are induced in both directions. Therefore, the internal stress distribution in antiferroelectrics differs from that of piezoelectrics.

Similar crack propagation processes were observed in the different layer-thickness samples, however, significant differences were recognized in the fracture toughness. Figures 4(a) and 4(b) plot the layer thickness dependence of the critical deformation cycles required for the initial crack generation and of the crack propagation speed per drive cycle (measured in PNZST). A dramatic improvement in the fracture toughness is obtained in the thinner layer sample, even though the driving electric field is the same of all samples. The reason is not clear, but it may be related to the ratio between the grain size and the layer thickness.

Displacement Changes during Failure: The destruction of the device brings a change in the induced displacement. Figures 5(a) and 5(b) show the variation of the induced displacement during the crack propagation process for the model actuators of PNNT and PNZST, respectively, with a layer thickness of 200 µm. The displacement is enhanced remarkably at the initial stage; this can probably be attributed to the bending deformation associated with the crack opening and closing process. Further increase in the number of deformation cycles leads to a decrease in the magnitude of the displacement. The effective electric field in the ceramics decreases because the narrow air gap is associated with complete crack formation.

Variation of Acoustic Emission: Acoustic emission (AE) events were counted during the destruction process of the PNZST sample with a layer thickness of 200 mm (Fig. 6). The AE count increases remarkably after the crack initiation, reaching a maximum at 60 cycles, where the crack propagation speed is maximum, and the largest displacement is observed. Later, the AE count leveled off after the crack was completed.

(a) Internal Electrode

(b) 100-300μm 3mm 6mm
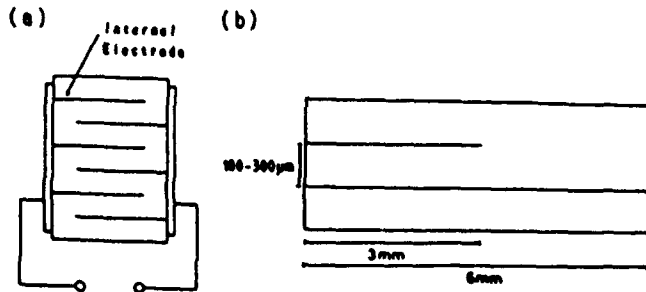
Fig. 1 Structure of (a) conventional multilayer actuator with an interdigital electrode, and (b) electrode configuration of a model actuator used in this study.

Monitor
CCD Camera
VTR
Objective Lens (x10)
Light
Sample
AE Sensor
Amp. Amp.
Displacement Sensor
Function Generator Voltmeter
Pre.-Amp.
Oscilloscope Computer
Discriminator
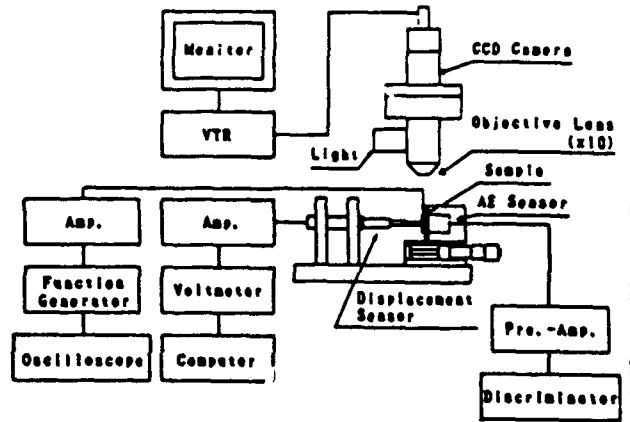
Fig. 2 Measuring system for the crack propagation experiments.

Initial State

Electrode Edge

Electric
Field:20kV/cm
Strain:0.26%
Layer
Thickness:280μm

2400 Cycles

3000 Cycles

Electrode edge

Initial State

Electric
Field:40kV/cm
Strain:0.3%
Layer
Thickness:200μm

36 Cycles

**48 Cycles**

360 Cycles

Electrode edge
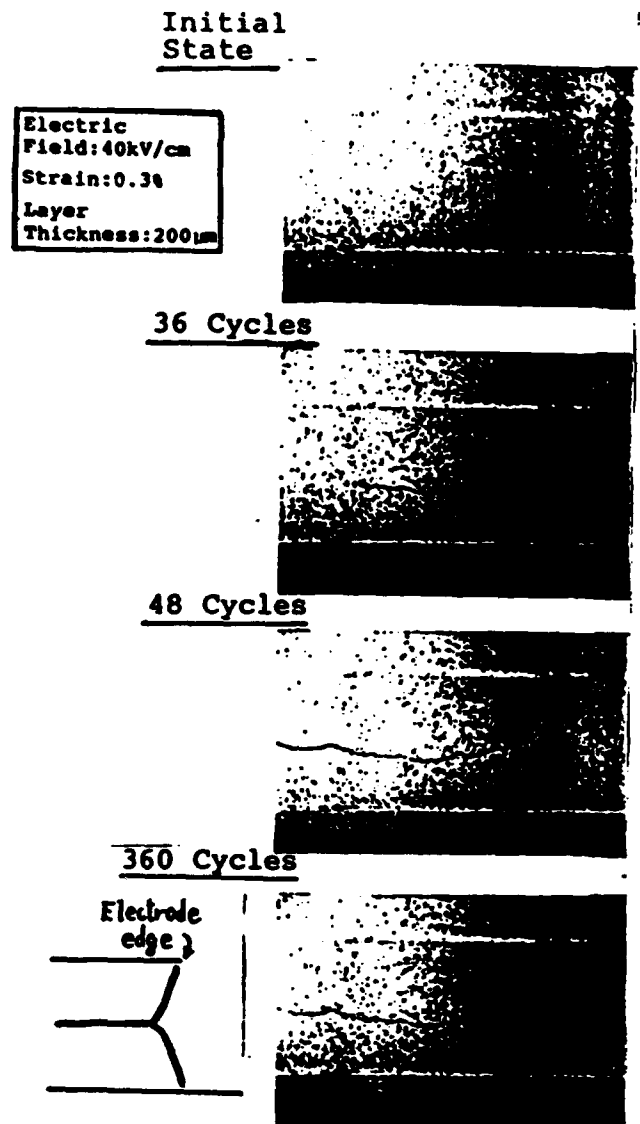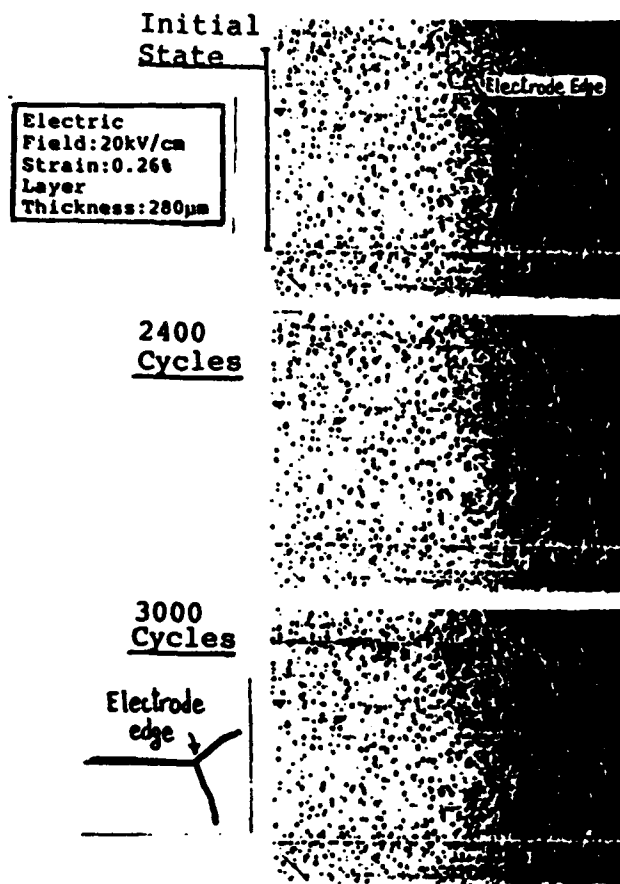
Fig. 3 Crack generation and propagation process in the multilayer model actuator. (a) Piezoelectric PNNT, and (b) antiferroelectric PNZST.
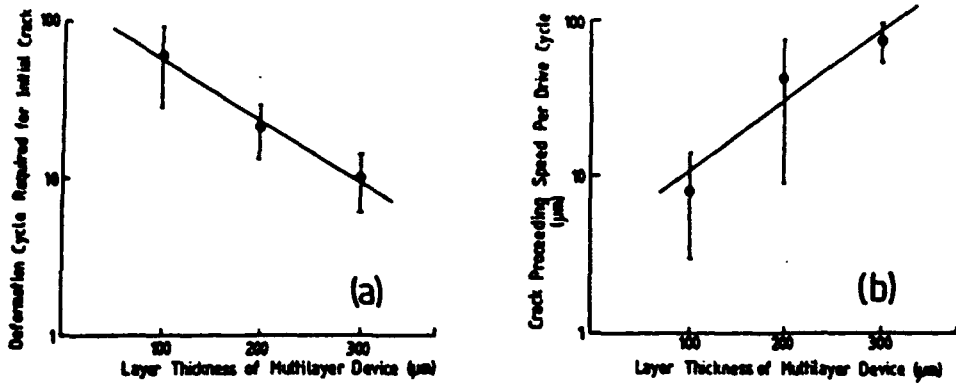
Fig. 4   Layer thickness dependence of the critical deformation cycle required for the initial crack generation (a), and of the crack propagation speed per drive cycle (b).
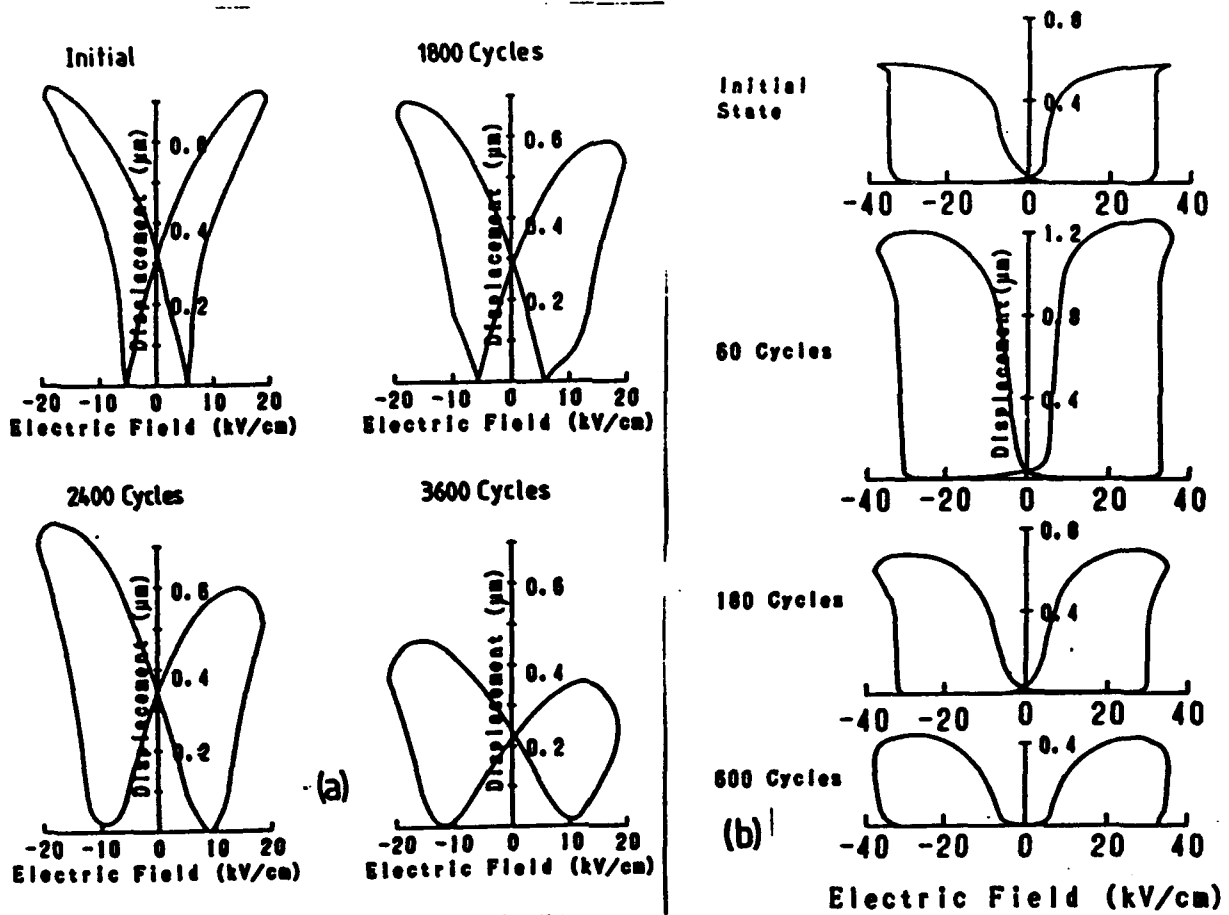

Fig. 5   Variation of the displacement during the destruction. (a) PNNT and (b) PNZST.
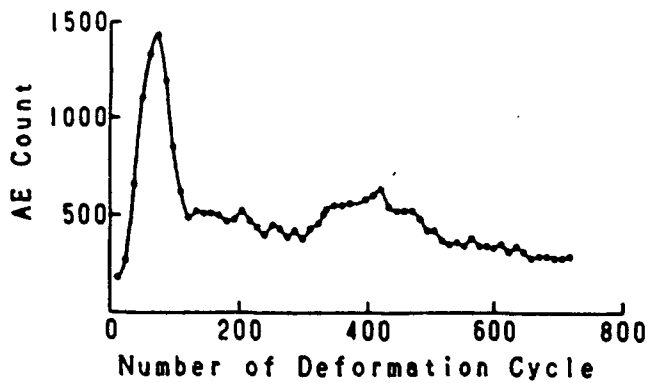
Fig. 6   Changes in acoustic emission count during the fracture process measured in a model actuator of PNZST.
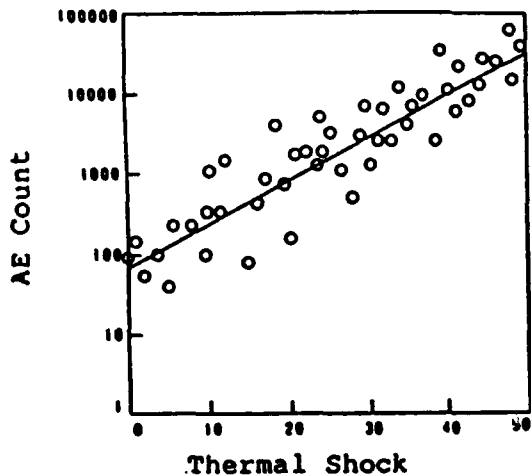

Fig. 7   AE count change monitored in a 200-layers sample of PNNT with aging time. The accelerated aging was performed by a thermal shock treatment.
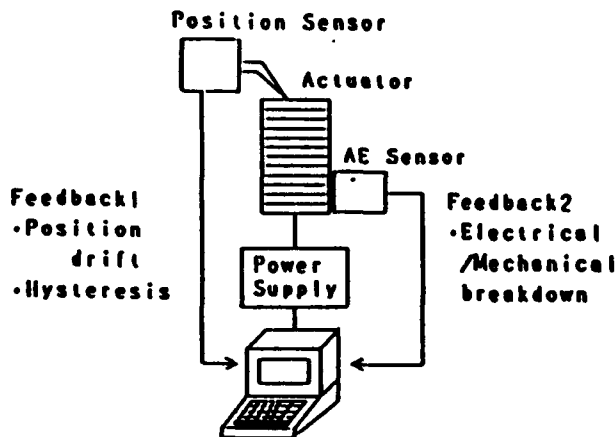

Fig. 8   Very smart actuator system with a reliability test function as well as position sensor.

The AE count change was also monitored for a 200-layers sample of PNNT ($10 \times 10 \times 20$ mm^3) with aging time.[4] An accelerated aging test was performed by a rapid-heat treatment up to 100°C in a second. Figure 7 shows that the AE count increases by three orders of magnitude at the final failure of the device in comparison with the virgin state. The monotonous increase of AE may be attributed to successive accumulation of cracks generated in the actuator device.

Summary and Discussion

The crack generation and propagation in multilayer ceramic actuators was observed dynamically during cyclical electric fields. In piezoelectrics, the crack initiated near the edge of the internal electrode and propagated basically in three directions: two cracks moved toward the outside electrostrictively inactive region forming an angle of 100° with each other, while the third moved along the ceramic-electrode interface. This behavior can be explained theoretically based on finite element calculations.[5]

On the contrary, in antiferroelectrics, the crack begins slightly inside the edge of the internal electrode and propagates along the center area between the pair electrodes. Later crack branches are generated around the electrode edge. Theoretical calculations are now in progress.

In both cases the apparent displacement becomes slightly larger than that of the virgin state, and the AE count increases drastically associated with the crack propagation.

Finally we propose a very smart actuator system containing a safety feedback function (Fig. 8), which can stop an actuator drive safely without causing any serious damages on to the work, e.g. in a precision lathe machine. The AE might be one of good predictors for actuator failure. A certain level of the AE count will indicate a timing to replace the ceramic actuator.

References

[1]   K. Uchino, Piezoelectric/Electrostrictive Actuators. Tokyo: Morikita Publ. Co., 1986.

[2]   K. Uchino, "Shape Memory Ceramics," in Proceedings MRS Int'l Mtg. on Advanced Materials, vol. 9, pp. 489, 1989.

[3]   Tokin Technical Catalogue, Multilayer Piezoelectric Actuator Series. Tokin Corp., 1986.

[4]   T. Hirose and K. Uchino, "Acoustic Emission in Ceramic Actuators," Ferroelectrics, vol. 87, pp. 295, 1988.

[5]   S. Takahashi, A. Ochi, M. Yonezawa, T. Yano, T. Hamatsuki and I. Fukui, "Internal Electrode Piezoelectric Ceramic Actuator," Jpn. J. Appl. Phys., vol. 22, Suppl. 22-2, pp. 157, 1983.

APPENDIX 37

Shape Memory Ceramics and Their Application to Latching Relays

Atsushi Furuta, Ki-Young Oh and Kenji Uchino

Department of Physics, Sophia University,
7-1 Kioi-cho, Chiyoda-ku, Tokyo 102

Basic characteristics of shape memory unimorphs have been measured in detail, and a new latching relay has been fabricated using the shape memory unimorph. This new relay has a very simple structure with compact size and light weight, as compared with the conventional electromagnetic type. The relay is turned ON at 350 V and turned OFF at −50 V with a short-pulse electric field. The response time is about 13 ms under an input electric energy of 7 mJ. The relay can be kept in an ON state for more than a day without applying any electric field.

1. Introduction

The shape memory effect is not only characteristic of certain metal alloys, but is also observed in ceramics. Figure 1 shows the transverse strains induced in the ceramic plates of $Pb_{0.99}Nb_{0.02}[(Zr_{0.6}Sn_{0.4})_{1-y}Ti_y]_{0.98}O_3$ (PNZST) under an applied electric field.[1-3] These strain curves can be classified into three patterns with changing Ti mole fraction.

The ceramic of Type I ($y = 0.060$) is originally antiferroelectric, but can be changed to ferroelectric by applying an electric field, and large strains are generated during the phase transition. It is worth noting that the magnitude of strain is three to four times as large as that of the conventional piezoelectrics. When the electric field is decreased, the phase of the ceramic is changed back to the initial antiferroelectric and the strain recovers. The square-type hysteresis of the strain curve is applicable to digital displacement transducers.
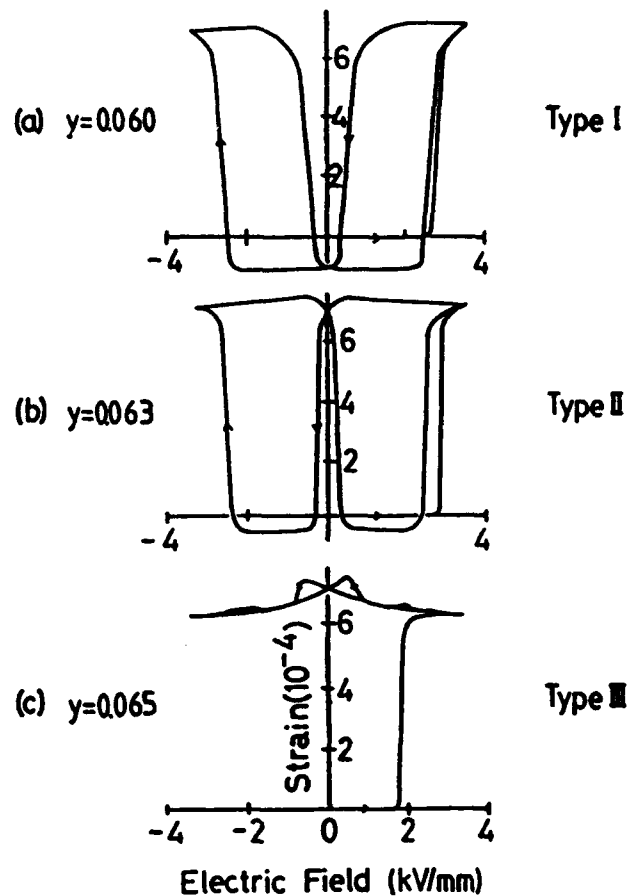
Fig. 1. Transversely induced strains in the $Pb_{0.99}Nb_{0.02}[(Zr_{0.6}Sn_{0.4})_{1-y}Ti_y]_{0.98}O_3$ ceramics at room temperature: (a) $y = 0.06$, (b) $y = 0.063$, (c) $y = 0.065$.

In the case of Type II ($y = 0.063$), once the ceramic changes from antiferroelectric to ferroelectric, the phase is maintained even when the electric field goes down to zero, and the deformation is memorized. To obtain the initial antiferroelectric state, a small reverse bias field should be applied to the sample.

On the contrary, the ceramic of Type III ($y = 0.065$) cannot recover the antiferroelectric state during the electric field cycle after the ferroelectric phase is induced. Thermal annealing up to 50°C is required to recover the initial state.

The strain characteristics of Type II and Type III are denoted as the shape memory effect. In particular, since the PNZST of Type II can be controlled easily by applying electric field, it is the most useful from a practical point of view. This kind of shape memory ceramic requires only a pulse electric field to obtain a permanent displacement, leading to electric energy savings as compared with conventional piezoelectrics, which require continuous application of field.

A latching relay, which will not change its original ON or OFF state without an intentional electric signal even when an accidental electricity shutdown occurs, is one of the best application candidates of the shape memory devices.

This paper describes trial manufacturing of a latching relay using shape memory ceramics, following basic characteristics of a shape memory unimorph as the drive source of the relay.

2. Sample Preparation and Experiments

The PNZST family ceramics of $Pb_{0.99}Nb_{0.02}[(Zr_{0.6}Sn_{0.4})_{1-y}Ti_y]_{0.98}O_3$ were prepared by the conventional sintering process. After mixing and drying the reagent-grade PbO, Nb_2O_5, ZrO_2, SnO_2 and TiO_2 raw materials, the powders were calcined at 850°C for 10 h and sintered at 1270°C for 2 h. The samples of 10 mm diameter and 0.2 mm thickness were used for basic strain measurements after being silver-electroded. The samples of 22 mm × 7 mm area and 0.2 mm thickness were used for fabricating unimorphs. Figure 2 shows the structure of the unimorph, which is composed of two ceramic plates, A and B, bonded together with adhesive. Plate A is coated with silver electrode. When an electric field is applied to plate A,
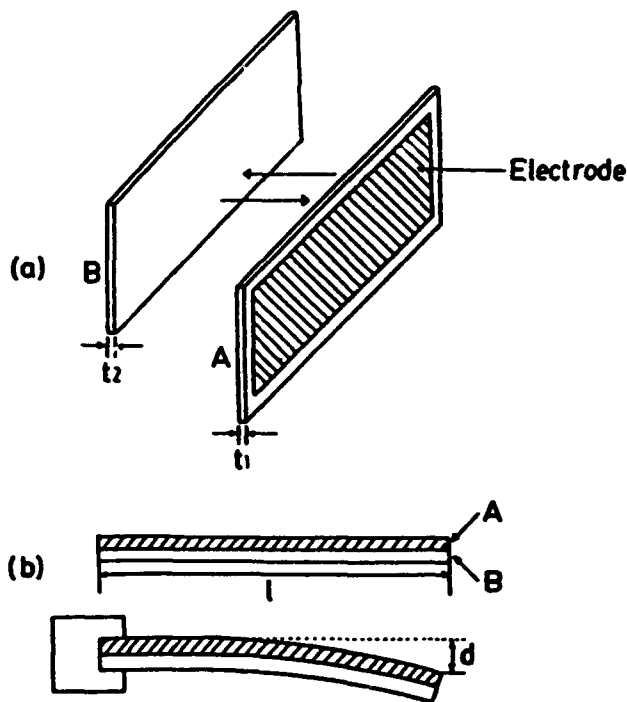

Fig. 2. Structure of a unimorph device.

the expansive strain is induced only in plate A, not in plate B; then finally the unimorph generates bending motion.

For measuring induced strains in single-plate samples, a contact-type strain sensor (Millitron, No. 1202) was used. For the tip displacement of the unimorph, d in Fig. 2, and load characteristics in the induced displacement, a noncontact-type displacement sensor (Kaman, KD-2300) was used.

3. Results

3.1 Characteristics of the shape memory unimorph

Figure 3 shows induced strains of the single-plate-type samples of $Pb_{0.99}Nb_{0.02}[(Zr_{0.6}Sn_{0.4})_{1-y}Ti_y]_{0.98}O_3$ ($y = 0.0625 - 0.0645$). Some results have been reported in ref. 4. The PNZST in the above composition range exhibits the shape memory effect. Figure 4 shows the tip displacements of the unimorph. It is


a) y=0.0625

d) y=0.0640

b) y=0.0630

e) y=0.0645

c) y=0.0635
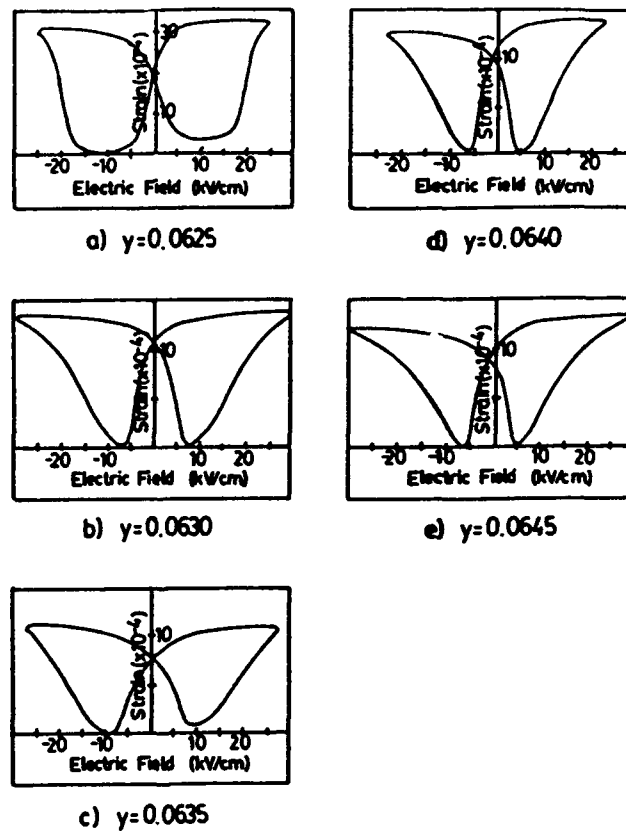
Fig. 3. Strain-vs-field characteristics in the single-plate-type samples of PNZST for various Ti mole fractions.

a) y=0.0625

d) y=0.0640

b) y=0.0630

e) y=0.0645

c) y=0.0635
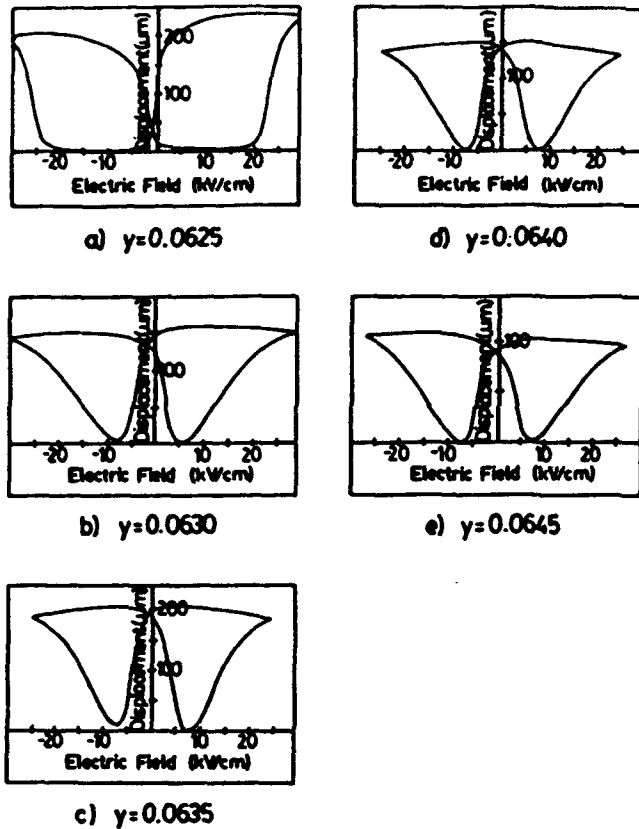
Fig. 4. Displacement-vs-field characteristics of the unimorphs of PNZST for various Ti mole fractions.

noteworthy that the sample with $y = 0.0625$, exhibiting the shape memory effect in the single plate, does not exhibit the shape memory characteristic in the unimorph design. Figure 5 shows the time dependence of the tip displacement of the unimorphs ($y = 0.0625$ and $y = 0.0630$). The recovery in the $y = 0.0625$ sample to the antiferroelectric phase is probably attributable to compressive stress generated during the bending process.

Figure 6 shows the temperature dependence of the unimorph bending measured in $y = 0.0630$. At 0°C, once the ferroelectric phase is induced, the ceramic will not recover antiferroelectricity under applied reverse bias electric field. On the other hand, at 40°C the electric field required to cause the phase transition becomes great and the unimorph loses the shape memory effect. To realize a complete shape memory phenomenon, the temperature should be controlled between 10°C to 30°C for this composition. A similar characteristic change is also observed when the Ti mole fraction is changed from $y = 0.060$ to $y = 0.065$.

Figure 7 shows the dynamical response of the unimorph ($y = 0.0630$). In the
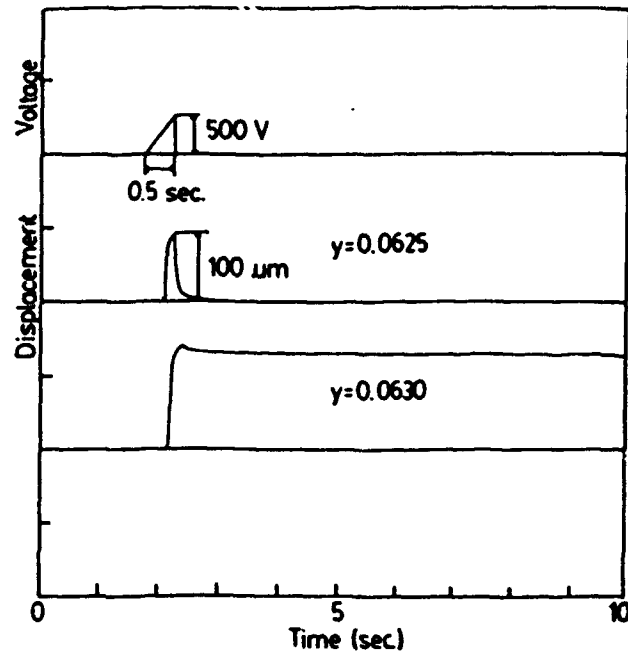
Fig. 5. Time dependence of the tip displacement change in the unimorphs.

case of the conventional piezoelectric, a continuous application of the electric field is required to maintain a constant displacement; meanwhile, the shape memory ceramic can be driven by a pulse electric field. When the unimorph is driven by a triangular pulse with a rise time of 3.0 ms (Fig. 7(a)), overshoots and ringing of the tip displacement are observed. It is important to note that the phase transition arises quickly enough to generate the following resonant vibration. When the rise time of the electric field is adjusted to 4.7 ms (Fig. 7(b)), which is the sum of the mechanical resonant period (2.2 ms) and the lag time, to cause phase transition (2.5 ms), the ringing can be suppressed completely. Too slow a rise time of 6.0 ms (Fig. 7(c)) again causes the ringing vibrations. Overshoots and ringing of the unimorph element would cause chattering in the latching relay and the response would become very slow. Therefore, an electric field with the rise time corresponding to the mechanical resonant period is required.

To operate the mechanical snap-action switch element, at least 20 gf of the generative force is necessary for the unimorph as well as 50 μm of the displacement. The relationship between the tip displacement and the load for the unimorph was measured using metal weights applied to the tip position (Fig. 8). Generative force of more than 50 gf can be practically induced both at the maximum and zero field. The magnitude of the maximum generative force of the shape memory unimorph, which is estimated from the intercept on the horizontal axis, is about 90 gf, which is
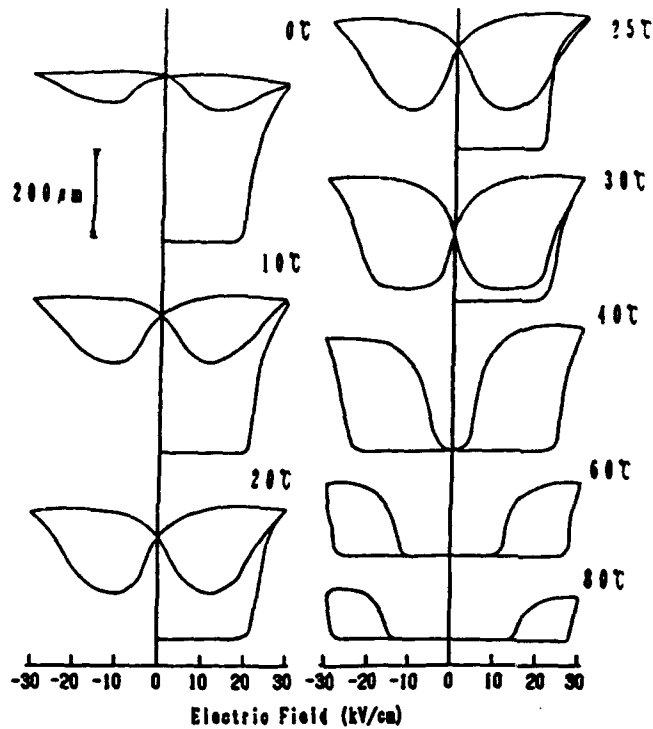
Fig. 6. Temperature dependence of the tip displacement in the unimorph with $y = 0.063$.

twice as large as that of the conventional piezoelectric bimorph. This is probably due to the strain bias caused by the spontaneous strain change from the antiferroelectric to ~he ferroelectric phase.

3.2 Characteristics of the latching relay

We have fabricated a new latching relay using the shape memory unimorph. Figure 9 shows the structure of the latching relay, which is composed essentially of a mechanical snap-action switch and a driving unimorph device. The snap-action switch is easily driven by a 50 μm displacement, having mechanically bistable states. The size of the relay is very compact, $20 \times 10 \times 10$ mm^3, as compared to a conventional electromagnetic type ($20 \times 26 \times 34$ mm^3). Figure 10 shows the basic ON/OFF function of the new relay. The relay is turned ON at about 350 V and turned OFF at -50 V. The voltage required for switching can be lowered by using multimorph structures. Dynamical response of the newly developed latching relay is shown in Fig. 11(a). The response of the conventional electromagnetic latching relay is also shown in Fig. 11(b) for comparison with the new relay. A pulse electric field with the mechanical resonant period of the shape memory unimorph is applied

212
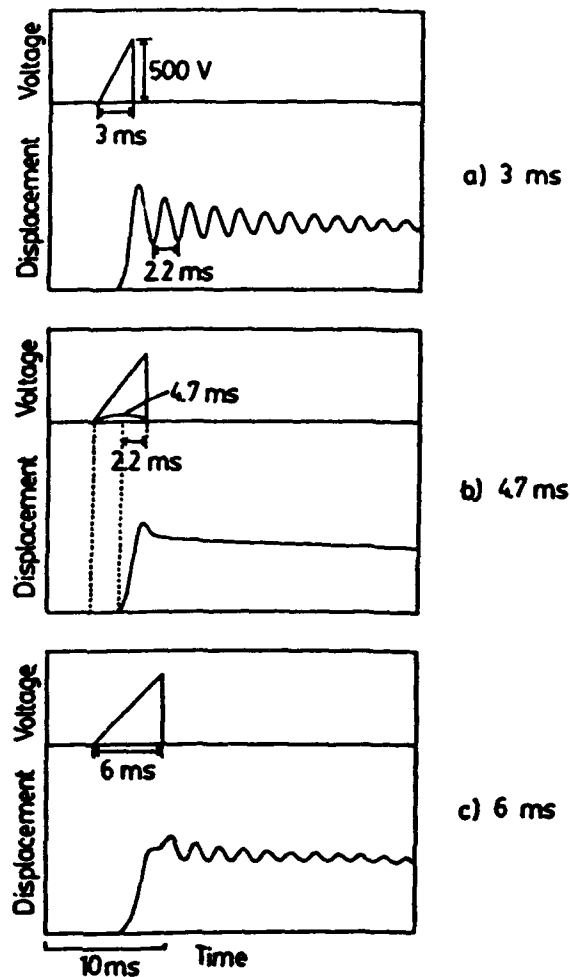
Fig. 7. Dynamical response of the tip displacement of the shape memory unimorph with $y = 0.063$ under various drive pulse conditions.

so as to suppress the ringing at the tip of the unimorph. Chattering was still observed, probably due to an additional mechanical soft leaf spring at the snap-action switch. The rise time of the new relay is 1.8 ms, which is much shorter than that of the electromagnetic relay (8.5 ms), although the former needs 13 ms to stabilize the ON state, which is slightly longer than the 9 ms of the latter relay; this suggests a potential capability of much faster response if the whole mechanical setup were adjusted to optimize conditions. The newly developed latching relay can be kept in the ON state for more than a day without applying any electric power. The drive power required to turn it ON is about 7 mJ. This energy requirement can be reduced by collecting electric energy in the discharging process. A camera strobe makes a suitable
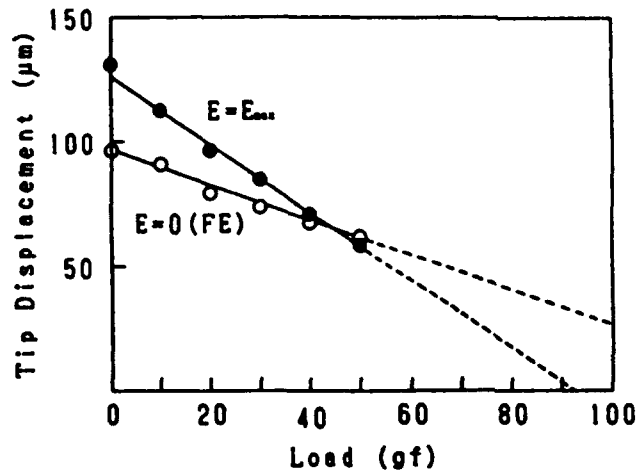
Fig. 8. Tip displacement of the shape memory unimorph ($y = 0.063$) as a function of the external load.
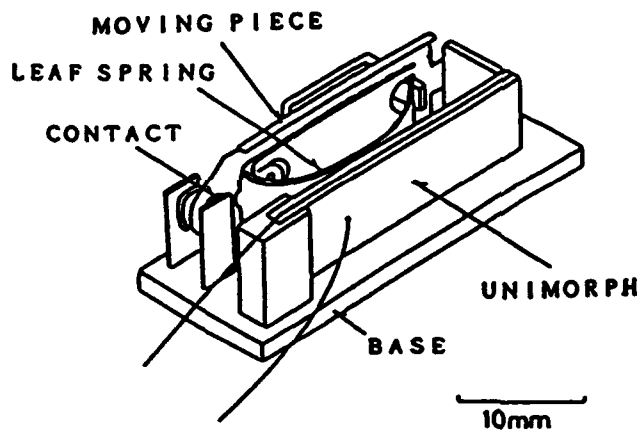
Fig. 9. Structure of the latching relay using the shape memory ceramic.

high-voltage supply for driving the relay, because the relay can be switched only by a short-pulse field of several ms.

4. Conclusions

a) Shape memory ceramic unimorphs have been fabricated as actuator elements. The unimorph shape memory effect can be observed at room temperature for the samples with Ti mole fraction $y = 0.0630$ to $y = 0.0645$ in the

214
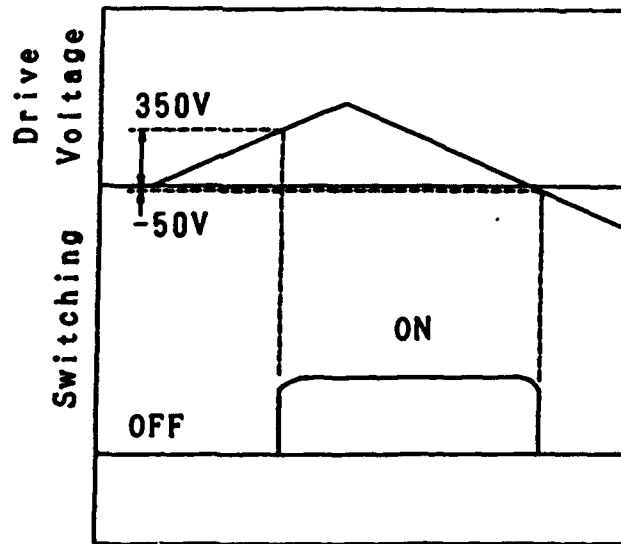
Fig. 10. Basic ON/OFF function of the latching relay using the shape memory ceramic.
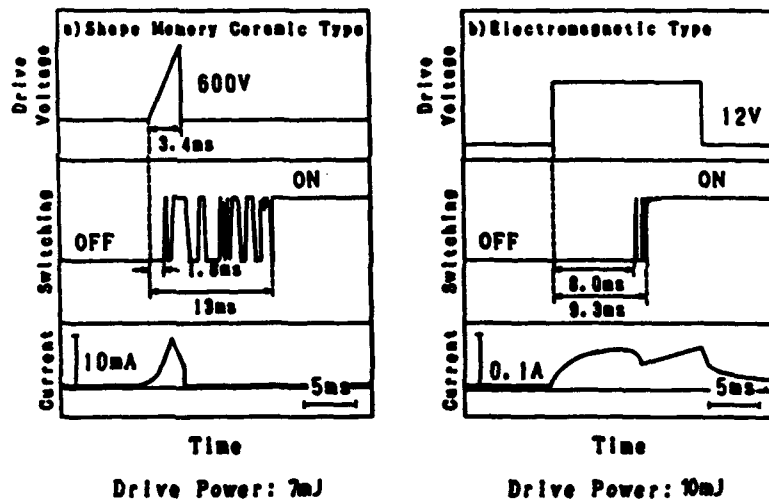
Fig. 11. Dynamical response of the latching relays: (a) shape memory ceramic type, (b) electromagnetic coil type.

Pb$_{0.99}$Nb$_{0.02}$[(Zr$_{0.6}$Sn$_{0.4}$)$_{1-y}$Ti$_y$]$_{0.98}$O$_3$ family.

b) Mechanical vibration overshoots and ringings at the tip of the unimorph can be completely suppressed by applying an electric field with rise time equal to the sum of the mechanical resonant period and the lag time to cause the phase transition.

c) A compact, lightweight latching relay using a shape memory ceramic ($y = 0.063$) has been fabricated and found to have a quick response compared with the conventional electromagnetic type. The relay is driven simply by applying pulse electric field, and is maintained in the ON state without application of any electric field; this reduces the electric power requirement significantly.

References

1 D. Berlincourt, H. H. Kruger and B. Jaffe: J. Phys. Chem. Solids 25 (1964) 675.
2 K. Uchino: Jpn. J. Appl. Phys. 24 Suppl. 24-2 (1985) 460.
3 K. Uchino: MRS Int'l. Mtg. on Adv. Mater. 9 (1989) 489.
4 K. Y. Oh, A. Furuta and K. Uchino: J. Ceram. Soc. Jpn. 98 [8] (1990) 905.

APPENDIX 38

Piezoelectric ceramics in smart actuators and systems

KENJI UCHINO
Materials Research Laboratory, The Pennsylvania State University
University Park, PA 16802-4801, USA

ABSTRACT: In these several years piezoelectric and electro-strictive actuators
have become very popular for micro-positioning in optical and precision
machinery fields. Aiming at wide commercialization of these actuators, many
investigations have been made in the improvement of ceramic materials for
actuators, designs of the devices and control and systemization of the
actuators. This paper reviews recent applications of piezoelectric/
electrostrictive ceramics from a viewpoint of "smart" actuators and systems.

1. INTRODUCTION

"Smartness" in the words of "smart" materials and structures is defined by
three functions of "sensing," "actuating," and "active control" of environmental
conditions with some intelligence. Dental braces made rom shape memory alloys and
electrochromic grass windows are often cited in the literatures as smart
materials. This paper reviews recent applications of piezoelectric/
electrostrictive and their related ceramics from a viewpoint of "smart" actuators
and systems.[1]

2. ACTUATOR MATERIALS

A _passively smart materials_ is exemplified by the lead magnesium niobate
(PMN) based ceramic, which can exhibit a large electrostriction ($\Delta l/l \sim 10^{-3}$)
witnout any hysteresis and aging effect during an electric field cycle (Fig. 1).[2]
A composite actuator structure called "moonie" has been developed to amplify the
small displacement induced in a multilayer piezoelectric device (Fig. 2). Passive
damper application is another smart usage of piezoelectrics, where mechanical
noise vibration is radically suppressed by the converted electric energy
dissipation through Joule heat when a suitable resistance is connected to the
piezoelectric plate.[3] Piezoelectric: carbon black: polymer composites are
promising useful designs for practical use.
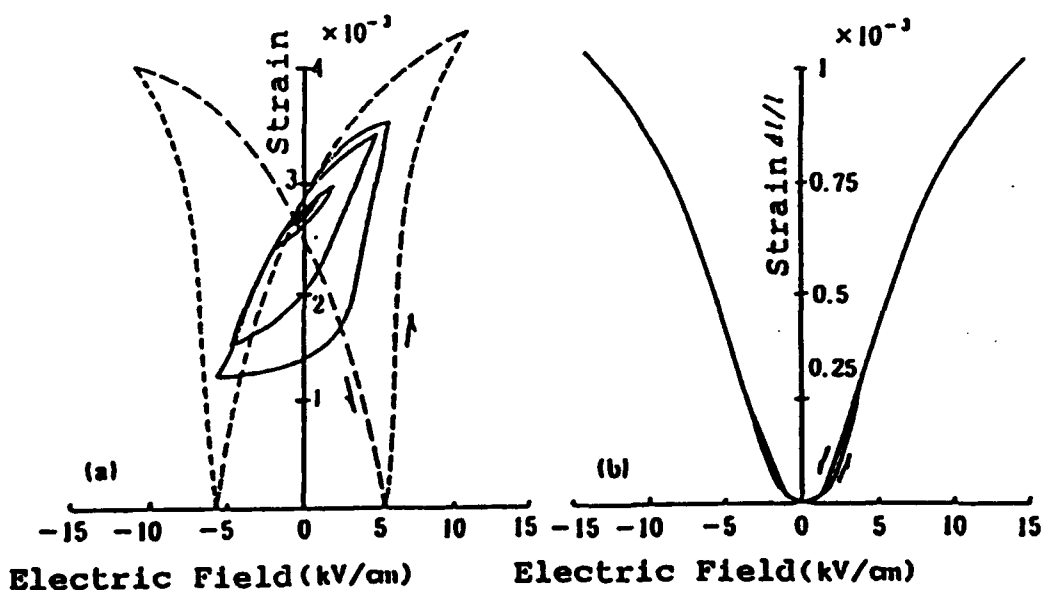
Figure 1 Electric field induced strain in a piezoelectric lead lanthanum
zirconate titanate (PLZT) (a); and in an electrostrictive lead
magnesium niobate(PMN) based ceramic (b).

An **actively smart material** is exemplified by the video tape head positioner made from a lead zirconate titanate (PZT) bimorph with sensor and actuator-divided electrodes.[4]

Monomorphs and shape memory ceramics belong to **very smart materials**. A monomorph device made of a semiconductive piezoelectric plate generates the Schottky barrier when metal electrodes are coated on the faces, providing non-uniform distribution of the electric field even in a compositionally uniform ceramic (Fig. 3). A superimposed effect of piezo-electricity and semiconductivity leads to a bending deformation in a total ceramic plate.[5] The strains associated with phase transitions such as an antiferroelectric-to-ferroelectric transition in lead zirconate stanate-based ceramics reach up to 0.4%, which is much larger than that expected in electrostrictors (Fig. 4). Moreover, this field-induced transition exhibits a shape memory effect in appropriate compositions, and such ceramics are useful for the applications to latching relay and a mechanical clamper.[6]

Figure 2 Structure of a composite
          actuator "moonie."

(a)

$x=0.60, y=0.055$

(b)

$x=0.70, y=0.045$
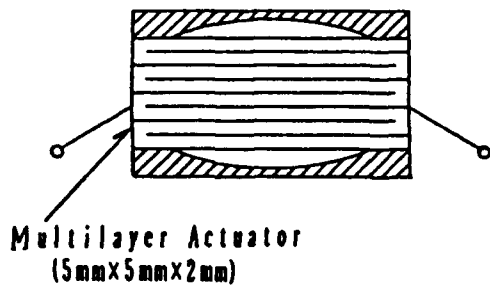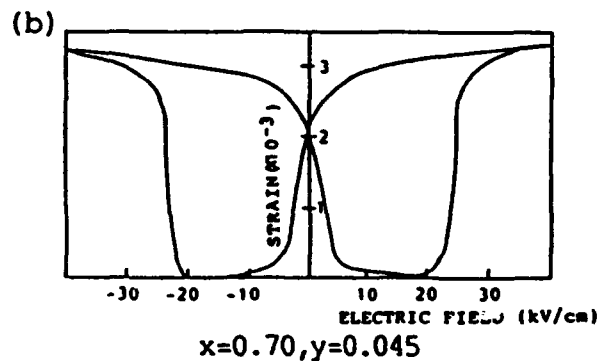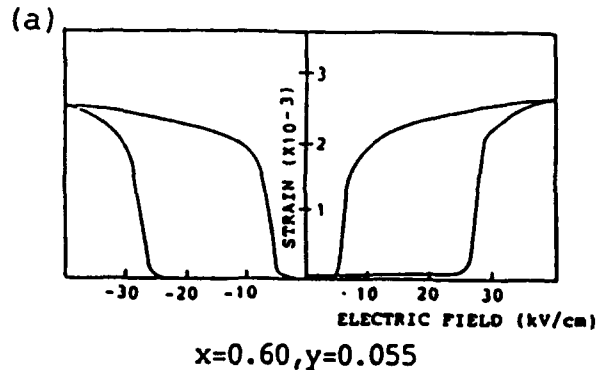
Figure 4 Longitudinal induced strains of
          $Pb_{0.99}Nb_{0.02}((Zr_xSn_{1-x})_{1-y}Ti_y)_{0.98}O_3$
          at room temperature.
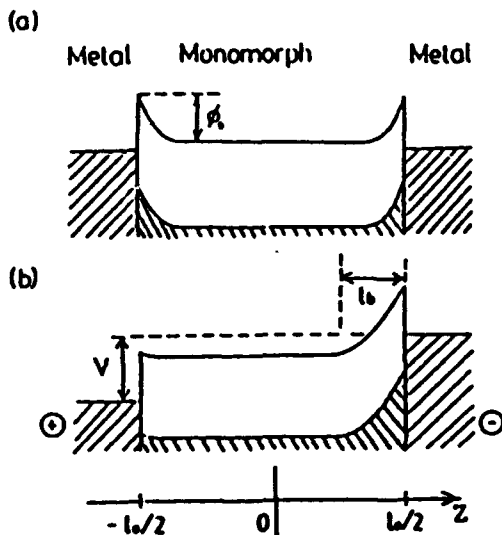
Figure 3 Electron energy band (Schottky
          barrier) models in monomorph
          devices (n-type semiconductor).

A photostrictive actuator is the best example of <u>intelligent materials</u> including sensing, actuating and drive/control functions in a unique material.[7] In certain ferroelectrics a phenomenon by which a constant electromotive force is generated with exposure of light has been observed. A photostrictive effect is expected as a result of the coupling of the photovoltaic and inverse piezoelectric effects. A remote control miniature walking robot, which is activated with illumination, is currently being fabricated (Fig. 5). Two photostrictive PLZT bimorphs were combined together and each plate exhibits a minute photo-induced displacement on the order of 150μm. Alternative illumination causes a slow moving of the ceramic device.

3. ACTUATOR SYSTEMS

Pulse voltage drive of piezoelectric actuators is only one-way control without a feedback system, but very important for improving the response of ceramic actuators.[8] Figure 6 shows transient vibrations of a bimorph excited after a pseudo-step voltage applied. The rise time is varied around the resonant period. It is concluded that overshoot or ringing of the tip displacement is completely suppressed when the rise time is precisely adjusted to the resonance period of the piezo-device.

A flight actuator consisting of a pulse-driven piezoelectric element and a steel ball is a very <u>suggestive mechanism</u>, even if it would not be denoted as a smart system. A 2mm steel ball can be hit up to 20mm by a 5μm displacement induced in a multilayer actuator with quick response.
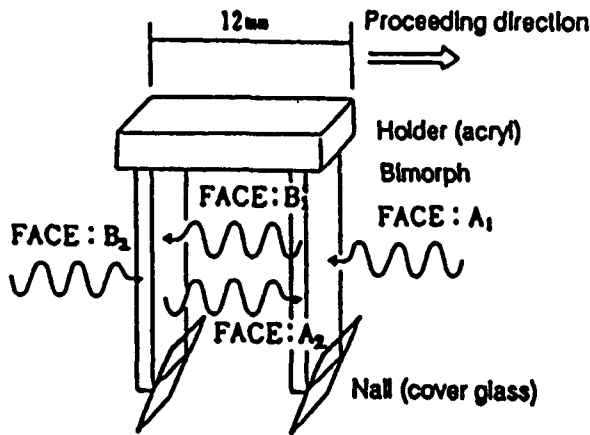
Figure 5 Photo-driven miniature walking device.
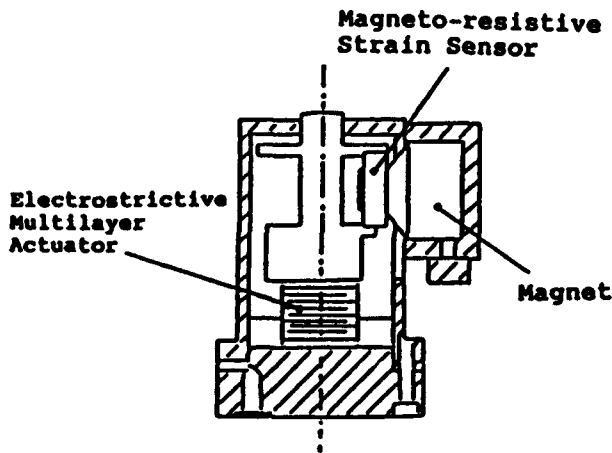
Figure 7 Micro displacement actuator with a magneto - resistive strain sensor.
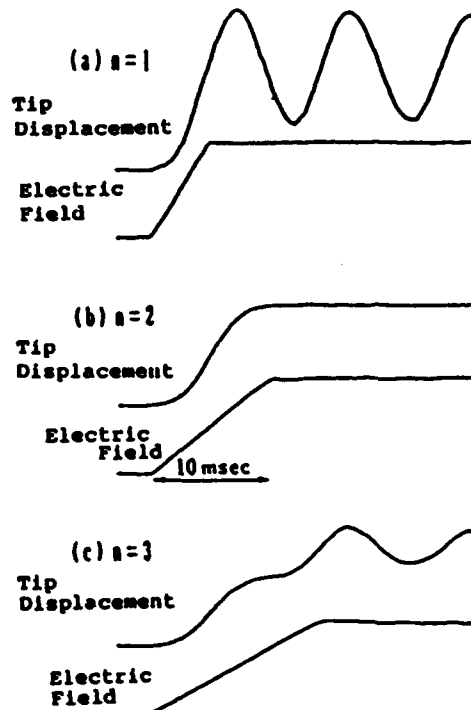
Figure 6 Transient vibration of a bimorph excited after a pseudo - step voltage applied. n is a time scale in the unit of a half of the resonance period.
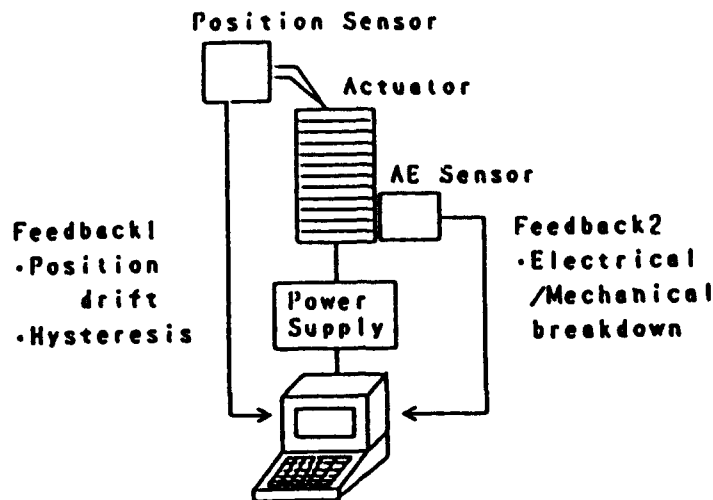
Figure 8   Very smart actuator system with a reliability test function as well as a position sensor.

A **smart system** is typically exemplified by a precision lathe machine. A micro displacement actuator has been manufactured using an electrostrictive multilayer actuator, a magneto-resistive strain sensor and an adaptive control circuitry (Fig. 7). The feedback control has suppressed the position deviation of the cutting edge when pushing stress is produced during cutting process. The cutting accuracy in less than ±0.01μm is now available.

A **very smart system** contains a reliability test system, which can stop an actuator system safely without causing any serious damages on to the work, e.g. in a lather machine. Acoustic emission measurement of a piezo-actuator under a cyclic electric field is a good candidate for estimating the life time of the actuators.[9]

4. CONCLUSION

The bright future of piezoelectric/electrostrictive actuators has been initiated and even greater commercial participation in their continued growth and application is anticipated.

REFERENCES

1. K. Uchino, *Piezoelectric / Electrostrictive Actuators*, Morikita Pub. Co., Japan (1986)
2. L.E.Cross, S.J.Jang, R.E.Newnham, S.Nomura and K.Uchino, Ferroelectrics **23**, 187 (1980)
3. K. Uchino and T.Ishii, J.Ceram. Soc. Jpn. **96**, 863 (1988)
4. A.Ohgoshi and S.Nishigaki, Ceramic Data Book '81, Industrial Products Tech. Assoc., Japan, p.35 (1981)
5. K.Uchino, M.Yoshizaki, K.Kasai, H.Yamamura, N.Sakai and H.Asakura, Jpn. J. Appl. Phys. **26**, 1046 (1987)
6. K.Uchino, Proc. MRS Int'l. Mtg. on Adv. Mats. **9**,489 (1989)
7. M.Tanimura and K.Uchino ,Sensors and Mater. **1**, 47 (1988)
8. S.Sugiyama and K.Uchino, Proc. 6th IEEE int'l Symp. Appl. Ferroelectrics, p.637 (1986)
9. T.Hirose and K.Uchino, Ferroelectrics **87**, 295 (1988)

APPENDIX 39

Electric Field Induced Piezoelectric Response in Ferroelectric Materials near the Paraelectric-Ferroelectric Transition

Q. M. Zhang, J. Chen, and L. E. Cross

Materials Research Laboratory, The Pennsylvania State University
University Park, PA 16802

Abstract: In many ferroelectric materials, the piezoelectricity can be induced by an applied electric field and the material will return to piezoelectric inactive state when the field is reduced to zero. Based on thermodynamic theory, the effect of temperature and applied electric field on the electromechanical response is analyzed for materials with a first order and continuous ferroelectric-paraelectric phase transitions. It is concluded that near the critical point of a first transition, a giant piezoelectric constant and a high electromechanical coupling factor can be achieved. Experimental results on a series of $(BaSr)TiO_3$ samples show that an exceptionally high induced piezoelectric constant can be obtained for the material with a first order transition.

I. Introduction

In many transducer applications, it is highly desirable to have materials with a high piezoelectric constant, dielectric constant, and electromechanical coupling factor as well as that these material properties can be tuned by electric and mechanical fields. Among the various avenues to achieve these features, the one which operates the materials near a phase transition point shows great promise and has received increased attention recently. In general, there are four types of phase transitions one can make use of: the paraelectric-ferroelectric transition in regular ferroelectric material, the diffused phase transition in relaxor material, the antiferroelectric-ferroelectric transition, and the ferroelectric-ferroelectric transition.[1-4] In this paper, the results of a recent theoretical and experimental investigation on the electromechanical behavior of a ferroelectric material near the ferroelectric-paraelectric transition will be presented. The emphasis here will be placed on how the induced material properties are tuned by the bias electric field and affected by temperature, and what the conditions are to achieve a high piezoelectric response in a material.

II. Theoretical treatment on the electromechanical behavior near the paraelectric-ferroelectric transition

In the paraelectric phase, the spontaneous polarization of a ferroelectric material is zero and there is no piezoelectric activity in the material. However, by applying a DC bias field on the material, a polarization can be induced and the material will exhibit non-zero piezoelectric constant. As will be analyzed in the following, how a material behaves in this induced state will critically depend on the order of the transition. As schematically drawn in figure 1(a), for a continuous transition, as one turns on external electric fields, the transition is smeared out and as a result, the material constants are reduced from their extreme values. On the other hand, for a first order phase transition, the effect of an external field is to narrow the width of the
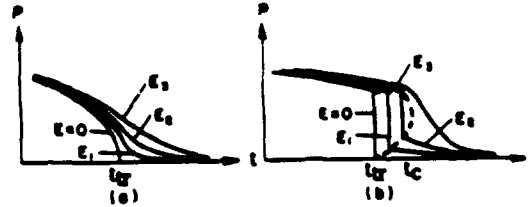
Figure 1. Polarization as a function of temperature with and without bias field E: (a) near a continuous transition; (b) near a first order transition.

coexistence region and to induce a critical state, as schematically drawn in figure 1(b), which will yield a high piezoelectric constant and electromechanical coupling factor. These features can be quantitatively analyzed using Landau-Denvonshire theory.[5] For simplicity, only the cubic to tetragonal transition will be considered here. However, the results obtained are general and applicable to more complicated systems.

Using the convention in the literature, the free energy G of the system near the transition has the form

$$G = (1/2)\, \alpha\, P^2 + (1/4)\, \beta\, P^4 + (1/6)\, \gamma\, P^6 - Q_{11}T_3P^2$$
$$-Q_{12}(T_1+T_2)P^2 - (1/2)\, s^P_{11}(T_1+T_2+T_3) \qquad (1)$$

where P is the polarization, T_i is the mechanical stress tensor component, $\alpha=\alpha_0(t-t_0)$, t is temperature, α_0, β, γ are constants, Q_{ij} is the electrostrictive constant, and s_{11}^P is the elastic compliance under constant electric displacement. For most materials, Q_{ij} and s_{11}^P are nearly independent of temperature and electric field. In eq. (1), the free energy for P=0 state is taken as zero. The difference between a first order transition and a continuous transition is reflected by the sign of β in eq. (1). For a first order transition, $\beta<0$ and for a continuous transition, $\beta>0$ and the transition occurs at $t=t_0$. From eq. (1), the basic equations which describe the response behavior of a material in the transition region can be derived.

$$E = \frac{\partial G}{\partial P} = \alpha P + \beta P^3 + \gamma P^5 - 2Q_{11}T_3P - 2Q_{12}(T_1+T_2)P \qquad (2)$$

$$\varepsilon = \frac{1}{(\alpha + 3\beta P^2 + 5\gamma P^4 - 2Q_{11}T_3 - 2Q_{12}(T_1+T_2))} \qquad (3)$$

$$d_{33} = 2Q_{11}\varepsilon P = \frac{2Q_{11}P}{(\alpha + 3\beta P^2 + 5\gamma P^4 - 2Q_{11}T_3 - 2Q_{12}(T_1+T_2))} \qquad (4)$$

$$s_{33}^E = s_{11}^P + \frac{4Q_{11}^2P^2}{(\alpha + 3\beta P^2 + 5\gamma P^4 - 2Q_{11}T_3 - 2Q_{12}(T_1+T_2))} \qquad (5)$$

$$k_{33}^2 = \frac{d_{33}^2}{\varepsilon\, s_{33}^E} \qquad (6)$$

To avoid confusion. the mechanical stress effect will not be considered here and hence T_i is set to zero in these equations. Eq. (2) relates the polarization to the bias electric field and temperature. and it is solved numerically.

For a continuous transition. without electric bias fields. at $t < t_0$.

$$P = \sqrt{\frac{\alpha_0(t_0-t)}{\beta}} \;,\; \varepsilon = \frac{1}{2\alpha_0(t_0-t)} \;,\; d_{33} = \frac{Q_{11}}{\sqrt{\beta\alpha_0(t_0-t)}} \quad (7)$$

Above t_0. both P and d_{33} become zero. In figure 2. the material properties as a function of temperature under a fixed DC bias field and as a function of DC bias electric field at several temperatures are plotted. The parameters used are: $\alpha_0 = 6.66 \ast 10^5$. $\beta = 9.48 \ast 10^8$. $\gamma = 3.94 \ast 10^{10}$. and $Q_{11} = 0.1$ (all in MKS units). The choice of these parameters is to provide a comparison with the response behavior of a first order transition later where the parameters for BaTiO$_3$ single crystal are used. Clearly. the DC bias field eliminates the critical behavior and reduces the dielectric constant substantially. As a result. the material does not exhibit a large piezoelectric constant and electromechanical coupling factor in the induced piezoelectric state.

In contrast to the continuous transition. for a material with a first order transition. these material constants will have a substantial increase as a DC electric bias field is applied. Without electric field. a first order transition will occur at

$$t_r = t_0 + \frac{3\beta^2}{16\,\alpha_0\gamma} \;.$$ With a DC bias field. a critical region will be

induced with the critical field $E_c = \frac{6\beta^2}{25\gamma} P_c$ and $P_c = -\frac{3\beta}{10\gamma}$. the

polarization at the critical field. The critical temperature is at

$$t_c = t_0 + \frac{9\beta^2}{20\,\alpha_0\gamma} .$$ Near the critical point,

$$k_{33} \to 1. \; \varepsilon \to |t\text{-}t_c|^{-1}. \text{ and } d_{33} \to P_c |t\text{-}t_c|^{-1} \quad (8)$$

In figure 3. the dependence of the dielectric constant, piezoelectric constant, and electromechanical coupling factor on the bias electric field and temperature for a first order transition material is presented. The parameters used here are those for BaTiO$_3$ single crystal: $\alpha_0 = 6.66 \ast 10^5$, $\beta = -9.48 \ast 10^8$, $\gamma = 3.94 \ast 10^{10}$, $Q_{11} = 0.1$. all in MKS units. and $t_0 = 110\,^\circ C$.[6]

Figures 2 and 3 demonstrate the drastical difference in the material properties near the transition region between a first order and a continuous transition:

(1) For a continuous transition, the peak dielectric constant decreases monotonically as the DC bias field increases, while for a first order transition, it will increase until reaches the critical field E_c. Afterwords, the peak value decreases when the bias field level is further increased. From the expression above, a strong first order transition (a large β) will yield a higher E_c. This feature may be useful for the electric energy storage application, where a high electric field and large dielectric constant are needed.

(2) Near the critical point of a first order transition, the electromechanical coupling factor can approach one which means a 100 % energy conversion between the electric and mechanical forms. Although in reality, due to the loss and material imperfections, the electromechanical coupling factor may be smaller than one, it will still be substantially larger near the critical region than those in the other regions.

(3) A large piezoelectric response can be achieved near and at the critical point of a first order transition. For a continuous transition, the piezoelectric constant also shows a divergence as the temperature approaches the transition point. However, the
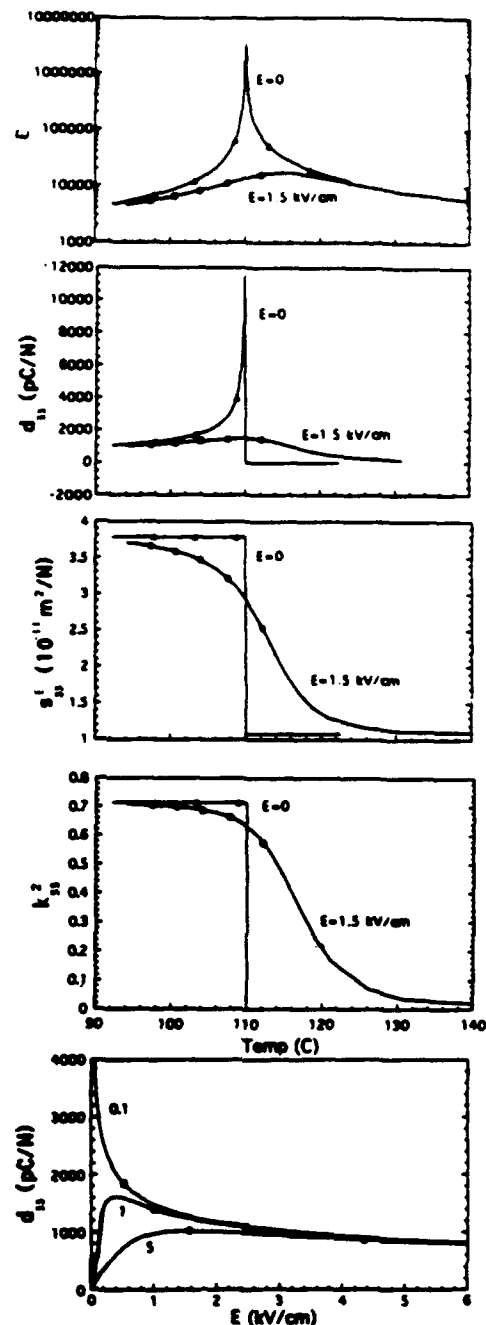
Figure 2. From the top to the bottom: the dielectric constant. the piezoelectric constant, the elastic compliance. and the electromechanical coupling factor near a continuous transition as a function of temperature with different bias field E; and the piezoelectric constant as a function of bias field E at different temperature (the labels for the curves are t-t_0). All the curves are calculated using equations (2) to (6) for a continuous transition.

anomaly is much weaker than that for a first order transition near the critical point, that is $(t$-$t_0)^{-1/2}$ vs. $(t$-$t_c)^{-1}$. In real material, a transition is always smeared out over a finite temperature and field range due to various imperfections. On
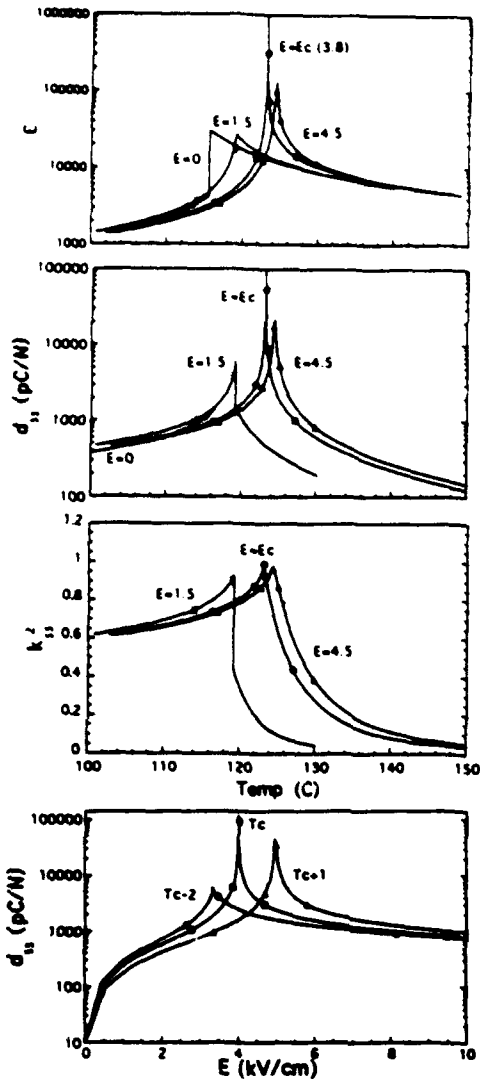
Figure 3. From the top to the bottom: the dielectric constant, the piezoelectric constant, and the electromechanical coupling factor as a function of temperature for a material with a first order transition under different bias field; and the induced piezoelectric constant as a function of bias field for different temperature, where t_c is the critical temperature. All the curves are calculated using eqs. (2) to (6) and the parameters used are those for BaTiO$_3$ single crystal.

the average, a first order transition will yield a much larger piezoelectric response. The stronger this first order transition is, the larger the piezoelectric response near the critical point will be. The penality for having a stronger first order transition is that the critical field E_c will escalate since it is proportional to β^2.

Although for a continuous transition, an anomaly in the piezoelectric constant will occur near the transition when there is no DC bias fields, the polarization of the material is not stable against the thermal depoling effect as the material is near the transition point. As a result, the piezoelectric response near a continuous transition is not stable. In addition, there is no increase in the electromechanical coupling factor near a continuous transition.

In practical applications, the materials used are often in the ceramic form. Hence, at a constant applied external field, the electric field in each grain is not the same, which will smear out the critical point and reduce the maximum value of the achievable piezoelectric constants. From the practical point of view, this may not be detrimental. A broad phase transition region means a broad operation temperature and/or field range which is often required for practical applications.

III. Experimental results

In searching for materials with a high piezoelectric response, the properties of a series of (Ba$_{1-x}$Sr$_x$)TiO$_3$ (BST) ceramic specimens at $x=0.35$, which have the transition near room temperature, with different dopants and processing conditions were evaluated. The experimental details and a detailed account of the results will be presented in a later publication. Since the saturated polarization and the electrostrictive coefficient are almost the same for all these samples, the magnitude of the induced piezoelectric response will be determined by the order of the transition in these samples. From the bias field dependence of the dielectric response, the order of the transiton in these specimens were identified. Both the dielectric behaviors typical for a first order transition and for a continuous transition were observed in these specimens. In figure 4, the dielectric constant as a function of temperature under different bias field for one specimen is shown and clearly, it is the behavior for a first order transition. The temperature difference t_c-t_{tr} is 1.1 °C which indicates a weakly first order transition (t_c-t_{tr} for BaTiO$_3$
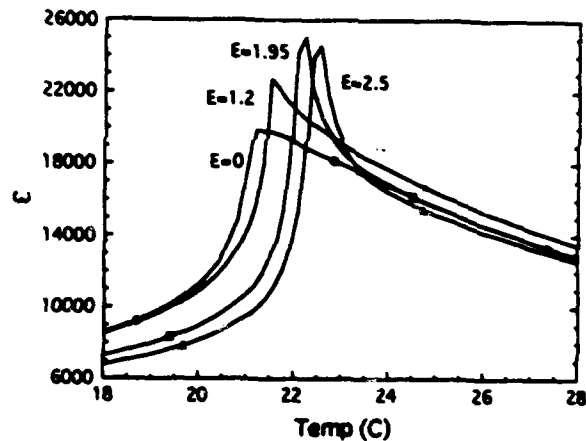
Figure 4. The dielectric constant for a BST sample which shows a first order transition as a function of temperature for different DC bias field. The unit for the bias electric field shown in the figure is kV/cm.

is about 9 °C) and $E_c=1.95$ kV/cm. The maximun induced piezoelectric constant d$_{33}$ for this material is 1,600 pC/N, which is far above any piezoelectric constant of the materials currently in use and reported. For the samples showing a continuous transition behavior, the induced piezoelectric constant is much smaller. Among them, the highest one is at 1,200 pC/N. This demonstrates the importance of the order of transition on the electromechanical response of a ferroelectric material.

The large difference in the electromechanical behavior between a first order transition and a continuous transition can be explained from the polarization hysteresis loops shown in figure 5. which are taken from the BST samples possessing first order transition and continuous transition respectively.

From the relation $d_{33}=2Q_{11}$ P ε. a high piezoelectric constant requires a material to have a large P and ε simultaneously. As shown in figure 5(a). which is for the BST sample with a first order transition. the highest dielectric constant maximum occurs at P=0. therefore. yields a large piezoelectric response. While for a continuous transition material. figure 5(b) shows that the highest dielectric constant maximum occurs at P=0. which certainly does not satisfy the condition for a high piezoelectric response.

IV. Summary and acknowledgment

In this paper. we show that, both theoretically and experimentally, a giant piezoelectric response with tunability can be achieved by operating a material near its paraelectric-ferroelectric transition for a material with a first order paraelectric-ferroelectric phase transition. A stronger first order transition is preferred to have a higher induced piezoelectric constant and electromechanical coupling factor. For a material with a continuous transition, there is no advantage to operate it near the transition region. This work was supported by the official of Naval Research.

References:
1. Wuyi Pan, Q. M. Zhang, A. S. Bhalla, and L. E. Cross, J. Am. Ceram. Soc. 71, C302 (1988).
2. L. E. Cross, S. J. Jang, R. E. Newnham, S. Normura, and K. Uchino, Ferroelectrics 23, 187 (1980).
3. Wuyi Pan, Q. M. Zhang, A. Bhalla, and L. E. Cross, J. Am. Ceram. Soc. 72, 571 (1989).
4. B. Jaffe, W. R. Cooke, Jr., and H. Jaffe, Piezoelectric Ceramics.
5. A. F. Devonshire, Phil. Mag. 3, 85 (1954).
6. F. Jona and G. Shirane, Ferroelectric Crystals (Oxford: New York: Pergamon Press, 1962).
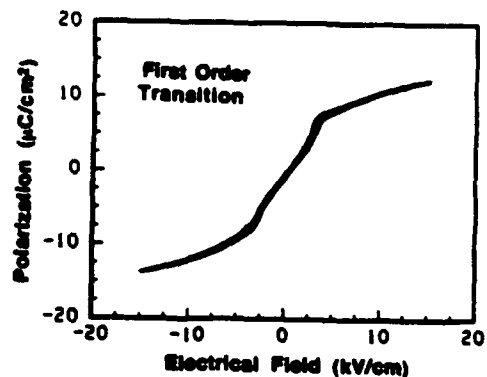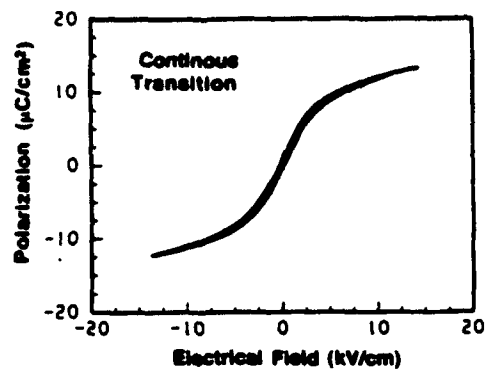
Figure 5. The polarization hysteresis loops for the BST samples with a continuous transition near t_0 and a first order transition near t_c. For a first order transition, the maximum dielectric constant peak occurs at $P=P_c$, while for a continuous transition, the maximum dielectric constant peak occurs at P=0.

INTEGRATION ISSUES

APPENDIX   40

Piezoelectric Performance of Piezoceramic-Polymer Composites with

2-2 Connectivity ---- A Combined Theoretical and Experimental Study

Q. M. Zhang, Wenwu Cao, J. Zhao, and L. E. Cross

Materials Research Laboratory, The Pennsylvania State University

University Park, PA 16802

Abstract:

The piezoelectric performance of piezoceramic polymer composites with 2-2 connectivity at low frequency has been analyzed theoretically. Due to the elastic coupling between the ceramic and polymer phases, the strain components in directions perpendicular and parallel to the ceramic-polymer interface are not uniform in either phases. As a result, most of the stress transfer between the two phases occurs at the region near the surface of the composite. In order to improve the piezoelectric performance of a composite, the polymer matrix should have a small Young's modulus and a large shear modulus, and a large aspect ratio. It may be also desirable to have the polymer matrix made of two different polymers with the stiffer one near the surface and the softer one in the interior of the composite. To compare with the theoretical calculations, surface profiles of a series of 2-2 composites with different aspect ratios were measured, and the experimental results show excellent agreement with the theoretical calculations. The non-uniform strain and stress in the direction parallel to the ceramic-polymer interface of a composite were also confirmed by experiments.

I. Introduction

One of the key design criteria of piezoceramic polymer composites is to optimize the stress transfer between the two constituents --- the piezoelectric ceramic and polymer matrix. Since the stress transfer between the two constituents depends on the dimensions and elastic properties of each phase in a complicated manner, as has been demonstrated by numerous experiments. there has been a constant effort to establish a quantitative understanding of how various design parameters affect the performance of a piezocomposite.[1-5] One of the most frequently used models in analyzing the properties of a composite is based on the isostrain approximation. i.e.. the assumption that the elastic displacements in the two constituents are equal in the ceramic poling direction. However, the results derived using the isostrain approximation often overestimated the stress transfer between the two phases. Also, the prediction that the piezoelectric performance of a composite should be independent of the aspect ratio of the ceramics in a composite, derived from the isostrain approximation, was apparently incorrect. As a matter of fact, the aspect ratio is one of the most important parameters in adjusting the performance of a composite.[3-5]

Recently, in an effort to improve the modeling of piezocomposites, we have introduced a simple model based on the static force balance condition to describe the mechanical and the piezoelectric response of a composite under external stress or electric fields.[6,7] The model provided the trend of how the elastic properties of each phase and especially the aspect ratio of the ceramics affect the performance of a composite, and was in good agreement with experimental results. Hence, it provided a much better base for relating the performance of a composite to the design parameters. However, quantitatively, there still existed some discrepancy between experimental results and theoretical predictions. For example, in order to fit the experimental surface profile of a composite, a much larger Poisson's ratio for the polymer matrix has to be used. The discrepancies are the result of the approximation made in the model that the strain in both phases along the piezoceramic poling direction (the z-direction, as will be introduced later in this paper) is a constant (or independent of z-coordinate). In this paper. we

will eliminate this assumption and treat the piezocomposites using the basic static elastic equations:[8]

$$\sum_{k=1}^{3} \frac{\partial T_{ik}}{\partial x_k} = 0 \qquad (1)$$

In equation (1), i and k=1, 2, and 3 (or x, y, and z as will be used later in this paper) correspond to the three orthogonal coordinates x, y, and z. Although a standard procedure for solving (1) has been developed, it involves complicated mathematical calculations for a composite structure, which quite often do not yield much physical insight.[9] To avoid this, numerous approximations were made in the literature to simplify (1) so that a closed form solution can be obtained for composites.[10-12] In trying to adapt these results to the piezoceramic polymer composites, we found that among these theoretical studies, there is a common shortcoming, i.e., there always exists an undetermined adjustable parameter in the final results, which is not desirable for a model required to give quantitative predictions.

For a piezocomposite with 2-2 connectivity, as shown in fig. 1, we will show in this paper that one can greatly simplify (1) by making use of the features of a typical 2-2 composite. The calculated results from this approach indicate that the strain field in both the x and z-directions is not uniform. It also shows that most of the stress transfer between the two constituents occurs near the surface of a composite. The results confirm that when a composite thickness 2L is much larger than the width of ceramic plates and polymer gap (d and a), the performance of a composite at low frequency can be analyzed by the isostrain approximation.

In order to compare with the theoretical results, we have also carried out a series of measurements on the surface profile of 2-2 composites with different aspect ratio using a double beam laser dilatometer.[13] The theoretically calculated profile and experimentally measured one agree with each other in numerical value even without use of adjustable parameters. We have also made a 2-2 composite with multilayer structure so that the z-dependence of the local stress field can be probed and the result also agrees with the theoretical prediction. It is conceivable that the method used here to measure the local stress field may be generalized to the structure

composites in which the piezoceramic elements can serve as sensors to monitor the change in the local stress field. In this manner, one may be able to verify the detailed theoretical predictions about the stress pattern in these composites.

II. Piezoelectric Response of 2-2 Composites under an Electric Field

In the earlier publication,[6] we have shown that when a composite is subjected to an external electric field along the ceramic poling direction, the surface displacement profile is not uniform. The displacement in the polymer region is always less than that in the piezoceramic region. From this non-uniform strain distribution, one is able to calculate the stress transfer between the two phases.[6,7] Since the ceramic plates are poled in the z-direction, we are mainly concerned with the stress transfer in that direction. Hence, we only consider the following elastic equation

$$\frac{\partial T_{zz}}{\partial z} + \frac{\partial T_{xz}}{\partial x} = 0 \qquad (2)$$

As shown in Fig. 1 the y-dimensions of a typical 2-2 composite is much larger than the thickness 2L and repeating distance (a+b) in the x-direction of the composite, hence all the quantities involved are assumed to be independent of y-coordinate. Through the stress-strain relationship, (2) can be converted to[10]

$$(\lambda+\mu)\frac{\partial \varepsilon}{\partial z} + \mu \nabla^2 u_z = 0 \qquad (3)$$

where λ and μ are the Lame coefficients (μ is shear modulus), $\varepsilon = u_{xx} + u_{yy} + u_{zz}$, and ∇^2 is the Laplacian operator. For simplicity, we assume that both ceramic and polymer are elastically isotropic (the elastically anisotropic case can also be treated utilizing the procedure outlined in this paper). λ and μ are related to the Young's modulus Y and Poison's ratio σ through

$$\mu = \frac{Y}{2(1+\sigma)} \qquad \text{and} \qquad \lambda = \frac{Y\sigma}{(1+\sigma)(1-2\sigma)}$$

When an electric field E_3 (E_3 is a constant) is applied on a composite, one has the following constitutive relations in the ceramic:

$$T_{xx} = c_{11}^c u_{xx} + c_{12}^c u_{yy} + c_{12}^c u_{zz} - e_{31} E_3 \qquad (4a)$$

$$T_{yy} = c_{12}^c u_{xx} + c_{11}^c u_{yy} + c_{12}^c u_{zz} - e_{31} E_3 \qquad (4b)$$

$$T_{zz} = c_{12}^c u_{xx} + c_{12}^c u_{yy} + c_{11}^c u_{zz} - e_{33} E_3 \qquad (4c)$$

where c_{ij}^c are the elastic constants (the superscript c refers to the ceramic) and e_{ij} are the piezoelectric stress constants for the ceramic. Similar equations can be written for the polymer matrix except that all $e_{ij}=0$ and c_{ij} are those for the polymer.

From earlier experimental and theoretical results and the dimensionality arguments, the strain u_{yy} in both polymer matrix and ceramic plate can be assumed to be constant. For a composite material, in general, T_{xx} is not equal to zero when it is subjected to an electric field. However, this non-zero T_{xx} is the result of the stress transfer in the z-direction between the two constitunents and it is, therefore, small compared with the stress in the z-direction. Since we are mostly concerned with the stress transfer in the z-direction, the error of assuming $T_{xx}=0$ to the z-direction stress transfer will be on the order of σ^2 (σ is the Poisson's ratio).[6] Under these approximations, the strain u_{xx} and u_{zz} are related by

$$u_{xx} = \frac{-1}{c_{11}^c}(c_{12}^c A_y + c_{12}^c u_{zz} - e_{31} E_3) \qquad (5a)$$

$$u_{xx} = \frac{-1}{c_{11}^p}(c_{12}^p A_y + c_{12}^p u_{zz}) \qquad (5b)$$

where (5a) is for the ceramic plate and (5b) for the polymer matrix. u_{yy} is the same in both phases and is denoted as a constant A_y. Substituting (5) to (3) yields

$$K^2 \frac{\partial^2 u_z}{\partial z^2} + \frac{\partial^2 u_z}{\partial x^2} = 0 \qquad (6)$$

where

$$K^2 = [(\lambda + 2\mu) - (\lambda + \mu)\lambda / c_{11}] / \mu$$

$$= Y(2-\sigma) / [2\mu(1-\sigma^2)] \qquad (7)$$

(6) can be used for both ceramic plate and polymer matrix, except different elastic constants should be used for different phases. Apparently, u_z is a function of both x and z. Following the standard procedure in solving the partial differential equation, we assume u_z as $u_z = f(x)g(z)$. Substituting this into (6), one gets two ordinary differential equations:

$$\frac{K^2}{g(z)} \frac{\partial^2}{\partial x^2} g(z) = -\beta^2 \quad \text{and} \quad \frac{1}{f(x)} \frac{\partial^2}{\partial x^2} f(x) = \beta^2 \qquad (8)$$

The solution to (8) which satisfies the boundary condition that $u_z=0$ at $z=0$, and the symmetry of the problem $\frac{\partial u_z}{\partial x}=0$ at $x=0$ for the polymer matrix and at $x=(a+d)/2$ for the ceramic plate is

$$u_z^c = A^c z + \sum_{n=0}^{\infty} B_n^c \sin(\alpha_n z)\cosh[\beta_n^c(x-(a+d)/2)] \quad (\tfrac{a}{2} \leq x \leq d + \tfrac{a}{2}) \quad (9a)$$

$$u_z^p = A^p z + \sum_{n=0}^{\infty} B_n^p \sin(\alpha_n z)\cosh(\beta_n^p x) \quad (-\tfrac{a}{2} \leq x \leq \tfrac{a}{2}) \quad (9b)$$

where A^c, A^p, B_n^c, and B_n^p are the integration constants, $\beta_n^c = K^c \alpha_n$ and $\beta_n^p = K^p \alpha_n$. α_n is the eigenvalue, which will be determined from the boundary condition. K^c and K^p are defined in (7) for the ceramic plate and polymer matrix, respectively. Due to the periodic nature of the composite, we only write down the solution for a unit cell of the composite at $-a/2 < x < a/2+d$.

The following boundary conditions are used to determine the integration constants:

$$T_{zz}=0 \quad \text{at } z= \pm L.$$

$$u_z^c = u_z^p \quad \text{and} \quad T_{xz}^c = T_{xz}^p \quad \text{at } x=a/2,$$

$$u_{y}^c = u_{y}^p = A_y.$$

The relation between the shear stress T_{xz} and the shear strain u_{xz} is

$$T_{xz} = \mu\left(\frac{\partial u_z}{\partial x} + \frac{\partial u_x}{\partial z}\right)$$

Making use of (4) and (9), one arrives at

$$\alpha_n = (2n+1)\pi/(2L) \quad (n=0,1,2,\ \ ) \quad (10a)$$

$$B_n^p = \frac{2(-1)^n}{L(\alpha_n)^2} \frac{(A^c-A^p)\,[\mu^c(K^c + \frac{c_{12}^c}{c_{11}^c K^c})\sinh(\beta_n^c\frac{d}{2})]}{(\mu^c(K^c+\frac{c_{12}^c}{c_{11}^c K^c})\sinh(\beta_n^c\frac{d}{2})\cosh(\beta_n^p\frac{a}{2}) + \mu^p(K^p+\frac{c_{12}^p}{c_{11}^p K^p})\cosh(\beta_n^c\frac{d}{2})\sinh(\beta_n^p\frac{a}{2}))} \quad (10b)$$

$$B_n^c = \frac{2(-1)^{n+1}}{L(\alpha_n)^2} \frac{(A^c-A^p)\,[\mu^p(K^p + \frac{c_{12}^p}{c_{11}^p K^p})\sinh(\beta_n^p\frac{a}{2})]}{(\mu^c(K^c+\frac{c_{12}^c}{c_{11}^c K^c})\sinh(\beta_n^c\frac{d}{2})\cosh(\beta_n^p\frac{a}{2}) + \mu^p(K^p+\frac{c_{12}^p}{c_{11}^p K^p})\cosh(\beta_n^c\frac{d}{2})\sinh(\beta_n^p\frac{a}{2}))} \quad (10c)$$

$$A^p = \frac{C_2^p}{C_1^p} A_y \quad (10d)$$

and

$$A^c = \frac{C_2^c}{C_1^c} A_y + (e_{33} - \frac{c_{12}^c}{c_{11}^c} e_{31})\frac{E_3}{C_1^c} \quad (10e)$$

where C_1^c, C_2^c, C_1^p, and C_2^p are defined in the Appendix. The superscripts p and c stand for polymer matrix and ceramic plate, respectively, and this convention will be used through out this paper. For the sake of simplicity, B_n^c and B_n^p are rewritten as

$$B_n^c = (A^c - A^p) B_{n0}^c$$
$$B_n^p = (A^c - A^p) B_{n0}^p$$

It is clear that B_{n0}^c and B_{n0}^p depend only on the properties of the composite and will not change with the experimental conditions.

Incidentally, $\beta_0^p = \frac{\pi}{2L} \sqrt{\frac{Y \; (2-\sigma)}{\mu 2(1-\sigma^2)}}$ in (9b), which is the prefactor in the cosh function of the first term describing the non-uniform strain profile in the polymer matrix in the x-direction, is quite similar to that obtained in our earlier analysis except there the strain in the z-direction is assumed to be uniform.[6,7] Since β_n^p describes the strain decay in the polymer phase in the x-direction, for more efficient stress transfer between the two constituents, a smaller β_n^p is preferred, which implies that the polymer should have a smaller Young's modulus and a large shear modulus. A composite with a larger L will also improve the stress transfer. These conclusions are the same as those derived from our earlier theoretical model.[6,7]

Finally, A_y can be determined from the force balance condition (Newton's third law) in the y-direction, which requires that the total force experienced by the ceramic plate should be equal in magnitude and opposite in sign to that in the polymer matrix

$$\int_0^L \int_{a/2}^{(a+d)/2} T_{yy}^c \, dx \, dz + \int_0^L \int_0^{a/2} T_{yy}^p \, dx \, dz = 0$$

From this

$$A_y = \frac{III^E E_3}{\frac{L}{2}(dC_A^c + a \, C_A^p) - C_B (II^c + II^p)}$$

where C_A^c, C_A^p, C_B, II^c, II^c and III^E are defined in the Appendix.

Equation (9) shows that the strain profile not only depends on the x-coordinate but also depends on the z-coordinate. The coupling between the polymer and ceramic changes the strain pattern in both directions.

In order to verify these theoretical results, the surface profiles of several 2-2 composites with different thickness (2L) were measured using a double beam laser dilatometer. The 2-2 composites were made from PZT-500 ceramics[14] and Spurrs epoxy[15] with the dimensions of a=1.3 mm and d=1.0 mm. The 2-2 composite samples with different thicknesses 2L used in the surface profile measurement were cut from one original piece. Shown in fig. 2 is the comparison of experimentally measured surface profiles with those calculated using (9) at the surface of the composites ($z= \pm$ L). All the input parameters are fixed in the calculation, which are taken from the data either from the manufacturer or from the other measurements.[14,15] During the process of making these 2-2 composite samples, there was some degree of depoling due to the heating of the ceramic plate to higher temperature. The d_{33} value was reduced from 400 pm/V (poled by the manufacturer) to a lower value of 356 pm/V and the d_{31} value was also reduced in the same proportion. In the theoretical calculation, these reduced values were used. For clarity, not all experimentally measured surface profiles are shown in fig. 2. In Table I, the ratio of u_z^p at x=0 to u_z^p at x=(a+d)/2 from all the samples measured and the corresponding theoretically calculated values are listed, since this is the most sensitive parameter reflecting the non-uniform strain distribution in the x-direction of a composite. Excellent agreement between the experimentally measured profiles and theoretically predicted ones was achieved over a large range of aspect ratio without adjustable parameters, and the theoretical fitting parameters (listed in Table II) agree with the earlier measured results. The results here also demonstrate that the surface profile becomes more or less uniform as the aspect ratio becomes large.

Fig. 3 show the strain profile in the z-direction calculated using (9) for both ceramic plate and polymer matrix for three aspect ratios (d/L=0.4, 0.2, and 0.05) with 40 % ceramic content for 2-2 composites made of PZT-500 plates and Spurrs epoxy. The parameters used in the calculation are given in Table II except d_{33}=400 pm/V and d_{31}=-175 pm/V are used here. For the ceramic plate, the strain u_{zz} plotted is averaged over x, and for the polymer, the value was taken at x=0:

$$\overline{u_{zz}^c} = A^c + \frac{2}{dK^c} \sum_{n=0}^{\infty} B_n^c \cos(\alpha_n z) \sinh[\beta_n^c d/2] \qquad (11a)$$

$$u_{zz}^p = A^p + \sum_{n=0}^{\infty} B_n^p \alpha_n \cos(\alpha_n z) \qquad (11b)$$

Figs. 2 and 3 shows clearly that the strain depends both x and z. It also shows that near the surface the piezoelectric response of the ceramic plate is very close to that of pure ceramic (d_{33}=400 pm/V) while the strain in the polymer near z=L is nearly zero. In other words, the elastic coupling between the two phases does not affect very much the piezoelectric response of the ceramic plate and elastic response of the polymer matrix near the surface region ($z= \pm L$). On the other hand, although the strain in the z-direction shows large changes with z-coordinate for composites with a small aspect ratio, the strain in the z-direction is almost a constant for composites with large aspect ratio, for which the constant strain approximation in the z-direction and isostrain approximation in the x-direction should be appropriate. These results also justify the assumption made earlier in this paper that u_{yy} is a constant for a 2-2 composite since the y-dimension is much larger than the ceramic plate width d and polymer matrix gap a.

III. Piezoelectric Response under Hydrostatic Pressure

When a 2-2 piezoceramic polymer composite is subjected to a hydrostatic pressure (-p), the elastic response of both ceramic plate and polymer matrix is still described by (1), (2), and (3) except that (4) becomes

$$T_{xx} = c_{11}^c u_{xx} + c_{12}^c u_{yy} + c_{12}^c u_{zz} \qquad (12a)$$

$$T_{yy} = c_{12}^c u_{xx} + c_{11}^c u_{yy} + c_{12}^c u_{zz} \qquad (12b)$$

and $\qquad T_{zz} = c_{12}^c u_{xx} + c_{12}^c u_{yy} + c_{11}^c u_{zz} \qquad (12c)$

for the ceramic plates. For the polymer matrix, one just replace c_{ij}^c in (11) by c_{ij}^p, the stiffness constant of the polymer phase used. From $T_{xx} = -p$, the relation between u_{xx} and u_{zz} becomes

$$u_{xx} = \frac{-1}{c_{11}}(p + c_{12}u_{zz} + c_{12}A_y)$$

which can be used for ceramic plates and polymer matrix.

The elastic displacement u_z for the two phases are those in (9a) and (9b). The boundary conditions now are

$$T_{zz} = -p \quad \text{at } z = \pm L,$$

$$u^c_{zz} = u^p_{zz} \quad \text{and} \quad T^c_{xz} = T^p_{xz} \quad \text{at } x = a/2,$$

$$\text{and} \quad u^c_{yy} = u^p_{yy} = A_y.$$

$\alpha_n = (2n+1)\pi/(2L)$, B^p_n, and B^c_n are those in (10a) and (10b). A^c, A^p and A_y now are different from those in the electric field driven situation

$$A^c = \frac{-p}{c^c_{11} + c^c_{12}} + \frac{C^c_2}{C^c_1} A_y \qquad (13a)$$

$$A^p = \frac{-p}{c^p_{11} + c^p_{12}} + \frac{C^p_2}{C^p_1} A_y \qquad (13b).$$

Taking into account the external stress (-p) in the y-direction, the force balance condition in that direction requires

$$\int_0^L \int_{a/2}^{(a+d)/2} T^c_{yy}\,dxdz + \int_0^L \int_0^{a/2} T^p_{yy}\,dxdz = -p(a+d)L/2 \qquad (14)$$

where T^p_{yy} and T^c_{yy} are the stresses in the polymer matrix and ceramic plate, respectively. (14) states that the total force experienced by the composite in the y-direction should be the same as that exerted by the hydrostatic pressure. Hence, the strain in the y-direction, A_y, can be determined from (14),

$$A_y = \frac{(III^b - (a+d)L/2)\,p}{\frac{L}{2}(dC^c_A + a\,C^p_A) - C_B(II^c + II^p)} \qquad (15)$$

where C^c_A, C^p_A, C_B, II^c, II^p and III^b are all defined in the Appendix.

The non-uniform strains and stresses in the ceramic plate imply that the piezoelectric hydrostatic response in the ceramic is not uniform, it depends on both x and z coordinates. For example, the local piezoelectric hydrostatic response can be found from the relation

$$E_3 = -[g_{33}T_{zz} + g_{31}(T_{xx} + T_{yy})] = -g^{eff}_h(-p) \qquad (16)$$

where g^{eff}_h is introduced as the local effective piezoelectric hydrostatic coefficient, which is a function of both x and z coordinates. Utilizing the results derived above, one can get

$$E_3 = -[-p\{g_{33}\frac{c^c_{12}}{c^c_{11}} + g_{31}(1 + \frac{c^c_{12}}{c^c_{11}})\} + A_y(g_{31}c^c_1 - g_{33}c^c_2) + u^c_{zz}(g_{33}C^c_1 - g_{31}C^c_2)] \qquad (17)$$

Apparently, the third term, which contains u^c_{zz}, is responsible for the variation of the hydrostatic response with x and z coordinates.

The z-dependence of the piezoelectric response predicted by (17) was verified experimentally. The local stress field was probed in a 2-2 composite with multilayer structure (see schematic in fig. 4). The multilayer 2-2 composite was made of PZT-500 ceramic and Spurrs epoxy with total eleven layers. The ceramic plates were glued together using silver epoxy which also serves as electrodes for each layer. The charge output under an AC hydrostatic pressure (50 Hz) was measured for each layer with the electrodes of other layers shorted together. The experimentally measured quantity corresponds to $\overline{E}_3$, which is E_3 averaged over x on the ceramic plate

$$\overline{E}_3 = - \left[-p\left\{ g_{33} + g_{31}\left(1 + \frac{2c_{12}^c}{c_{11}^c + c_{12}^c}\right)\right\} + A_y g_{31} \frac{(c_{11}^c + 2c_{12}^c)(c_{11}^c - c_{12}^c)}{c_{11}^c + c_{12}^c} + \right.$$
$$\left. 2(g_{33}C_1^c - g_{31}C_2^c)\frac{(A^c - A^p)}{dK^c} \sum_{n=0}^{\infty} B_{n0}^c \cos(\alpha_n z)\sinh(\beta_n^c \frac{d}{2}) \right] \qquad (18)$$

The experimental result and theoretical calculation are compared in fig. 5 and the agreement between the two is satisfactory.

The effective hydrostatic piezoelectric coefficient $\overline{g_h}$ of the sample can be found by averaging $\overline{E}_3$ in (18) over z ($E_3^{ave} = \frac{1}{L} \int_0^L \overline{E}_3 dz$) and $\overline{g_h} = E_3^{ave}/p$. $\overline{d_h}$ for the sample is $\overline{g_h}\overline{\epsilon}$. $\overline{\epsilon}$ is the averaged dielectric permitivity of a composite $\overline{\epsilon} = v_c \epsilon^c + (1-v_c)\epsilon^p$, where v_c is the volume content of ceramics in a composite, ϵ^c and ϵ^p are the dielectric permitivity of the ceramic plate and polymer, respectively. Usually, ϵ^c is much larger than ϵ^p, which results in $\overline{\epsilon} = v_c \epsilon^c$. Hence,

$$\overline{d_h} = v_c \gamma d_h \qquad (19)$$

where

$$\gamma = [(d_{33} + d_{31}(1 + \frac{2c_{12}^c}{c_{11}^c + c_{12}^c})) - III^y \frac{(c_{11}^c - c_{12}^c)(c_{11}^c + 2c_{12}^c)}{c_{11}^c + c_{12}^c} d_{31}$$
$$- \frac{2(d_{33}C_1^c - d_{31}C_2^c)}{dLC_2^c}(C_B III^y + C_D)II^c]/d_h$$

where $d_h = (d_{33} + 2d_{31})$ is the hydrostatic piezoelectric coefficient of the ceramic plate, and γ is the stress transfer factor, which measures how much stress is transferred from the polymer matrix to ceramic plates. In fig. 6, $\overline{d_h}$ is plotted against the ceramic content in the composite for different aspect ratio. The results for (a+d)/L=0.01 and 0.05 are almost identical, which indicates that the aspect ratio effect saturates at (a+d)/L~0.05. In other words, when L becomes larger, the

results derived here approaches those derived from the isostrain approximation and there is no further improvement in the piezoelectric performance of a composite with a smaller $(a+d)/L$.

In fig. 7, the tensile stress T_{zz} for the ceramic plate is plotted as a function of z-coordinate for 2-2 composites with different aspect ratio. The ceramic content is kept at 40 % and the composite is subjected to a hydrostatic pressure of 1 N/m^2. In the figure, T_{zz} is the average over $x=a/2$ to $x=a/2+d$. Most of the parameters used in the calculation are listed in Table II except $d_{33}=400$ pm/V and $d_{31}=-175$ pm/V (the value for PZT-500 from the manufacturer)[14]. In fig. 8, the strain u_{zz} as a function of z is plotted for both ceramic plate and polymer matrix [(11a) and (11b)]. The result is similar to that in fig. 3 where the sample is under an electric field.

In order to have a stress transfer between the two phases in a composite, it is necessary that a strain gradient exists between the two phases in the x-direction. The larger this gradient is, the more the stress will be transferred between the two phases. Fig. 8 shows clearly that the stress transfer between the polymer matrix and ceramic plate mainly occurs near the surface of the composite $(z= \pm L)$. For composites with large aspect ratio, the portion of polymer participating in the stress transfer is relatively small, i.e., most of the polymer does not contribute to the stress transfer. In fact, the polymer in the interior region acts only as the elastic loading which reduces the effective stress transfer between the two phases. Therefore, a composite with the polymer matrix made of very stiff polymer near surface region (near $z= \pm L$), and very soft polymer in the interior (near $z=0$) can have a much better piezoelectric performance.

IV. Summary and Acknowledgment

Starting from the basic elastic equations, the static piezoelectric performance of piezoceramic polymer composites with 2-2 connectivity has been analyzed theoretically. The results show that due to the elastic coupling between the two constituent phases, the strain is not only non-uniform in the x-direction, but also in the z-direction. Most of the stress transfer between the two phases occurs at the region near the surface of a composite, the materials in the interior of the

composite does not contribute significantly to the stress transfer. The results confirm that the isostrain model may be used for composites with very large aspect ratio without introducing much error. In order to improve the piezoelectric performance of a composite, the composite should be made of polymer matrix with a small Young's modulus and a large shear modulus, and a large aspect ratio. It may be desirable to have the polymer matrix made of two different polymers with the stiffer one near the surface and the softer one in the interior of the composite.

Surface profiles of a series of 2-2 composite with different aspect ratio were measured using a double beam laser interferometer and the experimental results show excellent agreement with the theoretical calculations. The non-uniform strain in the z-direction of a composite was also confirmed by experiment.

It should be noted that these conclusions reached here are based on static elastic relations, they are valid only for low frequencies, that is, for frequencies well below various resonance modes in a composite. Similar analysis on the performance of a piezocomposite near its thickness resonance frequency will be pursued in the future.

Appendix

$$C_1^c = (c_{11}^c - \frac{(c_{12}^c)^2}{c_{11}^c}) \text{ and } C_2^c = -(c_{12}^c - \frac{(c_{12}^c)^2}{c_{11}^c})$$

$$C_1^p = (c_{11}^p - \frac{(c_{12}^p)^2}{c_{11}^p}) \text{ and } C_2^p = -(c_{12}^p - \frac{(c_{12}^p)^2}{c_{11}^p}).$$

$$C_A^p = C_1^p - \frac{(C_2^p)^2}{C_1^p} \quad \text{and} \quad C_A^c = C_1^c - \frac{(C_2^c)^2}{C_1^c}$$

$$C_B = \frac{C_2^c}{C_1^c} - \frac{C_2^p}{C_1^p}$$

$$C_D = (\frac{1}{c_{11}^p + c_{12}^p} - \frac{1}{c_{11}^c + c_{12}^c})$$

$$II^c = \sum_{n=0}^{\infty} C_2^c \frac{(-1)^n \sinh(\beta_n^c \frac{d}{2})}{\beta_n^c} B_{n0}^c$$

$$II^p = \sum_{n=0}^{\infty} C_2^p \frac{(-1)^n \sinh(\beta_n^p \frac{a}{2})}{\beta_n^p} B_{n0}^p$$

$$III^E = \frac{1}{C_1^c}(e_{33} - \frac{c_{12}^c}{c_{11}^c} e_{31})(II^c + II^p) + \frac{Ld}{2}((1 - \frac{c_{12}^c}{c_{11}^c})e_{31} + \frac{C_2^c}{C_1^c}(e_{33} - \frac{c_{12}^c}{c_{11}^c} e_{31}))$$

$$III^h = (\frac{1}{c_{11}^p + c_{12}^p} - \frac{1}{c_{11}^c + c_{12}^c})(II^c + II^p) + aL(\frac{c_{12}^p}{c_{11}^p + c_{12}^p}) + dL(\frac{c_{12}^c}{c_{11}^c + c_{12}^c})$$

$$III^y = \frac{III^h - (a+d)L/2}{(dC_A^c + aC_A^p)L/2 - C_B(II^c + II^p)}$$

References:

1. R. E. Newnham, D. P. Skinner, and L. E. Cross, "Connectivity and piezoelectric-pyroelectric composites," Mater. Res. Bull., Vol. 13, pp. 525-536, 1978.

2. W. A. Smith, B. A. Auld, "Modeling of 1-3 composites: Thickness-mode oscillations." IEEE Trans. Ultrason., Ferroelec., Freq. Contr., Vol. 38, pp. 40-47, 1991.

3. K. A. Klicker, "Piezoelectric composites with 3-1 connectivity for transducer applications". Ph. D. Thesis, Penn State University, University Park, PA, 1980.

4. T. R. Gururaja, A. Safari, R. E. Newnham, and L. E. Cross, "Piezoelectric ceramic-polymer composites for transduder applications", in Electronic Ceramics, ed. L. M. Levinson, pp. 92-128. New York: marcel Dekker, 1987.

5. W. A. Smith, " Modeling of 1-3 composite piezoelectrics: hydrostatic response", IEEE Trans. Ultrason., Ferroelec., Freq. Contr., Vol. 40, pp. 41-49, 1993.

6. Q. M. Zhang, Wenwu Cao, H. Wang, and L. E. Cross, "Strain profile and piezoelectric performance of piezocomposites with 2-2 and 1-3 connectivities", in Proc. 1992 IEEE 8th Inter Symp. Appl. Ferroelec. (ISAF8) at Clemson Univ., 1992, pp. 252-254.

7. Wenwu Cao, Q. M. Zhang, and L. E. Cross, Theoretical study on the static perfromance of piezoelectric ceramic-polymer composites with 2-2 connectivity", IEEE Trans. Ultrason., Ferroelec., Freq. Contr., Vol. 40, pp. 103-109, 1993.

8. L. D. Landau and E. M. lifshotz, Theory of Elasticity, 3rd ed. (Pergamon Press, Oxford 1986).

9. W. Nowacki, Thermoelasticity, second ed. (Pergamon Press, Oxford 1986).

10. J. A. Nairn, "A variational mechanics analysis of the stress around breaks in embeded fibers", Mach. of mater. vol. 13, pp. 131-154, 1992.

11. H. L. Cox, "The elasticity and strength of paper and other fibrous materials", Br. J. Appl. Phys., Vol. 3, pp. 72-79, 1952.

12. A. Kelly and W. R. Tyson, "Fiber strengthened materials", J. Mech. Phys. Solids. vol. 10. pp. 329-350, 1963.

13. Q. M. Zhang, S. J. Jang, and L. E. Cross, "High-frequency strain response in ferroelectrics and its measurement using a modified Mach-Zehnder interferometer", J. Appl. Phys., vol. 65. pp. 2807-2813, 1989.

14. PZT-500 is the trade-mark of Piezo Kinetics Inc. for one of its PZT ceramics. The data are from Data sheet of Piezo Kinetics Inc., Bellefonte, PA, 1992.

15. C. G. Oakley, "Analysis and development of piezoelectric composites for medical ultrasound transducer applications", Ph. D. Thesis, Penn State University, University Park, PA, 1991.

Table I. The comparison of experimentally measured and theroetically calculated non-uniform strain distribution of 2-2 composites (d=1.0 mm, a=1.3 mm)

L (mm)	u_ξ^p/u_ξ (exp.)	u_ξ^p/u_ξ (theo.)
5.2	0.88	0.87
4.06	0.84	0.836
3.1	0.79	0.787
2.15	0.72	0.70
1.35	0.5	0.538

Table II. The parameters used for PZT-500 ceramics and Spurrs Epoxy in the calculation for Table I and figure 2

PZT $Y^c = 5.43 \ (10^{10} \ N/m^2)$, $\mu^c = 2.06 \ (10^{10} \ N/m^2)$, $\sigma^c = 0.31$, $c_{11}^c = 1.156 \ (10^{11} \ N/m^2)$

$c_{12}^c = 0.75 \ (10^{11} \ N/m^2)$, $d_{33} = 356$ (pm/V), $d_{31} = -156$ (pm/V), $\varepsilon^c = 1700 \ \varepsilon_0$

Spurrs Epoxy $Y^p = 4.8 \ (10^9 \ N/m^2)$, $\mu^p = 1.76 \ (10^9 \ N/m^2)$, $\sigma^p = 0.364$

$c_{11}^p = 8.27 \ (10^9 \ N/m^2)$, $c_{12}^p = 4.7 \ (10^9 \ N/m^2)$, $\varepsilon^p = 4 \ \varepsilon_0$

Figure captions:

Figure 1. Schematic drawing of a 2-2 piezoceramic-polymer composite. The ceramic plates are marked by shaded areas, the width of ceramic plate is d and the width of polymer matrix gap is a, and the sample thickness is 2L. z is the poling direction of the ceramic plate.

Figure 2. Comparison between measured and calculated surface displacement profiles (in the x-direction) for a composite subjected to a low frequency electric field. The black dots are the experimental data points and the solid lines are theoretical results. The ceramic regions have a high displacement value than the polymer regions. The displacement profile of the composite was measured using a double beam laser dilatometer at a frequency of 250 Hz. The dimensions of the composites are a=1.3 mm, d=1.0 mm, with (a) 2L=10.4 mm and (b) 4.3 mm, respectively.

Figure 3. The effect of the aspect ratio on the non-uniform strain profile in the z-direction for both ceramic plate $\overline{u^c_z(z)}$ (solid lines) and polymer matrix $u^p_z(z)$, (dashed lines). $\overline{u^c_z(z)}$ is the average displacement of the ceramic plate and $u^p_z(z)$ is the polymer displacement at x=0. the applied electric field is 1 V/m along the z-direction, a=3 mm and d=2 mm with three different thicknesses: (a) 2L=10 mm; (b) 2L=20 mm; (c) 2L=80 mm.

Figure 4. Schematic drawing of the multilayer 2-2 composite, which consists of eleven ceramic layers glued together using silver epoxy with the thickness of each ceramic layer being 0.79 mm. The dimensions of the composite are: a=1.3 mm, d=1.06 mm, 2L=8.7 mm. The electrodes for each layer are numbered from 1 to 12.

Figure 5. The charge output from the electrode pairs: 1 and 2, 2 and 3, 3 and 4, 4 and 5, 5 and 6, 6 and 7 (shown in black dots) and their comparison with the theoretically calculated result (solid line). The data point at z=0 is for pair 6 and 7, and the point near the composite surface (z=4.35)

is for pair 1 and 2. When the charge output, for example, from the second layer was measured (between the electrodes 2 and 3), the electrodes 1 and 2 were connected together and the electrodes 3 to 12 were also connected together.

Figure 6. The calculated piezoelectric hydrostatic constant $\overline{d_h}$ of 2-2 composites as a function of the ceramic volume content v_c for different aspect ratio. The parameters used in the calculation are listed in table II except here $d_{33}=400$ pm/V and $d_{31}=-175$ pm/V. The top curve is for $(a+d)/L=0.05$ and the bottom one is for $(a+d)/L=1$.

Figure 7. The tensile stress T_{zz}^c for the ceramic plate as a function of z for 2-2 composites with different L. The ceramic width $d=2$ mm and the width of polymer gap $a=3$ mm. The composites are subjected to a hydrostatic pressure of -1 N/m^2.

Figure 8. The effect of the aspect ratio on the non-uniform strain profile in the z-direction for both ceramic plate $\overline{u_{zz}^c(z)}$ (solid line) and polymer matrix $u_{zz}^p(z)$ (dashed line), where $\overline{u_{zz}^c(z)}$ is that averaged over the ceramic plate and $u_{zz}^p(z)$ is at $x=0$ when the composite is subjected to a hydrostatic pressure $-p= -1$ N/m^2. The 2-2 composite has $a=3$ mm and $d=2$ mm.

d a

Ceramic
plate

Polymer

Fig 3

F : 4

Fig. ら

Fig. 7

u_{zz} (10^{-11})

−1.5

−1.6

−1.7

−1.8

−1.9

L=5 mm

u_{zz} (10^{-11})

−1.5

−1.6

−1.7

−1.8

−1.9

L=20 mm

0   0.2   0.4   0.6   0.8   1   1.2

z/L
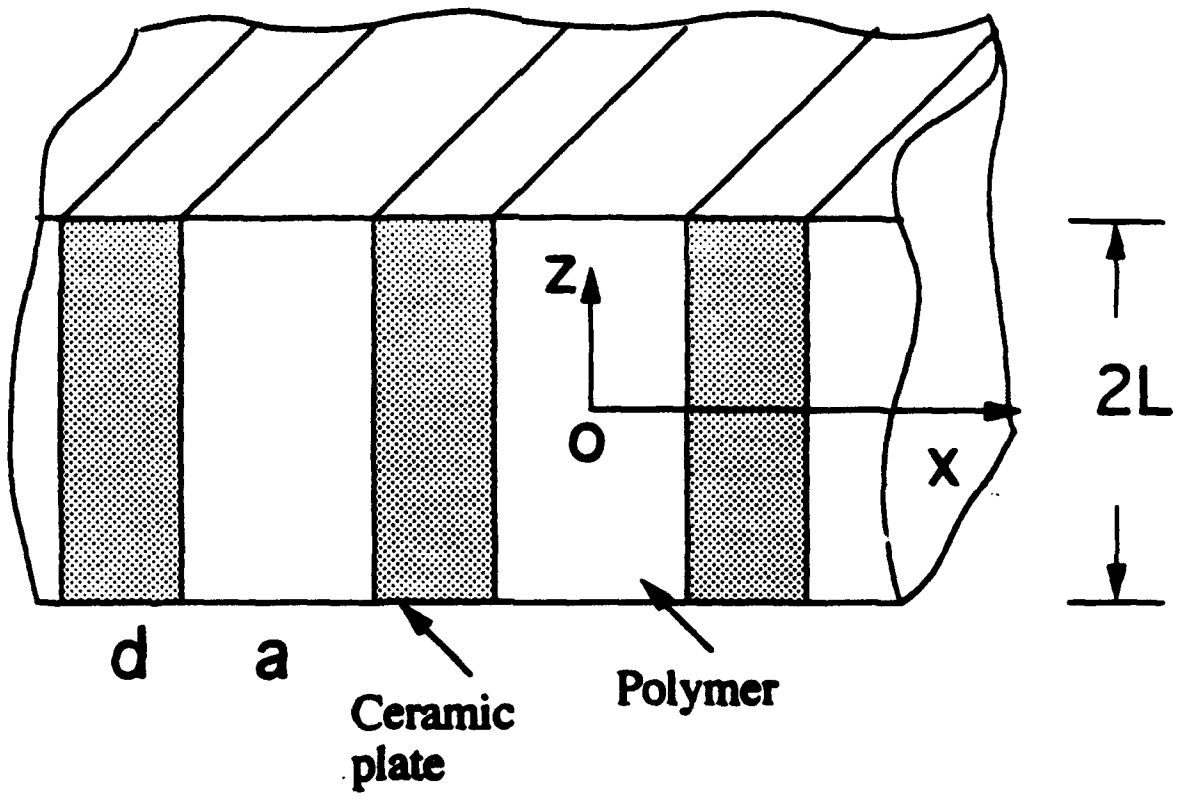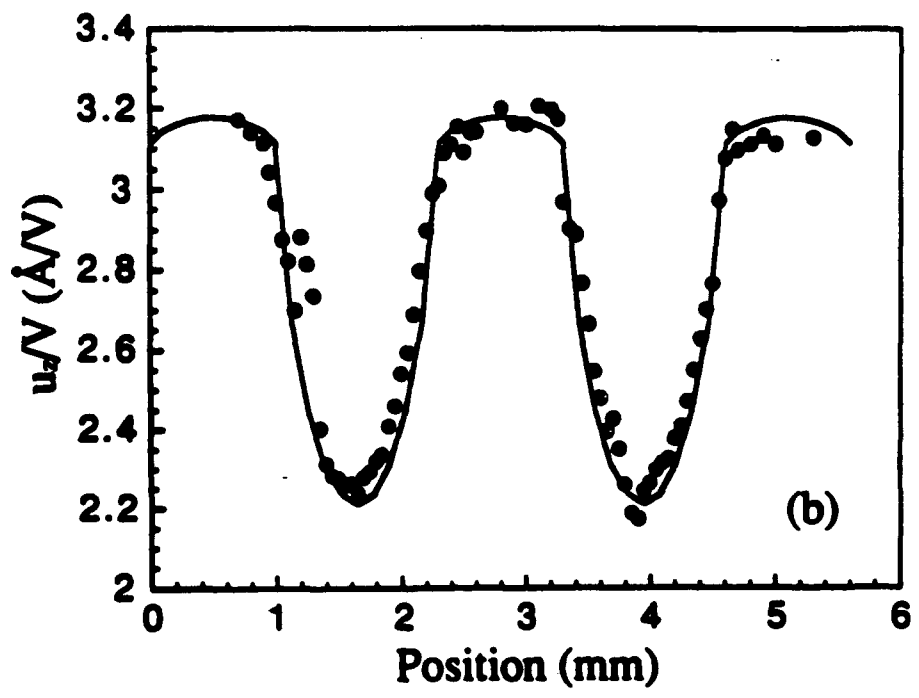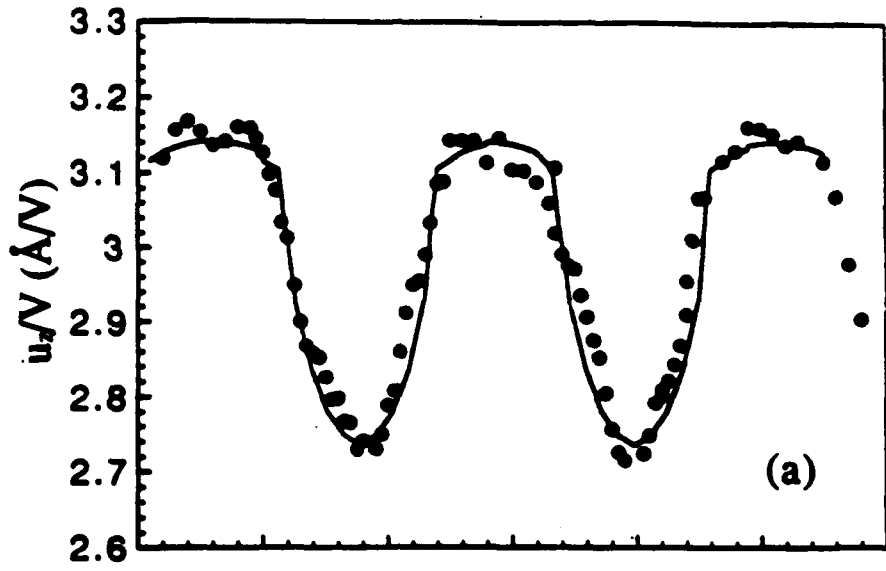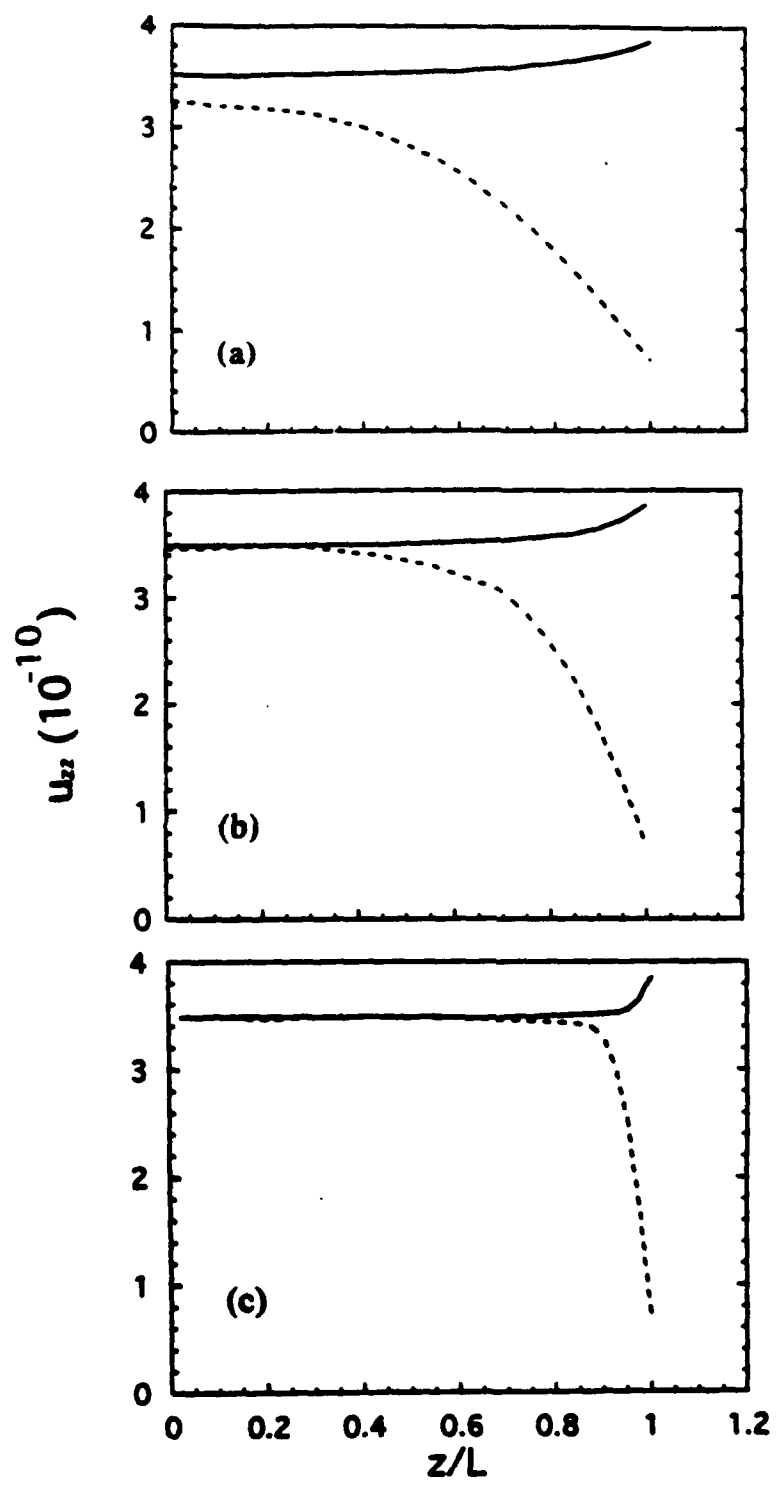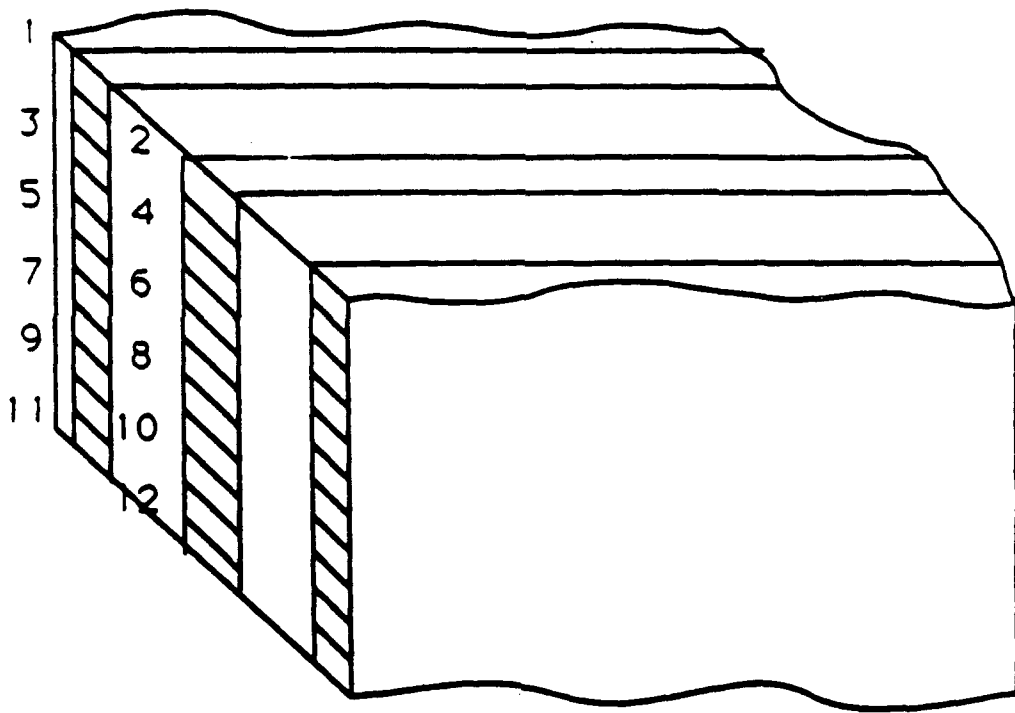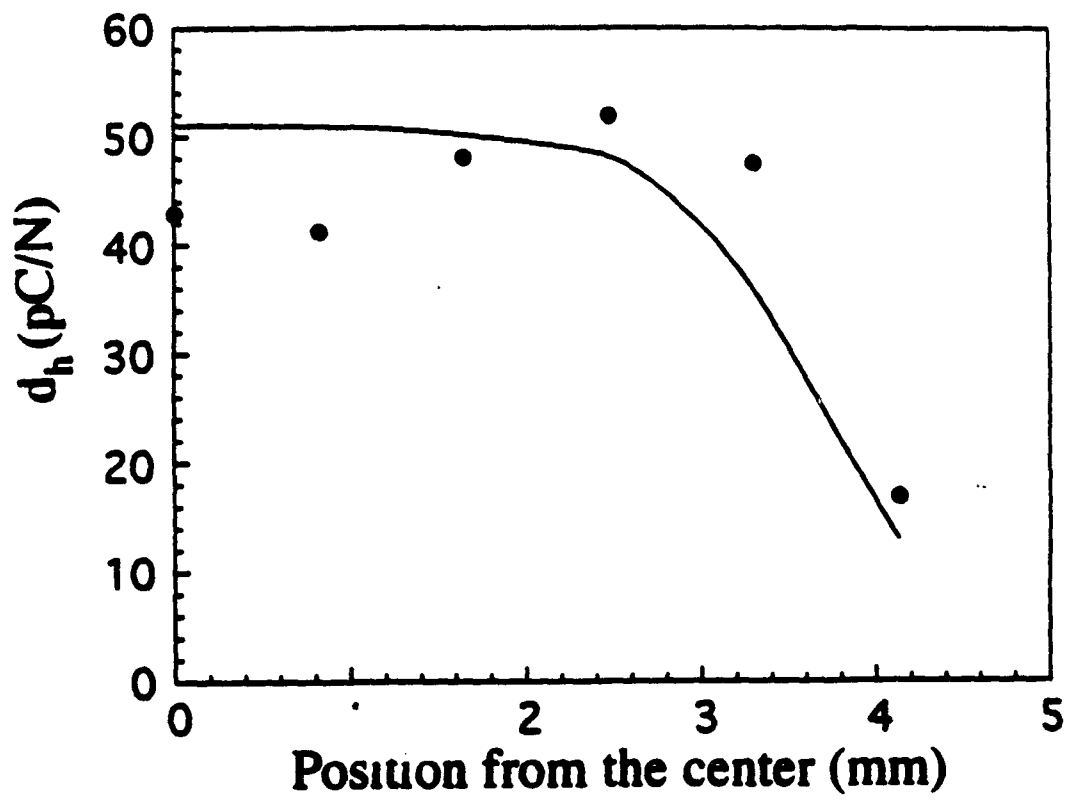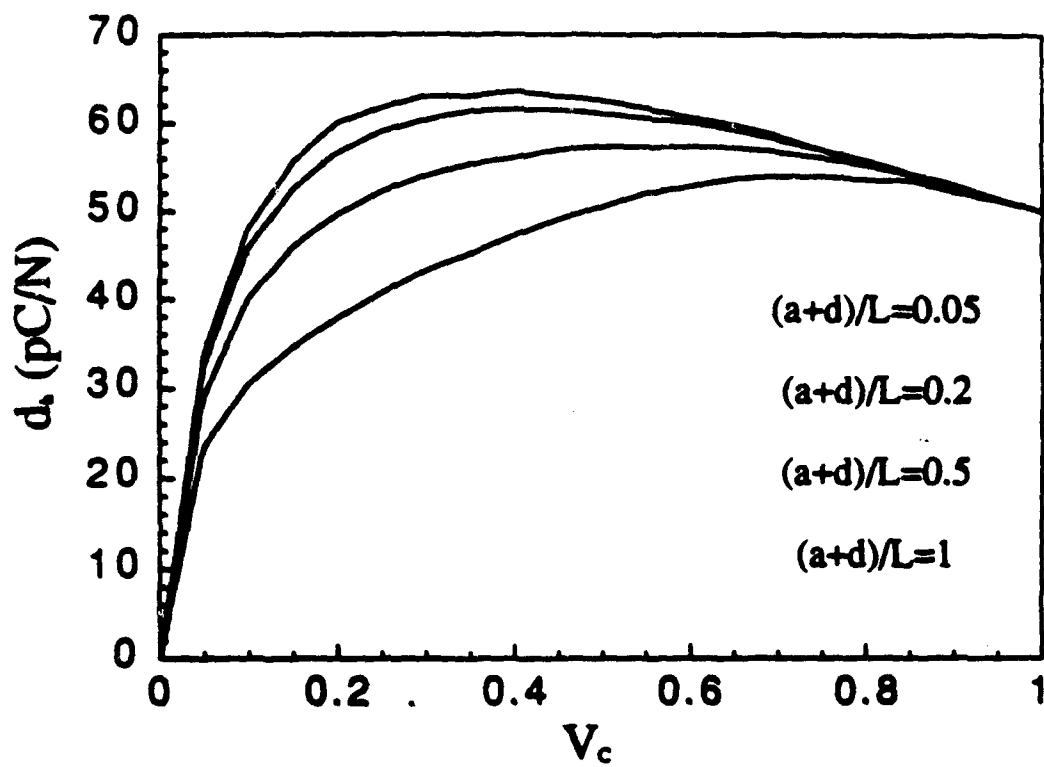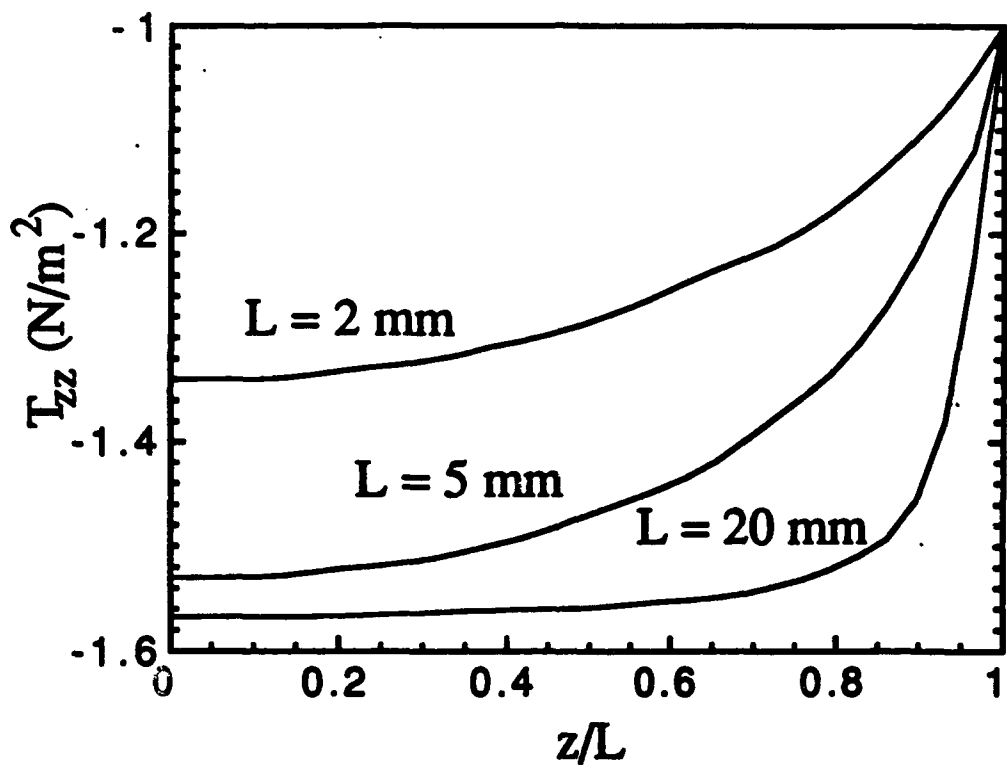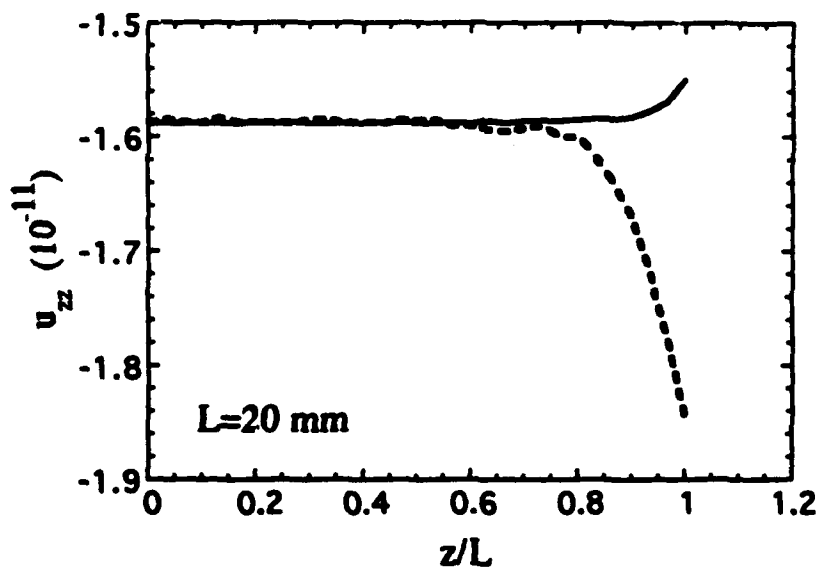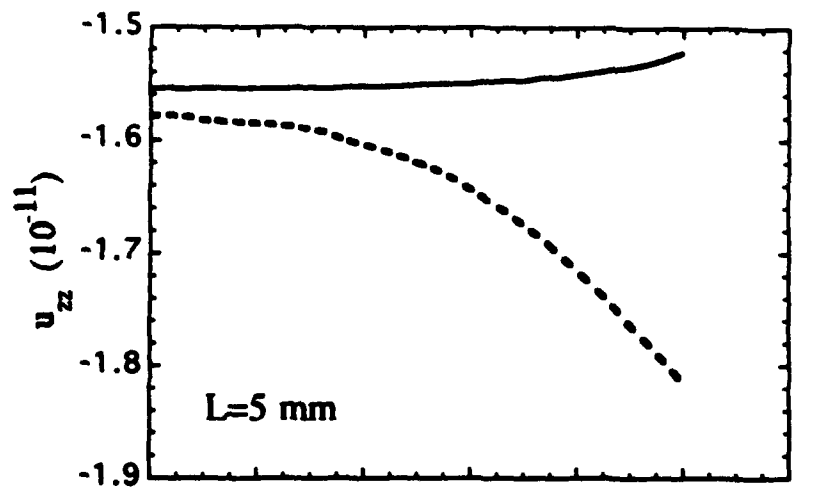
New figure 5

APPENDIX   41

Title: Modeling and Design of 1-3 Tubular Composite for Smart Transducer Applications

Authors: J. Chen, Q.M Zhang, L.E. Cross, and C. M. Trottier*

ABSTRACT

A new type of 1-3 piezocomposite has been developed recently for advanced transducer applications. The composite made of piezoelectric ceramic tubes embedded in a polymer matrix has many unique features, such as tunability on acoustic impedence and piezoelectric response. The stress analysis indicates that the elastic parameters of polymer matrix have significant effects on the performance of 1-3 tubular piezocomposites. By optimizing the structure of composite and the elastic properties of the polymer matrix, the piezocomposite has a exceptionally large hydrostatic response, d_h, and a very high receiving sensitivity. A low electric impedence and large effective piezoelectric constants suggest that the transducers in the form of the 1-3 tubular piezocomposites are superior to normal 1-3 rod piezocomposites in hydrostatic applications.

INTRODUCTION

1-3 piezocomposites have been developed for over a decade. Because of the capability of tailoring material properties, such as acoustic impedence and piezoelectric responses, in a wide range, 1-3 piezocomposites have been successfully applied in advanced transducers, including medical imaging transducers in megahertz frequency regime and underwater acoustic transducers [Garuraja, 1987]. However, when frequencies fall in kilohertz regime, namely for those applications involving imaging through air, such as autonomous vehicle guidance, manufacturing assembly, nondestructive test and vibration control, the conventional 1-3 rod piezocomposite suffers some difficulties, such as the need of a high operation voltage, high electric impedance, and that the acoustic impedance of the transducers is still too high for air transducers which substantially reduces the energy transfer efficiency. The recent developments of 1-3 piezocomposites show that the composites using piezoelectric ceramic tubes have several advantages over conventional 1-3 rod piezocomposites in these applications. Previous work [Zhang et al. 1993a] has demonstrated that because the electric field is applied in the wall thickness direction of piezoelectric tubes, the 1-3 tubular piezocomposite is able to be operated under low voltages which is desirable for low frequency transducers operated at the thickness resonance mode. In addition, the effective transverse piezoelectric constant d_{31} can be changed from negative to positive depending on the Poisson's ratio of the polymer matrix, the dimensions and piezoelectric constants as well as the volume content of the ceramic tube, while the effective longitudinal piezoelectric constant d_{33} remains substantially large. As a result, the hydrostatic coefficient, $d_h=d_{33}+2d_{31}$, becomes exceptionally large. Another advantage is

J. Chen, Q.M. Zhang and L.E. Cross
Materials Research Laboratory
The Pennsylvania State University, University Park, PA 16802.
Michael Trottier, FMI, Inc., Biddeford, Maine 04005

that ceramic tubes can be encaped with air which will significantly reduce the acoustic impedence of a composite.

The performance of 1-3 piezocomposites depends on their structural design and the component selection. There are a number of parameters which are critical to the performance of 1-3 tubular piezocomposites, such as elastic constants of the polymer matrix and ceramic tube size. Analytical studies [Smith and Auld, 1991, Zhang et al. 1993b] of 1-3 rod piezocomposites have made significant contributions to the understanding of the material responses as acoustic transducers which is also helpful in understanding the performance of tubular composites. Increasing the tunability of acoustic impedence, eliminating undesired vibration modes, and enhancing the sensitivity of the composites are the basic goals to design advanced piezocomposites for sensor and actuator applications. In this paper. we will present a detailed analysis on the effect of various design parameters on the piezoelectric responses of 1-3 tubular composites based on the results of recent theoretical and experimental investigations.

MODELING

One of the major concerns in the underwater applications is the piezoelectric response of a composite under hydrostatic condition, while in air acoustic applications, the response to the uniaxial stress is of more importance. Therefore, establishing theoretical models to simulate the stress transfer between ceramic tubes and polymer matrix under both hydrostatic and uniaxial stress conditions will help us to understand and improve the composite performance. Previous study [Zhang et al, 1993b] indicated, in 1-3 rod piezocomposites, the majority of stress transfer is concentrated in the surface regime. A rigid thin face plate is helpful to improve the stress transfer from polymer matrix to ceramic elements and reduce the self-loading effect of the composite. Therefore, face plates have to be taken into consideration in our theoretical model.

Two configurations of 1-3 tubular composites are modeled: (1) 1-3 tubular composites with homogenous polymer matrix; (2) 1-3 tubular composites with rigid face plates. In these calculations, the stress transfer between polymer matrix and ceramic tubes and surface displacement profile of the composite under different pressure conditions were evaluated. The hydrostatic piezoelectric constant (d_h), receiving sensitivity (g_h), and effective longitudinal piezoelectric constant d_{33}^e are evaluated. In these calculations, the parameters of PZT 5H piezoelectric ceramic tubes are used: d_{33} =593 x 10^{-12} m/V, d_{31}=-274 x 10^{-12} m/V, Y_{33}^E=4.8 x10^{10}N/m^2 and s_{33}^E= 21 x10^{-12} m^2/N (Mogan Matroc, Inc.).

(1) Homogenous Matrix

A 1-3 composites with a homogenous polymer matrix will be treated first. The ideal working condition of 1-3 piezocomposites is that the polymer matrix moves in phase with the ceramic component, a situation which can be described by the iso-strain model. Therefore, the iso-strain model is utilized in the following modeling. The comparison is also made with a single end capped piezoelectric ceramic tube and 1-3 rod composites.

By approximating the unit cell of 1-3 tubular composites and adopting the polar coordinate system as what shown in Figure 1, under iso-strain model , the non-zero strain components are

$$u_{rr} = \frac{\partial u_r}{\partial r}; \quad u_{\phi\phi} = \frac{u_r}{r}; \quad u_{zz} = \frac{\partial u_z}{\partial z} \tag{1}$$

The basic piezoelectric constitutive relations can be expressed as

$$T_z = c_{11} u_{zz} + c_{12} u_{\phi\phi} + c_{12} u_{rr} - e_{31} E$$

$$T_r = c_{11} u_{rr} + c_{12} u_{zz} + c_{12} u_{\phi\phi} - e_{33} E \qquad (2)$$

$$T_\phi = c_{11} u_{\phi\phi} + c_{12} u_{rr} + c_{12} u_{zz} - e_{31} E$$

where T_z, T_r, and T_ϕ are the stress components in the three directions, c_{ij} are the elastic stiffness constant, e_{ij} are the piezoelectric stress constant, and E is the applied electric field on the wall of piezoceramic tubes along the r direction. For the situation when the composite is subjected to a hydrostatic pressure P, the boundary conditions are: at $r = R$, there is no stress transfer in the r direction, $T_r = P$; at $r = r_2$, T_r is continuous through the interface; at

$r=r_1$, $T_r = 0$; and at the two surfaces normal to the z-direction, $\int_{r1}^{r2} T_z^c 2\pi r dr + \int_{r2}^{R} T_z^p 2\pi r dr$

$= \pi R^2 P$, where L is the thickness of the composite, r_1 and r_2 are the inner and outer diameters of the ceramic tube respectively. Based on these boundary conditions, one can obtain the strain components and then through equation (2), the stress components T_z, T_r. and T_ϕ. superscript c and p represent in ceramic and polymer regimes respectively.

The voltage generated by the 1-3 tubular piezocomposite under hydrostatic pressure P is

$$V_r = \int_r [g_{33}T_r + g_{31}(T_\phi + T_z)]2\pi r dr \qquad (3)$$

where g_{33} and g_{31} are piezoelectric coefficients of ceramic tubes and the integration is from $r=r_1$ to $r=r_2$.

The effective piezoelectric coefficient of piezocomposite, therefore, can be defined as

$$g_h^e = \frac{V_r}{PL} \qquad (4)$$

and
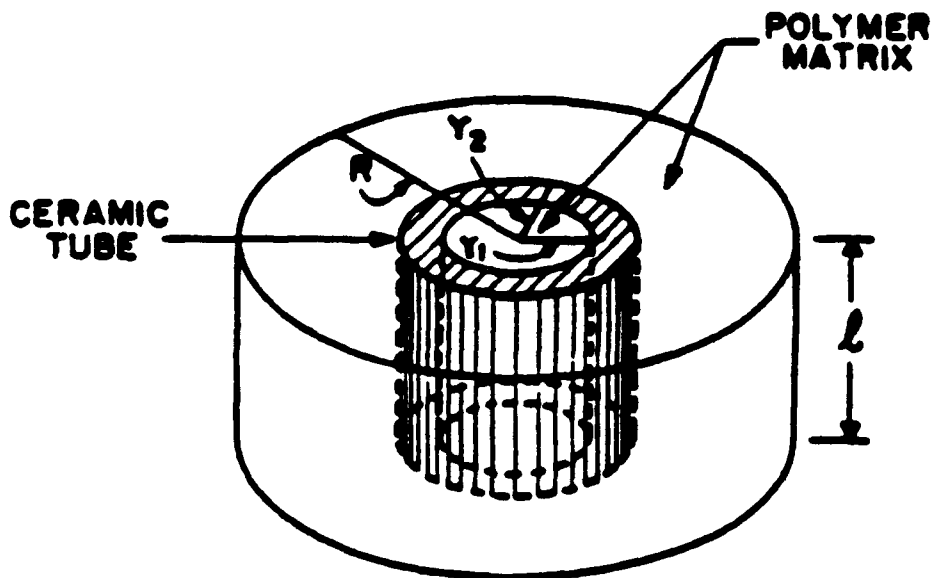
Figure 1. The schematic draw of an unit cell of 1-3 tubular piezocomposite. R, r_2 and r_1 are the radii of unit cell, tube outer and inner respectively.

$$d_h^e = g_h^e \cdot \bar{\varepsilon} \tag{5}$$

where ε is the effective permittivity of the piezocomposite, which is

$$\bar{\varepsilon} = \frac{2\varepsilon L^2}{R^2 \ln\left(\frac{r_2}{r_1}\right)} \tag{6}$$

Therefore, the effective hydrostatic piezoelectric constant d_h^e can be expressed as

$$d_h^e = \frac{2L}{PR^2 \ln\left(\frac{r_2}{r_1}\right)} \int_r [d_{33}T_r + d_{31}(T_\phi + T_z)]2\pi r dr \tag{7}$$

The equation (1), (2) and (7) are solved and the results are plotted in following figures. Figure 2a shows how the hydrostatic piezoelectric response d_h of tubular composites varies with the volume fraction of the end capped tube (r_2^2/R^2) for different Poison's ratios of the polymer matrix. Here the tube volume content in a composite is defined as r_2^2/R^2, and ceramic content as $(r_2^2-r_1^2)/R^2$, refering to Figure 1. The diameters of piezoelectric ceramic tubes in the calculation are OD(outer diameter)=0.05" and ID(inner diameter)=0.03". Young's modulus of the polymer matrix is E=4.8x10^9 (the same as that of Spurs epoxy). It is clear that the hydrostatic sensitivity d_h of 1-3 tubular piezocomposite is always lower than that of end capped piezo-ceramic tube. For a 1-3 tubular piezocomposite with Spurs epoxy matrix, d_h is decreased significantly with the tube volume fraction is reduced and at lower volume fraction, is much lower than than of the end capped tube. However, for a composite with a polymer matrix of a low Poisson's ratio, for example σ=0.15, d_h can be very close to that of the single tube, which is the d_h value at 100% volume fraction. Therefore, except for a polymer with a negative Poison's ratio, 1-3 tubular composite hydrostatic sensitivity (d_h) is always less than that of the end capped piezoceramic tube, which is different from the 1-3 rod piezocomposite. The advantage of the composite structure is to integrate tubes into a polymer matrix, which can be used for large area applications, provides lower and adjustible acoustic impedance and density, improved mechanical integrity, and possibily a larger hydrostatic figure of merit, while the reduction in d_h is small. For example, the 1-3 tubular piezocomposite of 20 % volume content and a polymer matrix of σ=0.15, hydrostatic piezoelectric constant d_h value is about 85% of that of the end capped ceramic tube, however its weight density and mechanical strength are superior to a signal ceramic tube.

The hydrostatic figure of merit of a 1-3 tubular composite, however, can be much higher than that of an end capped tube, see Figure 2b. For example, with a Poison ratio of σ=0.25, the hydrostatic figure of merit for composite in all the volume fraction is higher than that of a single tube (100% tube volume content) if the stress transfer between the tube and polymer matrix follows the isostrain model. A smaller Poisson's ratio of the polymer matrix can have a higher hydrostatic figure of merit.
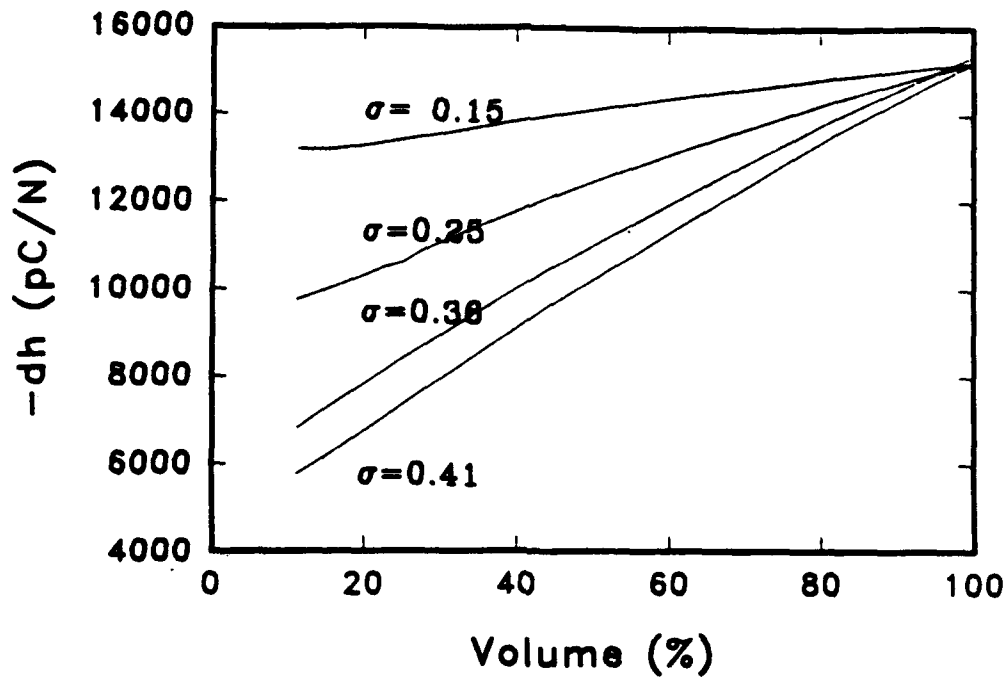
Figure 2a. Hydrostatic response of 1-3 tubular piezocomposites as a function of the tube volume content and Poisson's ratio of the polymer matrix
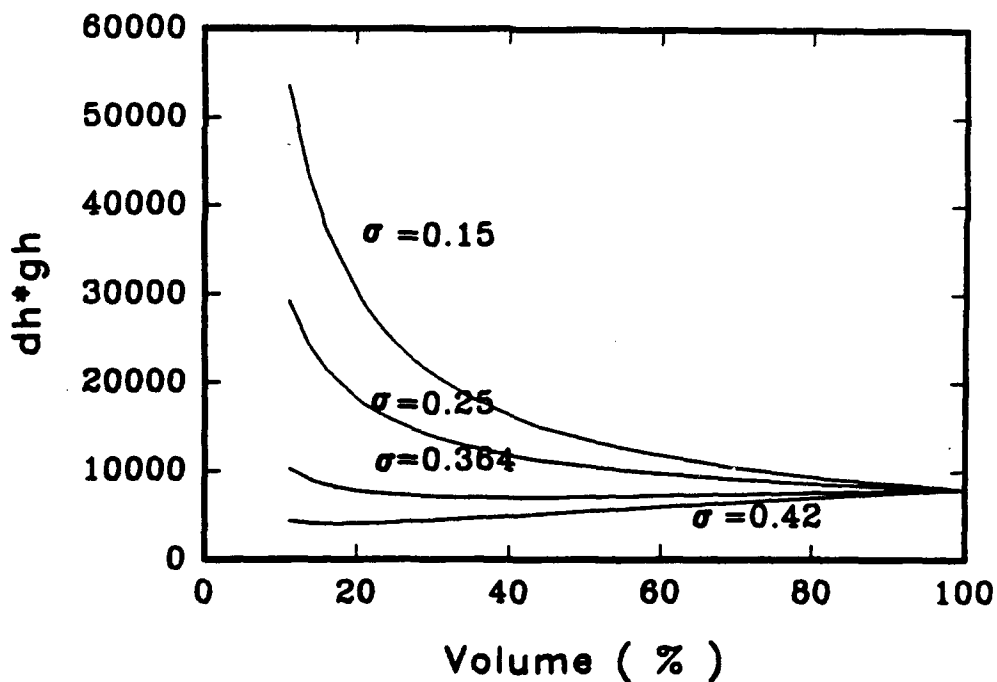

Figure 2b. The figure of merit of 1-3 tubular piezocomposites varies with the tube volume content and Poisson's ratio of the polymer matrix

A reduction on Young's module of polymer matrix can also improve hydrostatic sensitivity d_h of 1-3 tubular composite. Figure 3 shows the relationship between d_h and the Young's module of polymer matrix at different Possion's ratios. At the tube volume content considered (30%), d_h reaches its saturation value when Young's module of matrix is reduced to 10^9 N/m^2. Further reduction in the Young's modulus of the polymer matrix will not improve the hydrostatic response. Apparently, in hydrostatic case, the Possion's ratio is a more important parameter than Young's module of polymer matrix.

(2) Face Plate Case

From the analysis presented above, it is clear that a proper selection of polymer matrix can increase the hydrostatic piezoelectric sensitivity of 1-3 tubular piezocomposite significantly. On the other hand, if the aspect ratio of the ceramic tube is not very large, the stress transfer between the polymer matrix and ceramic tube will deviate from that of the iso-strain model. Hence, the performance of the 1-3 tubular composites can be improved by optimizing the composite structure. It has been demonstrated [Zhang et al , 1993b] that the stress transfer between polymer matrix and ceramic elements is non uniform in the thickness direction of 1-3 composites. The most of stress in a 1-3 composites is transferred in the surface region in the z (thickness)-direction. Therefore, a rigid polymer surface layer will offer an effective stress transfer between the polymer matrix and ceramic tubes and make it approach that of the iso-strain value. It can be expected that the combination of rigid surface layer and soft matrix will further improve the figure of merit of a 1-3 tubular piezocomposite. In addition, using a soft polymer matrix can lower the acoustic impedance, especially when the polymer matrix is in foamed structure. By controlling the porosity in the matrix, the acoustic impedence of piezocomposites and the Poisson's ration of the polymer matrix can be adjusted in a wide range .

To model the piezoelectric responses in the rigid face plate case, a thin plate elastic equation is used to calculate the displacement field on the composite surface. In the modeling, the composite is subjected to an uniaxial stress P1 in the z-axis direction. The basic equation is [Landau and Lifshitz, 1986]:

$$D \Delta^2 u - P = 0 \qquad (8)$$

where $D = \dfrac{h^3 Y}{12(1-\sigma^2)}$, h is the thickness of the face plate, Y and σ are the Young's modulus and Poisson's ratio of the face plate respectively. The stress P in the equation depends on P_1 and parameters of the composite. By solving the above equation, we can obtain the displacement field of the composite in the z-direction and then piezoelectric responses.

The displacement field at the composite surface can be divided into three regions (refer to Figure 1.):

Region i. inside the ceramic tube, $r<r_1$

$$u = a_1 + \frac{P_1}{64D} r^4 + b_1 r^2 \qquad (9)$$

Region ii. in the ceramic tube wall region, $r_1<r<r_2$

$$u = K \quad \text{(constant)} \qquad (10)$$

Region iii. outside the ceramic tube wall, $r_2<r< R$

$$u = a_2 + \frac{P_1}{64D} \sum_{i=1} \left|\vec{r} - \vec{r_i}\right|^4 + b_2 \sum_{i=1} \left|\vec{r} - \vec{r_i}\right|^2 + c_2 \sum_{i=1} \left|\vec{r} - \vec{r_i}\right|^2 \ln\left|\vec{r} - \vec{r_i}\right| + d_2 \sum_{i=1} \ln\left|\vec{r} - \vec{r_i}\right| \qquad (11)$$

where a_1, a_2, b_1, b_2, c_2, d_2 are the integration constants which can be determined from the boundary conditions: at polymer-ceramic interfaces, polymer phase has the same displacement as the ceramic phase ; at r=R, $\frac{\partial u}{\partial r} = 0$. P_1 is pressure in z-axis direction. The results are plotted in the figures 4-8.

Figure 4 shows the piezoelectric performance of 1-3 tubular composite (25% tube volume content) as a function of the elastic parameters of the polymer matrix under an uniaxial stress. Different from the hydrostatic case, the longitudinal piezoelectric response of composite is less sensitive to Poisson's ratio of the polymer matrix within 0.15-0.364 range. (The Poisson's ratio of the polymer has a large effect on the effective d_{31} coefficient of the composite.) However, the longitudinal piezoelectric response of the composite is more sensitive to the stiffness of the matrix polymer. When the stiffness of the polymer is larger than 1×10^8 N/m^2 the longitudinal piezoelectric response of the composite decreases dramatically as the stiffness of the polymer matrix increase. In the calculation, a spurs epoxy (Young's modulus is about 4.8 $\times 10^9$ N/m^2) is used as the rigid face plate with a thickness of 1 mm. It is obvious that to achieve a high piezoelectric response the face plate has to be 10 times stiffer than the matrix polymer. Figure 5 shows the relationship between the Young's modulus of the face plate and piezoelectric response of the composite. At the same tube volume content, a larger tube size requires a more rigid face plate.

As an alternative to the increasing Young's modulus of the face plate, increasing the thickness of the face plate also improves the stress transfer within the composite. Figure 6 illustrates the piezoelectric response as a function of the face plate thickness and different tube OD size. Under the same tube volume content (25% in this case), the piezoelectric response increases as the thickness of the face plate increases. there is a threshold value in the thickness of face plates, beyond this value the piezoelectric response of the composite is saturated and will not change with the face plate thickness. The composite with a smaller tube OD needs a thinner face plate to reach the threshold value. The result is not surprising because the distance between two ceramic tubes is shorter in the case of a smaller size tube than that of a larger size tube, even if they have the same tube volume content (i.e. same OD/R ratio).

Figure 7 illustrates the piezoelectric response of the composite as a function of OD of ceramic tubes with a fixed wall thickness and volume percent. The piezoelectric response of the composite varies as either the Young's modulus or the thickness of the face plate changes which gives more flexibility in the design of 1-3 tubular composites.

As we have mentioned above, the piezoelectric response of the composite is also closely related to the ceramic tube volume content. Figure 8 is a calculated result of the pieoelectric response as a function of the ceramic tube volume constant with different Young's modulus of polymer matrix. As expected, the piezoelectric response of the composite increases with the increase of the tube volume content. Therefore, in the design of a composite, there is a minimum tube volume content for a reasonable piezoelectric response. From Figure 8, we can see that this minimum value varies with the elastic properties of the polymer matrix. In the calculated region, the softedr the polymer is, the lower the minimum tube volume content can be. This may be attributed to the fact that the 1-3 tubular piezocomposite with a softer polymer matrix has a smaller self-loadir effect.

EXPERIMENTAL

To verify the results of theoretical analysis, two types of 1-3 tubular piezocomposites were fabricated: one with single polymer matrix and another with a soft polymer matrix and rigid plates on the two faces. The piezo ceramic tubes were poled in radial direction at 20 kV/cm. The piezoelectric responses of these samples were measured by laser dilatometer and hydrostatic setup. The results are described as follow:
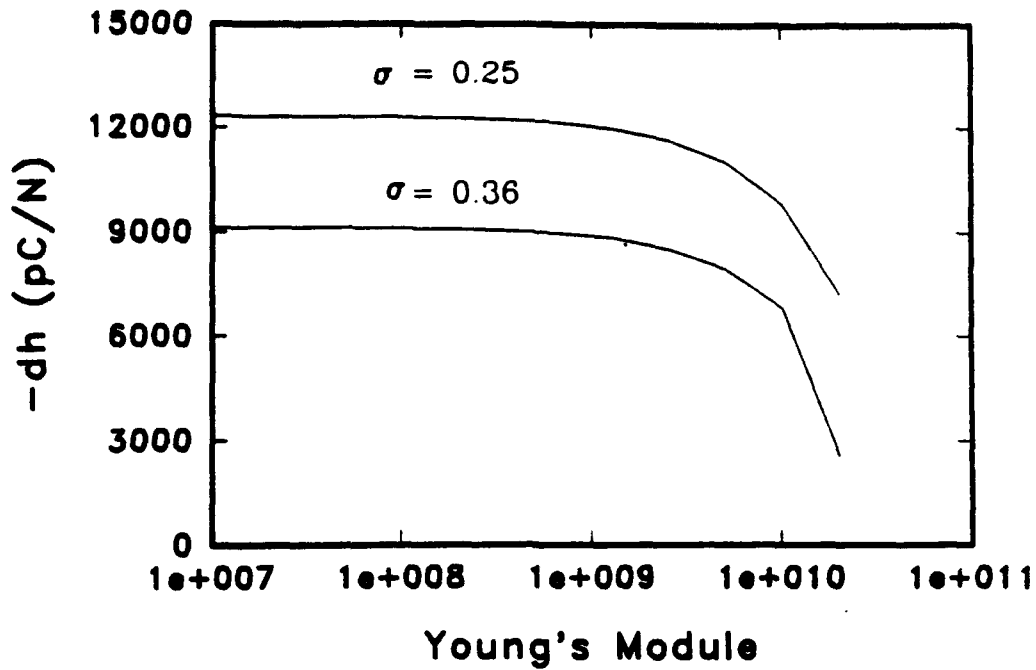
Figure 3. Hydrostatic response of 1-3 tubular piezocomposites as a function of Young's modulus and Poisson's ratio of the polymer matrix
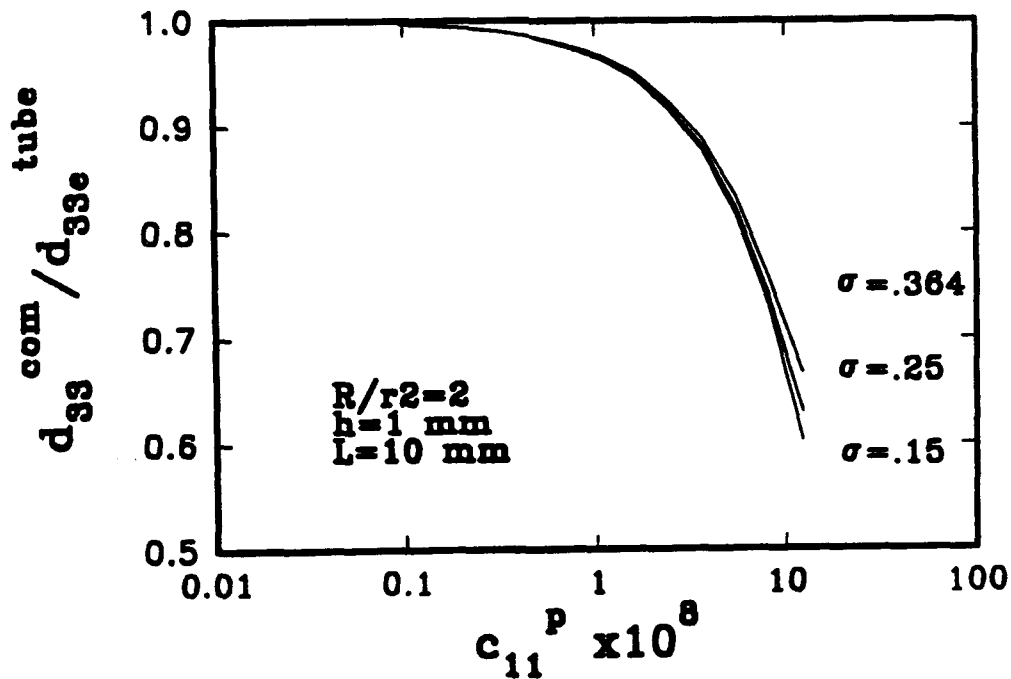

Figure 4. The longitudinal piezo response of 1-3 tubular piezocomposites varies with the stiffness and Poisson's ratio of the polymer matrix. (d_{33}^{com} and d_{33e}^{tube} are effective piezo constants of composites and tubes respectively)
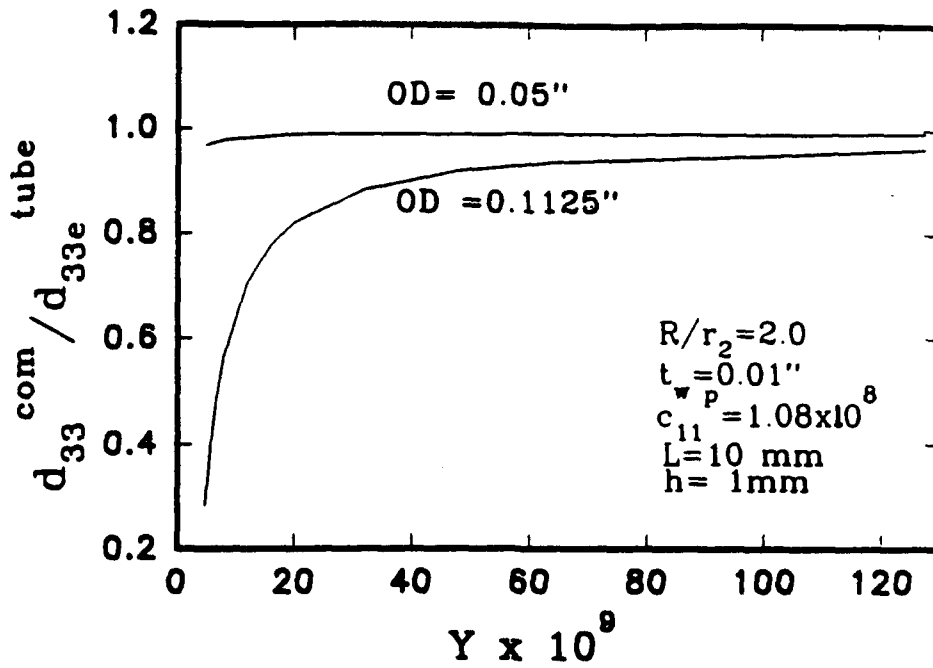
Figure 5. The longitudinal piez response of 1-3 tubular piezocomposites as a function of Young's modulus of face plates.(d_{33}^{com} and d_{33e}^{tube} are effective piezo constants of composites and tubes respectively)
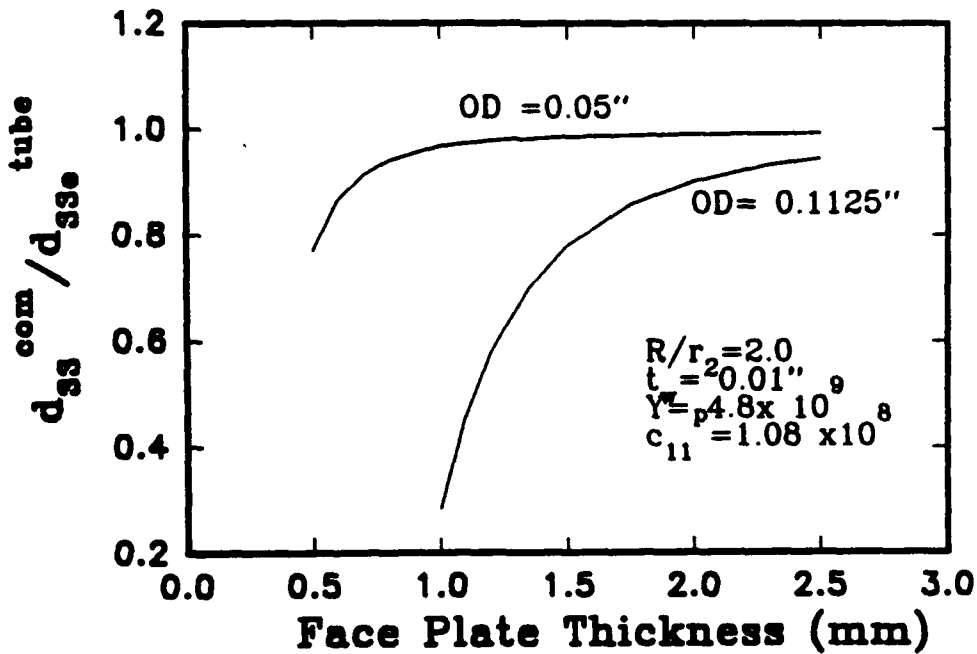
Figure 6. The longitudinal piezo response of 1-3 tubular piezocomposites varies with the thickness of face plates.
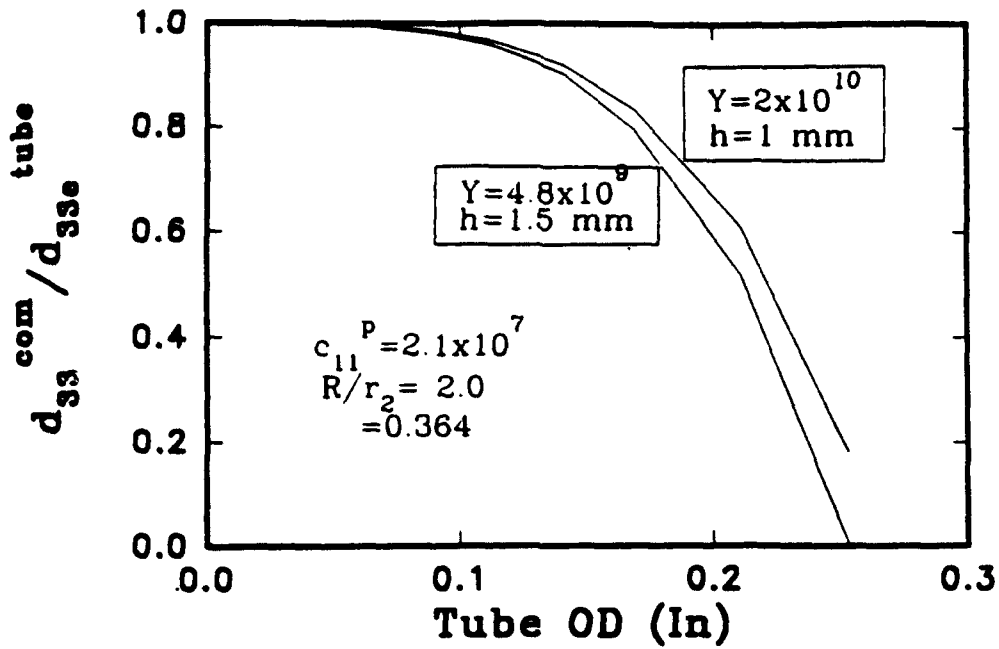
Figure 7. The longitudinal piez response of 1-3 tubular piezocomposites as a function of the outer diameter of piezo tubes.($d_{33}{}^{com}$ and $d_{33e}{}^{tube}$ are effective piezo constants of composites and tubes respectively)
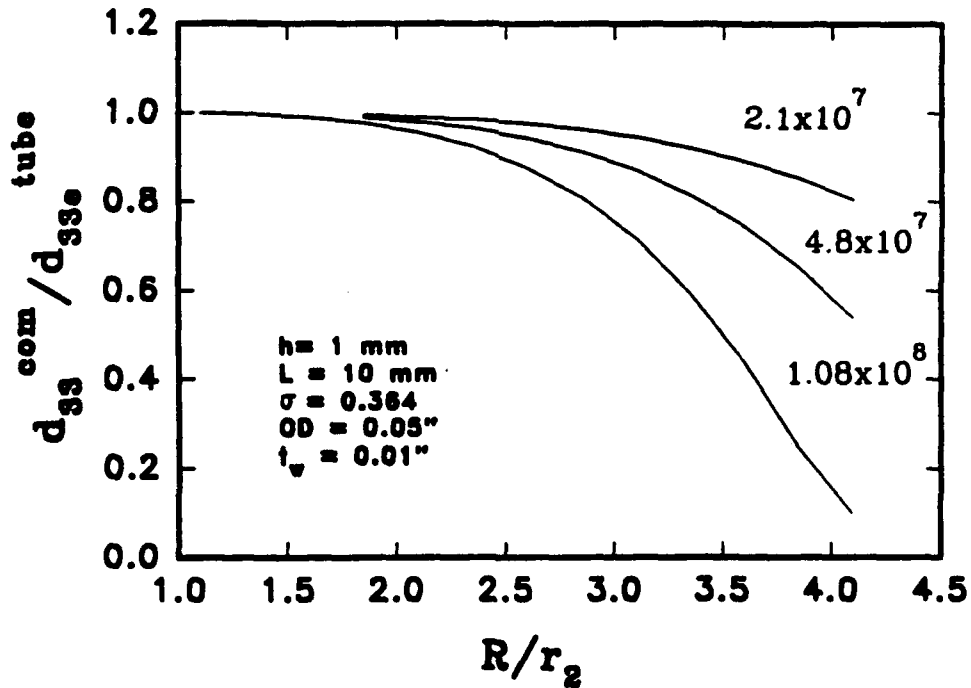

Figure 8. The longitudinal piezo response of 1-3 tubular piezocomposites varies with the volume content of ceramic tubes and the stiffness of polymer matrix.

(1) 1-3 tubular piezocomposites with a uniform polymer matrix were made with the tube content from 5% to 40%. Spurs epoxy ($\sigma=0.36$, $Y=4.8\times10^9$) and was used for the polymer matrix and PZT-5H tube with 0.05" OD and 0.03" ID were used as active phases. The results are listed in table I. For the composites of 30% and 40% tube volume content, the hydrostatic response is almost the same as that predicted by the model calculation (see figures 2a and 2b), while the d_h and $d_h g_h$ values of 5% and 20% piezocomposites are lower than the model prediction. The deviation may be attributed to the fact that, at low tube volume content, the polymer matrix does not transfer the stress as effectively as predicted by the isostrain model.

To compare the effect of polymer softness and Poisson's ratio on the hydrostatic sensitivity of tubular composites, several 1-3 tubular piezocomposites were made using both spurs epoxy (hard polymer matrix) and a soft polymer (FMI polymer) as the matrix material. For 5% ceramic tube volume content, the composite with spurs epoxy matrix has a d_h value of -1267.9 pC/N while the d_h value for the composite with FMI soft polymer matrix is -892 pC/N. The smaller dh values in the soft polymer matrix composite is attributed to the large Poisson's ratio of matrix which is consistent with the modeling. Table 1 lists the piezoelectric properties of 1-3 tubular piezocomposites with various tube volume contents.

(2) 1-3 tubular composites with rigid face plates were made with the tube content from 5% to 20%. As indicated by the theoretical calculation, a rigid surface layer can offer an effective stress transfer from the polymer matrix to the piezoelectric tubes without changing the softness of the major polymer matrix, and the soft polymer matrix can reduce the self-loading and acoustic impedence of the composite. This unique feature gives one a flexibility in designing tubular composites which have high piezoelectric activities and various acoustic impedance's. The initial combination of the samples is using spurs epoxy as face plates and foamed polyurethane as matrix. The polyurethane was foamed by 50 volume % micro balloons. The measurement shows ; ; 5% tubular piezocomposite with face plates (thickness - 1mm) has a d_h value of 1707 pC/N which is higher than the composite of a homogenous polymer matrix (1267.9 pC/N for spurs epoxy and 892 pC/N for FMI soft polymer). Based on theoretical calculations, see Figure 5, it can be expected that increasing the stiffness of the face plates and reducing the Poisson's ratio of the polymer matrix will further improve the piezoelectric performance of the composite. A 20% 1-3 tubular composite with face plate has demonstrated that d_h is 8200 pC/N under 200 Pa pressure which is also higher than that of no face plate and close to the calculated value by the iso-strain model.

As a summery, Table 2 lists some properties of several convensional piezo materials to compare with 1-3 tubular piezocomposites. It is obvious that 1-3 tubular piezocomposites have superior properties than other materials in hydrostatic transducer applications.

CONCLUSIONS

1. Poisson's ratio of polymer matrix plays a major role in the hydrostatic response of 1-3 tubular piezocomposite. A polymer matrix with lower Poisson's ratio, for example $\sigma=0.15$, can have a higher d_h value than that with a higher Possion ratio, and have a larger figure of merit than that of a single piezocreamic tube, especially, at lower ceramic tube volume content.

2. The rigid face plates can improve the pieoelectric response and reduce the acoustic impedence of the composites. The increase of face plate thickness or stiffness can improve the effective stress transfer between polymer matrix and ceramic tubes.

3. The elastic stiffness of the matrix polymer should be at least about 10 times smaller than that of the face plate to increase the piezoelectric response of the composites. Further reducing the elastic stiffness of the polymer has no advantage in the increase of the piezoelectric response, and reduces the mechanical strength of the composite. The optimium elastic stiffness of the soft polymer matrix is in the range of 10^7-10^8 m^2/N.

TABLE 1. PIEZOELECTRIC PROPERTIES OF 1-3 TUBULAR PIEZOCOMPOSITES

	d_h (pC/N)	$d_h{}^*g_h$ ($10^{-15}m^2/N$)	Effective d_{33} (pC/N)
Single Tube	-18706	11605	6800
5 % Composite	-1268	3024	3200
20 % Composite	-5630	7192	6000
30 % Composite	-8226	9917	
40 % Composite	-9862	10195	

TABLE 2. COMPARISION OF PROPERTIES OF SOME PIEZOELECTRIC MATERIALS

	PZT 5H*	PVDF	1-3 Rod Composite (20%)	1-3 Tubular Composite (20%)
Density (kg/m^3)	7500	1800	2800	2300
Permittivity	1800	10	780	290000
Loss Tangent %	2	5	3	3
d_{33} (pC/N)	593	-30	480	>6000
d_h (pC/N)	45	9	>100	>5000
$d_h g_h$ $x10^{-15}$ (m^2/N)	150	830	>2000	>6000

* PZT 5H- Mogan Matroc, Inc.

REFERENCES

Gururaja, T.R., Safari, A., Newnham, R.E. and Cross, L.E., 1987, "Piezoelectric Ceramic-Polymer Composites for Transducer Applications" pp92-128 *Electronic Ceramics*. edit by L.M. Levinson, Marcel Dekker, New York, New York.

Landau, L.D. and Lifshitz, E.M., 1986, *Theory of Elasticity*, Pergamon.

Smith, W.A. and Auld,A. 1991, "Modeling 1-3 Composite Poezoelectrics: Thickness-Mode Oscillations" IEEE Trans. on Ultra. Ferro., and Frequency Control, pp40-47, vol. 38, No.1,

Zhang, Q.M. et al., 1993a, Journal of Materials Science (28), pp3962

Zhang, Q.M. et al., 1993b, Journal of Applied Physics (73), pp1403.

APPENDIX 42

PIEZOELECTRIC RELAXATION OF P(VDF-TrFE) COPOLYMER

H. WANG, Q. M. ZHANG and L. E. CROSS
Materials Research Laboratory, The Pennsylvania State University, University Park, PA 16802, USA

Abstract   The dielectric and piezoelectric relaxations of poly(vinylidene fluoride-trifluoroethylene)(75/25) copolymer over the temperature interval of -100 to 60 °C are reported in this paper. A two-dimension model is proposed to explain the experimental results. The expressions of piezoelectric d constants from the direct and the converse effects, dielectric constant and the elastic compliances are derived as functions of the physical properties of crystalline and amorphous regions. The numerical calculations of the model are in good agreement with the experimental results.

INTRODUCTION

The studies of dielectric, mechanical and piezoelectric dispersion are important in describing the dissipation behavior of a piezoelectric material. In many applications, such as acoustic target location and multielement 360° scanning sonar transducer, the knowledge of complex piezoelectric coefficients is useful. The relaxation phenomenon is related to the microstructure of a material and, therefore, is important in understanding the structure-property relations of a material. Due to the nature of the mesoscopic morphology of semicrystalline polymers, which consist of crystalline and amorphous regions, the relationship among dielectric, elastic, and piezoelectric relaxations can be different from that of piezoelectric ceramics which has been studied relatively well.[1,2] In typical piezoelectric polymers, several relaxation mechanisms can coexist due to local mode motion, side chain motion, and segment motion of main chains, and relaxation occurs in both crystalline and amorphous regions. Piezoelectric relaxation has been studied on a number of polymeric materials.[3,4] However, for PVDF and its copolymers, the only commercialized piezoelectric polymers, information is very limited at present. Recently, we have carried out a systematic investigation of complex dielectric, elastic and piezoelectric coefficients of P(VDF-TrFE) copolymer.[5] It is found that near the glass transition temperature, the piezoelectric properties also exhibit relaxation. However, the relaxation frequency of piezoelectric coefficients is different from that of dielectric constants. This is similar to previous experimental results of other piezoelectric polymers, in which dielectric, piezoelectric and elastic relaxations occurred at different frequencies. To explain this phenomenon, a two-dimension model is proposed to derive the piezoelectric, dielectric, and elastic compliance coefficients of polymeric materials. Numerical calculations show they are in good agreement with the experiment results.

COMPLEX PIEZOELECTRIC COEFFICIENTS

The constitutive equations for a piezoelectric material are:[6]

$$D_m = d_{mj} T_j + \varepsilon_0 K_{mn} E_n \qquad (1a)$$

$$S_i = s_{ij} T_j + d_{ni} E_n, \qquad (1b)$$

where stress T_j and electric field E_n are taken as the independent variables, and electric displacement D_m and strain S_i the dependent variables, respectively; K_{mn}, s_{ij} and d_{mj} are dielectric constant, elastic compliance and piezoelectric strain coefficient of the material, respectively; ε_0 is the free space permittivity. The complex material coefficients are defined by the following equations:[7]

$$K^*_{mn} = K'_{mn} - j\, K^{\bullet}_{mn}, \quad s^*_{ij} = s'_{ij} - j\, s^{\bullet}_{ij}, \text{ and } d^*_{mj} = d'_{mj} - j\, d^{\bullet}_{mj}. \qquad (2)$$

For a homogeneous material, the piezoelectric strain coefficients d_{mj}, determined by the direct effect using Eq. (1a), is the same as that by the converse effect using Eq. (1b). However, for complex materials, such as piezoelectric polymers, this equality needs to be verified because of the complicated boundary conditions. For a material with complex coefficients, the response process of the material is not thermodynamically reversible. Although it has been shown, through the irreversible thermodynamics, that Eqs. (1) are still valid for a single phase material, it is not clear and is interesting to know whether or not, for multiphase materials, the complex piezoelectric constants measured through the direct effect and through the converse effect will be equal.

EXPERIMENTAL WORKS AND RESULTS

P(VDF-TrFE) (75/25) copolymer samples used in this study were purchased from Atochem North America Inc.. The complex piezoelectric coefficients d_{mj} of the copolymer through the converse effect were measured by a laser ultra-dilatometer.[8]


FIGURE 2 Complex dielectric constant as a function of temperature.

FIGURE 1 Complex piezoelectric coefficients as functions of temperature.

Shown in Fig. 1 are the tensile complex d coefficients thus determined as a function of temperature. For comparison, the complex dielectric constant K_{33} is shown in Fig. 2. Apparently the peak temperature of dielectric loss is different from that of imaginary part of piezoelectric constants. The complex d_{33} constant of the samples through the direct effect was measured by a high sensitivity, phase sensitive d_{33} meter that was developed recently in this laboratory.[9] The room temperature results for the copolymer are: $|d_{33}'|=31.0$ pC/N and $|d_{33}''|=0.62$pC/N, which are consistent with those measured from the converse effect within the data scattering. To our knowledge, these are the first experimental results of a complex piezoelectric coefficient from the direct and converse effects.

CALCULATION OF THE COMPLEX COEFFICIENTS

There has been a number of models to predict and explain the piezoelectric properties of PVDF type materials.[10,11] However, the observed relaxation behaviors of the copolymer can not be explained by these models. In order to understand the experimental results and to explore the interactions between crystalline and amorphous regions involved in the piezoelectric responses, a model is proposed to derive the expressions of material coefficients as functions of the properties of crystalline and amorphous regions. For simplicity, only two dimension case is considered. The material is approximated as piezoelectric crystallites dispersed in nonpiezoelectric, isotropic amorphous matrix, as shown in Fig. 3, in which the 3-direction is the polar direction. The mechanical properties of the crystalline regions are also assumed to be isotropic. Because of the nonuniformity of the material and the interaction between crystalline and amorphous regions, the material is divided into four regions. For the crystalline region, the constitutive relations of the direct and the converse effects are:

$$S_3^c = s_{11}^c(T_3 + \frac{F_3^{II}}{\beta_c}) + s_{12}^c \frac{F_\perp^I}{\alpha_c}, \tag{3a}$$

$$S_1^c = s_{12}^c(T_3 + \frac{F_3^{II}}{\beta_c}) + s_{11}^c \frac{F_\perp^I}{\alpha_c}, \tag{3b}$$

$$S_3^c = d_{33}E_3^c + s_{11}^c \frac{F_3^{II}}{\beta_c} + s_{12}^c \frac{F_\perp^I}{\alpha_c}, \tag{3c}$$

$$S_1^c = d_{31}E_3^c + s_{12}^c \frac{F_3^{II}}{\beta_c} + s_{11}^c \frac{F_\perp^I}{\alpha_c}, \tag{3d}$$

respectively, where T_3 is the external stress in the direct effect and E_3^c is the electric field on the crystalline region in the converse effect; d_{33} and d_{31} are the intrinsic piezoelectric constants of crystalline regions; F^I and F^{II} are forces applied by the region AI and AII to the crystalline region, respectively; superscript c stands for the crystalline region. Similar equations can be written for the other regions. Using the boundary conditions, which are based on the static force equilibrium and equal strains at boundaries, all these equations can be solved, and the piezoelectric constant from the direct effect $\overline{d_{33}}^d$ and from the converse effect $\overline{d_{33}}^c$, dielectric constant $\overline{K_{33}}$, and the elastic compliance $\overline{s_{11}}$ can be derived. For brevity, the detailed derivations are omitted here. The final results are:
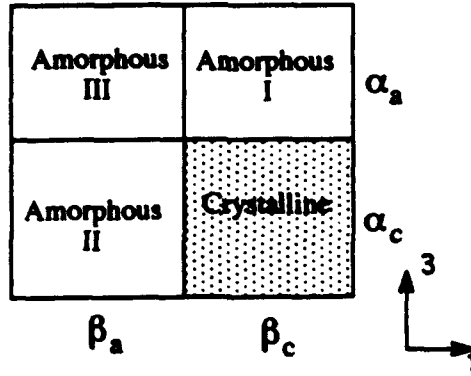
FIGURE 3   The two-dimension model.
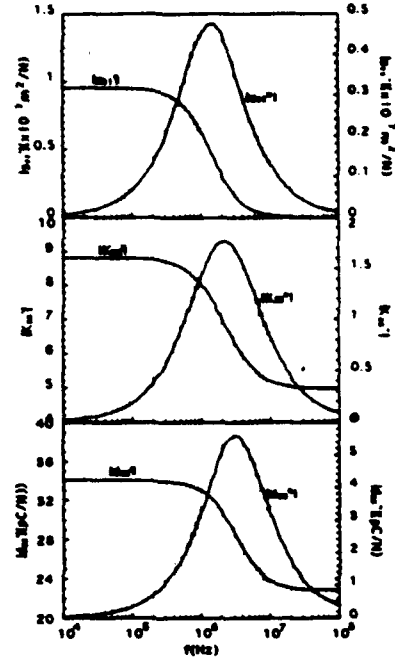
FIGURE 4   Calculated s^*, K^*, and d^* as functions of frequency.

$$\overline{d_{33}}^d = \frac{K^c\alpha_a\beta_c}{K^a\alpha_c + K^c\alpha_a}\{d_{33}\{1 + \frac{1}{AB-CD}[\frac{\beta_a}{\beta_c}\frac{1}{\alpha_a}(\frac{1}{\alpha_a}+\frac{1}{\alpha_c})(\Delta s_{12}A - \Delta s_{11}D)$$

$$-\frac{1}{\beta_c}(\Delta s_{11}B - \Delta s_{12}C)]\} + d_{31}\frac{1}{AB-CD}$$

$$[\frac{\alpha_a}{\alpha_c}\frac{1}{\alpha_a}(\frac{1}{\beta_a}+\frac{1}{\beta_c})(\Delta s_{11}B - \Delta s_{12}C) - \frac{1}{\alpha_c}(\Delta s_{12}A - \Delta s_{11}D)]\} \tag{4}$$

$$\overline{d_{33}}^c = \frac{K^a}{K^a\alpha_c + K^c\alpha_a}\frac{s_{11}^a}{\beta_a}\frac{1}{AB-CD}[(d_{31}C - d_{33}B) - \frac{\beta_a}{\sigma^a}(1 + \frac{\alpha_c}{\alpha_a})(d_{33}D - d_{31}A)] \tag{5}$$

$$\overline{K_{33}} = K^a\beta_a + \frac{\beta_c K^c K^a}{K^c\alpha_a + K^a\alpha_c} \tag{6}$$

$$\overline{s_{11}} = (\alpha_c s_{11}^c + \alpha_a s_{11}^a) + \frac{1}{AB-CD}\{[\frac{\beta_a}{\beta_c}\frac{1}{\sigma}s_{11}^c(1 + \frac{\alpha_c}{\alpha_a}) + \Delta s_{12}](\Delta s_{12}A - \Delta s_{11}D)$$

$$-[\frac{\alpha_a}{\sigma^a}\Delta s_{12}(\frac{1}{\beta_c}+\frac{1}{\beta_a}) + \frac{1}{\beta_c}(\alpha_a s_{11}^a - \alpha_c s_{11}^c)](\Delta s_{11}B - \Delta s_{12}C)\} \tag{7}$$

Where K^c and K^a are dielectric constant ⌣ ystalline and amorphous regions, respectively; $\sigma^a = -s_{12}^a / s_{11}^a$ is the Poisson ratio of amorphous regions; Δs_{ij} ($= s_{ij}^a - s_{ij}^c$) is the elastic compliance difference of amorphous and crystalline regions; A, B, C, and D are quantities depending on the mechanical properties of both crystalline and amorphous regions:

$$A = \frac{\alpha_a}{\alpha_c}(\frac{1}{\beta_c} + \frac{1}{\beta_a})\frac{1}{\sigma^a}s_{12}^c - (\frac{s_{11}^c}{\beta_c} + \frac{s_{11}^a}{\beta_a}) \tag{8a}$$

$$B = \frac{\beta_a}{\beta_c}(\frac{1}{\alpha_c} + \frac{1}{\alpha_a})\frac{1}{\sigma^a}s_{12}^c - (\frac{s_{11}^c}{\alpha_c} + \frac{s_{11}^a}{\alpha_a}) \tag{8b}$$

$$C = (\frac{s_{11}^c}{\beta_c} + \frac{s_{11}^a}{\beta_a})(\frac{1}{\alpha_c} + \frac{1}{\alpha_a})\frac{\beta_a}{\sigma^a} + \frac{1}{\alpha_c}(s_{12}^a - s_{12}^c) \tag{8c}$$

$$D = (\frac{s_{11}^c}{\alpha_c} + \frac{s_{11}^a}{\alpha_a})(\frac{1}{\beta_c} + \frac{1}{\beta_a})\frac{\alpha_a}{\sigma^a} + \frac{1}{\beta_c}(s_{12}^a - s_{12}^c) \tag{8d}$$

Similarly, piezoelectric constant $\overline{d_{31}}$ from both the direct and the converse effects and the elastic compliance $\overline{s_{12}}$ can be derived. Apparently, Eqs. (4)-(7) are too complex to reveal the physical insight of the problem. To study the relaxation behaviors of these coefficients, numerical calculations of these equations were carried out. Compared with relaxation of the properties of amorphous regions, the relaxation frequencies of dielectric and piezoelectric constants of crystalline regions could be much higher. Hence, to study the effect of glass transition that occurs in amorphous regions, we assumed relaxation only occurs in amorphous regions with Debye type:

$$s_{ij}^a(\omega) = s_{ij}^a(\infty) + \frac{s_{ij}^a(0) - s_{ij}^a(\infty)}{1 + j\,\omega\tau}, \text{ and } K^a(\omega) = K^a(\infty) + \frac{K^a(0) - K^a(\infty)}{1 + j\,\omega\tau}, \tag{9}$$

where τ is the relaxation time. The parameters used in the calculation are listed in Table I. The typical results are shown in Fig. 4 with the volume fraction of crystalline regions of 0.56.

TABLE I Parameters used in the calculations

K^{c12}	8.5	$s_{11}^c{}^{13}$	$5.0 \times 10^{-11} m^2/N$
$K^a(0)^{12}$	10.2	$s_{12}^c{}^{13}$	$-0.5 \times 10^{-11} m^2/N$
$K^a(\infty)^{12}$	3.0	$s_{11}^a(0)$	$5.0 \times 10^{-7} m^2/N$
d_{33}^5	-40pC/N	$s_{11}^a(\infty)$	$5.0 \times 10^{-11} m^2/N$
d_{31}^5	20pC/N	$s_{12}^a(0)$	$-2.5 \times 10^{-7} m^2/N$
τ^5	$1.13 \times 10^{-7} s$	$s_{12}^a(\infty)$	$-0.5 \times 10^{-11} m^2/N$
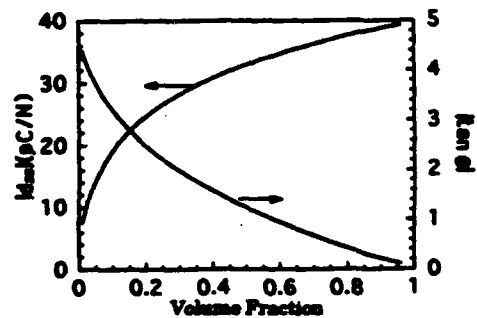
FIGURE 5 Complex d coefficient as functions of degree of crystallinity.

DISCUSSION

(1) As shown in Fig. 4, the model predicts that the relaxation peaks of dielectric, piezoelectric, and elastic coefficients can occur at different frequencies. The relaxation frequency of dielectric constant is lower than that of piezoelectric constant. Using the WLF relation, it can be deduced that in temperature domain, the relaxation peak of d

constants should occur at lower temperature compared with that of dielectric constant. This conclusion is consistent with the experimental results as shown in Figs. 1 and 2. The calculations also show the differences among three relaxation frequencies increase with the degree of crystallinity.

(2) The experimental results of dielectric constant indicate, in the temperature range of -80 to 60 °C, the only relaxation observed in this copolymer is β-relaxation, which is associated with the glass transition of non-crystalline molecules. On the other hand, for PVDF type polymeric materials, it is believed that the piezoelectricity only exists in the crystalline regions. Therefore, for the single crystal PVDF, there should be no relaxation at the glass transition temperature and frequency. The observed piezoelectric relaxation near the glass transition temperature clearly indicate that the piezoelectric response of the materials can be strongly affected by the properties of amorphous regions. Again, this confirms the results of the theoretical model in which no relaxation is assumed in crystalline regions, and relaxation behavior still occur in the piezoelectric properties of the material.

(3) Experimental evidence has shown that the piezoelectric response of polymeric materials strongly depends on the degree of crystallinity of the materials. The model predicts nonlinear relations between d_{33} constant and the volume fraction of the crystalline regions, as shown in Fig. 5. The decrease of the loss tangent is caused by the relaxation free assumption of the crystalline regions.

(4) For P(VDF-TrFE) (75/25) copolymer, the complex d_{33} coefficients measured through the direct and converse effect are equal. This result is consistent with the numerical calculations. Since this is the first and perhaps the only existing precise measurement of the complex piezoelectric coefficient, we do not intend to generalize the conclusion to other complex materials. Further theoretical and experimental studies are needed.

(5) When volume fraction of the crystalline regions is 90%, the calculated elastic compliance at low frequencies is 0.95×10^{-7} m^2/N, which is much greater than the measured compliance of the copolymer ($s_{11} = 3.32 \times 10^{-10}$ m^2/N). It is believed that this big difference is caused by the assumption that crystallite are isolated by amorphous medium. In fact, when the crystallinity is high, the model is not accurate because there must be some percolation of the crystalline regions which can significantly reduce the compliances of a material.

REFERENCES

1. G. Arlt and H. Dederichs, Ferroelectrics, 29, 47 (1980).
2. P. Gerthsen, K. H. Hardtl and N. A. Schmidt, J. Appl. Phys. , 51, 1131 (1980).
3. T. Furukawa and E. Fukada, Nature, 221, 1235 (1969).
4. M. date, S. Takashita and E. Fukada, J. Polymer Sci. A-2, 8, 61(1970).
5. H. Wang, Q. M. Zhang, L. E. Cross and A. O. Sykes, J. Appl. Phys., (1993).
6. IEEE Standard on Piezoelectricity, 176-1987.
7. R. Holland, IEEE Trans. Sonics and Ultraso. SU-14, 18 (1967).
8. W. Y. Pan, H. Wang and L. E. Cross, Jpn. J. Appl. Phys., 29, 1570 (1990).
9. H. Wang, Q. M. Zhang and L. E. Cross, Jpn. J. Appl. Phys., Accepted.
10. M. G. Broadhurst, G. T. Davis and J. E. McKinney, J. Appl. Phys., 49, 4992 (1978).
11. Y. Wada and R. Hayakawa, Ferroelectrics, 32, 115(1981).
12. S. Ikeda and M. Kutani, Jpn. J. Appl. Phys., 30, 3456 (1991).
13. K. Tashiro, M. Kobayashi, H. Tadokoro and E. Fudaka, Macromelecules, 13, 691 (1980).

APPENDIX   43

Effects of Face Plates and Edge Strips on Hydrostatic Piezoelectric Response of 1-3 Composites

J. Zhao, Q.M. Zhang*, and Wenwu Cao

Materials Research Laboratory, The Pennsylvania State University

University Park. PA. 16802

Abstract: Piezoceramic-polymer composites with 1-3 connectivity provide higher hydrostatic figure of merit $d_h g_h$ and low density, which make them attractive for underwater applications. By incorporating rigid face plates on the composite electrode surfaces, the transverse piezoelectric response can be reduced effectively and d_h increases significantly. When edge strips are put on the lateral dimensions, the hydrostatic response of the composite may be further improved, depending on the ratio of the sample thickness to the sample lateral dimensions and the elastic properties of the edge strips. In this work the effects of the rigid face plates and the edge strips on the piezoelectric response of 1-3 composites with different lateral dimensions were investigated. All the experimental features can be well accounted for by using the shear-coupling model developed recently by us and the isostrain model. Based on these results the relationship between d_h of face plated 1-3 composite and the elastic properties of the polymer matrix as well as other design parameters is derived, which can serve as a guideline to optimize the material selection for 1-3 composites with larger hydrostatic response.

Key words: composite materials, piezoelectricity

* Author to whom all the correspondence should be addressed.

1

I. Introduction

Piezoelectric ceramic-polymer composites with 1-3 connectivity possess many promising features which make them attractive for hydrostatic applications.[1-5] As has been demonstrated, both theoretically and experimentally, with a small aspect ratio of the ceramic rods and a proper ceramic content, the piezoelectric hydrostatic figure of merit $d_h g_h$ (d_h and g_h are the piezoelectric hydrostatic charge and voltage coefficients respectively) of a composite can be substantially higher than the constituent ceramic phase.[2,6] However, to fully utilize the potential of a 1-3 composite for hydrostatic applications, several issues have to be addressed. Small aspect ratio of ceramic rods will incur a high manufacturing cost and low reliability of the rods. The Poisson's ratio effect, which reduces the effective pressure on the polymer matrix in the ceramic rod poling direction by a factor of $(1-2\sigma)$ where σ is the Poisson's ratio of the polymer phase, drastically cuts down the effectiveness of the stress transfer from the polymer to the ceramic rods.[7] In the past, a great deal of efforts have been devoted to address these issues and some progress has been made. One of the effective ways to improve the hydrostatic response of a 1-3 composite is to glue rigid face plates on the two electrode surfaces, as schematically drawn in figure 1(a). Throughout this paper, the following convention will be used: the 3-direction (or the z-direction) is along the ceramic rod axial (poling) direction, the 1 and 2-directions (or x and y-directions) are in the plane perpendicular to the poling directions.

The effect of rigid face plates on a 1-3 piezocomposite can be summarized as follows: (1) it improves the stress transfer between the ceramic rods and polymer matrix in the ceramic poling direction so that the composite approaches the isostrain situation; (2) it improves the bonding between the ceramic rods and polymer matrix; (3) it reduces Poisson's ratio effect and the d_{31} effect. The effect (1) has been investigated and the results have been reported in another publication.[8] The reason for effect (2) is quite obvious. In this paper, the results of a recent investigation on effect (3) will be presented and in all the discussion, the stress transfer in the 3-direction is assumed to be that of isostrain results due to the face plates.

2

elastic stiffness of the plates is much higher than that of the composite in the lateral dimensions, most of the pressure in these directions will be born by the face plates, which reduces the effective d_{31} and d_{32} coefficients of the whole sample and increases d_h since $d_h=d_{33}+d_{31}+d_{32}$. In addition to that, the much reduced lateral pressure on the polymer matrix greatly reduces the Poisson's ratio effect.

Based on an earlier work by Wang et al.[9] to treat the clamping effect of the face plates on 1-3 composites and the isostrain model[2,3,5] to calculate the effective material properties of the composite, a theoretical treatment will be presented in this paper, which quantitatively analyzes how various parameters affect these two effects and provides a general guideline to the design of a face plated 1-3 composite.

For a face plated 1-3 composite, as shown schematically in figure 1(a), the clamping effect of the face plates in the lateral dimensions is through shear force, a situation quite similar to a 2-2 composite. As has been demonstrated earlier,[2,10] the effectiveness of this clamping effect will depend on the sample dimension, especially, the ratio of the 1-3 composite thickness t to its lateral dimension L. To evaluate this dimensional effect, experiments were carried out systematically on 1-3 composites with different ratio of t/L. The results are in excellent agreement with the theoretical calculation based on the shear coupling model.[10]

To improve the stress transfer in the lateral directions between the face plates and 1-3 composite, one can put edge strips on the end faces of the face plated 1-3 composite, as schematically drawn in figure 1(b). The effect of the edge strips on the hydrostatic response of 1-3 composite with different dimensions was also investigated and will be reported in the paper.

II. Experiments.

Two 1-3 composites with 15 % volume content ceramic rods and different polymer matrix were made and tested. The polymer matrix for the first composite (labeled as composite I) is Spurrs epoxy and the second one (labeled as composite II) is polyurethane mixed with 50 % volume of

3

properties.[11] The ceramic rods of lead zirconate titanate (PZT) used for the two composites were manufactured by CPSS Co. (MA). The composition of the rods is similar to that of PZT-5H and the diameter of the rods is 1.10 mm. The piezoelectric and dielectric properties of the PZT rods used for the two composites are also listed in table I. Both composites were poled at a poling voltage of 25 kV/cm at room temperature for three minutes.

The initial dimensions of the composite with Spurrs epoxy matrix are: $t =5.62$ mm, $L_2= 27$ mm, and $L_1=38.5$ mm. Brass plates with thickness $t=0.79$ mm were used as the face plates and J-B weld cement of J-B weld Co. was used to glue the brass plates to the composite. Glass reinforced polymer (GRP) plate ($t=1.6$ mm) and alumina plate ($t=3.5$ mm) were tested for edge strip materials. The bonding between the edge strip and face plated 1-3 composite was provided by a 5 minute epoxy of Devcon Corporation.

The initial dimensions of the composite with polyurethane mixed with 50 % microballon matrix are: $t=5.54$ mm, $L_2=35$ mm, and $L_1=52.5$ mm. Since the elastic stiffness of the polymer matrix here is much lower than that of spurrs epoxy, a GRP plate ($t=1.6$ mm) was used for the face plates. Silver epoxy (Insulating Materials Inc.) was used to glue the face plates and 1-3 composite together. For this structure, only alumina plates ($t=3.5$ mm) were used as edge strips. The elastic properties of the face plate materials as well as the plates thickness are summarized in table II.[12]

The effective dielectric constant ϵ, the piezoelectric hydrostatic charge coefficient d_h, piezoelectric d_{33} coefficients were evaluated for these composites. Surface profile scans using a double beam laser dilatometer were also made to characterize the nonuniform strain distribution in the face plated 1-3 composites.[13] The dielectric constant was measured using a HP multi-frequency RLC meter (HP 4192A). The d_h was measured by a comparison method where the test sample and a standard sample with known d_h value are subjected to the same quasi-static pressure (50 Hz) and the charge outputs from the two samples were compared. d_{33} coefficient of the samples was measured using both a Berlincourt d_{33} meter and a laser dilatometer. The effective d_{31} coefficient of the composites was evaluated using a laser dilatometer and will be discussed in detail later in the

4

The dimensional effect of face plated 1-3 composites was investigated by reducing the sample length L_1 while keeping L_2 constant. All the relevant material parameters were evaluated for samples with different L_1.

To distinguish the hydrostatic charge coefficient d_h measured for a 1-3 composite without face plates and with face plates, d_h and d_h' are used corresponding to the two situations. The same convention will also be used for the other parameters when needed.

III. Experimental results for composite I.

Shown in figure 2 is d_h^f of face plated 1-3 composite with Spurrs epoxy matrix measured at different L_1. For comparison, d_h of the composite without face plates was also measured and it is 43 pC/N. Clearly, without face plates, d_h of the composite is not any better than the ceramic rods even though its $d_h g_h$ value is improved owing to the smaller effective dielectric constant of the composite. Face plates significantly increases the hydrostatic piezoelectric response of a composite. Figure 2 also shows that d_h^f decreases drastically with decreasing L_1, which is caused by the incomplete clamping of the face plates on the 1-3 composite for samples with large t/L ratio.

If the composite is effectively clamped in the lateral dimensions by the face plates, it is expect that the whole sample will exhibit very small d_{31} and d_{32} coefficients. Figure 3(a) shows the lateral strain profiles, measured by the double beam laser dilatometer, in the 1-direction of face plated composite for different L_1 while L_2 was kept constant and the samples were driven with an electric field of 1V/m. These surface profiles are quite similar to those of 2-2 composites measured earlier, which is consistent with the fact that a 1-3 composite with face plates can be viewed as one repeating unit of a large 2-2 composite. Because of the non-uniform strain profile in the lateral directions, d_{31}^f should be calculated using the relation $d_{31}^f = \bar{S}_1/E_3$ where $\bar{S}_1$ is the averaged strain in the 1-direction and E_3 is the applied electric field in the 3-direction. The results are plotted in figure 3(b). For the composite without face plates, $d_{31} = -128$ pC/V. Evidently, the value of d_{31} is greatly reduced by the face plates especially when t/L_1 is small. As L_1 decreases, the clamping effect of

· 5

face plates becomes less effective which leads to the rapid increase of d_{31}^f.

In practice, a face plated 1-3 composite may not reach the limit $t/L \rightarrow 0$ for which d_h^f reaches maximum. Therefore, it is useful to know how much d_h^f of a face plated 1-3 composite is off from its limiting value. From our earlier work on 2-2 composites,[10] it can be shown that both d_h and d_{31} follow approximately a linear relationship with t/L. Indeed, the data here, when plotted against t/L_1, fall on a straight line, as shown in figure 4. Hence, the limiting value of d_h^f and d_{31}^f can be extrapolated from the figure. For this composite structure, in the $t/L_1 \rightarrow 0$ limit, d_h^f should reach 180 pC/N and d_{31}^f -15.5 pC/N. Since this d_h^f value is for the sample with L_2=27 mm, in the limit of both t/L_1 and $t/L_2 \rightarrow 0$, d_h^f should be above 200 pC/N. For the sample investigated, at L_1=38.5 mm and L_2=27 mm d_h^f value is 160 pC/N, which is already about 80 % of the limiting value.

To improve the clamping effect of the face plates on 1-3 composites, edge strips were added on this face plated composite. Shown in figure 5 are the comparison of strain profiles of the sample of t/L_1=0.196 with and without edge strips. Two different edge strips were used here, one is GRP plate (thickness=1.6 mm) and the other is alumina plate (thickness=3.5 mm). It is evident that the edge strips improve the uniformity of the strain profiles. For the alumina plates, the measured d_{31} value is -18.5 pC/N, which is very close to the limiting value of d_{31}^f at $t/L_1 \rightarrow 0$. However, the effect of GRP plates is much smaller due to its relatively lower elastic stiffness and small thickness.

The comparison of the hydrostatic charge coefficient d_h between the three configurations (without edge strips, with GRP edge strips, and with alumina edge strips) is shown in figure 2. The effect of GRP edge strips is not significant. When an edge strip is used in face plated composite structure, it will influence the composite response in two opposite ways. On one hand, it reduces d_{31} for samples with finite ⁀ ., hence enhances d_h. On the other hand, it will clamp the composite in the 3-direction in the region near it, which leads to the reductions of d_{33} and d_h. This latter effect is illustrated in figure 6 where the surface profiles in the ceramic poling direction (the 3-direction) for face plated composite with and without edge strips are compared. The interface between the edge strip and the face plated composite is located at x=0. Due to the cancellation of the two competing effects, the GRP edge strips do not change d_h very much as has been shown in

6

figure 2. In the limit of $t/L \rightarrow 0$, the three configurations should yield the same d_h. That is, as far as the hydrostatic response is concerned, the edge strips do not make much difference when t/L is very small. However, the edge strips do have the effect of reducing shear stress concentration at the side boundaries of the face plate-1-3 composite interface, which improve the mechanical integrity of the composite structure.

IV. Experimental results for composite II.

The polymer matrix of polyurethane mixed with microballoon has much smaller Young's modulus and Poisson's ratio compared with Spurrs epoxy as listed in table I. Without face plates, the composite II has a d_h of 45 pC/N and a d_{31} of -130 pC/N. Although softer polymer matrix reduces the polymer self-loading, the much reduced shear modulus of the polymer matrix also reduces the stress transfer between the polymer matrix and ceramic rods resulting in a small d_h. With GRP face plates, d_h value is increased significantly as shown in figure 7(a). Similar to the composite I, d_h^f also exhibits a strong t/L_1 dependence. The dimensional dependence of d_{31}^f was also measured and is plotted in figure 7(b). Though d_{31}^f value here is comparable to those of composite I, d_h^f is clearly much higher for the composite with a soft polymer matrix. As will be shown later in the paper, this increase is due to the reduction in the polymer matrix self-loading which produces a higher effective stress level in the ceramic rods.

The influence of 3.5 mm thick alumina edge strips on the hydrostatic response of this face plated composite is also shown in figure 7(a). The improvement of the edge strips on this face plated composite is only about 10% at most. This is the result of edge strip clamping on d_{33} response of the composite since with a soft polymer matrix, the elastic stiffness in the 3-direction is much smaller than that of the edge strips and the effect of clamping in the 3-direction will be more severe in composite II.

For composite II, the plots of d_h^f and d_{31}^f as a function of t/L_1 did not fall on a straight line. It was also found that the dielectric constant and piezoelectric constant d_{33}^f of the sample decreased as the sample dimension L_1 decreases. All these are quite different from the results of composite I.

7

Careful inspection on composite II reveals that some PZT rods in the composite were broken when the sample was recycled during the hydrostatic measurement and during the cutting process to reduce L_1. To correct this, the dielectric constant ε of individual PZT rods was measured and the data is used to calculate the percentage α of the broken rods in the samples by assuming the sample dielectric constant do not depend on the sample lateral dimensions if no ceramic rod is broken in the sample. Using this method, the measured d_{33}^f, d_h^f and d_{31}^f were corrected by dividing them by the factor of $(1-\alpha)$ at the corresponding L_1 value. After this correction, d_{33}^f becomes almost independent of the sample lateral dimension as we have expected. The results after the correction for d_h^f and d_{31}^f are plotted in figure 8 and indeed, the data follow a linear relationship with $1/L_1$. From the linear extrapolation, the limiting values of d_h^f and d_{31}^f at $1/L_1 \rightarrow 0$ are obtained and they are 440 pC/N and -6.6 pC/N respectively. Therefore, the hydrostatic figure of merit for this configuration can be as high as $50,600*10^{-15}$ m^2/N.

In table III, the values of d_h, d_{31}, d_h^f, d_{31}^f, measured at smallest t/L_1 ratio, and the values of d_h^f, d_h^f at $t/L_1 \rightarrow 0$, as well as the hydrostatic figure of merit for the two composites are listed. Needless to say, the exceptionally high $d_h g_h$, high d_h, light weight, and relative easiness of manufacturing face plated 1-3 composites make them superior compared with currently available hydrophone designs.

V. Theoretical treatment of clamping effect of face plates on 1-3 composites

From the experimental results in the sections III and IV, it is clear that in order to have a high hydrostatic response of a face plated 1-3 composite, a polymer matrix with a low Young's modulus is preferred. On the other hand, a 1-3 composite made of soft polymer matrix such as foamed polyurethane used here has the problem of low mechanical integrity, which may result in failure of a device. In practice, one has to balance these two effects. In this section, we will present a theoretical treatment which relates various design parameters to the hydrostatic response of a face plated 1-3 composite.

Clamping effect of stiff face plates on a soft piezoelectric material has been analyzed by Wang et

8

$$d^f_{31} = d^f_{32} = \frac{\overline{d_{31}}}{1 + \frac{2(\overline{s_{11}} + \overline{s_{12}})}{\gamma(s^b_{11} + s^b_{12})}} \qquad (1)$$

$$d^f_{33} = \overline{d_{33}} + \frac{\overline{s_{13}}(d^f_{31} + d^f_{32} - 2\overline{d_{31}})}{\overline{s_{11}} + \overline{s_{12}}} \qquad (2)$$

$$d^f_0 = \overline{d_{33}} + \overline{d_{31}}\frac{2\gamma(s^b_{11} + s^b_{12}) - 4\overline{s_{31}}}{\gamma(s^b_{11} + s^b_{12}) + 2(\overline{s_{11}} + \overline{s_{12}})} \qquad (3)$$

where the quantities on the left hand side of the equations are those for the face plated samples. The quantities with a bar on the top (such as $\overline{d_{31}}$) on the right hand side of the equations are those for the soft piezoelectric material and the superscript b refers to the face plate. $\gamma = \frac{t}{t^b}$ is the thickness ratio of the piezoelectric material to the face plate. Equations (1), (2), and (3) are derived under the condition that the lateral strains in the face plate and the soft piezoelectric material are equal, a situation corresponds to t/L→0 limit here.

To use these equations for the face plated 1-3 composite, the effective material properties have to be evaluated. Though the behavior of composites without face plates can be quite different from that calculated based on the isostrain model, it is shown that the difference of the strain profile between the polymer and ceramic rods in the 3-direction becomes very small for composites with thick face plates, and the composite can be treated using the isostrain model.[8]

The basic assumption for the isostrain model used here is that the strains in both the polymer and ceramic rods in the 3-direction are equal while the stresses in the 1- and 2-directions in the two constituents are the same. Based on these assumptions, it can be derived

$$\overline{d_{33}} = \frac{D}{T_3} = \frac{V^c s^p_{33} d^c_{33}}{V^c s^p_{33} + (1 - V^c) s^c_{33}} \qquad (4)$$

$$\overline{s_{33}} = \frac{S_3}{T_3} = \frac{s^p_{33} s^c_{33}}{V^c s^p_{33} + (1 - V^c) s^c_{33}} \qquad (5)$$

where the superscripts p and c refers to the polymer and ceramic, respectively.

Assuming the sample is subjected to a stress T_1 in 1 or 2 direction, from the constitutive

9

relations and isostress assumption, one can get

$$S_3^c = s_{33}^c T_3^c + s_{13}^c T_1 \qquad (6)$$

$$S_1^c = s_{11}^c T_1 + s_{13}^c T_3^c \qquad (7)$$

$$S_2^c = s_{12}^c T_1 + s_{23}^c T_3^c \qquad (8)$$

For the polymer phase, similar equations can be obtained by simply replacing superscript c by p. Further more,

$$V^c T_3^c + (1-V^c) T_3^p = 0 \qquad (9)$$

$$\overline{D_3} = d_{33}^c T_3^c V^c + d_{31}^c T_1 V^c \qquad (10)$$

$$\overline{S_2} = V^c S_2^c + (1-V^c) S_2^p \qquad (11)$$

$$\overline{S_1} = V^c S_1^c + (1-V^c) S_1^p \qquad (12)$$

Solving these equations yield:

$$\overline{s_{13}} = \frac{\overline{S_3}}{T_1} = \frac{s_{33}^c s_{13}^p (1-V^c) + V^c s_{11}^p s_{13}^c}{V^c s_{33}^p + s_{33}^c (1-V^c)} \qquad (13)$$

$$\overline{s_{11}} = (1-V^c)\left[s_{11}^p + s_{13}^p (s_{13}^p - s_{13}^c) V^c c_a\right] + V^c\left[s_{11}^c - s_{13}^c (s_{13}^p - s_{13}^c)(1-V^c) c_a\right] \qquad (14)$$

$$\overline{s_{12}} = (1-V^c)\left[s_{12}^p + s_{13}^p (s_{13}^p - s_{13}^c) V^c c_a\right] + V^c\left[s_{12}^c - s_{13}^c (s_{13}^p - s_{13}^c)(1-V^c) c_a\right] \qquad (15)$$

$$\overline{d_{31}} = d_{33} V^c c_a\left[s_{13}^c (s_{13}^p - s_{13}^c)(1-V^c)\right] + d_{31} V^c \qquad (16)$$

where $c_a = 1/((1-V^c) s_{33}^c + s_{11}^p V^c)$. From these relations, d_h^f and d_{31}^f are calculated for the two composite structures investigated. Some of the material parameters used for the calculations have been listed in tables I and II and the elastic compliance data for PZT-5H are used for the ceramic rods, which are listed in table IV. ($\gamma=7.1$ for spurrs epoxy composite and $\gamma=3.46$ for polyurethane composite). The calculated results for the composite with Spurrs epoxy matrix (composite I) are, $d_h^f = 171$ pC/N and $d_{31}^f = -17.6$ pC/N; and for the composite with foamed polymer matrix (composite II), $d_h^f \approx 480$ PC/N and $d_{31}^f = -0.2$ PC/N. These values are in very good agreement with the experimental data when extrapolated to t/L_1 and $t/L_2 \rightarrow 0$ limit. It indicates that the theoretical results here provide quite accurate prediction on the hydrostatic response of a face plated 1-3 composite.

10

From the above equations, the relationship between the hydrostatic response of a face plated 1-3 composite and s_{11}^P and σ of the polymer can be derived:

$$d_h^f = d_{33}s_{11}^P V^c c_a + [V^c d_{31} - V^c(1-V^c)d_{33}c_a(s_{13}^c + \sigma s_{11}^P)]$$
$$\left\{ \frac{2\gamma(s_{11}^f + s_{12}^f) - 4c_a[V^c s_{11}^P s_{13}^P - s_{33}^c \sigma s_{11}^P(1-V^c)]}{\gamma(s_{11}^f + s_{12}^f) + 2[V^c(s_{11}^c + s_{12}^c) + (1-V^c)s_{11}^P(1-\sigma) - 2V^c c_a(1-V^c)(s_{13}^c + \sigma s_{11}^P)^2]} \right\} \quad (17)$$

Figure 9(a) shows the dependence of d_h^f on s_{11}^P for three different Poisson's ratio of the polymer matrix: $\sigma = 0.15$, 0.3, and 0.4. GRP is used here as face plates. The ceramic used in the calculation is PZT-5H.[14] The ceramic rods content of 15% and a γ of 3.5 are used in the calculation. From figure 9(a), it is clear that the effect of the Poisson's ratio of the polymer phase on d_h^f depends critically on the elastic compliance of the polymer. When the elastic compliance of the polymer matrix is below, for example, $5*10^{-8}$, there is little change in d_h when the Poisson's ratio is increased from 0.15 to 0.4. However, a drastical decrease of d_h^f with σ occurs for polymers with smaller elastic compliance. Further more, there is not much decrease in d_h^f when s_{11}^P is reduced from $5*10^{-8}$ (close to the value of the foamed polyurethane used for the composite II) to $5*10^{-9}$, a polymer ten times hard than the polymer matrix used for the composite II. With an elastically stiffer polymer matrix, the mechanical integrity of the device is improved significantly while there is not much loss in the hydrostatic response. This illustrates that for a composite with a polymer matrix ten times stiffer than the polymer matrix for the composite II, there is little reduction in the hydrostatic figure of merit while there is a substantial increase in its mechanical integrity. Apparently, spurrs epoxy is not a suitable choice either for the polymer matrix for the face plated 1-3 composite discussed here.

Figure 9(b) shows the dependence of d_h^f on s_{11}^P with different ratio γ (thickness ratio of 1-3 composite to the face plate) with $\sigma = 0.3$ for the polymer matrix, which should provide valuable information on the selection of face plate thickness in reference with the thickness of 1-3 composite.

VI. Summary.

The hydrostatic response of a 1-3 composite can be significantly increased by using face plates

11

to (1) improve the stress transfer in the 3-direction; (2) reduce the Poisson's ratio effect and d_{31} effect; (3) improve the mechanical integrity of the composite structure. In this paper, we show that for a face plated 1-3 composite with a soft polymer matrix and 15% ceramic rod content, its hydrostatic figure of merit $d_h g_h$ can reach more than $50,000*10^{-15}$ (m^2/N). However, due to the nature of the shear coupling between the face plates and 1-3 composite, the hydrostatic response of a face plated 1-3 composite will depend on the sample lateral dimensions. The hydrostatic response will increase as the ratio of the thickness to the lateral dimension (t/L) becomes small, for a large t/L ratio, improvement of the hydrostatic response due to the face plates is not significant. One possible method to increase d_h for samples with a large t/L ratio is to use edge strips. However, the study here shows that the effect is not significant due to the two opposite roles an edge strip plays on a face plated 1-3 composite. Therefore, the key to increase hydrostatic response is to use small t/L ratio for a face plated 1-3 composite.

To balance the requirement of high hydrostatic sensitivity and mechanical integrity, a proper polymer matrix with the right elastic properties should be used. In the paper, we showed that the two face plated composites tested represent the two extreme cases with the Spurrs epoxy matrix on the hard side and the polyurethane with 50% microballon on the soft side of the polymer matrix spectrum. A polymer matrix with its elastic properties in between the two would be a good choice to balance the two requirements as mentioned above. In general, the theoretical results presented here can provide a useful guideline for the optimum design of face plated 1-3 composites.

VII. Acknowledgment.

Table I. Some properties of the polymer matrix and PZT rods for the two composites

	s_{11}^P (m^2/N)	σ^P	$d_{33}(pC/N)$	$d_{31}(pC/N)$	ε
Composite I	$2*10^{-10}$	0.36	450	-208	2333
Composite II	$5*10^{-8}$	0.2	481	-222	2533

Table II. Properties of face plates

	t (mm)	s_{11} (m^2/N)	s_{12}
GRP	1.6	$2.63*10^{-11}$	$-0.789*10^{-11}$
Brass	0.79	$0.97*10^{-11}$	$-0.32*10^{-11}$

Table III. Summary of the properties of the two composites

	d_{31} (pC/N)	d_h	d_{31}^f	d_h^f	d_{31}^f (limit)	d_h^f(limit)	$d_h^f g_h^f$ (limit) (m^2/N)
Composite I	-128	43	-34.8	154	-17	181	7378 (10^{-15})
Composite II	-130	45	-23.9	414	-6.6	438	50,600 (10^{-15})

* d_{31} and d_h are for 1-3 composite without face plates, d_{31}^f and d_h^f are for 1-3 composites with face plates at their initial dimension, d_{31}^f (limit) and d_h^f(limit) are taken from figures 4 and 8.

References:

1. R. E. Newnham, D. P. Skinner, and L. E. Cross, Mat. Res. Bull. 13, 525 (1978).

2. K. A. Klicker, Ph. D. Thesis, The Pennsylvania State University, 1980.

3. T. R. Gururaja, Ph. D. Thesis, The Pennsylvan tate University, 1984.

4. W. A. Smith and B. A. Auld, IEEE Trans. UFFC, 38, 40 (1991).

5. M. J. Haun and R. E. Newnham, Ferroelectrics 68, 123 (1986).

6. Wenwu Cao, Q. M. Zhang, and L. E. Cross, J. Appl. Phys. 72, 5814 (1992).

7. Q. M. Zhang, Wenwu Cao, H. Wang, and L. E. Cross, Proc. IEEE ISAF8 252, (1992).

8. Wenwu Cao, Q. M. Zhang, J. Zhao, and L. E. Cross, Preprint and to be published.

9. H. Wang, Q. M. Zhang, L. E. Cross, and A. O. Sykes, Submitted to Ferroelectrics (1993).

10. Q. M. Zhang, Wenwu Cao, J. Zhao, and L. E. Cross, Submitted to IEEE Trans. UFFC. (1993).

11. C. G. Oakley, Ph. D. Thesis, The Pennsylvania State University, 1991.

12. CRC Handbook of Chemistry and Physics, CRC Press, Inc. 1980-1981.

13. Q. M. Zhang, S. J. Jang, and L. E. Cross, J. Appl. Phys. 65, 2808 (1989).

14. PZT-5H is the trade mark of Mrogan Matric Inc., Vernitron Div. for its La doped PZT. From the data sheet, $d_{33}=593(pC/N)$, $d_{31}=-275$, $s_{11}=1.65*10^{-11}(m^2/N)$, $s_{12}=-0.478*10^{-11}$, $s_{33}=2.08*10^{-11}$, $s_{13}= - 0.845*10^{-11}$.

Figure captions:

Figure 1. (a) Schematic drawing of a face plated 1-3 composite; (b) schematic drawing of a face plated 1-3 composite with edge strips at two end faces in the 1-direction.

Figure 2. The hydrostatic charge coefficient of composite I (Spurrs epoxy matrix) as a function of the sample lateral dimension L_1. Curve 1 is for the composite without edge strips, curve 2 is for the composite with alumina edge strips, and curve 3 is for the composite with GRP edge strips. Solid lines are drawn to guide eyes.

Figure 3. (a) The lateral strain S_1 profile of the composite I under 1 V/m driving electric field for different t/L_1 ratio. The label for each curve is the ratio t/L_1. The incomplete clamping of the face plates on 1-3 composite is reflected by the non-uniform strain profile of S_1; (b) The dependence of d_{31}^f on the sample lateral dimension L_1.

Figure 4. The linear relationship between d_h^f, d_{31}^f and $1/L_1$.

Figure 5. The comparison of the strain profile S_1 for the face plated composite I at $t/L_1=0.196$. Curve a is for the composite with alumina edge strips, curve b is for the composite with GRP edge strips, and curve c is the one without edge strips. The composites were driven under 1V/m electric field.

Figure 6. The effect of edge strips on the longitudinal strain S_3. For the comparison, S_3 for the composite without edge strips is shown in curve a. Curve b is for the composite with GRP edge strips and curve c is for the alumina edge strips. The interface between the face plated composite and edge strip is at $x=0$.

15

Figure 7. (a) The dependence of d_h^f on the sample lateral dimension L_1 for the composite II. Curve a is for the composite without edge strips and curve b is that with alumina edge strips. (b) The dependence of d_{31}^f on the sample lateral dimension L_1 for the composite II.

Figure 8. The modified d_h^f and d_{31}^f (corrected for the broken rods in the composite) as a function of $1/L_1$.

Figure 9. (a) The dependence of d_h^f of a face plated 1-3 composite, which has 15% PZT 5H rod content and GRP face plates with $\gamma=3.5$, on the compliance s_{11} of the polymer matrix. Three Poisson's ratios are used: $\sigma=0.15, 0.3,$ and 0.4 as labeled on the figure. The curves are calculated using equation (17); (b) The dependence of d_h^f of a face plated 1-3 composite, which has 15% PZT 5H rod content and GRP face plates, on the compliance s_{11} of the polymer matrix for different γ (the thickness ratio of the face plate t_b and the 1-3 composite t).

16

(a)

(b)

Fig. 2

(a)

0.16   0.24   0.49

Position Z (mm)

Lateral Strain -S_1 (10^{-12})

(b)

$-d_{31}^f$ (pC/N)

Lateral dimension L_1 (mm)
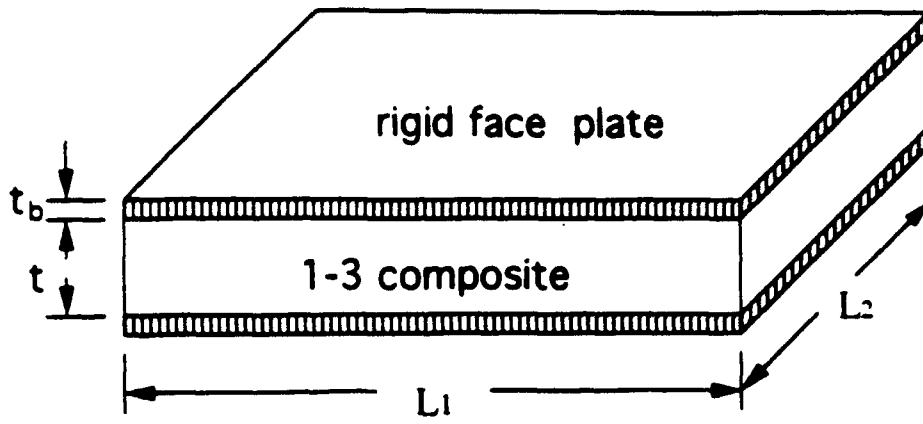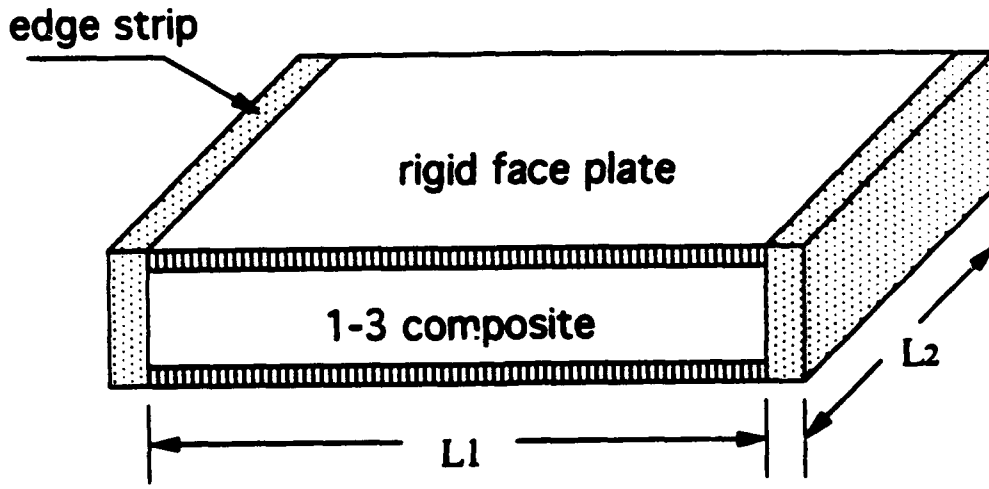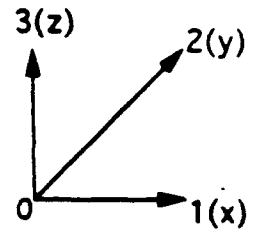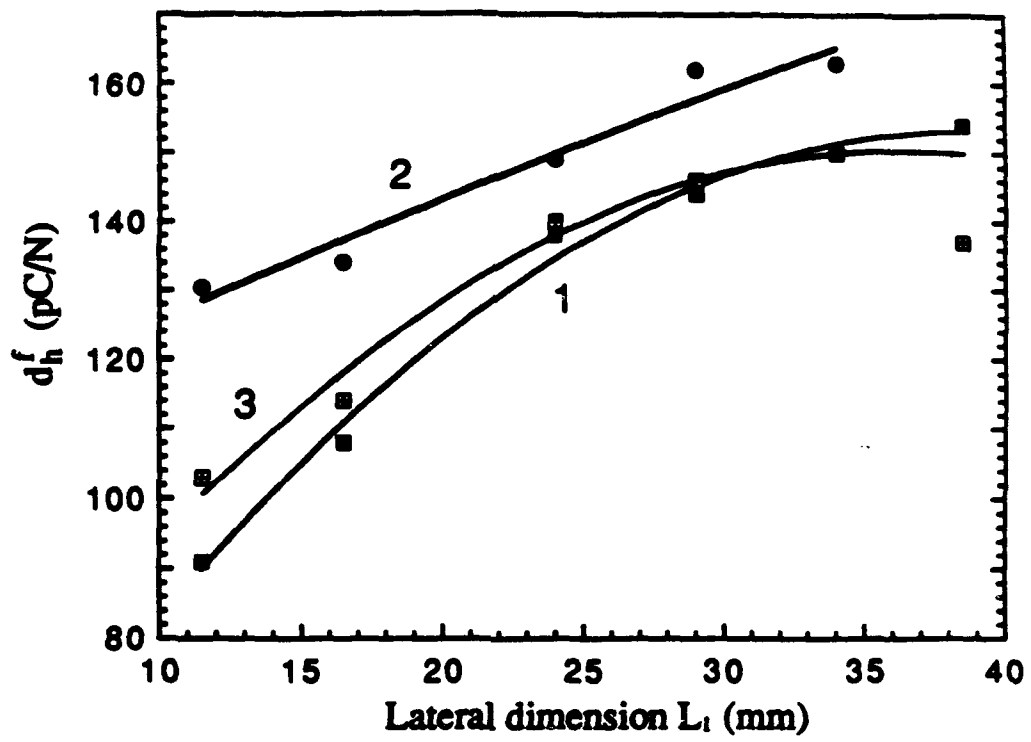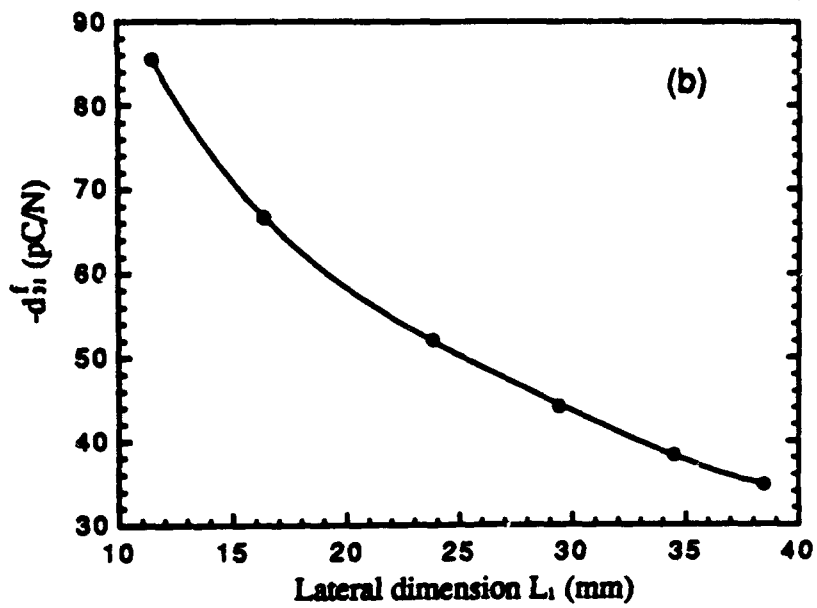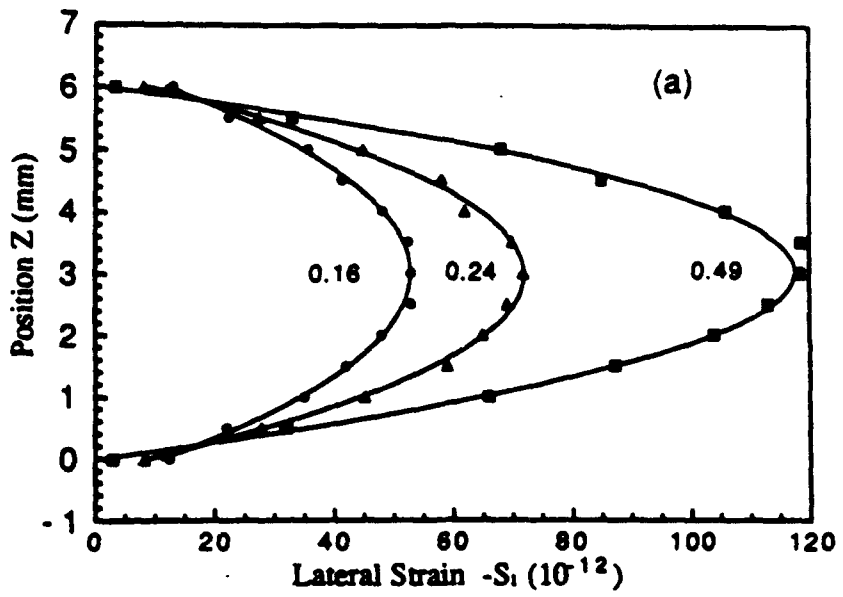
Fig. 3
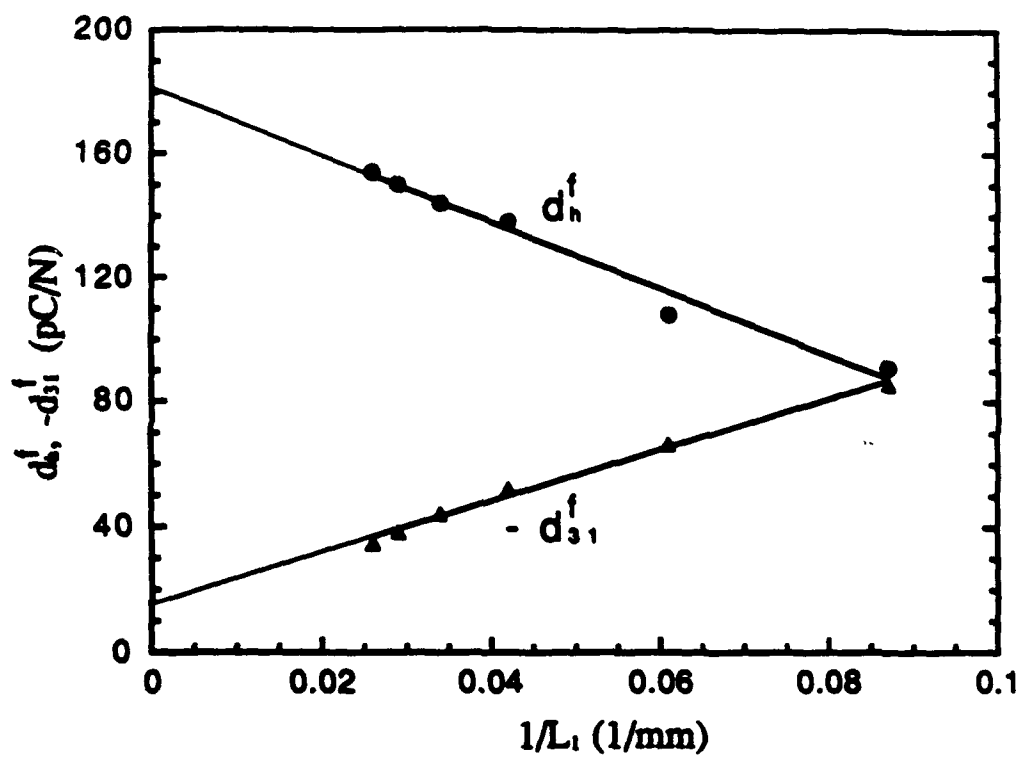
Fig. 4

Fig. 5

Fig. 6

Fig. 7

Fig. 8

Fig. 9